NORTHWESTERN UNIVERSITY

Advancing the Delivery and Therapeutic Potential of Biologics with Spherical Nucleic Acids

A DISSERTATION

SUBMITTED TO THE GRADUATE SCHOOL

IN PARTIAL FULFILLMENT OF THE REQUIREMENTS

for the degree

DOCTOR OF PHILOSOPHY

Field of Chemistry

By

Caroline Danielle Kusmierz

EVANSTON, ILLINOIS

September 2021

ABSTRACT

Advancing the Delivery and Therapeutic Potential of Biologics with Spherical Nucleic Acids

By: Caroline Danielle Kusmierz

The translation of proteins as effective intracellular drug candidates is limited by the challenge of cellular entry and their vulnerability to degradation. To advance their therapeutic potential, cell-impermeable proteins can be readily transformed into protein spherical nucleic acids (ProSNAs) or encapsulated into liposomal spherical nucleic acids (L-SNAs), structures defined by the dense packing of highly oriented DNA into spherical morphologies. Such nanostructures are stable, exhibit enhanced pharmacokinetics, and are routes for transfecting proteins into cells in highly active forms. Furthermore, this modular structure constitutes a plug-and-play platform in which the core and nucleic acid shell can be independently varied to achieve desired properties and function. Small structural changes in the chemical makeup of an SNA's components can affect the entire construct's bioactivity; thus, this thesis investigates the structure-activity relationships of the SNA as it relates to the delivery and biodistribution of biologics.

Chapter 1 introduces design rules identified through the ten years of research in the biological applications of the SNA and how these trends have been applied successfully to gene regulation, immunomodulation, and protein delivery. In the context of ProSNAs, Chapter 2 explores how structural changes to the shell's linker and DNA sequence profoundly impact the overall uptake, activity, and pharmacokinetics of an enzymatic protein. For example, DNA-based linkers and G-quadruplex-forming sequences significantly improve cellular uptake *in vitro*. When translated to murine models, the ProSNA with a DNA-only shell exhibits increased blood

circulation times and retention of their enzymatic activity in tissue. In Chapter 3, by employing aptamers designed to bind receptors abundant along the blood-brain barrier, a ProSNA's biodistribution can be specifically directed to the brain. Alternatively, by encapsulating proteins derived from pathogens into L-SNAs decorated with an immunostimulatory DNA shell, vaccines can be deliberately designed for cancer or infectious diseases. Chapter 4 discusses the utility of L-SNA cancer vaccines for triple-negative breast cancer immunotherapy. In particular, the chemical identity of the constituent lipid and antigen source modulates the L-SNA's properties and immunomodulatory activity, revealing a synergy between the cancer lysate preparation and liposome composition in formulating immunotherapeutic L-SNAs. Beyond oncology, Chapter 5 reports the development of a new SNA platform for infectious disease vaccines. For SARS-CoV-2, inoculation with SNA vaccines generate specific neutralizing antibodies on par with current commercial alternatives. Due to the structural diversity of proteins, each protein presents its own set of opportunities and challenges for various applications. This work illustrates the importance of understanding and manipulating an SNA's structural design to greatly advance the potential of proteins in medicine for years to come.

ACKNOWLEDGEMENTS

I would not have made it to this point without the insight, guidance, and encouragement from an amazing group of friends and colleagues around me. The scientific foundation and life lessons I have developed in graduate school changed me completely. I am a stronger and more confident version of myself, and I attribute these lessons to the relationships I have built over the past six years. First and foremost, I thank my advisor, Professor Chad Mirkin, for the privilege of being a member of a large and diverse group. You gave me the freedom to develop my own scientific interests and provided a diverse and well-resourced environment to achieve my goals. Moreover, you pushed me to have more confidence in my abilities and motivated me to strive for the best. I also thank my committee members, Professor Milan Mrksich, Professor Nathan Gianneschi, and Professor Tom O'Halloran for being available and willing to discuss my progress and provide feedback whenever possible. When I first joined the lab, Dr. Anthony Sprangers was my incredible mentor. He came to me when I had no clear direction for a project and taught me all the biological techniques that would later be the foundation of my research. I owe an enormous debt of gratitude to my mentors-turned best friends: Professor Katherine Bujold, Professor Cassandra Callmann, and Professor Devleena Samanta. Katherine, you were always a positive light to me when I was unsure of myself and my project. You are my cheerleader and encouraged me to think positively and that everything will work out in the end. Cassi, you pushed me to take risks and try new things. Your charisma and authenticity are qualities I will always admire and strive to achieve. Devleena, in addition to being a great laugh and friend, your valuable scientific insight always kept me thinking about ways to improve my projects. Whenever you complimented my data or presentation, I always felt validated because I knew your positive feedback was genuine. Going to work surrounded by fun, motivated and inspiring young scientists made my graduate experience much more enjoyable: Dr. Sasha Ebrahimi, Dr. Michelle Teplensky, Max

Distler, Matt Vasher, Jasper Dittmar, EunBi Oh, Dr. Ben Partridge, Wuliang Zhang, Jungsoo Park, John Cavaliere, Oliver Hayes, Cindy Zheng, Dr. Kacper Skakuj, Dr. Janet McMillan, and Dr. Gokay Yamankurt. Many thanks to the support staff who were entirely devoted to helping me and my fellow colleagues succeed: Dr. Tanushri Sengupta, Dr. Sara Rupich, Dr. Caroline Ko, Pam Watson, Elizabeth Forest, and Dr. Sarah Hurst. In addition to my scientific family, I thank my family and friends back home. My in-laws, Bill and Debra, you are the most encouraging and caring people I know, and your reassurance kept me going. My best friend Courtney, you were always a phone call away and someone I could always rely on. My sister Reneé, you celebrated my achievements and made me feel proud of myself. My cousin Karen, your stories from back home always gave me a smile, and your successes motived me to pursue the path I am on now. My dad (Tata), you were the person who instilled my love for science and always pushed me to work to my capabilities. My mom, you are my guardian angel and gave me the strength I didn't know was in me. My husband Nick, you are my best friend and I would not have been able to do this without you. You are always there for me, and I look forward to what the future will offer us.

LIST OF ABBREVIATIONS

Angiotensin-Converting Enzyme 2	ACE2
Alexa Fluor 647	AF647
Antigen-Presenting Cell	APC
Antisense Oligonucleotides	ASO
Blood-Brain Barrier	BBB
Beta-Galactosidase	β-Gal
Bio-Layer Interferometry	BLI
Bone Marrow-Derived Dendritic Cell	BMDC
Chimeric-Antigen Receptor T Cell	CAR-T
Circular Dichroism	CD
Central Nervous System	CNT
Unmethylated Cytosine Linked To Guanine	CpG
Cell-Penetrating Peptide	CPP
Cryogenic Transmission Electron Microscopy	cryo-TEM
Cerebral Spinal Fluid	CSF
Dna-Grafted Block Copolymer	DBC
Dendritic Cell	DC
Dynamic Light Scattering	DLS
1,2-Dimyristoyl- Phosphatidylcholine	DMPC
1,2-Dioleylphosphatidylcholine	DOPC
1,2-Dipalmitoylphosphatidylcholine	DPPC
1,2-Distearoyl- Phosphatidylcholine	DSPC
Extracellular Domain	ECD

Enhanced Permeability And Retention	EPR
Enzyme Replacement Therapy	ERT
Fetal Bovine Serum	FBS
Förster Resonance Energy Transfer	FRET
Glioblastoma Multiforme	GBM
Glucocerebrosidase	GCase
G-Quadruplexes	GQ
Hexaethylene Glycol	HEG
Human Epidermal Growth Factor Receptor 2	HER2
Hypochlorous Acid	HOCl
Human Peripheral Blood Mononuclear Cells	hPBMC
Inductively Coupled Plasma Mass Spectroscopy	ICP-MS
Immunofluorescent Histochemistry	IFC
Intrathecal	IT
Dissociation Constant	Kd
Lysosomal Storage Disorder	LSD
Liposomal-Sna	L-SNA
Matrix-Assisted Laser Desorption/Ionization Mass Spectroscopy	MALDI-MS
Myeloid Derived Suppressor Cell	MDSC
Major Histocompatibility Complex I	MHC-I
Microrna	miRNA
Mammary Tumor Virus-Polyoma Middle Tumor Antigen	MMTV-PyMT
No-Observed-Adverse-Event Level	NOAEL
Nanoparticle	NP
Ortho-Nitrophenyl-β-Galactoside	ONPG

Ovalbumin	OVA
Pathogen-Associated Molecular Pattern	PAMP
Phosphate Buffer Saline	PBS
Polyethylene-Glycol	PEG
Paraformaldehyde	PFA
Phosphodiester	PO
Polyinosinic Acid	Poly-I
Protein Spherical Nucleic Acid	ProSNA
Phosphorothioate	PS
Receptor-Binding Domain	RBD
Spike	S
Subarachnoid Space	SAS
Scrambled	Scr
Sodium Dodecyl Sulfate Polyacrylamide Gel Electrophoresis	SDS PAGE
Small Interfering Rna	siRNA
Spherical Nucleic Acid	SNA
Spacer 18	Sp18
Scavenger Receptor Type A	SR-A
Tumor-Associated Antigen	TAA
Phase Transition Temperature	TC
Transferrin	TfR
Toll-Like Receptor	TLR
Tumor Microenviroment	TME
Triple-Negative Breast Cancer	TNBC

DEDICATION

To my mom, Corina Quiroga Da Silva.

Thinking of you always kept me going.

TABLE OF CONTENTS

LIST OF FIGURES

LIST OF TABLES

CHAPTER 1. INTRODUCTION

Nanotechnology holds significant promise in improving disease diagnosis and treatment by rectifying limitations once found with small molecule drugs. By integrating biologics and oligonucleotides into nanoparticle formulations, we can increase specificity to disease targets and precisely tailor formulations for patient-specific treatments. Nanoparticles (NPs) can be engineered to include an assortment of customizable handles such as size, electrostatic charge, stimuli responsiveness, and targeting moieties that can be optimized for a specific application. However, effective intracellular drug delivery and biodistribution remain a challenge as NPs face many physical and biological barriers—such as cell membranes, enzymatic degradation, and rapid clearance—limiting the fraction of administered NPs to reach the target therapeutic site. Advances in nanomedicine that could facilitate the clinical translation of nanoparticles focus on leveraging chemical and material engineering innovations to overcome such barriers. One such innovation is the Spherical Nucleic Acids (SNA), a new and unnatural form of DNA. SNAs consist of a nanoparticle core densely functionalized with radially orientated oligonucleotide strands. In this privileged structure, the SNA interacts with living systems differently from its linear counterpart resulting in rapid and significant cellular uptake without the need for transfection agents. The biological properties of the SNA derive from the multivalency of the oligonucleotide shell and are core-independent. Thus, they have expanded to encompass many types of NPs—polymer, inorganic, liposomal, protein—and applied to various therapeutic applications. This introduction will discuss design rules identified through the ten years of research in the biological applications of the SNA and how these trends have been applied successfully to gene regulation, immunomodulation, and protein delivery.

1.1. Properties of Spherical Nucleic Acids

1.1.1. Scavenger Receptor-A Mediates Cellular Uptake.

For any downstream biological application, the first barrier encountered by the SNA is the cellular membrane. This natural enclosure protects and regulates the cell from the invasion of any foreign material, so by their very nature, linear oligonucleotides cannot transverse this membrane alone. In a pivotal 2006 Science paper[4], the Mirkin Group realized an unexpected property of SNAs: the reorganization of DNA into a dense, radial arrangement centered around an NP core promotes strong binding affinity to membrane receptors triggering endocytosis. This breakthrough opened the doors for new therapeutic applications of the SNA and the intracellular delivery of sensitive cargo, particularly oligonucleotides. In a 2010 mechanistic study on the uptake of SNAs using pharmacological inhibitors[5], Patel et al. identified the predominant uptake mechanism. Both polyinosinic acid (Poly-I) and fucoidan—well-known ligands for scavenger receptors—reduced the uptake of gold-core SNAs as measured by inductively coupled plasma mass spectroscopy (ICP-MS). A more detailed study in 2013 expounded more on the mechanism, attributing SNA

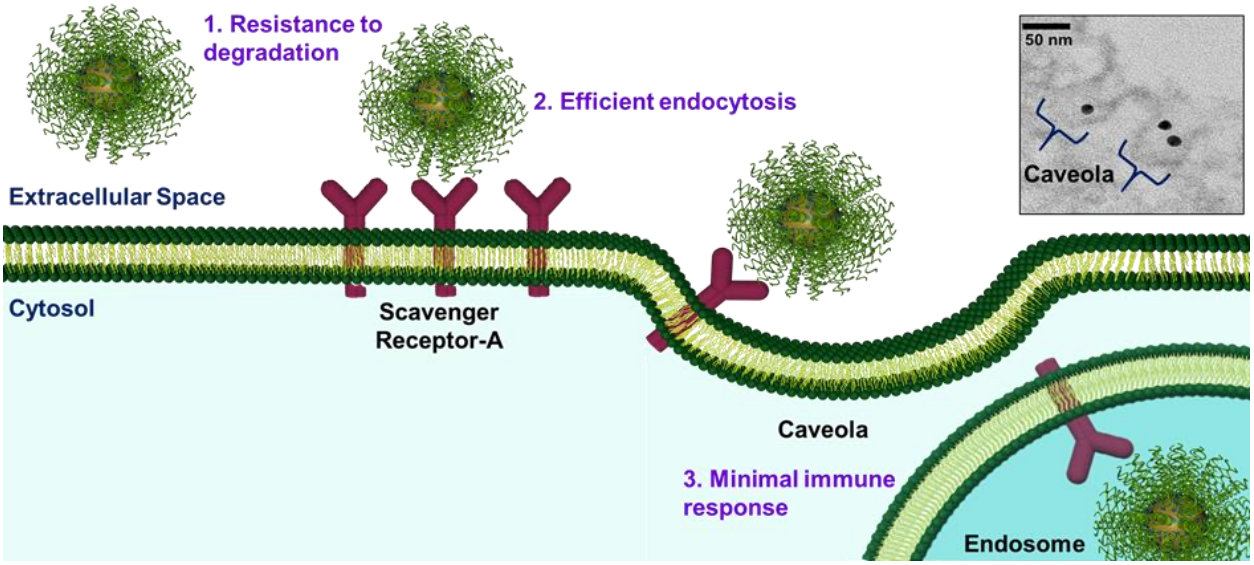

Figure 1. Mechanism of endocytosis of spherical nucleic acids (SNAs). SNAs engage with scavenger receptor-A resulting in rapid caveolae mediated endocytosis. Oligonucleotides that are densely conjugated to a nanoparticle core are more resistant to degradation, when compared to free, linear strands. Furthermore, there is minimal immune response once SNAs are endocytosed.

uptake to a lipid-raft-dependent and caveolae-mediated pathway principally driven by Scavenger Receptor Type A (SR-A).[6] By knocking down the receptor's expression, ICP-MS revealed an 80% decrease in uptake of SNAs. They also demonstrated a positive correlation between SR-A expression and the degree of endocytosis of SNAs in different cell types (A549, 3T3, C166, HaCaT). This receptor plays the predominant uptake role for SNAs composed of various cores, including inorganic[7], proteins[8], liposomes[9], and hollow, core-less[10] SNAs. For the liposomal-SNA (L-SNA), fucoidan inhibition studies validate the importance of SR-A on mediating cellular uptake regardless of DNA attachment chemistry (i.e., cholesterol, tocopherol, lipid-conjugated)[11-13]. Beyond the ability of SNAs to actively enter many cell types, the internationalization of the SNA is fast, where significant uptake is quantified after just 30 minutes[6]. Furthermore, the constructs are predominantly trafficked through an endosomal pathway[14]. In architectures, where the SNA comprises multiple components (i.e., encapsulated cargo, multi-sequence DNA shell), the individual components are trafficked together and colocalize regardless of identity.[15-17]

1.1.2. The Correlation Between SNA Loading Density and Cellular Uptake.

Following the introduction of the SNA in 1996, some early research was devoted to optimizing DNA loading density to increase hybridization events with complementary strands.[18] Early designs used a thymidine DNA spacer to distance the strands further from the NP's surface, increasing DNA coverage. Moreover, synthetic methods such as salt-aging and sonication were introduced to screen charge repulsions between neighboring oligonucleotide strands and the gold surface. In its final iteration, Hurst and Lytton-Jean et al. devised a polyethylene-glycol (PEG) spacer to further increase the DNA shell packing density on a gold NP[2]. Concurrently with the development of these DNA loading strategies, **t**he first and perhaps most crucial biological trend was elucidated: high oligonucleotide density—irrespective of core—increases cellular uptake**.** Giljohann et al. first uncovered this hallmark property when quantifying the uptake of gold SNAs

with increasing DNA density and discovered a correlation between high oligonucleotide loading and cellular uptake.[1]

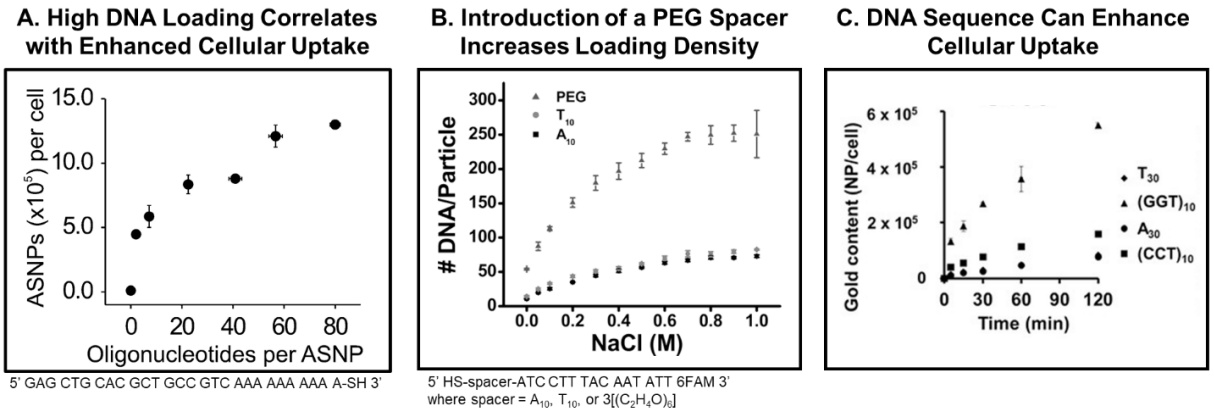

Figure 2. SNA Cellular Uptake Trends. A) Cellular uptake is dependent on the density of the oligonucleotides loading on the surface of the nanoparticle, where higher densities lead to greater uptake.[1] B) A lack of repulsions between neighboring strands with PEG linkers and the decrease interaction between the PEG and the gold surface allows for higher loading densities of DNA on gold NPs.[2] C) SNAs composed of G-quadruplex DNA shells show the highest uptake with C166 cells, when compared to SNAs with other nucleobases.[3]

As the SNA evolved to introduce more biocompatible cores—such as the liposome, polymer, and protein—the Mirkin Group devised different attachment chemistries to facilitate higher loading densities. For example, by anchoring DNA to the liposome head group rather than an intercalating hydrophobic tail (cholesterol), Meckes and Banga et al. demonstrated a significantly higher DNA loading density for lipid-tailed L-SNAs compared to the cholesterol-tail analogs.[11] This adjustment correlated to an enhancement in cellular uptake for the lipid-tail L-SNAs in U87-MG cells and RAW-Blue macrophages. Moreover, in the generation of DNA-grafted block copolymer (DBC) micelle-SNAs, Zhang, Hao, and Calabrese et al. synthesized two different structures where the DNA was either grafted to the monomer as an end group (linear) or as a brush.[19] Both DBC micelle-SNAs had similar hydrodynamic diameters (~40 nm) but vastly different loading densities 190 strands or 302 strands, respectively. These different loading densities correlated to a difference in cellular uptake efficiency in HeLa cells. Likewise, when the number of DNA is much lower, as with molecularly-pure SNAs, there continues to be a correlation between uptake and

the number of strands. For example, Li and Zhang et al. synthesized SNAs using single-molecule building blocks, which can accommodate 8 strands for the POSS-SNA or 12 strands for the C_{60}-SNA.[20] By both confocal microscopy and flow cytometry, the C_{60}-based conjugates were taken up two times faster and more effectively than the POSS-SNA, just by increasing the number of DNA by 4 strands.

1.1.3. G-Quadruplex Sequences Increase Cellular Uptake.

In the 2010 paper, which elucidated the mechanism of SNA uptake, Patel et al. performed an inhibition cellular uptake assay with telomere-like DNA.[5] These strands are guanine (G)-rich sequences that can self-assemble into specialty secondary structures called G-quadruplexes (GQs), characterized by the formation of G-quartets nucleated by physiologically relevant cations (e.g., K+). The resulting central cavity—composed of guanine bases—contracts the negatively charged phosphate backbone culminating in a more polyanionic ligand. Pretreatment with these sequences inhibited nanoparticle entry due to their natural affinity for the Scavenger Receptor-A. Many hypothesize that the highly negative nature of these sequences enhances their affinity to the lysine-rich region of the collagenase domain in the receptor.[21, 22] Considering that GQs have a natural affinity towards the receptor, Chinen et al. first assembled G-rich sequences into an SNA to assess whether these oligonucleotides can fold appropriately after being densely functionalized onto a nanoparticle core.[23] They demonstrated that the GQ structure remains intact and stabilized when formulated as an SNA using circular dichroism (CD) spectroscopy. By treating cells with GQ-SNAs, Narayan et al. found significantly higher uptake with these G-rich SNAs when compared to control SNAs (thymidine-rich, cytosine-rich, adenine-rich), and this enhancement in uptake is solely dependent on GQ folding.[3] Upon shortening the G-rich motif, the resulting G-quadruplex structure and any corresponding increase in cellular uptake were lost. When tested in mouse models, GQ-SNAs demonstrate a preference for macrophage-rich cells and tissues,

specifically those who express an abundance of scavenger receptors. For example, GQ-gold SNAs exhibit enhanced internalization in the liver and spleen when compared to their T-rich counterparts.[24] Furthermore, many studies show that marginal zone macrophages act in immune surveillance and are excellently position to capture blood-borne pathogens and regulate the subsequent adaptive immune response. Guan et al. provided downstream evidence for the affinity of G-rich SNA to these macrophages. They showed that GQ-gold SNAs could induce a temporary cytokine release when injected intravenously, providing further evidence on the sequence-specific affinity of G-rich SNAs to macrophages.[25]

1.2. Therapeutic Applications of Spherical Nucleic Acids

1.2.1. Gene Regulation and the Importance of Oligonucleotide Stability.

In the first therapeutically relevant application of the SNA, Rosi, et al. densely conjugated antisense oligonucleotides (ASO) onto a gold nanoparticle to showcase its potential for gene regulation.[26] Subsequently, microRNA (miRNA)[27], small interfering RNA (siRNA)[28], and ribozymes[29] have been formulated into SNAs to regulate protein expression in cells. The SNA's therapeutic efficacy has been illustrated *in vivo*, exemplified by the ability of SNAs to regulate Bcl2L12 mRNA in glioblastoma multiforme (GBM)[30] or EGFR overexpression in many skin malignancies[31]. In 2021, a phase 0 human clinical trial determined the safety, pharmacokinetics, and activity of siRNA-gold SNAs specific to the GBM oncogene Bcl2L12[32]. In this trial, patients with GBM were systemically administered a 1/50 of the no-observed-adverse-event level (NOAEL) dose determined in cynomolgus monkeys. Analysis of resected GBM tissue demonstrated that intravenously administered gold SNAs distributed throughout the tumor, and uptake into glioma cells correlated with a reduction in tumor-associated Bcl2L12 protein expression. Future clinical testing will assess the dose-dependence of gene knockdown and the efficacy of SNAs in prolonging patient survival in combination with standard therapies.

When employing SNAs for gene regulation, the delivery of intact oligonucleotides to the cytoplasm is of utmost importance. In this regard, there are multiple examples where the oligonucleotides, when immobilized on the nanoparticle surface, have increased serum stability (2-6 times increase in half-life depending on the specific design parameters).[33] This enhanced stability has been attributed both to lack of accessibility for serum nucleases due to increased steric hindrance and—in the specific case of DNase I—enhanced local ion concentration around the oligonucleotide shell.[34, 35] Still, in the presence of biological milieu, non-specific degradation continues to take place. As was visualized in TEM micrographs of cells treated with gold SNAs by Wu et al., as nucleases degrade the DNA shell within the endosome, the gold NPs are no longer stabilized and aggregate.[14] They determined that the aggregation is due to DNA degradation by DNases rather than pH effects or thiol displacement of the strands. With this in mind, unnatural modifications can be made to the shell to prevent non-specific degradation and improve gene regulation. These adjustments were first implemented by Seferos et al. by the introduction of locked nucleotides, where they showed a 20% improvement in knockdown efficiency of the survivin gene.[36] Sprangers et al. further illustrated the idea of stabilizing the oligonucleotide by replacing the phosphodiester (PO) DNA backbone with a phosphorothioate (PS) linkage that is more resistant to nucleases.[37] As a result, they exhibited higher nuclear localization and knockdown efficiency of long nontargeting RNA Malat1.

In the case of siRNA-SNAs, Barnaby et al. found that the RNase A can access duplex cut sites near the NP surface.[38] They demonstrated that by situating these cut sites further from the NP surface, with the introduction of a linker region, they could extend the half-life of siRNA duplexes in serum. Furthermore, as evidenced previously with ASO, when designer oligonucleotides replace these cut sites, the serum half-life of the siRNA duplex improves ten-fold. At first glance, it is seemingly detrimental for proteins to access sequences close to the NP core; however, Yamankurt et al. determined that Dicer must cleave the siRNA duplex from the

NP in the first step of the RNAi pathway.[39] Using this information, Yamankurt et al. introduced the doubly thiolated SNA, where both sense and antisense are conjugated to the gold NP, rather than relying solely on base-pair hybridization to deliver the antisense strand. This modification increases the duplex density, subsequently increasing the dosage of the therapeutically relevant components. Therefore, when designing SNAs for gene regulation, it is prudent to acknowledge that proteins will have access to the oligonucleotides throughout the shell. Therefore, it is essential to determine any non-specific cleavage products—which will be different for each sequence—and introduce specialty modifications at those sites. In addition to introducing stability to the shell to prevent non-specific degradation, the SNA core can be formulated to have a potential release mechanism for delivering oligonucleotides into the cytosol following cell entry. By utilizing biodegradable polymer cores that can dissociate at a lower pH or using positively charged guanidinium DNA backbone[40] to destabilize the endosome, we can increase the probability of intact nucleotide cargo reaching the cytosol.

1.2.2. Cancer Immunotherapy and the Rational Design of SNA Cancer Vaccines

In 2009, Dhar et al. first noted that SNAs—upon internalization—predominantly reside within vesicles.[41] Wu et al. later elucidated the intracellular fate of the SNA, after extensive colocalization experiments, and established that they are predominantly trafficked through the endocytic pathway.[14] This new revelation introduced a new opportunity to design the next generation of SNAs that take full advantage of their location inside endosomes and to modulate the immune system via toll-like receptors (TLRs) that reside there. The immune system is sensitive to molecular patterns commonly associated with infection or damaged cells. TLRs are a class of proteins that detect a variety of these cues to initiate an immune response. For example, TLR-9 recognizes and initiates a response to the DNA sequence CpG (unmethylated cytosine linked to guanine), which is abundant in microbial DNA. Chemical conjugation of antigens

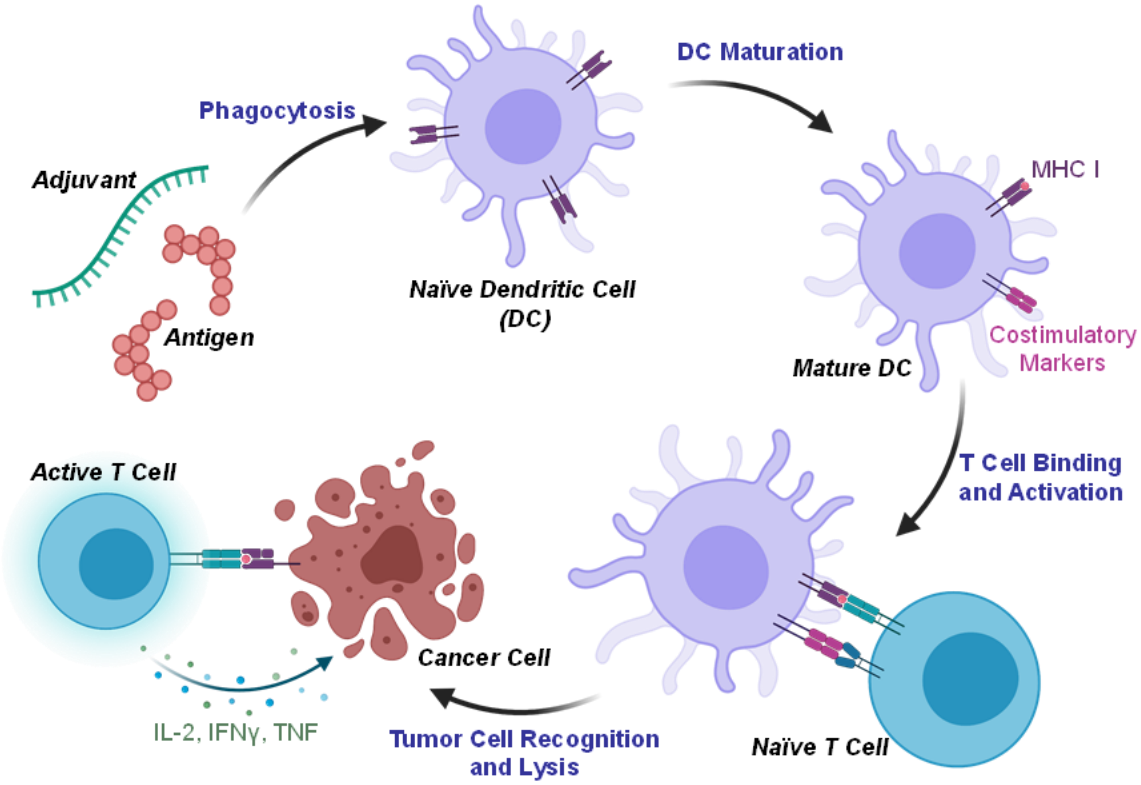

Figure 3. Cancer vaccine cycle. This cycle can be divided into four major steps, starting with the co-delivery of tumor-associated antigens and CpG adjuvants to dendritic cells (DCs). T cells recognize peptides presented by MHC I, are activated, and then trafficked to the tumor. When the T cell recognizes its antigen and becomes activated, it kills malignant cells through the secretion of cytokines.

(peptides or polysaccharides that direct the immune response against the desired target) to CpG DNA can result in a powerful and directed immune response. This immune response is exploited in cancer immunotherapy, which relies on the cell-mediated cytotoxic response to recognize and eliminate tumor cells that have undergone genetic modifications.[42, 43] Several research groups have demonstrated that tumor immunity can be enhanced by providing signals necessary to activate CD8+ T cells.[44, 45] This is realized by first training dendritic cells (DCs) to mature through the endocytosis of adjuvant and antigen. These matured DCs present three signals to CD8+ T cells: 1) surface antigens on a major histocompatibility complex I (MHC-I) protein;[46] 2) costimulatory membrane proteins (e.g., CD28, CD80, CD86, and CD40);[47] and 3) secrete

activating cytokines (e.g., interleukins and interferons). T cells that bear T cell receptors that match the antigen-MHC-I complex on the DC surface will engage with the mature DC and become primed. Primed T cells divide rapidly, resulting in multiple clones that can recognize and induce apoptosis in any cell that displays the same antigen-MHC-I complex.

Radovic-Moreno first realized this potential for cancer immunotherapy by formulating gold SNAs composed of immunomodulatory nucleic acids, which can agonize or antagonize toll-like receptors.[12] In a landmark 2015 publication, they established that SNAs—synthesized from either gold or liposomal cores—could be functionalized with CpG sequences, which can activate DCs. This activation can be further directed by the inclusion of an antigenic peptide sequence such as ovalbumin (OVA). By conjugating an antigenic peptide to the end of a complementary sequence that can hybridize to the external CpG shell, they demonstrated a profound and durable tumor growth remission in an E.G7-OVA lymphoma synergetic flank model. Since then, subsequent studies have delineated the design parameters, which, when tuned, can have a profound impact on the potency and specificity of cancer immunotherapy SNAs. Chemistry such as oligonucleotide sequence, DNA anchoring group, antigen linker chemistry, and SNA structure can be rationally altered to raise antitumor responses.

In its simplest form, SNAs induce higher immune activation than their unmodified linear counterparts. This improvement is attributed to the privileged structure of the SNA, which promotes cellular uptake and facilitates high co-delivery of both adjuvant and antigen to DCs. Immune activity can be further improved by increasing the oligonucleotides' serum stability. First, by replacing the naturally occurring phosphodiester (PO) with a more synthetic phosphorothioate (PS) analog, there is an increase in immune activity due to enhanced nuclease resistance.[48] In the same vein, we can boost immune activity by stabilizing the association of the DNA to the liposome core. Typically, SNA cancer vaccines are designed using LSNAs, which are dynamic systems that can readily dissociate in biological milieu. Therefore, to increase LSNA stability and

consequently immune activation, Meckes et al. increased DNA association by changing the hydrophobicity of the DNA anchor.[11] In a 2018 paper, Meckes illustrated that LSNAs formulated with lipid-conjugated DNA strands (more hydrophobic anchor) have a >20-fold extended half-life compared to cholesterol-tail analogs (less hydrophobic anchor) in 10% serum. Accordingly, with the more stable LSNAs, they confirmed an enhancement in cellular uptake and co-delivery of liposomes and DNA. Furthermore, the lipid-tail LSNAs also exhibit a modest increase in immune activation at lower concentrations and a significantly faster activation of RAW-Blue macrophages, presumably a consequence of more rapid uptake by cells.

In addition to the importance of DNA stability, another relevant parameter is the conjugation chemistry and location of the peptide antigen. Skakuj et al. studied the impact of different linkers (cleavable vs. non-cleavable), which conjugate an antigenic peptide (gp100) to DNA on LSNAs.[49] By comparing the CD8+ T-cell proliferation following incubation of splenocytes with L-SNAs, they show that a cleavable linker—particularly the traceless version—leads to better T-cell proliferation and subsequent higher cytokine release. Wang et al. then compared three SNA architectures, which varied in the position of the peptide antigen.[16] They tested the immunoactivities of SNAs consisting of the same constituents (CpG and antigen) but varied in the location of the antigen. The three architectures tested were: 1) encapsulating the antigen within the liposome (encapsulation model; SNA-E); 2) anchoring the antigen to a cholesterol liposomal intercalation moiety (anchor model; SNA-A); or 3) conjugating the antigen to a complementary DNA strand which can hybridize to the CpG adjuvant sequence (hybridization model; SNA-H). After evaluating the co-delivery efficiency of these design architectures, the hybridization model demonstrated the best co-delivery of both the CpG and antigen and the most significant retention in the endocytic pathway and endoplasmic reticulum over a 24-h period. Due to a combination of two factors in the hybridization model: 1) slower kinetics and processing of antigen and adjuvant 2) and better co-delivery, the antigen presentation fortuitously overlaps with the timing for the

expression of the costimulatory marker CD86. When tested *in vivo*, the hybridization model resulted in more secretion of proinflammatory cytokines (IL-12p70, IL-1α, IL-6, TNF-α) and antigen-specific T cells. When used to treat tumor-bearing mice, treatment with SNA-H led to tumor regression and survival of 100% of the animals in the group through 60 days. Furthermore, when these mice were reinoculated with new cancerous cells, a tumor did not grow, demonstrating the immunological memory generated by treatment with SNAs. Finally, they showed that a prophylactic vaccine with SNA-H led to the best outcomes, resulting in a 15-day delay in tumor initiation.

During these investigations it is apparent that the high co-delivery of both adjuvant and antigen to the same immune cell is of prime importance when designing SNAs for cancer vaccines. By strengthening the attachment of the DNA shell to the liposome core or increasing the likelihood for co-delivery through antigen/adjuvant hybridization, we can increase the immune response from SNAs. Therefore, future development should focus on further stabilizing these constructs to increase uptake and enhance co-delivery of components *in vivo*.

1.3. Introduction of Thesis Topics

This thesis explores the structure-function relationships of SNAs in the context of the delivery of biologics. Biologics are drug products semi-synthesized in a living system and consist of proteins, oligonucleotides, sugars, or a combination thereof. The application of biologics in therapeutics is far outpacing the development of small molecule drugs due to their high specificity and complexity of functions not easily realized by synthetic molecules.[50] Currently, there are three main strategies for using protein therapeutics: 1) replace a protein that is deficient or abnormal through enzyme replacement therapy; 2) protect against a deleterious foreign agent such as a virus or cancer with vaccines; or 3) block, stimulate, or tag a target such a receptor or molecule with monoclonal antibodies.[51] Presently, I will explore how the valuable biological properties of

the SNA can be adapted to fit these first two methods (enzyme replacement therapy and vaccines).

1.3.1. Delivering Deficient Proteins Through Enzyme Replacement Therapy

Many disorders stem from a deficiency of enzymes and, therefore, an accumulation of abnormal metabolic products. Commonly the best course of action is to replace the deficient enzyme with a recombinant protein, typically produced in large quantities using a bacterial expression system such as *E. coli*.[52] The first example of enzyme replacement therapy (ERT) was the utilization of insulin to treat diabetes, first approved by the US FDA in 1982. In the ensuing 40 years, the FDA has seen a remarkable expansion in the number of therapeutic applications of proteins. More than 239 proteins and peptides have been approved for clinical use by the FDA, with many more in development. Although there have been many successes in ERT, poor protein stability and distribution are major challenges in developing efficient and cost-effective therapeutics. The cellular uptake of functional proteins is impeded by their inherent instability, large sizes, and charged surfaces. Additionally, their half-life is considerably affected by degrading proteases and fast clearance rates. Researchers have developed conjugation strategies to facilitate intracellular delivery and extend blood circulation of proteins to address these limitations.

Strategies include, but are not limited to, conjugation of cell-penetrating peptides (CPPs), polymer coatings such as polyethylene glycol (PEG), or physical encapsulation in nanocarriers.[53] CPPs are short cationic peptide sequences, high in lysine and arginine residues, which can permeabilize membranes to deliver various cargos; however, their poor cell selectivity and toxicity limit their clinical use.[54] The most common strategy is functionalizing proteins with polymers such as PEG, reducing clearance and inhibiting degradation upon systemic delivery. However, there have been instances that result in a non-specific immune reaction to PEG and this strategy does

not facilitate cellular uptake.[55] Finally, proteins can be encapsulated in nanocarriers such as liposomes or polymeric micelles, which may suffer from low encapsulation yield and high polydispersity, leading to difficulties in quality control and mass production.[56]

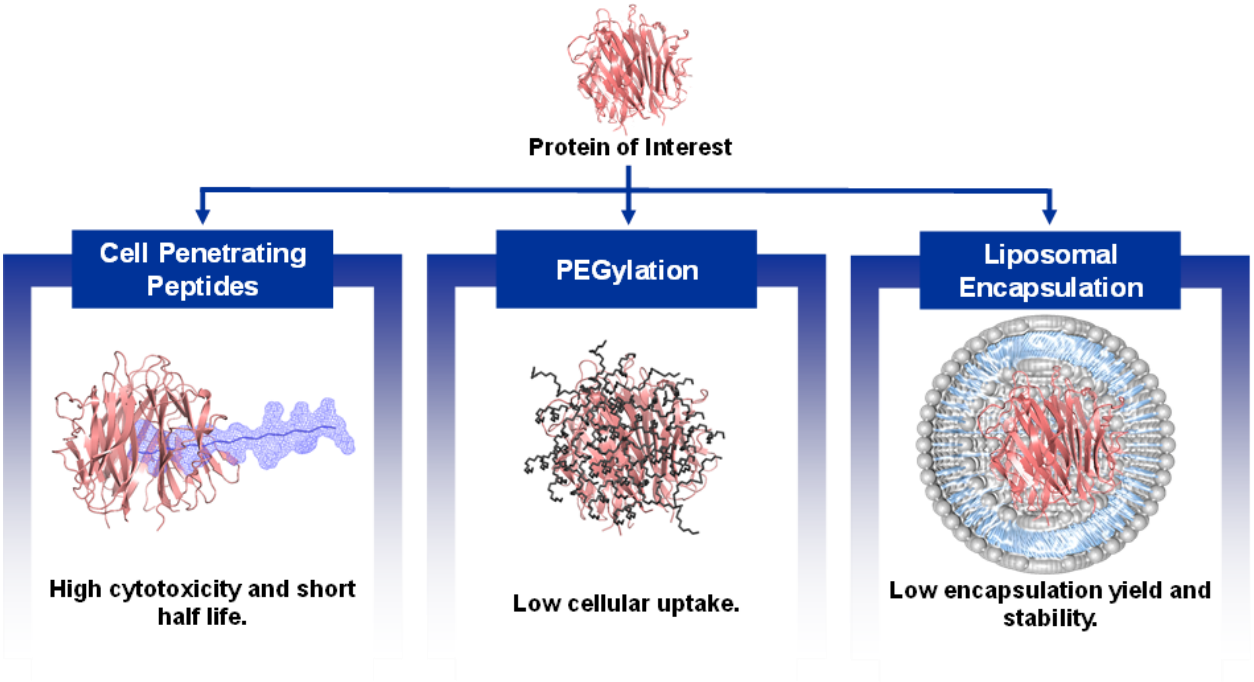

Figure 4. Systematic of different protein delivery strategies. A) Conjugation of short cationic cell penetrations peptides to proteins facilitates cellular uptake at the risk of high cytotoxicity. B) PEGylation is the process of conjugating long polymer chains to the surface of proteins to prolong their blood circulation time and mask degradation. C) Encapsulation of proteins within nanocarrier systems, such as liposomes, may facilitate endocytosis through targeting ligands or charged phospholipid headgroups.

To address these limitations, the Mirkin group has developed a chemical strategy for transforming cell membrane-impermeable proteins into Protein Spherical Nucleic Acids (ProSNAs) that can enter cells at low concentrations. In the original communication, Brodin *et al*. reported a strategy for chemically modifying surface accessible lysine residues on the hydrolytic enzyme β-Galactosidase (β-Gal) with DNA, facilitating cellular uptake of the protein in cells with no disruption to the enzyme's activity.[8]

1.3.1.1. Defining The Design Parameters for In Vivo Enzyme Delivery Through Protein Spherical Nucleic Acids (Chapter 2)

I sought to explore the DNA shell design parameters of ProSNAs and how structural changes to the DNA ligands can profoundly impact the SNA's biological properties. I found that in terms of attachment chemistry, DNA-based linkers promote a 7-fold increase in cellular uptake while maintaining enzymatic activity *in vitro* compared to originally used hexaethylene glycol (HEG, Spacer18) linkers. Additionally, the employment of G-quadruplex (GQ)-forming sequences increases cellular uptake *in vitro* up to 4-fold. I applied these SNA design rules to the lysosomal enzyme glucocerebrosidase (GCase) and demonstrated over a 25-fold increase in cellular delivery after a 30 min treatment in a microglial brain cell line. When translating to murine models, the β-Gal ProSNA with a DNA-only shell exhibits increased blood circulation times and higher accumulation in major organs, including lung, kidney, and spleen. Importantly, β-Gal ProSNAs with an all-oligonucleotide shell retain their enzymatic activity in tissue, whereas the native protein loses all function. Taken together, these results highlight the value of structural design in guiding ProSNA biological fate and activity and represent a significant step forward in the development of intracellular protein-based therapeutics.

1.3.1.2. Strategies to Increase Brain Delivery of Protein Spherical Nucleic Acids (Chapter 3)

When studying the pharmacokinetic profile of ProSNAs in a mouse model, I saw a profound increase in the distribution of β-Gal ProSNAs to all major organs (lung, heart, spleen, kidney, liver) except the brain. The brain is a hard-to-access organ following systemic injection due to the seemingly impenetrable barrier delineating the blood and the brain known as the blood-brain barrier (BBB). For GBM treatment, gold siRNA-SNAs were shown to bypass this barrier and accumulate in tumors for gene regulation; however, there was a 500-fold decrease in gold NP brain distribution in tumor-free mice.[30] This is likely due to a compromised BBB and enhanced

permeability and retention (EPR) effect due to the fast-growing GBM tumor. Therefore, there lacks a consistent strategy to deliver SNAs to brains with intact BBBs.

The BBB is formed by tight junctions between capillary endothelial cells which protects the brain from exogenous materials in the bloodstream. Lipid-soluble molecules such as CO_2, O_2, and H_2O freely cross the barrier, and larger substances are transported by active carriers such as transferrin and glucose. As such, I posited whether these transporter receptors could be hijacked to facilitate transcytosis of ProSNAs across the BBB. The transferrin receptor is highly abundant in endothelial cells lining the BBB and mediates the transport of iron into the brain through a carrier protein transferrin.[57, 58] Since 2008, a series of publications have evolved and truncated aptamers with high-affinity binding to the mouse transferrin receptor.[59-61] An aptamer is an oligonucleotide or peptide sequence that can bind to a target molecule or receptor when folded into a specialty secondary structure. By synthesizing ProSNAs with a transferrin-aptamer shell, I increased brain targeting by 3-fold and facilitated transcytosis into the brain of a large protein, β-Gal, that would typically be excluded from the central nervous system due to its large molecular size.

In addition to receptor-mediated transcytosis, I also explored noninvasive (intranasal) and invasive (intrathecal) administration pathways to increase brain delivery. The intranasal route has emerged as a promising approach to deliver nanoparticles to the brain. The drug evades liver elimination and has greater access to the central nervous system through the olfactory region in the nasal cavity. However, when administrating ProSNA intranasally, the SNAs became stuck in the nasal mucus layer, precluding brain delivery. As a more direct (yet invasive) route, I directly injected ProSNAs in the cerebral spinal fluid (CSF) via intrathecal injection. CSF flows in the subarachnoid space (SAS), which surrounds the brain and spinal cord. I hypothesized that by intrathecally injecting the ProSNA into the CSF, the protein would distribute through the SAS, bypassing the BBB and improving access to the brain. To test this, I administered ProSNAs to

healthy mice via direct injection into the spine. Based on *in vivo* fluorescence measurements taken over multiple days, I visualized a significant increase in the lifetime and accumulation of ProSNAs in the brain compared to the native protein. This confirmed that ProSNAs distribute differently from their native counterparts following intrathecal injections and provides evidence that intrathecal injection is a viable pathway to increase brain penetration of SNAs.

1.3.2. Protein Vaccines

In order to develop immunity, T cells must be activated to display a short peptide sequence, or antigen, which derives from the proteome of the foreign organism or cancer cell. For example, vaccination against polio was achieved by inoculating attenuated virus, thus arming the immune system with molecular cues to defect the infection. The Mirkin group has demonstrated great success in using immunostimulatory SNAs to reverse tumor growth and prevent cancer recurrence by co-delivering antigens and adjuvants; however, these studies used model (OVA) or known cancer antigens (E6, gp-100). Moreover, there has been no published evidence on using immunostimulatory SNAs as a vaccine for viral infections. Therefore, in my final two thesis chapters, I will first discuss how SNAs can be rationally designed to treat triple-negative breast cancer (TNBC)— a cancer with no known tumor-associated antigen (TAA). Finally, I will describe early research in employing SNAs as a vaccine to generate neutralizing antibodies against SARS-CoV2.

1.3.2.1. Immunostimulatory Spherical Nucleic Acids as Cancer Vaccines for Triple Negative Breast Cancer (Chapter 4)

The primary objective of cancer vaccines is to mobilize the host immune system against tumors. In contrast, tumors proliferate because they have developed a way to evade the immune system predominantly by crippling cytotoxic CD8+ T cells through the production of suppressive cytokines or by down-regulating antigen presentation.[62] Standard cancer therapeutic strategies,

such as chemotherapy, radiation, or tumor resection, cause transient immune suppression which, in turn, can decrease the immune system's ability to combat cancer recurrence.[63] Current development into cancer therapies that stimulate the immune system to kill tumor cells include vaccination with antigen peptides[64], DCs[65], and chimeric-antigen receptor T cells (CAR-T)[66]; however, these approaches are restricted to a subset of patients whose tumors express known tumor-associated antigens (TAAs). Moreover, cancer cells undergo high mutation rates, resulting in the loss of a specific TAA's expression. An alternative to single-antigen vaccines is to use cell lysates isolated from a patient's tumor as the TAA source.[67-73] This broadens the set of proteins processed and presented by immune cells to stimulate a robust T cell response. Moreover, oxidizing tumor cells before lysate preparation by hypochlorous acid (HOCl) significantly increases immunogenicity.[74, 75] To explore the potential of SNAs to treat cancer with no known TAA—such as TNBC—we synthesize L-SNAs that encapsulate lysates derived from TNBC cell lines in their core and present CpG on their surfaces, as well as analogs that contain lysates from TNBC cells that were oxidized with HOCl prior to lysis (OxLys-SNAs), and evaluated their antitumor properties in mouse models of TNBC. In addition to validating L-SNAs relevance as a cancer vaccine for TNBC, we defined design parameters of the lysate-loaded SNAs as a function of liposome composition. By varying the length and degree of saturation of the lipid tail used to formulate L-SNAs, we found correlations between the stability of the L-SNA and its *in vitro* cellular uptake and activation in DCs and *in vivo* antimetastatic and antitumor efficacy. Altogether, we established the utility of SNAs for personalized cancer therapy and validated that the method in which lysates are generated and how L-SNAs are packaged and delivered to the immune system has a profound impact on the resulting antitumor efficacy.

1.3.2.2. Spherical Nucleic Acids as a Platform for Infectious Disease Vaccines (Chapter 5)

In December 2019, a novel coronavirus (SARS-COV2) emerged, resulting in a global pandemic, with over 79 million confirmed cases and 1.75 million deaths worldwide in the year 2020.[76] The long incubation period, high infection rate, and long-term severe symptoms experienced by vulnerable populations make COVID-19 a concerning disease. Moreover, associated costs from quarantine restrictions and lockdowns implemented to mitigate spread have had unintended and severe consequences to the economy, mental health, and children's access to uninterrupted education. Only the rapid development and distribution of a vaccine to the population is the most effective approach to lift restrictions and stop this pandemic completely. Immunization against viruses has traditionally relied on the usage of heat-killed or attenuated pathogens; however, nanoparticle-based delivery platforms have become the next-generation vaccines, with Pfizer's and Moderna's vaccines becoming the first nanoparticle mRNA-based vaccines being clinically used.[77] In these vaccines, a cationic liposome is used to encapsulate and deliver mRNA that cells translate to produce spike (S) proteins. The spike is a structural protein on the SARS-CoV-2 membrane that facilitates viral entry into the host cell during the infection process. The spike protein subunits are responsible for binding to the angiotensin-converting enzyme 2 (ACE2) receptor (subunit S1) and facilitating host cell membrane fusion (subunit S2).[78] A segment of the S1 contains the receptor-binding domain (RBD), a target antigen for inducing neutralizing antibodies.[79, 80]

Based on the established effectiveness of immunostimulatory SNAs in increasing stability and facilitating synchronized delivery of both antigen and adjuvant to immune cells, we expanded the utility of the SNA to induce protective immunity against SARS-CoV-2. We developed SNA subunit vaccines which consist of structural components of SARS-CoV-2 that can prime a protective immune response in the host when administered together with adjuvants. Moreover,

SNAs are highly modular, allowing for their rapid modification to incorporate novel antigen variants as they arise. Presently, we have subcutaneously treated mice with L-SNAs that encapsulate the RBD protein and utilize CpG DNA (TLR9 agonist) as the dense shell that enables uptake into immune cells. After 14 days, a single dose of vaccine led to the production of significant levels of RBD-specific IgG antibodies, achieving >1000 ng/mL final neutralizing titer when assessed in a pseudovirus inhibition assay. These results are further enhanced following a second SNA dose, increasing the overall RBG-specific IgG titer to >8000 ng/mL. With these promising results, we identified a new frontier for SNAs as next-generation nanoparticle antiviral vaccines. As devastating as COVID-19 is, it served as an impetus for the scientific community to develop and distribute a life-saving vaccine at unprecedented speed. Nanotechnology platforms—such as the SNA—offer plug-and-play capabilities that can be tailored to seasonal or new variants of coronaviruses, underscoring the need for continued investment in SNA as a viral vaccine candidate.

CHAPTER 2. DEFINING THE DESIGN PARAMETERS FOR *IN VIVO* ENZYME DELIVERY THROUGH PROTEIN SPHERICAL NUCLEIC ACIDS

Material in this chapter is based upon published work:

Kusmierz C.D.; Bujold K.E.; Callmann C.E.; Mirkin C.A. Defining the Design Parameters for *in Vivo* Enzyme Delivery Through Protein Spherical Nucleic Acids. *ACS Central Sci.* **2020**, *6*, 815-822.

2.1. Introduction

When materials are structured on the nanoscale, they exhibit unique properties that can be exploited for various applications. DNA is a notable illustration of this concept; when densely radially functionalized onto a nanoparticle core in the form of a spherical nucleic acid (SNA), DNA achieves high cellular uptake through the engagement of scavenger receptors and is more resistant to nuclease degradation than its component nucleic acids.[4-6, 33, 82] These properties have enabled the development of SNAs as diagnostic tools and in therapeutic applications, ranging from gene regulation to immunotherapy.[12, 16, 26, 28, 30, 31, 39, 48, 49, 83-85] Because the three-dimensional architecture of the DNA shell is the primary driver for biological function, the SNA platform has been expanded to include biocompatible cores such as liposomes, polymers, and proteins.[8, 9, 11, 86] Protein SNAs (ProSNAs) are especially attractive because they address an unmet need in biologics development: facilitating the cellular delivery of large, hydrophilic, and charged macromolecules while maintaining their biological function.

The notion that DNA shell design parameters dictate the biological fate of SNAs is well-established. One such example is that high oligonucleotide loadings correlate with enhanced cellular uptake.[1] In previous work with gold nanoparticle-based SNAs, hexaethylene glycol (HEG), also known as Spacer 18 (Sp18), were introduced at the interface between the nanoparticle core and its oligonucleotide shell to mitigate the electrostatic repulsion between the negatively charged gold surface and the DNA, enabling denser packing.[2] However, a pivot in DNA shell design is required when synthesizing an SNA architecture from a protein core. Proteins typically offer fewer attachment sites and thus may not be affected by electrostatic repulsion to the same degree. Moreover, with many proteins, chemical modification of their surfaces can either positively or negatively influence different aspects of their function. For example, in the development of protein-based therapies, biocompatible polymer modification, or PEGylation, has been utilized to extend

the lifetime of susceptible proteins. However, such modifications generally lead to a loss in biological activity.[87-89]

In addition to the introduction of a linker region to the DNA shell of SNAs, another design rule identified with gold-based SNAs was their sequence-specific uptake behavior. Specifically that G-quadruplexes (GQs), which are guanine-rich sequences that can fold into unique secondary structures, contributed to higher cellular uptake and a difference in biodistribution.[3, 23, 24] This phenomenon is attributed to a favorable interaction between the scavenger receptor and a denser presentation of negative charge ascribed from the folding of the GQ.[21, 22, 90]

With insight into the potential benefits and detrimental effects of sequence design and polymer modifications, we sought to study the effects of incorporating (1) Spacer18 (a polymer mimic) in the DNA shell and (2) a GQ sequence on the cellular uptake, enzymatic activity, and biodistribution of ProSNAs, utilizing the previously established β-galactosidase (β-Gal) model system. We hypothesized that the nature and length of the linker would modulate the properties of the oligonucleotide shell of ProSNAs. Furthermore, the GQs will increase the uptake of the ProSNA akin to previous studies with the gold core. For this purpose, we used *in vitro* and *in vivo* models to investigate tunable parameters in the ProSNA DNA shell's linker design space in the interest of developing a set of general DNA shell design rules for biologic drug development.

2.2. Impact of linker design on cell uptake and activity.

β-Gal ProSNAs were synthesized using protocols previously established by our group. The protein was tagged with Alexa Fluor 647 (AF647) to facilitate tracking *in vitro* and *in vivo*. To evaluate the impact of DNA linker identity and length on the cellular uptake and enzyme activity of a β-Gal ProSNA, DNA was conjugated to the protein through surface-accessible lysine residues, with either T_{4n} or $(sp18)_{2n}$ (n = 1, 2, 3) near the conjugation site (**Figure 5A**). Each linker, T_4 or $(sp18)_2$, is approximately equivalent in length but varies significantly in chemical identity and

flexibility, which may impact the radial orientation of the oligonucleotide shell and ultimately affect the biological properties of the resulting ProSNAs. UV–vis spectroscopy showed that the DNA loadings were identical (30 DNA/ β-Gal, 3.7 pmol/cm2), regardless of the composition of the shell (**Figure 13**). Moreover, covalent conjugation of the DNA to the protein core was confirmed via a

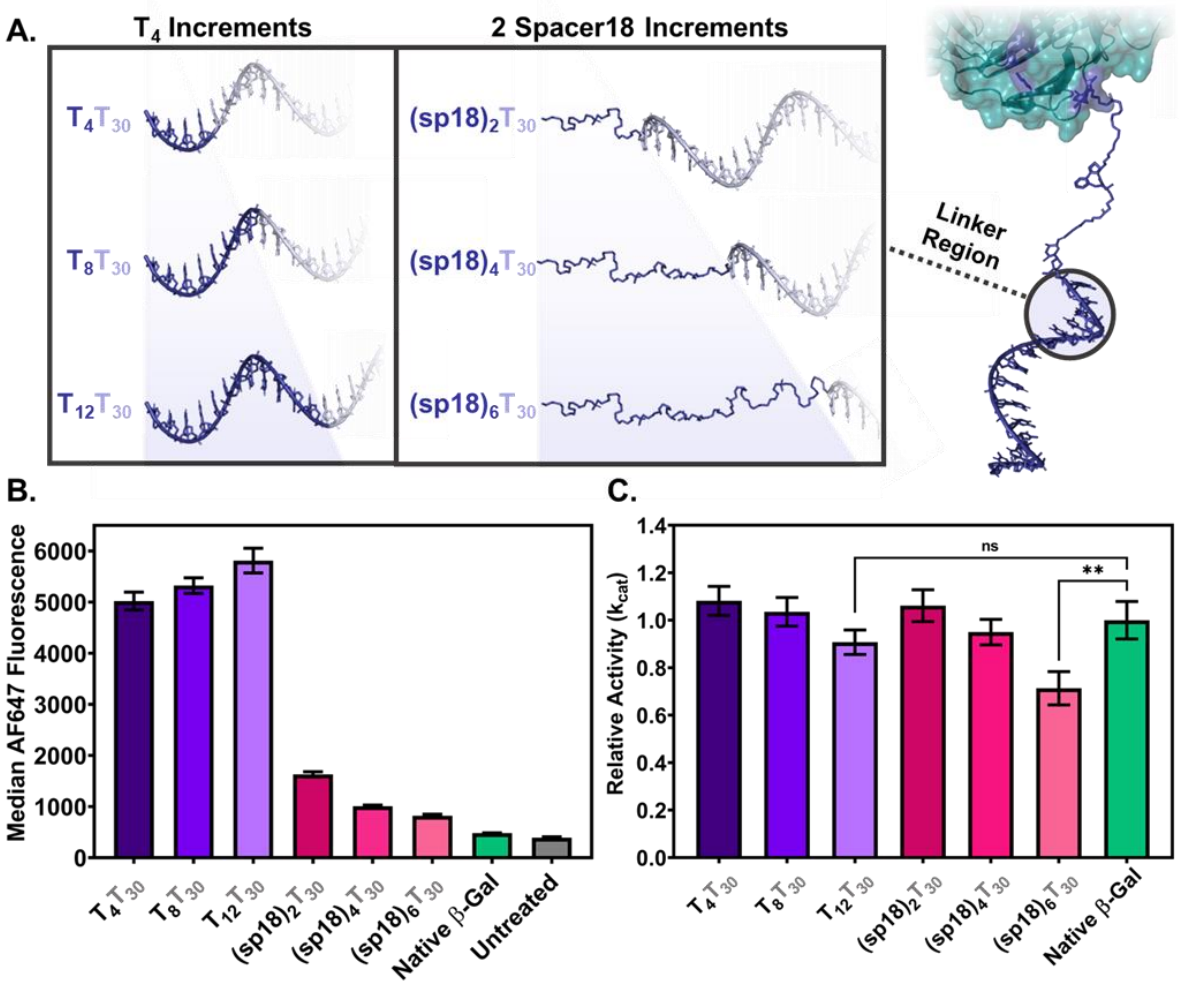

Figure 5. Impact of linker design on cellular uptake and enzymatic activity. (A) Cartoon representation of the surface of β-Gal at a lysine residue, which is covalently modified with a DNA strand. The "linker region", at the interface of β-Gal and a T_{30} oligonucleotide strand, varies in either increasing T_4 or 2 Spacer18 phosphoramidite increments. The representation was adapted from PDB ID 1PX3. (B) Cellular uptake of ProSNAs with increasing T_4 (purple) or Spacer18 (pink) linkers, as determined by flow cytometry. Fluorescence was measured in HeLa cells (n = 3) 4 h after treatment with 5 nM enzyme in serum containing media. All ProSNAs have equal loading density of 30 DNA/β-Gal. (C) Relative k_{cat} (n = 3) determined by an ONPG assay of ProSNAs with varying linker identity and the native protein. All ProSNAs have equal loading density of 30 DNA/β-Gal. The bars in the graphs represent the mean, and error bars show the standard error of the mean (SEM). An unpaired t test was performed with GraphPad Prism. n.s., not significant, ** P ≤ 0.01.

denaturing SDS-PAGE gel, which shows mobility shifts commensurate with the increased mass upon DNA addition (**Figure 14**). Importantly, in contrast to classical gold-based SNAs, the absence of Spacer18 did not significantly affect loading density onto ProSNAs, suggesting that each surface-accessible lysine on β-Gal was readily available for conjugation, independent of linker type.

One of the defining features of the SNA platform is its robust and unaided cellular uptake, which has been demonstrated in more than 60 cell lines.[10] Specifically, akin to other SNAs, the ProSNA was found to be taken up by cells through scavenger receptor-A (SR-A) mediated endocytosis through a receptor blocking study.[8] To establish the role of the linker on the cellular uptake of ProSNAs, HeLa cells were incubated with the six β-Gal ProSNA variants described above, and their uptake was monitored using flow cytometry by tracking the fluorescence of the protein core (**Figure 5B**). Surprisingly, the ProSNA with no Spacer18 was taken up to the greatest extent. Furthermore, internalization dramatically decreased with increasing Spacer18 length, even though these modifications were made adjacent to the protein surface and thus not expected to be accessible to the cell surface. In contrast, increasing the length of the DNA linker imparted only minor changes in cellular uptake. We speculate that these results originate from differences between the linkers in terms of persistence length and ability of the shell to adopt a radial arrangement away from the protein surface, resulting in a decreased affinity for SR-A.[3] The linker's deleterious uptake properties were further supported by switching the location of Spacer18 on the protein: cellular uptake recovers, confirming that placing Spacer18 near the protein surface is detrimental to internalization (**Figure 19Figure** 20). These findings were further reproduced in another cell line (**Figure 23**). Based on these results, we find that while gold-based SNAs benefited from the addition of Spacer18 linkers, the functionalization of protein cores should be carried out using linkers that are composed entirely of DNA to maximize cellular uptake.

A critical aspect, unique to ProSNAs in the context of protein delivery, is the retention of protein function after conjugation. To assess the effect of conjugating a large number of DNA strands on the protein surface on function, the enzymatic activity of the β-Gal ProSNAs was measured utilizing an ortho-nitrophenyl-β-galactoside (ONPG) assay, and Michaelis–Menten constants were calculated. Both linkers caused a loss of enzymatic activity as their length increased; however, this effect is more pronounced for the Spacer18 linker (**Figure 5C**). We speculate that Spacer18 is more detrimental to enzymatic activity because of an increased affinity of the Spacer18 linker for the protein surface when compared to DNA. To test this hypothesis, we placed the Spacer18 linker away from the protein surface by appending it at the end of a T_{30} strand and found that activity was improved (**Figure 26**). Considering that the reported isoelectric point for β-Gal is approximately 5.5, the protein is overall negatively charged at physiological conditions. Similarly, the DNA linkers provide a high density of negative charges through their phosphate backbone. These two elements combined are thus expected to promote electrostatic repulsion and favor a radial orientation of the oligonucleotide shell. On the other hand, Spacer18 linkers are less densely charged than DNA and may have other interactions with the protein surface. Based on these results, we conclude that with this protein, short DNA-only linkers maximize the enzymatic activity of ProSNAs.

2.3. G-Quadruplex Shell Enhances Cell Uptake *In Vitro*

We next assessed sequence-dependent cellular uptake and enzyme activity trends of ProSNAs under physiological conditions. Templated by their DNA sequence, particular strands will fold into secondary structures that can bind preferentially to receptors on the cell membrane. In previous work, our group demonstrated that SNAs constructed using guanine-rich sequences resulted in significantly higher uptake compared to thymine-, adenine-, or cytosine-rich control SNAs. G-rich sequences, which can fold into GQs, are a natural ligand for SR-A due to the

proposed favorable electrostatic interaction between the GQ and the lysine-rich collagenase region of the SR-A.[21, 22, 90] Because GQs are expected to interact preferentially with SR-A, we hypothesized that ProSNAs with a DNA shell that can form GQs would be able to enter cells in more significant amounts than SNAs composed of other nucleotides (**Figure 6A**). GQs exist in

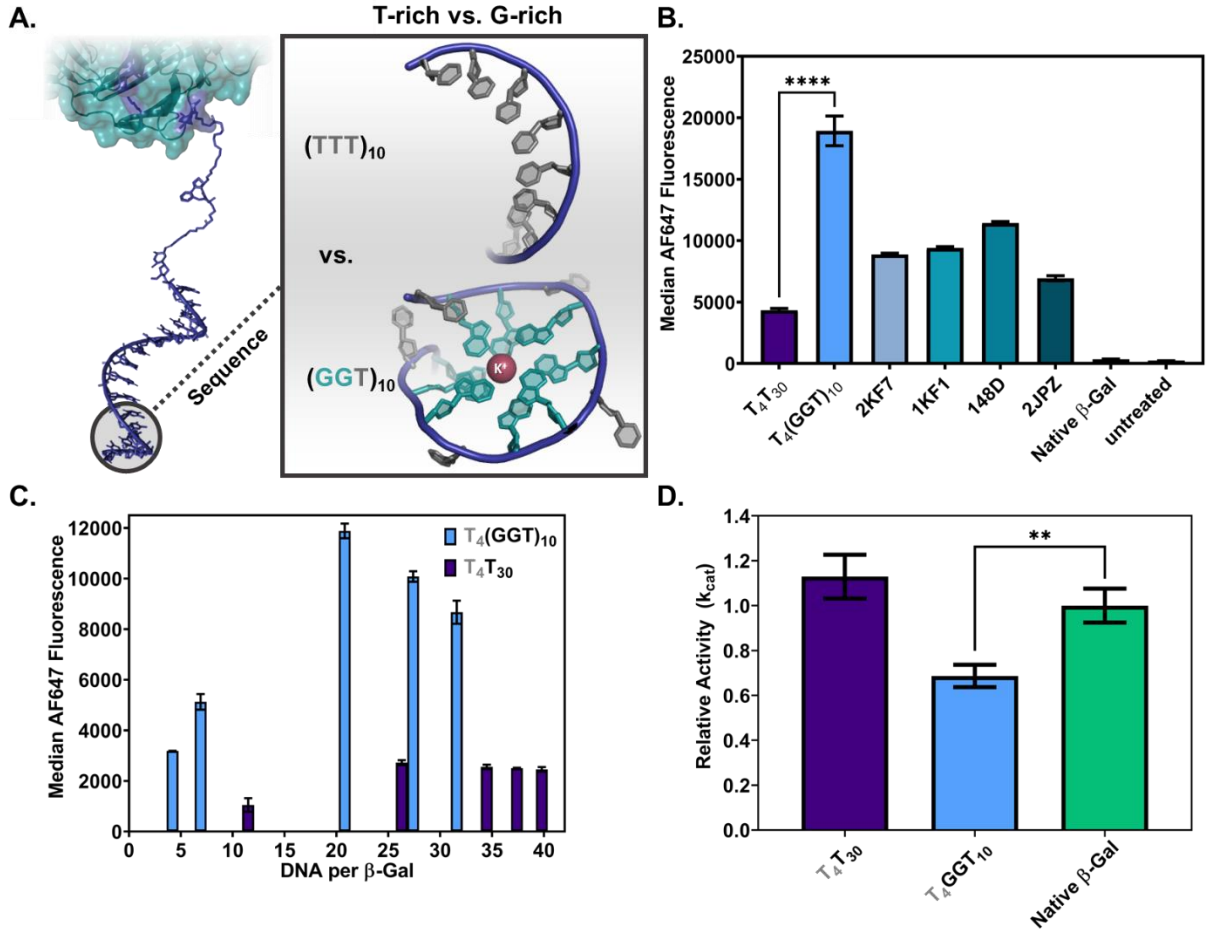

Figure 6. Impact of G-quadruplex sequences on cellular uptake and enzymatic activity. (A) Cartoon representation of the surface of β-Gal at a lysine residue which is covalently modified with a DNA strand. The inset represents either a T-rich and G-rich sequence structure. In the G-quadruplex topology, the guanine bases are selectively stabilized by a potassium cation. The representation was adapted from PDB ID 1PX3 and 2N3M. (B) Cellular uptake of ProSNAs with different G-quadruplex topologies, as determined by flow cytometry. 2KF7 (antiparallel basket), 1KF1 (parallel propeller), 148D (antiparallel chair), and 2JPZ (mixed chair) are named after their PDB ID. Fluorescence was measured in HeLa cells (n = 3) 4 h after treatment with 5 nM enzyme in serum containing media. (C) Cellular uptake of ProSNAs at different loading densities with either a T4T30 or T4(GGT)10 sequence, as determined by flow cytometry. Fluorescence was measured in HeLa cells (n = 3) 2 h after treatment with 10 nM enzyme in serum containing media. (D) Relative kcat (n = 3) determined by an ONPG assay of ProSNAs (both 20 DNA/β-Gal) and the native protein. The bars in the graphs represent the mean, and error bars show SEM. An unpaired t test was performed with GraphPad Prism. **P ≤ 0.01, ****P ≤ 0.0001.

various topologies based on their sequences; therefore, we investigated the impact of GQ folding on cellular uptake of the ProSNA *in vitro*. To facilitate attachment to β-gal, all GQ sequences were synthesized with a T_4 DNA-only linker, which was found to maximize both cellular uptake and enzymatic activity (*vide supra*).

To begin, we characterized all GQ strands by circular dichroism to confirm the chosen sequences fold into the appropriate GQ structure after the inclusion of a T_4 linker and DBCO-dT conjugation group (**Figure 17**). Then we synthesized ProSNAs using the previously reported method but under different buffer conditions. The G-quartet structure in a GQ's tetrad is selectively stabilized by a K^+ ion, which coordinates to each of the guanine bases. To linearize the strand, thus enabling more efficient loading, we replaced K^+ with Li^+ as the counterion in the reaction buffer. Lithium is the least stabilizing among type Ia and IIa cations; therefore, the GQ does not form under these conditions. After conjugation and ProSNA purification, the buffer was exchanged back to PBS (a potassium phosphate buffer) to facilitate GQ formation (**Figure 18**).

To determine which GQ topology results in the most significant enhancement in cellular internalization, HeLa cells were treated with each of the ProSNA GQ variants in serum containing media. According to flow cytometry, all GQs demonstrated an approximately twofold increase in uptake compared to the T-rich ProSNA (**Figure 2B**). More notably, the $T_4(GGT)_{10}$ ProSNA, which folds into a parallel GQ, increased uptake by fourfold. This enhancement in uptake with the $T_4(GGT)_{10}$ ProSNA was demonstrated over a range of loading densities with the highest cellular uptake seen at a loading of 20 DNA/β-Gal (**Figure 2C**).

The enhancement in cellular uptake with ProSNAs composed of a GQ shell stems from the DNA's unique secondary structure. However, this special folding imparts a small inhibitory effect on the enzyme's activity. An ONPG assay was used to calculate the kcat of the enzyme for ProSNAs with either T_4T_{30} or $T_4(GGT)_{10}$ DNA shells. After loading both ProSNAs equally (20 DNA/β-Gal), we calculated the kcat of the enzyme and found that there is an ~30% loss in activity

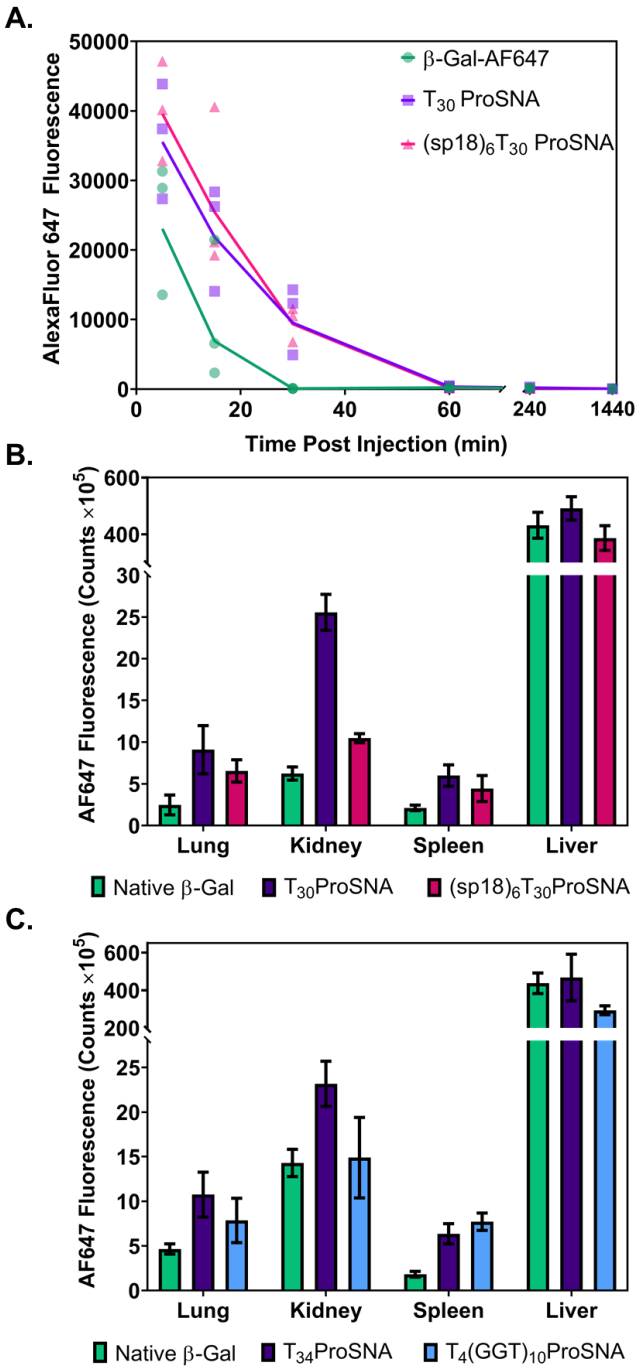

Figure 7. Pharmacokinetic profile of the ProSNA and native protein. (A) The clearance of two ProSNA variants with and without Spacer18 linker and native protein were studied by measuring the fluorescence in plasma. Raw data points as well as the geometric mean at each time point are depicted. (B, C) After a 1 h treatment with 4 mg of enzyme/kg mouse via a tail-vein injection; mice (n = 3) were sacrificed, perfused, and their organs dissected and fixed. Using IVIS, a region of interest was drawn around each organ, and the fluorescence counts were quantified. The bars in the graphs represent the mean, and error bars show SEM.

with a GQ shell (**Figure 2D**). This small loss in activity may stem from steric hindrance by the dense folding of the DNA around the enzyme. Nevertheless, it is subject to the intentions of the application whether this marginal loss in activity depreciates the gain in cellular uptake for a G-quadruplex DNA shell.

2.4. ProSNAs Demonstrate Enhanced Pharmacokinetics

We assessed whether these shell design considerations would translate from *in vitro* cell studies to a more relevant *in vivo* mouse model. Previous work using gold core SNAs highlighted the benefits of the oligonucleotide shell in enabling the biodistribution of SNAs to all major organs, which have been applied for the treatment of many diseases, including glioblastoma and many other forms of cancer.[16, 30] ProSNAs are a special case because there is an approximate order of magnitude difference in loading density (3.7 pmol/cm^2) when comparing to the classical gold SNAs (30–60 pmol/cm^2). Moreover, naked proteins are susceptible to degradation and typically show low cellular uptake. Therefore, we evaluated if this loading density would be sufficient to enable applications of ProSNAs *in vivo* and if these newly devised design rules would be able to amplify these effects further.

Based on cellular uptake and enzymatic activity findings *in vitro*, we hypothesized that Spacer18 would impede the internalization of ProSNAs within the tissue. For this purpose, we started by comparing constructs bearing either a T_{30} or $(sp18)_6T_{30}$ DNA shell, such that these two constructs would vary only in the presence of a Spacer18 linker. We assessed both the blood circulation time and temporal biodistribution following a single tail vein intravenous injection of either β-Gal ProSNAs or native protein in CD-1 mice, utilizing the Alexa Fluor 647 fluorescent-tag on the protein to track its distribution.

First, we measured the distribution half-life of these ProSNAs in plasma to determine the clearance rate of these protein constructs. Notably, both ProSNAs exhibit an increase in

circulation time (60 min), which is twice that of the native protein (30 min), regardless of the linker identity (**Figure 7A**). These similarities in the pharmacokinetic profiles of the SNAs highlight the influence of the DNA shell, regardless of linker, in transforming the biological properties of an SNA's nanoparticle core.

To evaluate the distribution of β-Gal in tissue, we measured the fluorescence of dissected and perfused organs utilizing an *in vivo* imaging system (IVIS). Quantification of radiant efficiency revealed that a majority of both ProSNA and native protein were sequestered by the liver, akin to previous observations with other nanoparticle systems.[91] However, the ProSNAs, in particular the T_{30} variant, exhibited distinct differences in biodistribution compared to the native protein (**Figure 7B**). Consistent with our hypothesis, we observed that the native protein is found primarily in the liver with limited distribution to other organs. In contrast, the addition of the oligonucleotide shell enabled a broader distribution of both ProSNAs. Importantly, an enhanced tissue accumulation was observed with the T_{30} ProSNA, mirroring our previous *in vitro* cellular uptake results (*vide supra*). This finding is of significance because it highlights the importance of using an all-DNA shell when designing ProSNAs because it dictates their *in vivo* behavior.

In addition to linker identity being a determinant of uptake for the ProSNA, DNA sequence was also established to enhance cellular uptake *in vitro*. Consistent with the previous experiment, we utilized IVIS to study the distribution of the ProSNA with two different sequence identities: T_{34} or $T_4(GGT)_{10}$. Both ProSNAs were loaded equally at 20 strands per protein, which we demonstrated resulted in the highest internalization for the GQ ProSNA in HeLa cells. CD-1 mice were treated with each construct via the tail-vein, and after a 1 h treatment, mice were sacrificed and perfused, and organs were dissected for IVIS analysis, which was used to track the AF647 fluorophore covalently conjugated to the protein. Based on fluorescence counts, both ProSNAs

accumulated in the dissected organs equally (**Figure 7C**). From this experiment, it is apparent that the nature of the linker is a more important determinant of *in vivo* ProSNA behavior.

2.5. Only ProSNAs Exhibit Enzymatic Activity in Tissue

The ultimate test to determine the potential of the SNA architecture as a delivery method for biologics was to assess whether the delivered enzyme retains its biological activity in tissue. Therefore, we performed a colorimetric activity assay specific to β-Gal on cryo-sectioned organs, allowing us to gain information on the suborgan compartmentalization of the SNA platform and its overall structural integrity. For this purpose, mice were intravenously administered ProSNAs or native protein. After 1 h, mice were sacrificed and perfused, and organs were cryosectioned and subsequently stained with 5-bromo-4-chloro-3-indolyl-β-d-galactopyranoside (X-Gal) to visualize the enzyme's activity via the appearance of a blue-colored insoluble product.[92] Strikingly, we observed blue coloring in both T_{34} ProSNA and $T_4(GGT)_{10}$ ProSNA treated mice (n = 3), which confirmed the successful delivery of active enzymes to tissues, while all organs treated with the native proteins (n = 3) exhibited no coloring (**Figure 8**). This is the first time that the ProSNA strategy has been tested in a living animal model, opening the door to various applications for relevant disease models.

In this context, we looked at the distribution of the blue stain within each organ, which revealed details about tissue localization of the ProSNA. A first striking observation was the presence of blue in the ProSNA-treated liver indicative of enzyme activity, whereas it was completely absent in the case of the native protein. This was unexpected since IVIS fluorescence signals in the liver from all treatment groups were nearly identical, suggesting that the oligonucleotide shell on the ProSNA was able to protect its structural integrity. The liver and lung displayed diffuse staining throughout the organ, whereas in the kidney and spleen, it was localized to tissue substructures. Specifically, the ProSNA is trapped within the glomerulus in the kidney,

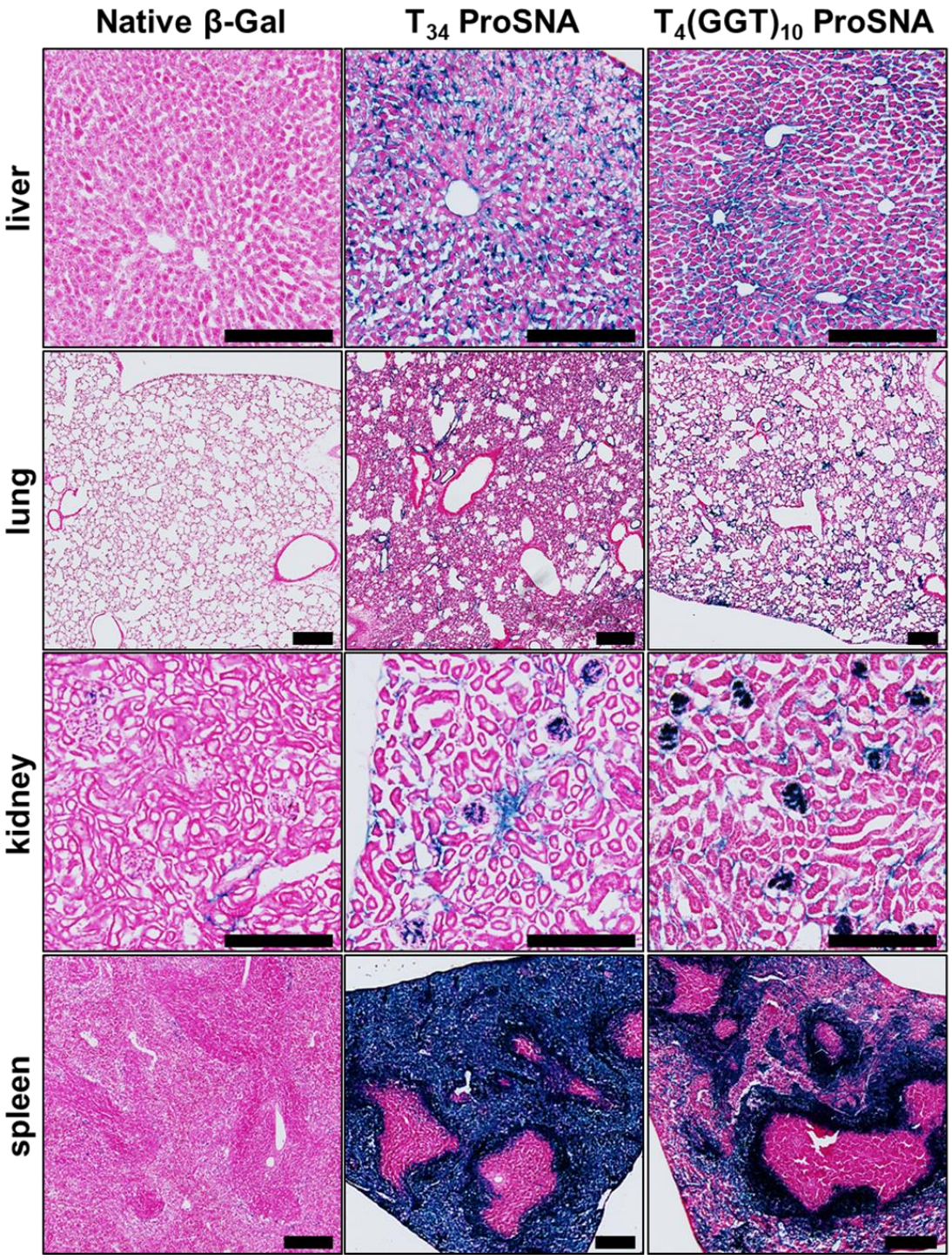

Figure 8. *In vivo* catalytic activity and tissue distribution of native β-Gal and ProSNA. Representative light micrographs of histology slides after incubation with the β-Gal substrate, X-Gal. The blue color apparent in tissue dissected from mice (*n* = 3) 1 h after intravenous injection of 6.5 mg enzyme/kg mouse results from the hydrolysis of X-Gal and the formation of an insoluble blue product. Scale = 250 μm.

which is a structural unit that acts as a filter with an average pore size of 3 nm.[93] We hypothesize that the ProSNAs are retained within this glomerular space and are thus prevented from entering the kidney tissue due to their inherent size. However, when the filtration size thresholds of the organs are larger, as is the case with the spleen, the ProSNA readily enters. Indeed, the spleen exhibits two distinct regions based on Nuclear Fast Red staining: red and white pulp. The white pulp is predominantly a sheath of lymphocytes (T and B) surrounding the artery, while the red pulp envelops the white pulp and consists mostly of macrophages, plasma, and a few lymphocytes.[94] Based on these images, the ProSNA is preferentially sequestered in the red pulp of the spleen. In particular, there is a difference in spleen distribution between the T-rich and GQ ProSNAs. The T-rich ProSNA distributes evenly throughout the red pulp. However, for the GQ ProSNA, the enzyme predominantly accumulates in a marginal zone at the junction between the red and white pulp. Regardless, we hypothesize that both ProSNA variants are taken up by macrophages (either marginal zone or red pulp), which take up the SNA due to the abundance of scavenger receptors on their cell membranes.[95]

2.6. Conclusions

We established the importance of DNA shell design in tuning the activity, cellular uptake, and overall biodistribution of ProSNAs. We find that the chemical composition of the linker is a crucial determinant of ProSNA properties: specifically, the replacement of the HEG linker with DNA leads to a recovery in both cellular uptake and enzymatic activity at no cost to loading density. Furthermore, we can harness the programmable topology of DNA structures to modulate cell interactions, as demonstrated with the GQ ProSNAs acting as preferential ligands for the scavenger receptor-A. In terms of biodistribution, the removal of the HEG linker resulted in a greater distribution in organs other than the liver. Conversely, both types of sequences facilitated protein delivery to a similar extent. Because the most critical parameter in protein delivery consists

in maintaining enzymatic activity, we demonstrate for the first time that the ProSNA strategy can be used to deliver functional enzymes to tissues, thus highlighting the relevance of this approach for biologics development. Considering the facile synthesis and conjugation of DNA onto proteins as well as its biocompatibility, these findings emphasize the relevance of applying the SNA architecture to therapeutically relevant proteins. We foresee that ProSNAs can be tailored to a breadth of applications from immunotherapy to enzyme replacement therapy in macrophage-relevant disease models.

2.7. Methods and Materials

2.7.1. Synthesis and Characterization of β-Galactosidase Protein Spherical Nucleic Acids

2.7.1.1. Oligonucleotide synthesis

Oligonucleotides were synthesized using standard phosphoramidite chemistry protocols on an ABI 392 using 1000 Å universal CPG solid supports (ChemGenes) and phosphoramidites, as well as coupling reagents purchased from Glen Research. The DBCO-dT-CE phosphoramidite was hand coupled in a glove box using a mild oxidizing agent ((1S)-(+)-(10-Camphorsulfonyl)-oxaziridine, CSO) to increase coupling efficiency and preserve the integrity of the strained alkyne in a water- and air-free environment. Synthesized strands were cleaved using 30% aqueous ammonia (Sigma Aldrich) for 16 h at room temperature and purified by HPLC using a reverse-phase C4 column (Shimadzu) running a gradient from 0 to 100% acetonitrile in triethylammonium acetate buffer (Sigma Aldrich) over 45 min. After HPLC purification, the final dimethoxytrityl group was removed in 20% acetic acid (Sigma Aldrich) for 2 h and extracted in ethyl acetate (Sigma Aldrich). The masses of the oligonucleotides were confirmed using matrix-assisted laser desorption ionization-time of flight (MALDI-MS) mass spectroscopy on a Bruker AutoFlex-III using

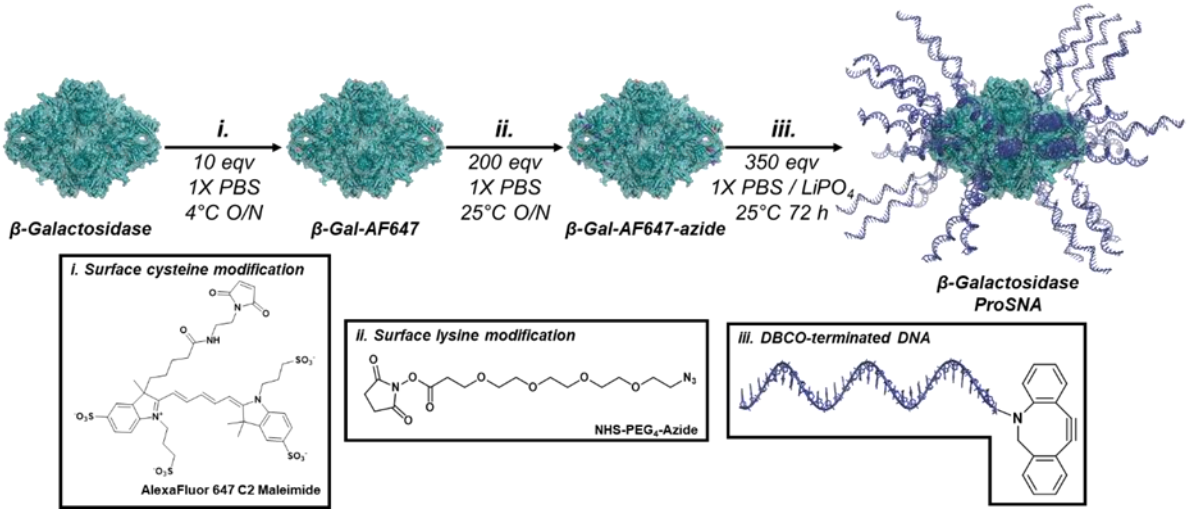

Figure 9. Synthesis scheme for ProSNAs. Cysteine residues are first modified with an Alexa Fluor 647 tag, then NHS-PEG_4-azide linkers are conjugated to surface accessible lysine residues. Using copper-free click chemistry, DBCO-terminated DNA strands can react with the azide-modified protein resulting in Protein Spherical Nucleic Acids (ProSNA). All reactions are held at pH 7.4 in phosphate containing buffers at either 4°C or ambient temperatures.

2',6'-dihydroxyacetophenone (Sigma Aldrich) as the matrix. Molecular weights and extinction coefficients were calculated based on estimates using the IDT OligoAnalyzer tool[96](**Table 1**).

Table 1. Oligonucleotide sequences, molecular weights, and extinction coefficients.

Name	Sequence (5' to 3')	MW Expected [Da]	MW Observed [Da]	ε_{260} [$M^{-1}cm^{-1}$]
T_4	DBCO-dT T_{34}	11054	10991	276000
T_8	DBCO-dT T_{38}	12271	12237	308400
T_{12}	DBCO-dT T_{42}	13488	13423	340800
$(sp18)_2$	DBCO-dT $(sp18)_2$ T_{30}	10526	10524	243600
$(sp18)_4$	DBCO-dT $(sp18)_4$ T_{30}	11215	11206	243600
$(sp18)_6$	DBCO-dT $(sp18)_6$ T_{30}	11903	11897	243600
T_{30} $(sp18)_6$	DBCO-dT T_{30} $(sp18)_6$	11903	11900	243600
$(sp18)_6$ only	DBCO-dT $(sp18)_6$	2840	2835	N/A
$T_4(GGT)_{10}$	DBCO-dT $T_4(TGG)_{10}$	11555	11558	322000
2KF7	DBCO-dT $T_4(G_3T_2A)_3G_3T$	8948	8984	255300
1KF1	DBCO-dT $T_4AG_3(T_2AG_3)_3$	8957	9002	260800
2JPZ	DBCO-dT $T_4(T_2AG_3)_4T_2$	10174	10202	293600

148D	DBCO-dT $T_4G_2T_2G_2TGTG_2T_2G_2$	6717	6702	175100

2.7.1.2. Synthesis of β-Galactosidase (β-Gal) Protein Spherical Nucleic Acids (ProSNA)

Molecular weights and extinction coefficients pertaining to synthesis and characterization of β-Gal ProSNAs are detailed in **Table 2**.

Table 2. Molecular weights and extinctions for chemical modifications onto β-Gal.

Name	MW [Da]	ε_{max} [$M^{-1}cm^{-1}$]
β-Galactosidase	464,000	1,142,000 (280nm) 596,268 (260nm)
Alexa Fluor® 647 dye	1250	265,000 (650nm)
NHS-PEG_4-azide	388	N/A

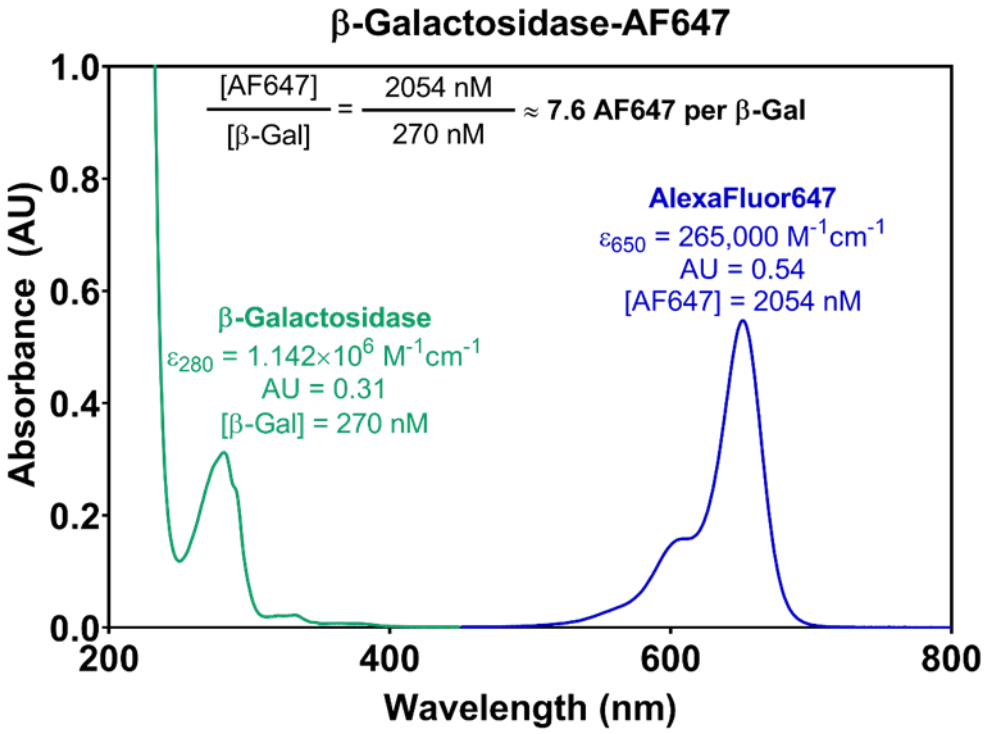

Figure 10. Representative UV-Vis spectrum of fluorophore modified β-Galactosidase. UV-Vis spectrum and calculation of the number of AF647 fluorophores on β-Gal in 1X PBS. Spectra were collected at ambient temperature with a 1 cm pathlength cuvette on a Cary5000 spectrophotometer. Inset calculations detail the steps used to calculate the number of fluorophores per protein.

2.7.1.2.1. Reaction of Surface-Accessible Cysteines with Alexa Fluor 647 (AF647).

β-Gal from an *E. coli* overproducer was purchased from Roche. The lyophilized protein was first dissolved in 1X phosphate-buffered saline (1X PBS; Thermo Fisher Scientific) and washed via 3 rounds of centrifugation using a 100 kDa centrifugal filter (Millipore), resuspending the protein in 1X PBS after each wash. Protein concentration was determined from its 280 nm absorbance peak collected on a Cary-5000 UV-Vis spectrophotometer in a 1 cm pathlength cuvette. Then, 10 equivalents of Alexa Fluor 647-C_2-maleimide (Thermo Fisher Scientific), dissolved in DMSO, were added to ~19 μM β-Gal in 1500 μL 1X PBS and the reaction was shaken (900 rpm) overnight at 4 °C. Unconjugated Alexa Fluor 647 was removed by repeated rounds of centrifugation using a 100 kDa filter until the filtrate did not have a detectable absorbance at 650 nm by UV-Vis. The number of Alexa Fluor 647 modifications per protein was calculated based on UV-Vis spectroscopy (**Figure 10**).

2.7.1.2.2. Reaction of Surface-Accessible Lysines with NHS-PEG_4-Azide.

200 equivalents of NHS-PEG_4-azide crosslinker (Thermo Fisher Scientific), dissolved in anhydrous DMSO at a concentration of 100 mM, were added to ~ 45 μM β-Gal-AF647 in 550 μL 1X PBS. The reaction was shaken (900 rpm) overnight at 25°C. Unconjugated linker was removed by 10 rounds of centrifugation using a 100 kDa filter. The number of azide modifications was assessed by MALDI-MS using sinapinic acid (Thermo Fisher Scientific) as a matrix in a Bruker AutoFlex-III (**Figure 11**).

$$\Delta\, {}^{m}/_{z_{monomer}} = \beta GalAF647Azide - \beta GalAF647 = 120349 - 116744 = 3605$$

$$\Delta\, {}^{m}/_{z_{tetramer}} = \Delta\, {}^{m}/_{z_{monomer}} \times 4 = 3605 \times 4 = 14420$$

$$\Delta\, {}^{m}/_{z_{tetramer}} \div MW_{NHSPEG_4azide} = \frac{14420}{388} = 37\ azide\ per\ protein$$

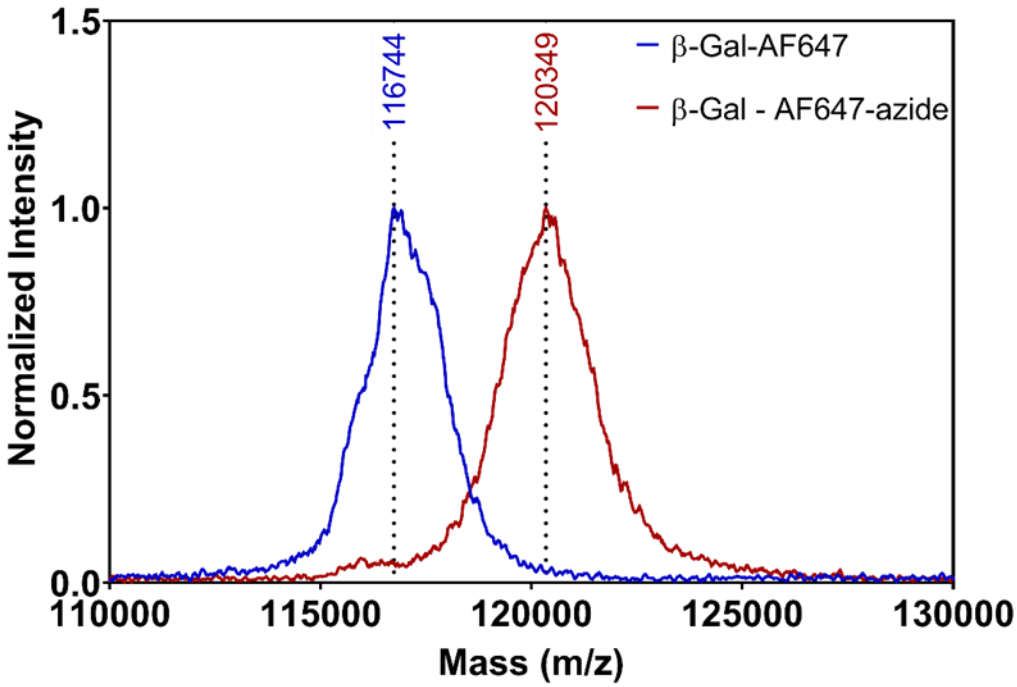

Figure 11. MALDI-MS spectra of azide modified and unmodified β-Gal-AF647. To calculate the number of azides per monomer, the mass difference between an unmodified and azide modified protein can be determined using MALDI-MS. The mass shown is of the monomer; therefore, to determine a mass change of the entire protein—a tetramer—this difference should be multiplied by 4.

2.7.1.2.3. Functionalization with DBCO-dT Terminated T-Rich Oligonucleotides.

350 equivalents of DBCO-dT terminated DNA strands were first lyophilized, then 6.5 μM β-Gal-AF647-azide in 450 μL 1X PBS was added to rehydrate the DNA. This solution was allowed to incubate for 72 h at 25 °C with shaking (900 rpm). Unreacted DNA strands were removed by successive rounds of centrifugation in a 100 kDa filter until the filtrate did not have a detectable absorbance at 260 nm. Typically, complete removal of DNA required 30-40 washing steps. The number of DNA strands per protein was calculated based on UV-Vis spectroscopy (**Figure 12**). Loading densities from ProSNAs described in this work appear in **Table 3** unless otherwise specified.

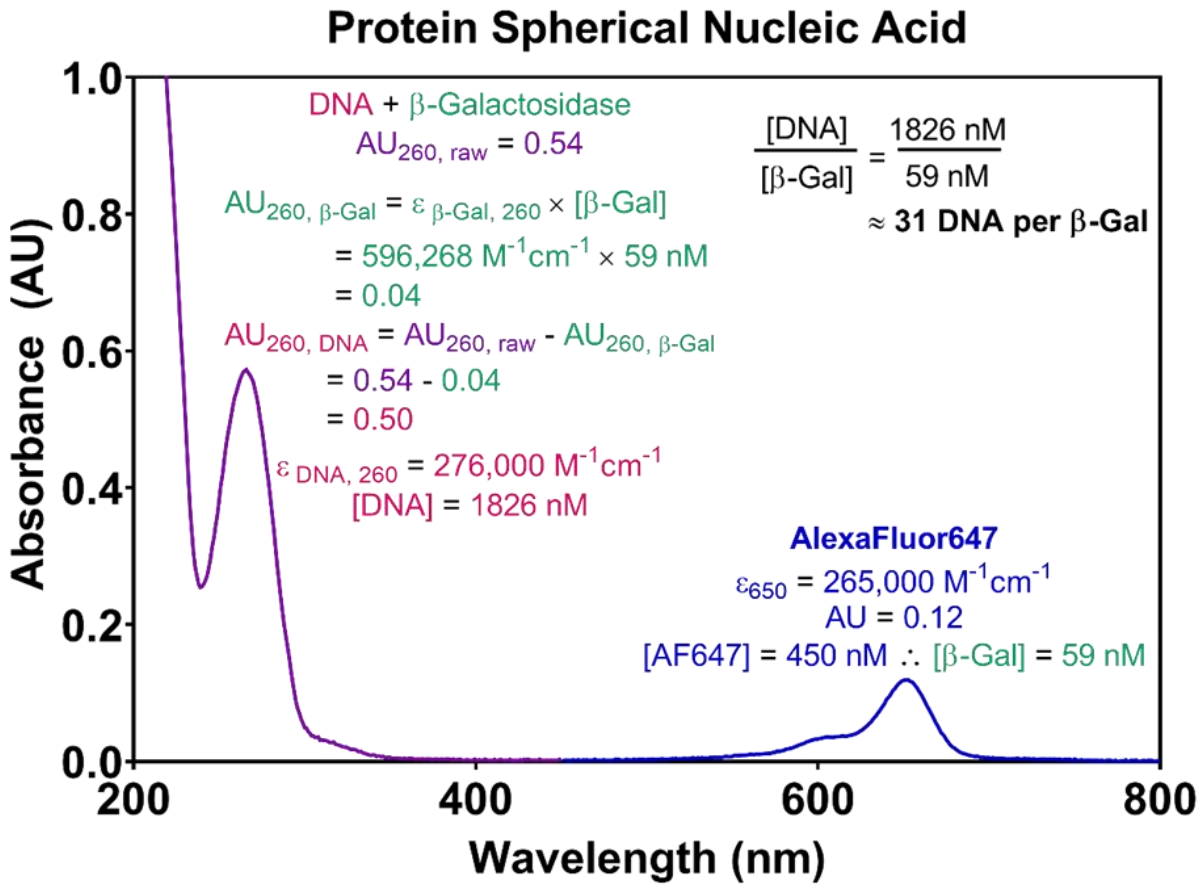

Figure 12. Representative UV-Vis spectrum of a protein spherical nucleic acid. UV-Vis spectrum and DNA loading calculations for a T_4T_{30} ProSNA in 1X PBS. Spectra were collected at ambient temperature with a 1 cm pathlength cuvette on a Cary5000 spectrophotometer. Inset calculations detail the steps used to calculate the number of T_4T_{30} DNA per protein.

2.7.1.2.4. Functionalization with DBCO-dT Terminated GQ Oligonucleotides.

β-Gal-AF647-azide was first buffer exchanged in lithium phosphate buffer (10 mM LiH_2PO_4, Sigma-Aldrich, pH 7.4) using five successive rounds of centrifugation in a 100 kDa filter. 350 equivalents of DBCO-dT terminated GQ DNA were lyophilized, then 6.5 μM β-Gal-AF647-azide in 450 μL $LiPO_4$ buffer were added to rehydrate the DNA. This solution was allowed to incubate for 72 h at 25 °C with shaking (900 rpm). Unreacted DNA strands were removed by successive rounds of centrifugation in a 100 kDa filter using the $LiPO_4$ buffer as the washing buffer until the filtrate did not have a detectable absorbance at 260 nm. Typically, complete removal of

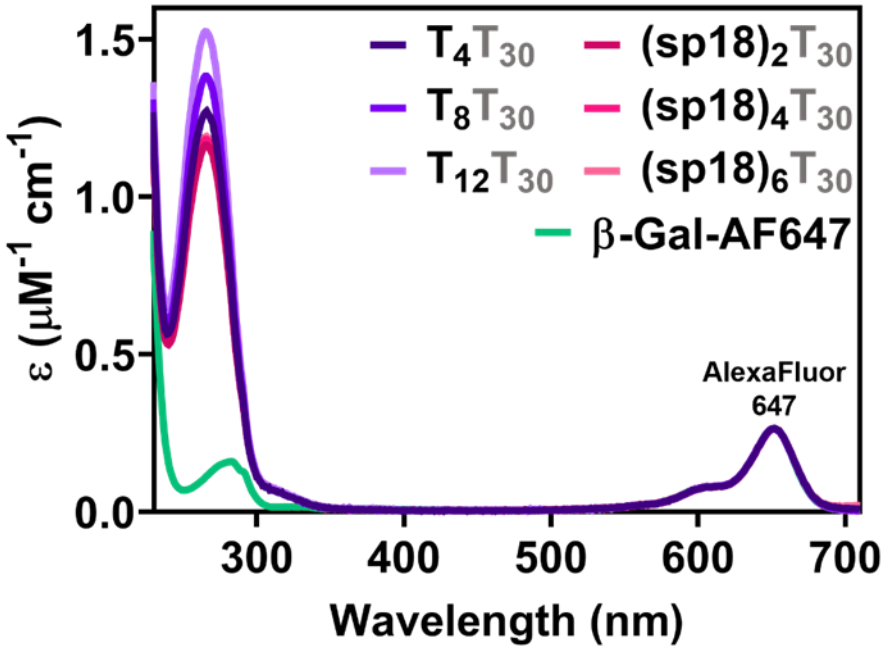

Figure 13. UV-Vis spectra of protein spherical nucleic acids. UV-Vis spectra of ProSNAs with different linker identities demonstrating their equal DNA loading. Spectra were collected at ambient temperature with a 1 cm pathlength cuvette on a Cary5000 spectrophotometer.

DNA required 30-40 washing steps. The number of DNA strands per protein was calculated based on UV-Vis spectroscopy (**Figure 12**). Loading densities from ProSNAs described in this work, unless otherwise specified, appear in **Table 3**. After complete removal of unconjugated DNA strands, ProSNAs were buffer exchanged back into 1X PBS buffer using five successive rounds of centrifugation in a 100 kDa filter.

Table 3. Oligonucleotide loading of ProSNA constructs (unless otherwise stated)

Name	Sequence (5' to 3')	DNA per β-Gal
T_4	DBCO-dT T_{34}	31
T_8	DBCO-dT T_{38}	30
T_{12}	DBCO-dT T_{42}	30
$(sp18)_2$	DBCO-dT $(sp18)_2$ T_{30}	32
$(sp18)_4$	DBCO-dT $(sp18)_4$ T_{30}	32

$(sp18)_6$	DBCO-dT $(sp18)_6$ T_{30}	33
T_{30} $(sp18)_6$	DBCO-dT T_{30} $(sp18)_6$	31
$T_4(GGT)_{10}$	DBCO-dT $T_4(TGG)_{10}$	32
2KF7[3]	DBCO-dT $T_4(G_3T_2A)_3G_3T$	35
1KF1[4]	DBCO-dT $T_4AG_3(T_2AG_3)_3$	35
2JPZ[5]	DBCO-dT $T_4(T_2AG_3)_4T_2$	37
148D[5]	DBCO-dT $T_4G_2T_2G_2TGTG_2T_2G_2$	37

2.7.1.3. SDS-PAGE Analysis of ProSNAs

Protein samples (2 pmol) were incubated at 80 °C for 5 min in 1X Laemmli Sample Buffer (Bio-Rad) and 355 mM 2-mercaptoethanol (Sigma-Aldrich) before loading. Samples were run on a 4-15% TGX mini-Protean pre-cast gradient gel (Bio-Rad) for 90 min at 100 V in 1X Tris/Glycine/SDS running buffer (Bio-Rad). Gels were stained using SimplyBlue SafeStain (Invitrogen) before imaging on a ChemiDoc™ MP Imaging System (**Figure 14-Figure** *16*).

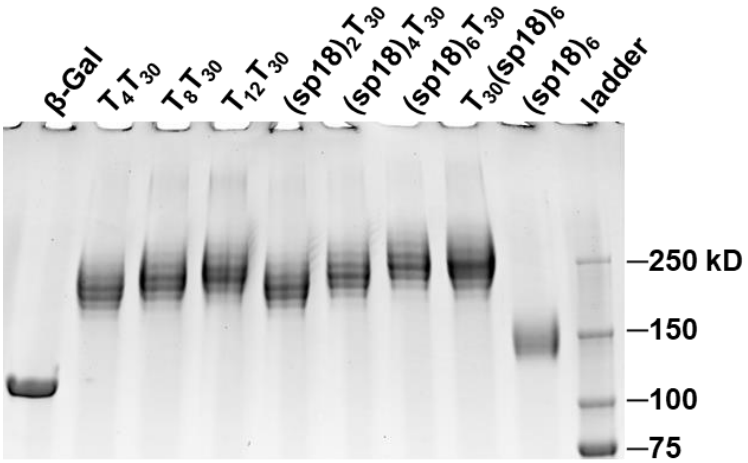

Figure 14. 4-15% SDS PAGE gel of native β-gal and ProSNA variants with different linker identity. Gel was run for 90 min at 100 V in 1X Tris/Glycine/SDS running buffer. Lower mobility bands are indicative of higher molecular weights for ProSNA variants and confirm the succesful conjugation of DNA strands onto the protein.

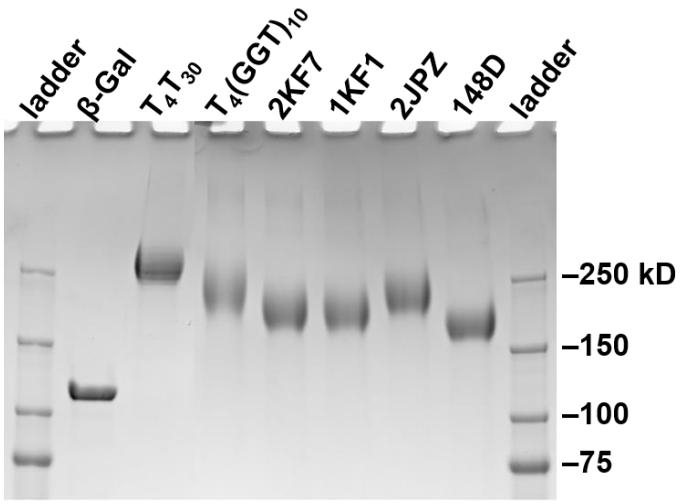

Figure 15. 4-15% SDS PAGE gel of native β-gal and ProSNA variants with different GQ topologies. Gel was run for 90 min at 100 V in 1X Tris/Glycine/SDS running buffer. Lower mobility bands are indicative of higher molecular weights for ProSNA variants and confirm the succesful conjugation of DNA strands onto the protein.

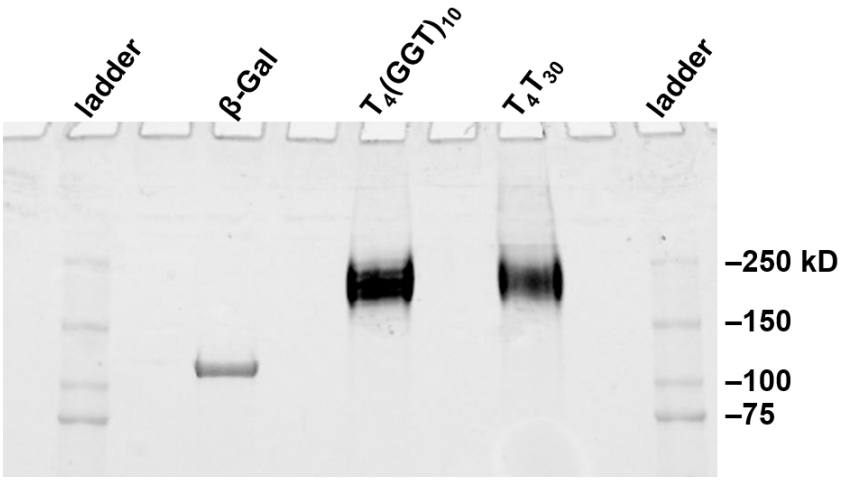

Figure 16. 4-15% SDS PAGE gel of native β-gal and ProSNA variants used for *in vivo* work. Gel was run for 90 min at 100 V in 1X Tris/Glycine/SDS running buffer. Lower mobility bands are indicative of higher molecular weights for ProSNA variants and confirm the succesful conjugation of DNA strands onto the protein.

2.7.1.4. Characterization of GQ Sequences and ProSNAs by Circular Dichroism

2.7.1.4.1. CD spectra of G-Quadruplex DNA strands in 1X PBS buffer

Circular dichroism (CD) spectra were recorded in a 10 mm pathlength cuvette at 25°C with a Jasco J-1700 spectropolarimeter equipped with a temperature controller at a concentration of 7.5 μM DNA in 1X PBS buffer (pH 7.4). The instrument parameters to record the CD spectra were:

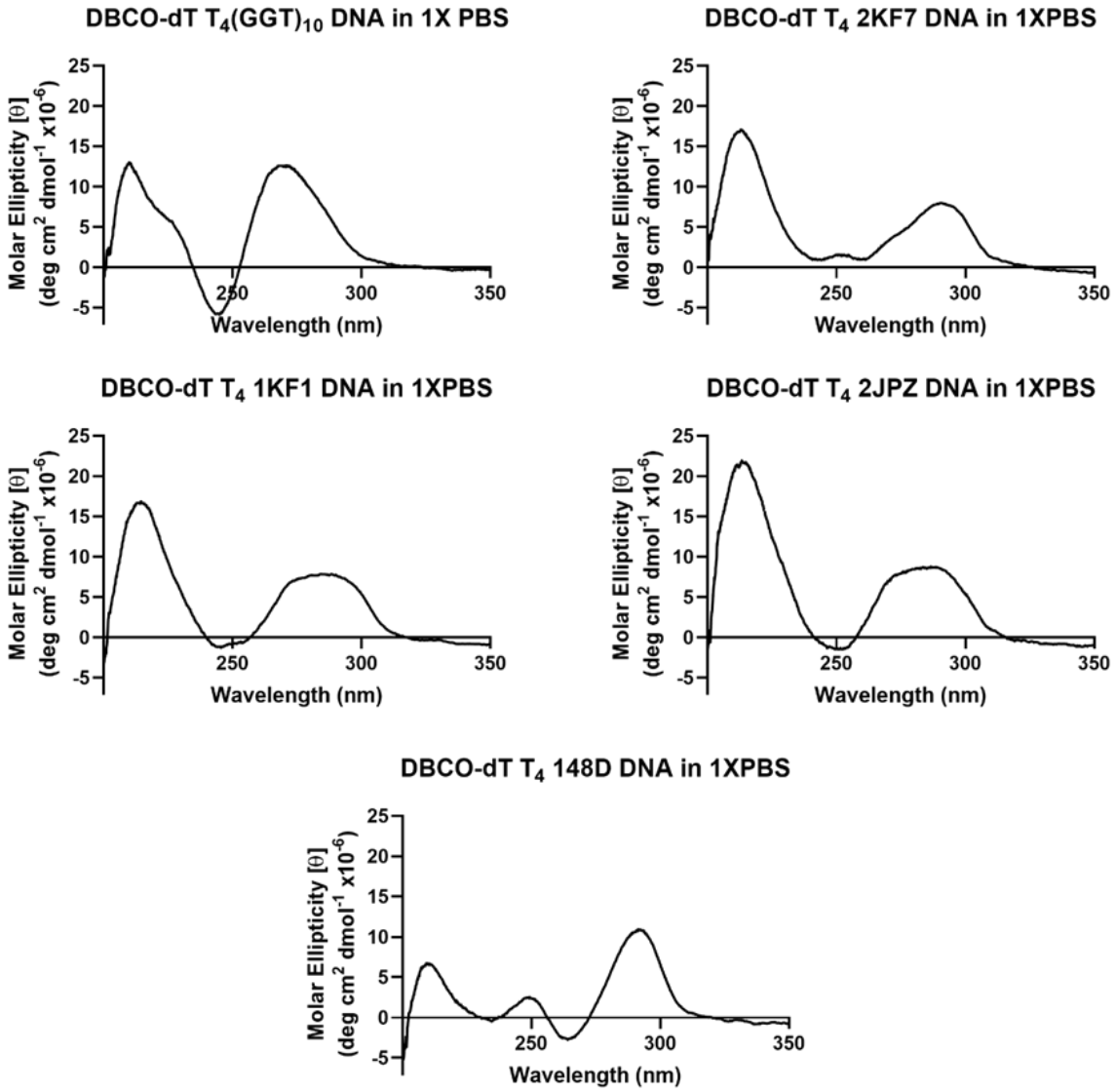

Figure 17. Circular dichroism (CD) spectra of free GQ DNA. CD spectra of 7.5 μM free DBCO-dT terminated strands with a T_4 DNA linker in 1X PBS. Sequences are detailed in Table S1.3. Spectra match the corresponding topology of (a) parallel, (b) antiparallel basket, (c) parallel, (d) mixed, and (e) antiparallel chair.

190-350 nm measurement range, 0.1 nm data pitch, 1 nm bandwidth, 50 nm/min scanning speed, and 5 accumulations. CD spectra were normalized to molar ellipticity ([θ], deg cm^2 $dmol^{-1}$) using $[\theta] = \frac{\theta \times 10}{c \times l}$ where θ is the CD ellipticity in millidegrees, c is the sample concentration in mol/L, and *l* is the pathlength in cm (**Figure 17**). Expected and observed peaks and troughs are tabulated in **Table 4.**

Table 4. G-Quadruplex Circular Dichroism Peak and Trough Signatures

Name	Sequence (5' to 3')	Expected **Peak** or *Trough*	Observed **Peak** or *Trough*
$T_4(GGT)_{10}$[97]	DBCO-dT $T_4(TGG)_{10}$	*245* **265**	**210** *245* **270**
2KF7[98]	DBCO-dT $T_4(G_3T_2A)_3G_3T$	*235* **250** *260* **290**	**215** *240* **250** *260* **290**
1KF1[99]	DBCO-dT $T_4AG_3(T_2AG_3)_3$	**215** *240* **290**	**215** *245* **280**
2JPZ[97]	DBCO-dT $T_4(T_2AG_3)_4T_2$	*240* **270** **290**	**215** *250* **280**
148D[97]	DBCO-dT $T_4G_2T_2G_2TGTG_2T_2G_2$	*230* **250** *270* **290**	**210** *230* **250** *265* **290**

2.7.1.4.2. Calculated CD spectra of Conjugated DNA strands on ProSNAs.

Circular dichroism (CD) spectra were recorded in a 1 mm pathlength cuvette at 22 °C with a Jasco J-1700 spectropolarimeter equipped with a temperature controller at a concentration of 300 nM β-Gal in 1X PBS buffer (pH 7.4) or 10 mM LiH_2PO_4 (pH 7.4). The instrument parameters to record the CD spectra were: 200-400 nm measurement range, 0.1 nm data pitch, 1 nm bandwidth, 200 nm/min scanning speed, and 10 accumulations. CD spectra were normalized to molar ellipticity ([θ], deg cm^2 dmol^{-1}) using $[\theta] = \frac{\theta \times 10}{c \times l}$ where θ is the CD ellipticity in millidegrees, c is the sample concentration in mol/L, and *l* is the pathlength in cm. Calculated spectra of the

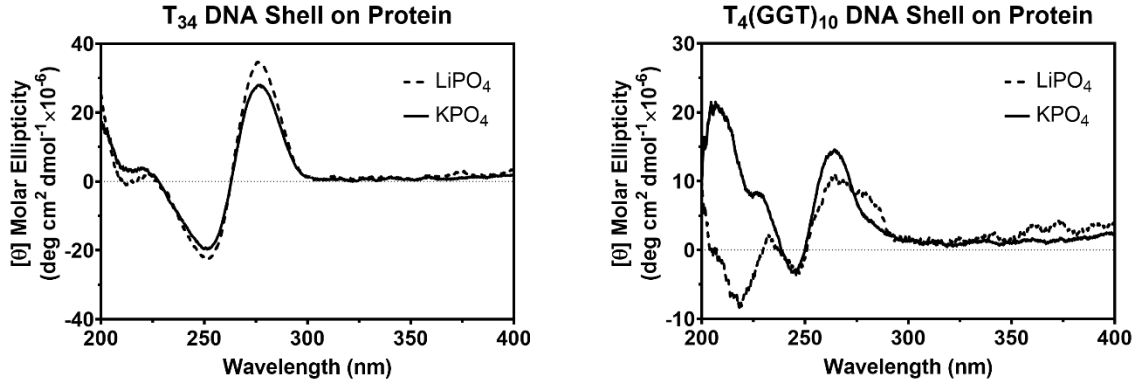

Figure 18. Calculated circular dichroism (CD) spectra of DNA conjugated to protein. Calculated spectra of T-rich or GQ DNA on protein in two different buffered conditions: KPO_4 (solid) and $LiPO_4$ (dashed). A strong shift in spectra for $T_4(GGT)_{10}$ DNA strands on the ProSNA indicates the loss of GQ secondary strucutre in the presence of a lithium based buffer.

DNA conjugated to the protein were obtained by subtracting the spectra of β-Gal-AF647 from the spectra of the ProSNAs in their respective buffers (**Figure 18**).

$$[\theta]_{DNA\ Conjugated\ to\ Protein} = [\theta]_{ProSNA} - [\theta]_{\beta-Gal-AF647}$$

2.7.2. *In Vitro* Investigations on ProSNA Variants

2.7.2.1. Cellular Uptake in HeLa Cells

HeLa cells (ATCC) were cultured in a 96-well plate in DMEM (Gibco) supplemented with 10% fetal bovine serum (Atlanta Biologicals) and 1% penicillin-streptomycin (Gibco). Once 80% confluent, cells were treated with either Alexa Fluor 647-modified native β-Gal or ProSNA variants for 2-4 h at 5-10 nM β-Gal (specific treatments are specified in figure captions). “Untreated”

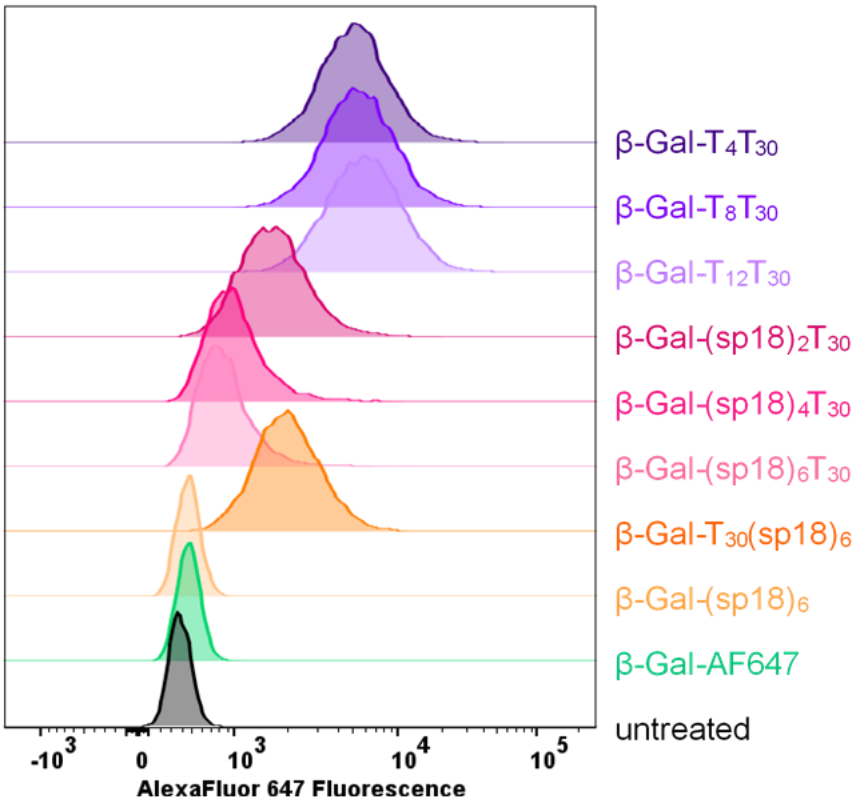

Figure 19. Representative histograms depicting cellular uptake of fluorophore modified ProSNA variants and native protein in HeLa cells. Flow cytometry was used to measure the upake of ProSNA variants or native protein in HeLa cells (*n* = 3) after 4 h treatments with 5 nM β-Gal in serum-containing media. Representative histogram of *n* = 1 per treatment, which shows the fluorescence intensity versus the number of events detected.

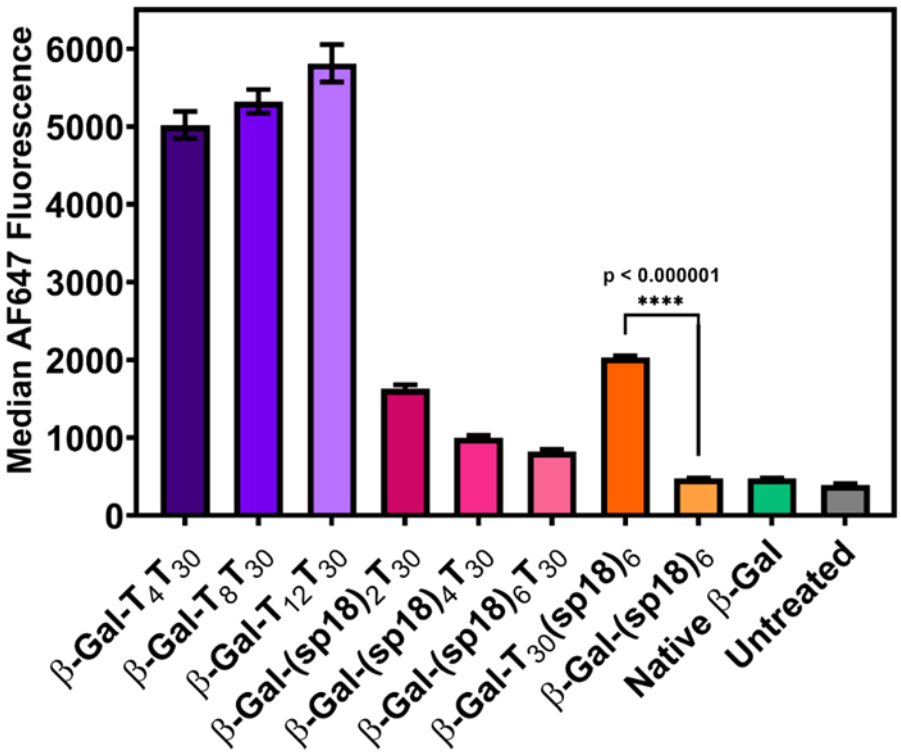

Figure 20. Median Alexa Fluor 647 fluorescence intensity from HeLa cells using flow cytometry. HeLa cells were treated with 5 nM β-Gal for 4 h in serum-containing media and subsequently analyzed by flow cytometry. The median fluorescence intensity of *n* = 3 wells was determined in FlowJo. The linker's deleterious uptake properties were further supported by switching the location of Spacer18 on the protein: cellular uptake recovers, confirming that placing Spacer18 near the protein surface is detrimental to internalization (orange bars).

samples refer to cells treated with the same volume of 1XPBS. Post-treatment, cells were washed with 1X PBS, trypsinized (Gibco), and fixed in 4% paraformaldehyde (Thermo Fisher Scientific) and subsequently analyzed by flow cytometry using a BD LSRFortessa measuring the fluorescence (excitation 640 nm, emission 655-685 nm) of at least 5000 single-cell events per sample. Raw FCS files were gated based on forward and side scatter intensities and analyzed on FlowJo (**Figure 19-Figure 21).**

2.7.2.2. Cellular Uptake in C166 Cells

C166 cells (ATCC) were cultured in a 96-well plate in DMEM (Gibco) supplemented with 10% fetal bovine serum (Atlanta Biologicals) and 1% penicillin-streptomycin (Gibco). Once 80%

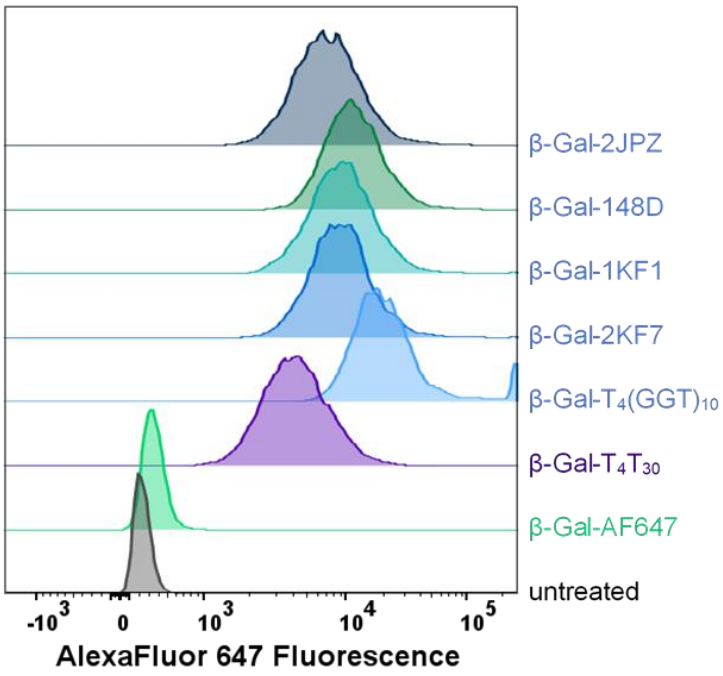

Figure 22. Representative histograms depicting cellular uptake of fluorophore modified ProSNA variants and native protein in HeLa cells. HeLa cells (*n* = 3) were treated with 10 nM β-Gal for 2 h in serum-containing media and subsequently analyzed by flow cytometry. Representative histogram of *n* = 1 per treatment, which shows the fluorescence intensity versus the number of events detected. Median MFI is plotted in Figure 6B.

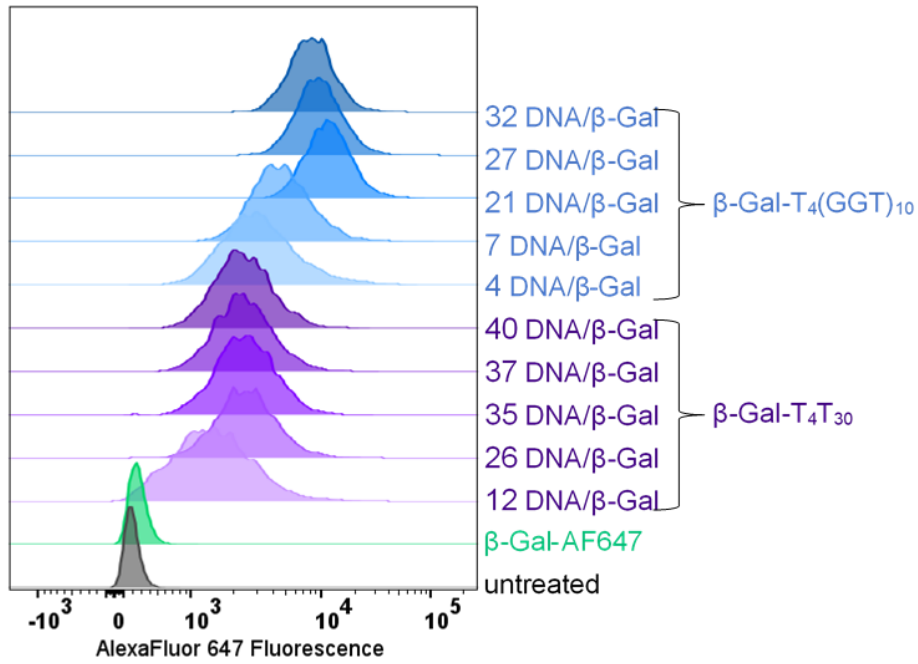

Figure 21. Representative histograms depicting cellular uptake of fluorophore modified ProSNA variants and native protein in HeLa cells. HeLa cells (*n* = 5) were treated with 10 nM β-Gal or ProSNA for 2 h in serum-containing media and subsequently analyzed by flow cytometry. Representative histogram of *n* = 1 per treatment, which shows the fluorescence intensity versus the number of events detected. Median MFI is plotted in Figure 6C.

confluent, cells were treated with either Alexa Fluor 647-modified native β-Gal or ProSNA variants for 4 h at 10 nM β-Gal. Post-treatment, cells were washed with 1X PBS, trypsinized (Gibco), and fixed in 4% paraformaldehyde (Thermo Fisher Scientific) and subsequently analyzed by flow cytometry using a BD LSRFortessa measuring the fluorescence (excitation 640 nm, emission 655-685 nm) of at least 5000 single-cell events per sample. Raw FCS files were gated based on forward and side scatter intensities and analyzed on FlowJo (**Figure 23**).

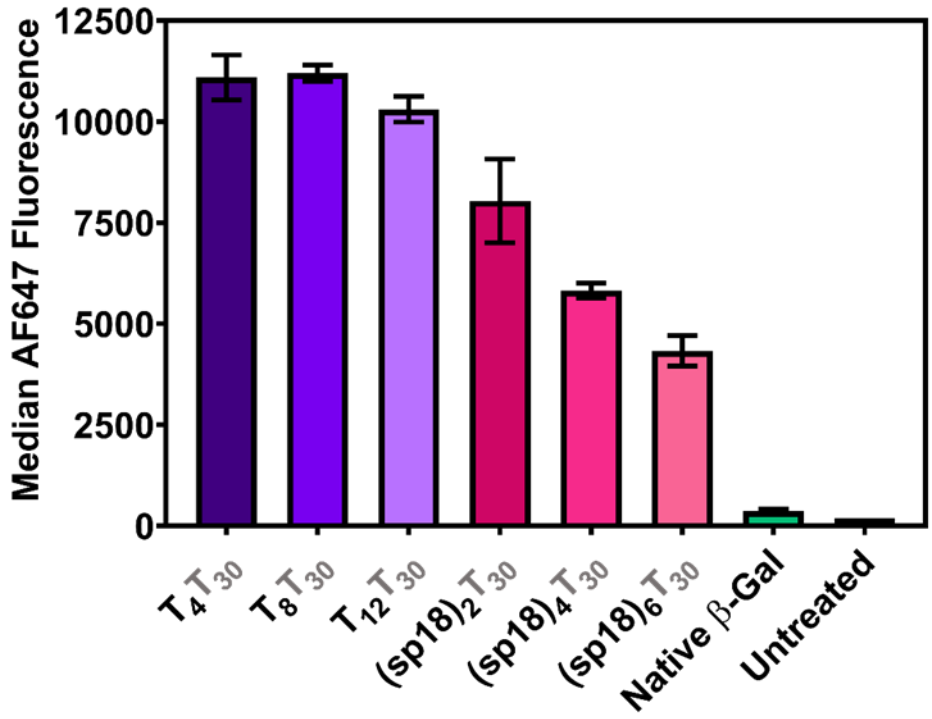

Figure 23. Median Alexa Fluor 647 fluorescence intensity from C166 cells using flow cytometry. C166 cells were treated with 10 nM β-Gal for 4 h in serum-containing media and subsequently analyzed by flow cytometry. The median fluorescence intensity of *n* = 3 wells was determined in FlowJo. The study demonstrates the generalizability of the linker's deletrious effect on a ProSNA's uptake in two differernt cell lines.

2.7.2.3. Kinetic Analysis of β-Galactosidase Activity

o-Nitrophenyl β-D-galactopyranoside (ONPG) was purchased from Thermo Fisher Scientific. Sodium phosphate, magnesium chloride, and 2-mercaptoethanol were obtained from

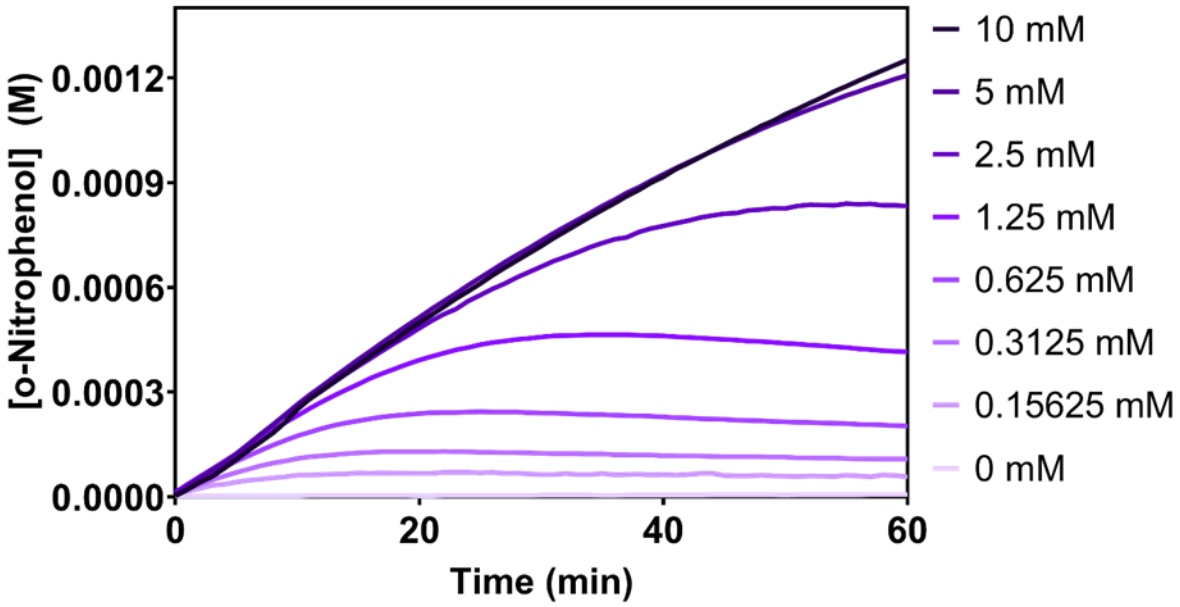

Figure 24. Representative kinetic reaction of the T_{34} ProSNA at various ONPG concentrations. The rate of ONPG turnover to o-nitrophenol in the prescence of 0.5 nM T_{34} ProSNA at indicated ONPG concentrations. The kinetic reactions were run in a 96 well plate and the absorbance at 420 nm was taken every 30 s using a BioTek Cytation5. In Excel, the absorbance readings were converted to concentrations of product and the slope in the linear portion of the curve ($R^2 \geq 0.99$) was calculated to the be the intial rate, V_o.

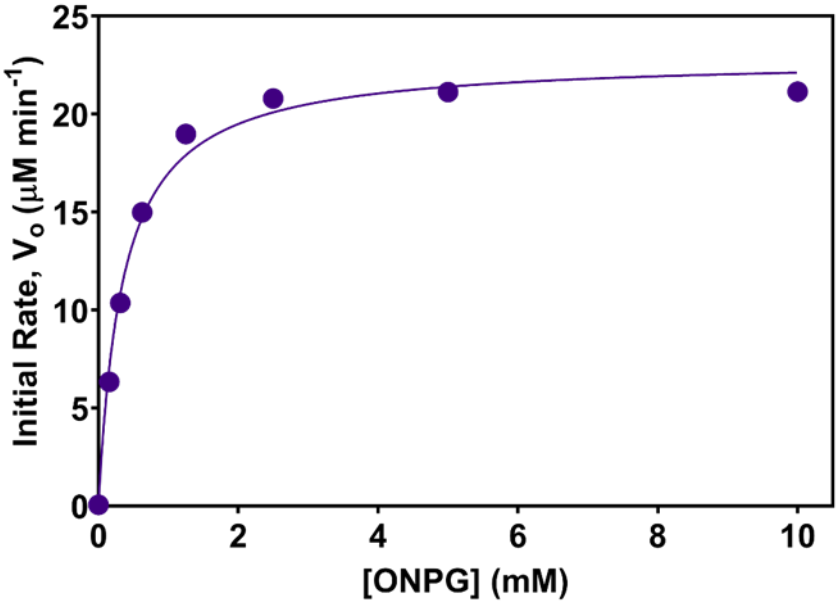

Figure 25. Representative graph of the effect of substrate concentration on the enzyme's inital rate. The initial rate of the T_{34} ProSNA was first determined kinetically (see Figure 24) and plotted against the ONPG substrate concentration. GraphPad Prism nonlinear regression software was then used to fit the data to a curve and thus determine the k_{cat} of the ProSNA variants.

Sigma Aldrich. All reactions were run in an assay buffer consisting of 100 mM sodium phosphate (pH 7.0), 1 mM $MgCl_2$, and 50 mM 2-mercaptoethanol. To determine Michaelis-Menten values, a dilution series of ONPG ranging from 4 mM to 0.0625 mM was made using the assay buffer as the diluent in a black 96-well clear bottom plate (Corning). Reactions were initiated by the addition of either native β-Galactosidase or ProSNA variants, to a final [β-Gal] of 0.5-1 nM, using a multichannel pipette (specified concentration in the figure caption). Absorbance readings were taken immediately at 420 nm every minute for a total of 45 min at ambient temperature with shaking between each reading in a BioTek Cytation 5 plate reader. To determine Michaelis-Menten values, the absorbance reading was converted to the concentration of *o*-nitrophenol using its extinction (ε_{420} = 4500 $M^{-1}cm^{-1}$) and a calculated plate pathlength of 0.23 cm. Excel was used to calculate the slope of the linear part of the line ($R^2 \geq 0.99$) in a graph of [*o*-nitrophenol] v. time

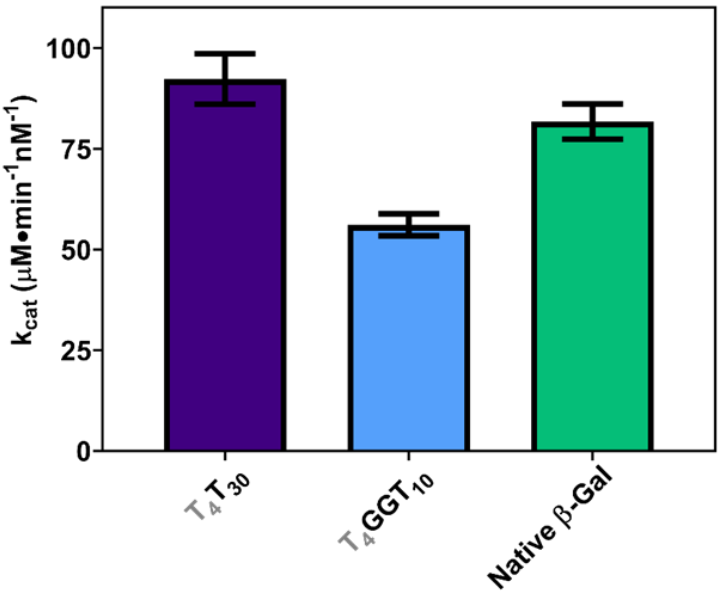

Figure 26. Average k_{cat} (*n* = 3) of the ProSNA variants and native protein. DNA modification of the protein with a T-rich sequence does not significantly affect its enzymatic activity; however, by introducing a GQ DNA shell, the activity of the enzyme decreases. The k_{cat} was determined by an ONPG assay of ProSNAs (both 20 DNA/ β-Gal) and the native protein. Relative activity is shown in Figure 2D of the main text. [β-Gal] = 1 nM

(**Figure 24**). Finally using GraphPad Prism nonlinear regression software, data were fit to a curve using the following model (**Figure 25**):

$$y = \frac{E_t\, k_{cat}\, x}{K_m + x}$$

The average k_{cat} of three separate trials is graphed in **Figure 27-Figure** *26*.

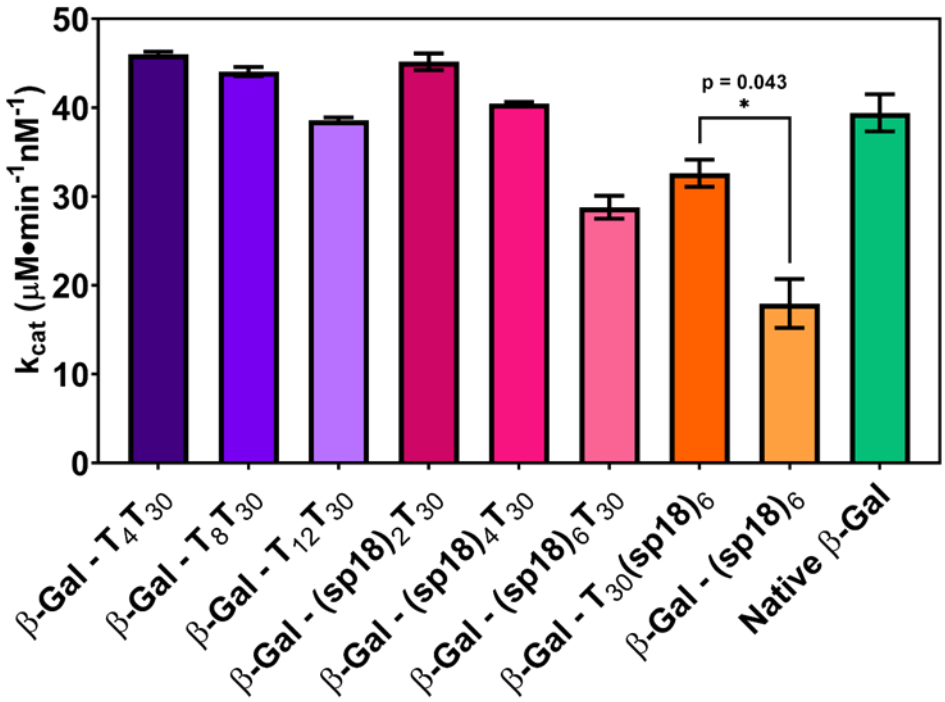

Figure 27. Average k_{cat} (*n* = 3) of the ProSNA variants and native protein. DNA modification of the protein does not significantly affect its enzymatic acitivity; however, with the addition of longer linker lengths, the activity of the enzyme decreases. This effect is more dramatic for the Spacer18 linkers (pink v. purple bars). In addition, there is a more than 50% decrease in activity after conjugating only Spacer18 (light orange) on the protein surface. This loss can be partially reversed by introducing a T_{30} oligonucleotide strand between the Spacer18 and the protein (dark orange). [β-Gal] = 0.5 nM

2.7.3. *In Vivo* Investigations Using Model ProSNA Variants

Female CD-1 mice (strain code: 022) were procured from Charles River Laboratory at 8 weeks of age and maintained in conventional housing. All animal experiments were carried out in accordance with the approved IACUC protocol issued by Northwestern University.

2.7.3.1. Blood Circulation Time

Pharmacokinetic studies were performed in female CD1 mice (28-30g). Alexa Fluor 647 modified native β-Galactosidase or ProSNA variants were administered in a single injection via the tail vein at a dose of 4 mg β-Gal / kg body weight. Blood (*n* = 3 per time point) was collected in a heparinized tube via retro-orbital blood draw and stored on ice. Blood was centrifuged at 1200 rpm for 7 min, and the fluorescence of the resulting supernatant, or plasma, was measured in a black 384-well plate using the BioTek Cytation 5 plate reader (excitation 640 nm, emission 680 nm).

2.7.3.2. Ex Vivo Near-Infrared Fluorescence (NIRF) Imaging

NIRF imaging studies were performed using a Caliper Life Sciences *In Vivo* Imaging System (IVIS) to determine the extent of protein accumulation in main organs at different time points post-injection. Female CD1 mice (28-30 g) were administered a single injection via tail vein at a dose of 4 mg β-Gal / kg body weight. At different time points post-injection, as specified in the figure, mice (*n* = 3 per time point) were humanely euthanized by cardiac perfusion while anesthetized. Tissues were harvested post-cardiac perfusion with 1X PBS and fixed in 4% paraformaldehyde for 1 h at 4 °C. Post-fixation, organs were washed three times with 1X PBS and stored in 1X PBS at 4 °C. Finally, organs were imaged using an IVIS system using 650 nm/700 nm excitation/emission filters and data was quantified by measuring fluorescence counts with the Living Image software. **Figure 28 - Figure 29** displays the IVIS images from each main organ post the indicated treatment time. **Figure 30** displays the IVIS image from each main organ post a 1 h injection.

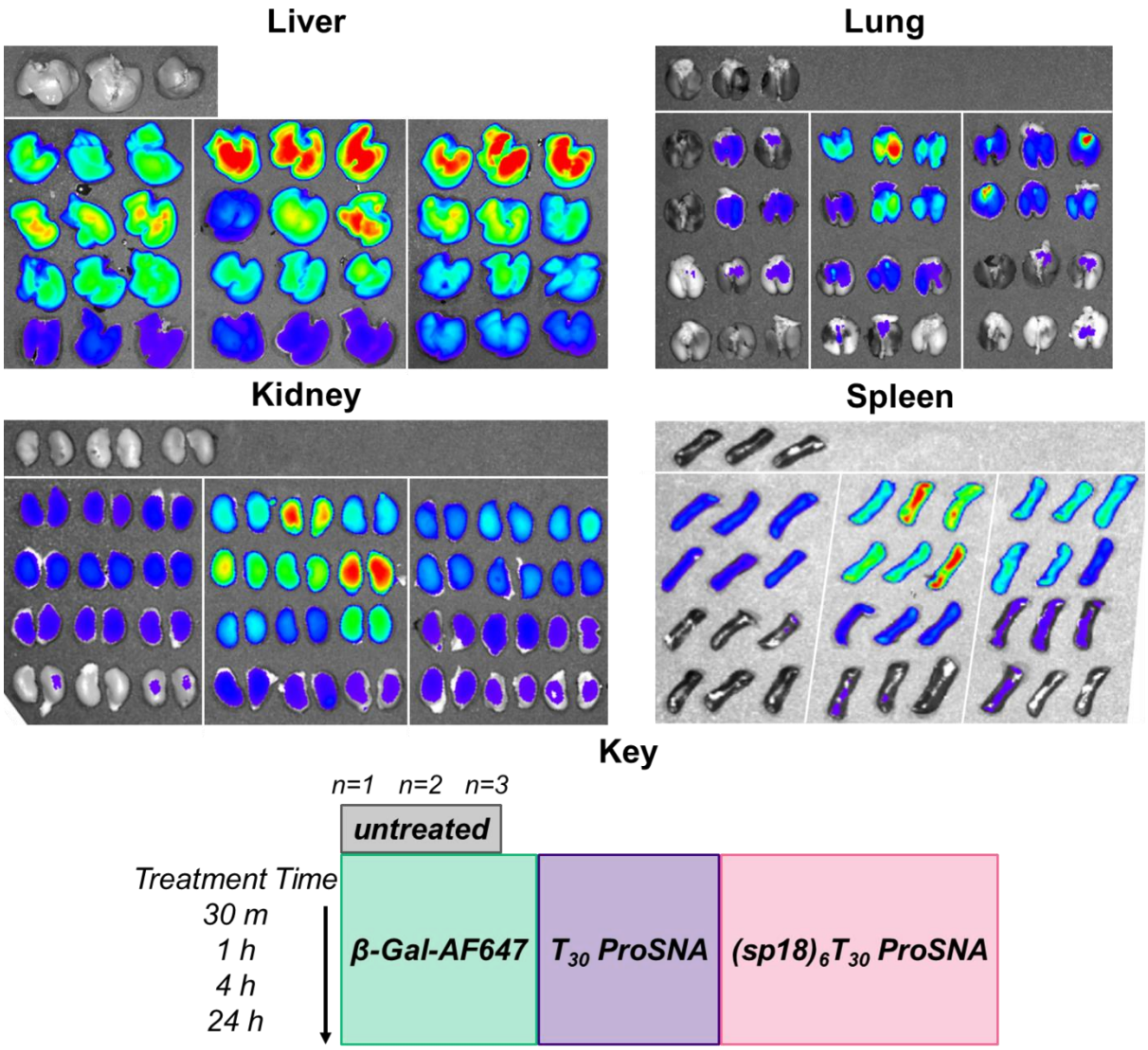

Figure 28. Temporal distribution of fluorophore modified ProSNAs and native protein in four main organs. The distribution of two ProSNA variants—with and without Spacer18 linker—and native protein were studied by measuring the fluorescence using IVIS (exictiation 650 nm, emission 700 nm) in four main organs: a) liver, b) lung, c) kidney, and d) spleen. Post the indicated treatment (see key; e), mice were sacrificed, perfused, and their organs dissected and fixed. T_{30} ProSNA demonstrates enhanced distribution and retention in imaged organs in comparison to the $(sp18)_6T_{30}$ ProSNA and native protein. Using the Living Image software, a region of interest was drawn around each organ and fluorescence counts were quantified (see Figure 7B).

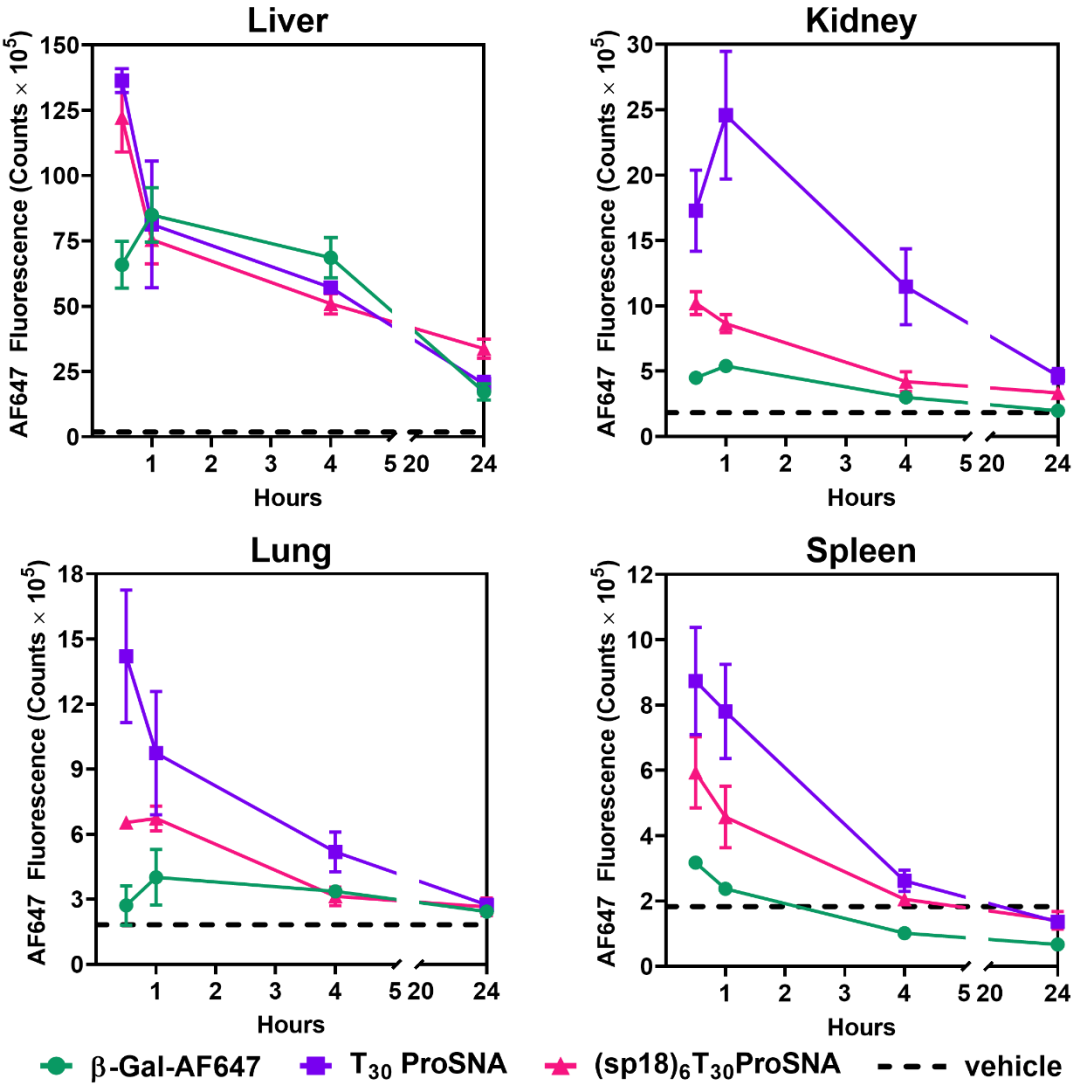

Figure 29. Temporal distribution of fluorophore modified ProSNAs and native protein in four main organs. The distribution of two ProSNA variants—with and without Spacer18 linker—and native protein were studied by measuring the fluorescence using IVIS (exictiation 650 nm, emission 700 nm) and reported versus time in four main organs: a) liver, b) lung, c) kidney, and d) spleen. Post the indicated treatment (x-axis), mice were sacrificed, perfused, and their organs dissected and fixed. T_{30} ProSNA demonstrates enhanced distribution and retention in imaged organs in comparison to the $(sp18)_6T_{30}$ ProSNA and native protein.

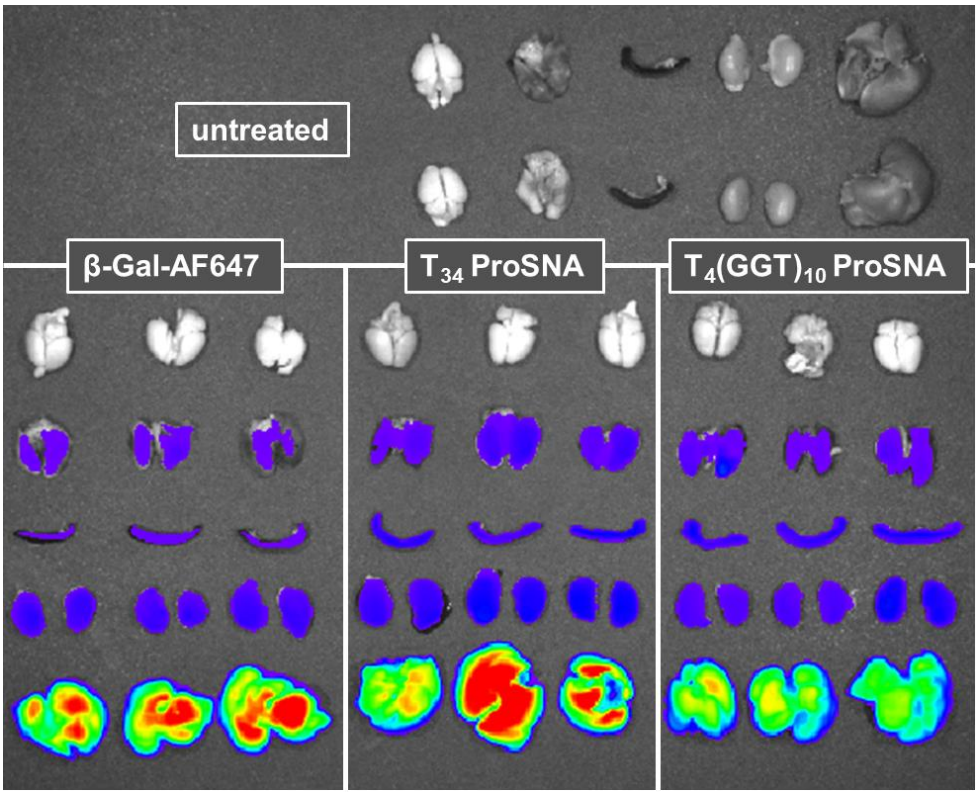

Figure 30. Temporal distribution of fluorophore modified ProSNAs and native protein in four main organs. The distribution of two ProSNA variants—T-rich and GQ sequence—and native protein were studied by measuring the fluorescence using IVIS (exictiation 650 nm, emission 700 nm) in five main organs: brain, liver, lung, kidney, and spleen. Post 1 h treatment, mice were sacrificed, perfused, and their organs dissected and fixed. Using the Living Image software, a region of interest was drawn around each organ and fluorescence counts were quantified (see **Figure 7C**).

2.7.3.3. Enzymatic Colorimetric Activity Assay of Main Organs

Female CD1 mice (29-35 g) were administered a single injection via tail vein at a dose of 6.5 mg β-Gal / kg body weight. One-hour post-injection, mice (*n* = 3) were humanely euthanized by cardiac perfusion while anesthetized. Each mouse was first perfused with 20 mL of 1X PBS, then 20 mL of 4% paraformaldehyde (PFA; Thermo Fisher Scientific), and main organs were dissected and stored in 4% PFA with shaking at 4 °C for 2 h. Organs were rinsed in many changes of 1X PBS and equilibrated overnight in 15% sucrose (Sigma Aldrich) in 1X PBS solution at 4 °C. The organs were subsequently transferred to a 30% sucrose in 1X PBS solution and stored at 4 °C until the organs sunk to the bottom of their respective container. Each organ was then

embedded in optimal cutting temperature compound and cryo-sectioned at 10 µm (kidney, liver, spleen) or 20 µm (lung) thickness. The slides were stored at -80 °C until staining. EGTA, sodium deoxycholate, potassium ferrocyanide, potassium ferricyanide, glutaraldehyde, xylene, Nuclear Fast Red, and aluminum sulfate were obtained from Sigma Aldrich. NP-40 Alternative was from Santa Cruz Biotechnology. X-Gal (5-bromo-4-chloro-3-indolyl-β-D-galactopyranoside), Permount, and ethanol were purchased from Thermo Fisher Scientific. **Table 5** provides the details of solutions used during the X-Gal histology staining protocol. Slides were first fixed in the *Fixative* solution for 10 min at room temperature. Subsequently, slides were washed in a *Wash Buffer* for 5 min three times. The slides were then stained at 37 °C for 6 h with shaking at 40 rpm in a *Reaction Buffer*. Slides were washed three times for 5 min in *PBS-Mg^{2+}* then once more in Milli-Q filtered (MQ) water. To counterstain, slides were stained for 5 min in a *Histology Counterstain* and quickly washed three times in MQ water. Slides were then dehydrated through ethanol and xylene baths as follows: 70% ethanol (EtOH) (1 min), 95% EtOH (2.5 min), 100% EtOH (3.5 min), xylene (twice, 3 min). A coverslip was then mounted to each slide using Permount. A BioTek Cytation 5 Imaging Multi-Mode Reader was used to image each slide at a 10X magnification. **Figure 31** is a microscope image of the entire organ section.

Table 5. X-Gal Staining Reagents

Solution Name	Component	[Component]	Diluent
Fixative	Glutaraldehyde EGTA $MgCl_2$	0.2% 5 mM 100 mM	1X PBS
Wash Buffer	Sodium deoxycholate NP-40 $MgCl_2$	0.01% 0.02% 2 mM	1X PBS
Reaction Buffer	Potassium Ferrocyanide Potassium Ferricyanide X-Gal	5 mM 5 mM 1 mg/mL	Wash Buffer
PBS-Mg^{2+}	$MgCl_2$	2 mM	1X PBS
Histology Counterstain	Nuclear Fast Red Aluminum Sulfate	0.1% 5%	Milli-Q Water

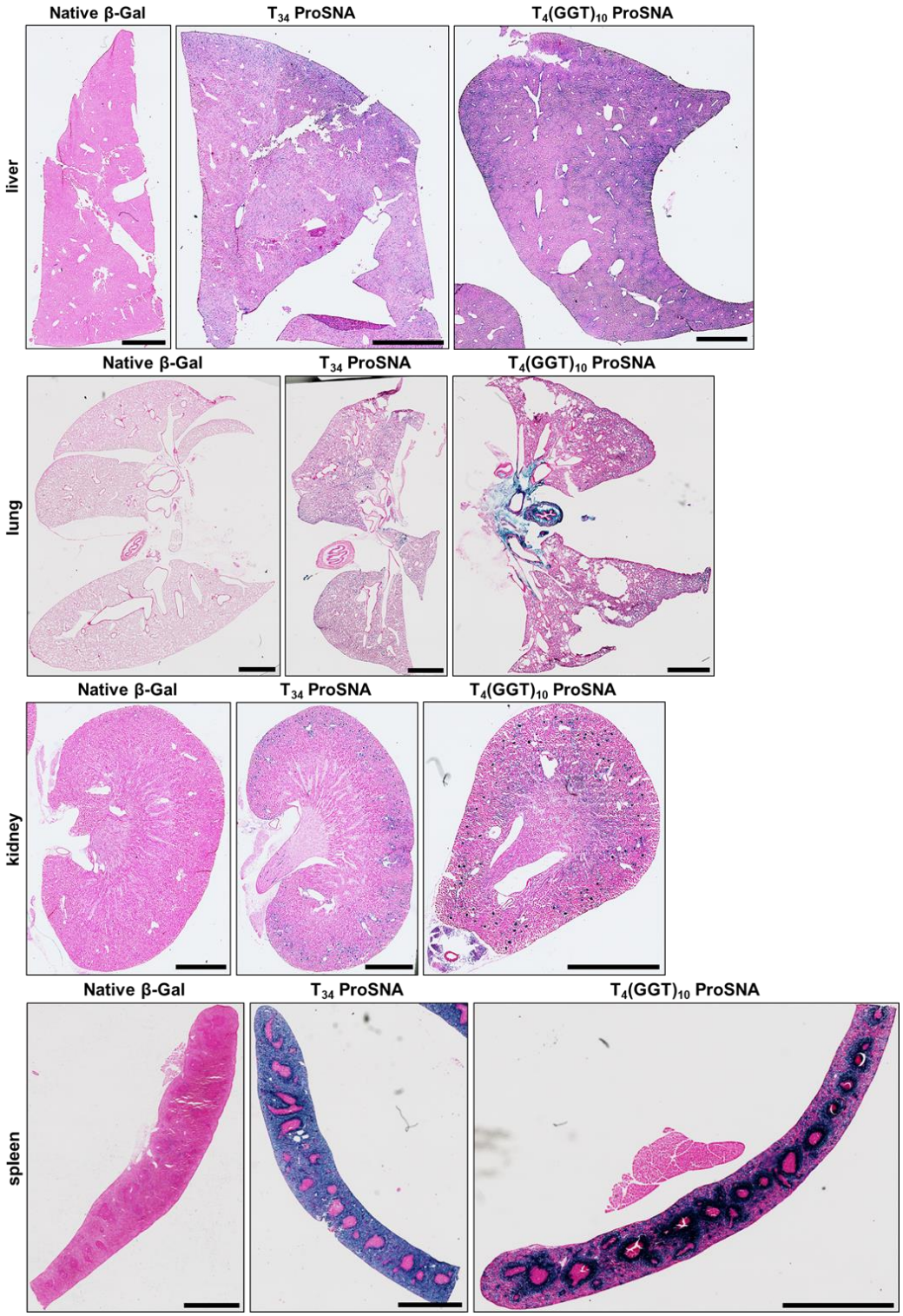

Figure 31. *In vivo* catalytic activity and tissue distribution of native β-Gal and ProSNAs. Representative light micrographs of histology slides after incubation with the β-Gal substrate, X-Gal. The blue color apparent in tissue dissected from mice (n = 3) 1 hour post intravenous injection of 6.5 mf enzyme/kg mouse results from the hydrolysis of X-Gal and the formation of an insoluble blue product. Scale = 2000 μm.

CHAPTER 3. STRATEGIES TO INCREASE BRAIN DELIVERY OF PROTEIN SPHERICAL NUCLEIC ACIDS

Material in this chapter is based upon on-going work:

Kusmierz C.D.; Callmann, C.E.; Mirkin C.A. “Transferrin Aptamers Increase the *In Vivo* Blood-Brain Barrier Penetration of Protein Spherical Nucleic Acids.” *In preparation*.

3.1. Introduction

The intracellular delivery of proteins is inherently challenging because of natural barriers that living systems have evolved to maintain homeostasis.[100] One such barrier—the cell membrane—restricts the simple diffusion of large and charged proteins from entering cells. Moreover, the abundance of proteases in the biological milieu reduces the lifetime of any exogenously delivered proteins. Despite these limitations, replacing defective enzymes with recombinant enzymes for lysosomal storage disorders (LSDs), thus restoring its enzymatic activity, has generally improved the quality of life for patients. Although many approved enzyme replacement therapies (ERT) have clinical success, the biodistribution of the enzymes into the difficult sites of pathology, such as the central nervous system (CNS), remains a challenge. In addition to LSDs, age-dependent neurodegenerative disorders, such as Parkinson's Disease and Lewy body dementia, have been linked to loss-of-function mutations of lysosomal enzymes. Therefore, a delivery method to overcome the limited access of enzymes to the CNS is needed.[101-103]

A significant obstacle that prevents the access of enzymes to the CNS is the blood-brain barrier (BBB).[104-106] The blood-brain barrier (BBB) is a highly selective barrier that prevents circulating blood solutes from reaching the CNS and is regulated by endothelial cells whose tight junctions form the impermeable walls of blood vessels. There has been a variety of strategies to penetrate the BBB or bypass it entirely. For example, local ultrasonic irradiation to the brain enhances the delivery of intravenously injected DNA-encapsulated microbubbles to brain tumors.[107-109] Alternative methods, such as direct injection of therapeutics into the cerebral spinal fluid (CSF) through intrathecal[110, 111] or intracranial[112] injections, are sometimes limited to disease targets on the surface of the brain or spinal cord, owing to a lack of drug diffusion.[111, 113, 114] In this chapter, three alternative strategies for facilitating protein delivery to the brain will be discussed

and span from DNA shell design strategies to promote BBB penetration to direct injection into the CNS.

3.2. Receptor-Mediated Transcytosis

The targeted delivery of proteins to the brain and central nervous system (CNS) is inherently challenging[104-106, 115] because of the many natural mechanisms and barriers that living systems have evolved to maintain homeostasis.[100] Firstly, unmodified proteins are rapidly degraded by serum proteases[116], which inherently limits their effective delivery to target sites. Moreover, the blood-brain barrier (BBB) is a highly selective barrier that prevents circulating materials from reaching the CNS and is regulated by endothelial cells whose tight junctions form the impermeable walls of blood vessels[117, 118]. Finally, even if the issues with proteolysis and the BBB are overcome, the cell membrane itself prevents the passive movement of exogenous materials into cells within the brain. As such, strategies to improve the intracellular delivery of proteins to the brain and CNS are warranted.

The BBB is a highly regulated barrier, where endothelial cells control the influx of nutrients and molecules into the brain via both passive and active pathways. Lipid-soluble substances (CO_2 and O_2) freely cross the BBB[119], while larger solutes gain access to the brain through active transport via receptors abundant in the endothelium[120, 121]. Accordingly, transport receptors, such as those for insulin[122, 123], glucose[124], or transferrin[57, 58, 125-130] (TfR), provide potential avenues for the transport of proteins across the BBB through chemical modifications with the respective ligands. Indeed, lysosomal enzymes modified with antibodies specific to both the insulin[122, 123] and TfR receptor[125, 129, 130] have shown significantly increased BBB penetration *in vivo*. Likewise, aptamers—short single-stranded DNA or RNA oligonucleotides that can assume secondary structures with high affinity and specificity to a target—have been evolved to transport oligonucleotides across the BBB via TfR receptors[128].

Spherical nucleic acids (SNAs) comprise a class of nanomaterials where oligonucleotides are densely functionalized around a nanoparticle core in a highly oriented manner.[4, 82] This spherical arrangement imparts biological properties to the composite oligonucleotides that are distinct from their linear counterparts, including rapid cellular uptake through scavenger receptor-mediated endocytosis and enhanced stability to degrading enzymes.[6, 11, 33, 38, 81] Importantly, proteins that are normally cell impermeable and highly susceptible to protease degradation are rendered permeable and protease-resistant when functionalized with oligonucleotides as protein spherical nucleic acids (ProSNAs).[8, 81] Previous work has found that the DNA shell not only protects the protein, but also alters its biodistribution following systemic administration.

Herein, we hypothesized that the intracellular delivery of proteins to cells within the CNS could be maximized using the ProSNA platform via covalent functionalization with DNA aptamers

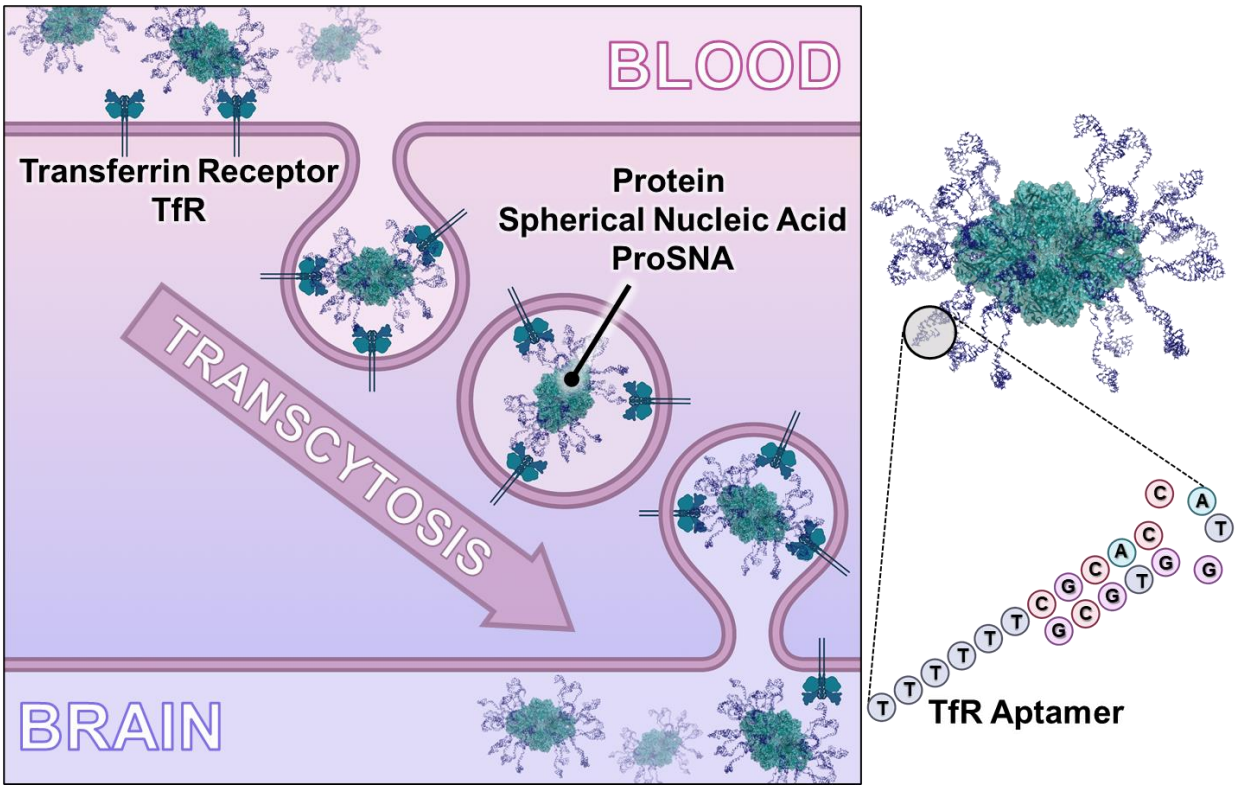

Figure 32. Receptor Mediated Transcytosis of ProSNAs Across the Blood-Brain Barrier. Cartoon representation of β-Gal ProSNAs being shuttled across an endothelial cell to the brain via the transferrin receptor. The surface of β-Gal is decorated with a shell of transferrin-specific aptamers covalently conjugated to surface lysine residues, resulting in a Protein Spherical Nucleic Acid (ProSNA). The representation was adapted from PDB ID 1PX3.

specific to the TfR receptor. DNA shell design is a critical parameter influencing the cellular uptake and biodistribution[3, 24, 25, 81, 131-133] of SNAs, and we reasoned that a ProSNA's distribution could be specifically directed by introducing a targeting sequence. Therefore, we synthesized ProSNAs bearing TfR aptamers using β-Galactosidase (β-Gal) as a model protein (Transferrin-ProSNAs, **Figure 32**) and assessed their uptake in an *in vitro* BBB model and their accumulation in cells within the CNS following intravenous injection into healthy mice.

3.2.1. DNA Transferrin Aptamers Associate with the Extracellular Domain of Transferrin Receptor.

The transferrin (TfR) aptamer sequence was selected based on prior research using SELEX to evolve and truncate aptamers, resulting in a 14-mer sequence with a strong binding affinity to the extracellular domain of the mouse transferrin receptor.[59-61] A scrambled DNA sequence, which differs from TfR by four bases in the loop region and has no receptor binding affinity, was synthesized as a control for aptamer-mediated uptake. With these materials in hand, their ability to bind the TfR receptor was assessed using bio-layer interferometry (BLI). In this experiment, the extracellular domain (ECD) of the transferrin receptor (containing an N-terminus polyhistidine tag) was first immobilized on the tip of a single-use Anti-Penta-His (HIS1K) coated fiber optic probe. After equilibration in PBS buffer, each probe was incubated in a TfR aptamer solution. The aptamer-receptor binding was measured by a shift in the wavelength of light reflected from the probe's tip (**Figure 33A**). The binding affinity was calculated by fitting BLI association and dissociation curves with a range of TfR aptamer concentrations (**Figure 33B**). Through these analyses, the dissociation constant (Kd) of the TfR aptamer binding to its receptor was determined to be 37.8 ± 9.06 μM (n = 3). This confirms that the TfR aptamer sequence efficiently binds the TfR receptor as designed and thus is an appropriate sequence for use in the synthesis of ProSNAs that can efficiently penetrate the BBB.

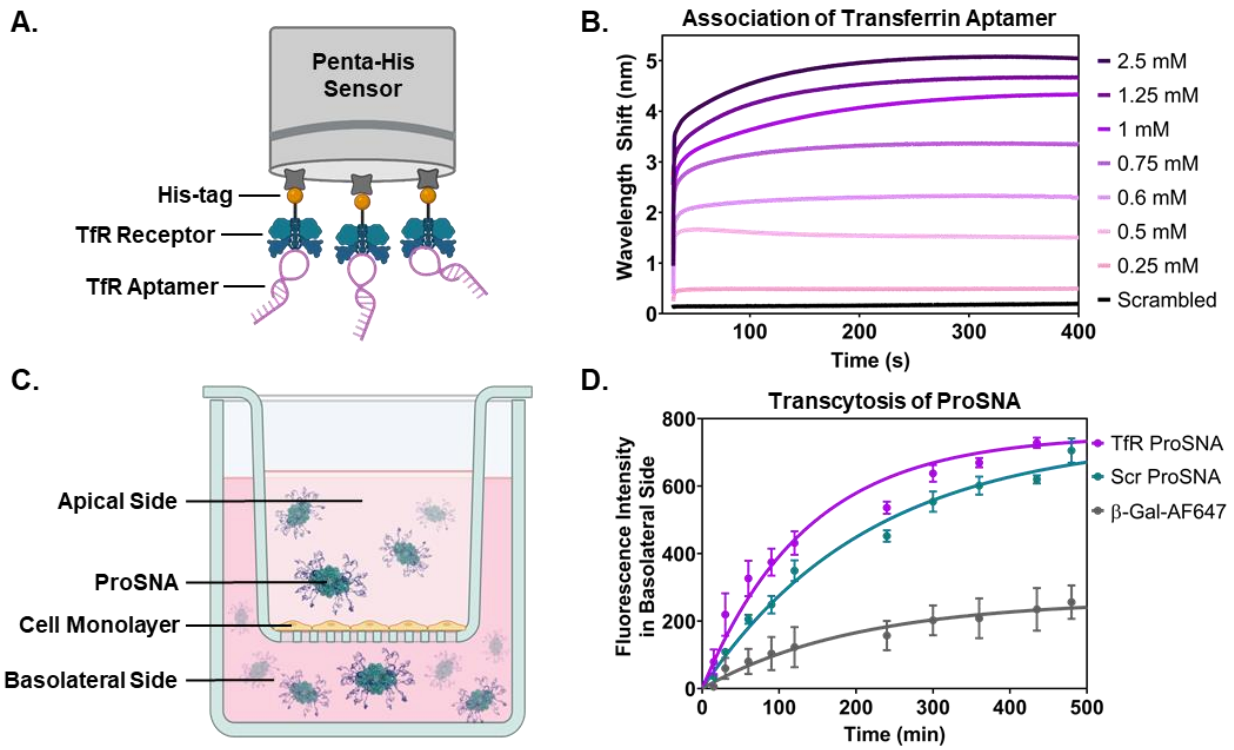

Figure 33. Bio Layer Interferometry and *in vitro* BBB Analysis Demonstrates Specificity of Transferrin Aptamer for Receptor. (A) Schematic of a BLI receptor-aptamer association experiment. The extracellular domain of the transferrin receptor is immobilized on the sensor's surface and the association of aptamers to the receptor is monitored by a change in optical thickness at the sen-sor's tip generating a wavelength shift. (B) The wavelength shift generated by the addition of different concentrations of transfer-rin aptamer (purple lines), or lack of signal by the scrambled aptamer (black line), establishes sequence specific affinity of ap-tamers to the receptor. Each line is the mean of n = 3 measurements. (C) Representation of ProSNAs crossing an in vitro BBB model. Cells were treated with fluorescently labeled proteins on the apical side of a transwell insert. (D) Fluorescence readings of the basolateral side were taken periodically and plotted to measure the protein's transcytosis efficiency. Each point represents the mean of n =3 measurements, the error bars show SD, and the line is a nonlinear regression fit graphed using GraphPad Prism.

3.2.2. Transferrin-ProSNAs Are Successfully Synthesized through the Functionalization of β-Galactosidase with Transferrin Aptamer DNA.

Protein SNAs bearing either TfR aptamers (Transferrin-ProSNAs) or the scrambled DNA sequence (Scr-ProSNAs) were synthesized using published protocols[8, 81]. β-Gal was chosen as a model system to assess brain delivery efficacy because it is a large (464 kDa) protein, easily amenable to DNA conjugation, and does not naturally traverse cell membranes. To track the distribution of β-Gal *in vivo*, an Alexa Fluor647 (AF647) fluorophore tag was conjugated to surface-accessible cysteines on the protein. Following successful fluorophore labeling, the lysine

residues were modified with azide-functionalized-PEG_4, which was subsequently reacted with DBCO-dT-terminated aptamer DNA strands through a strained-promoted alkyne azide cycloaddition. A thymidine DNA spacer (T4) was appended to the 3' end of each sequence to distance the aptamer from the protein surface and promote sequence folding. Covalent DNA conjugation to the protein core was confirmed using sodium dodecyl sulfate polyacrylamide gel electrophoresis (SDS-PAGE), which showed mobility shifts commensurate with the increased mass following DNA addition (**Figure 41**). Using circular dichroism (CD) spectroscopy, it was confirmed that the secondary structure of β-Gal was not altered following fluorophore and DNA conjugation (**Figure 42**).

3.2.3. Transferrin-ProSNAs Penetrate Cell Monolayer Faster in an *In Vitro* BBB Model.

With Transferrin-ProSNAs in hand, we sought to determine the extent to which the aptamer is able to promote receptor-mediate transcytosis.[121] For these experiments, bEnd.3 mouse brain endothelial cells, known to highly express the TfR receptor[57, 134], were cultured to form a monolayer and simulate the tight endothelial junctions that comprise the BBB. Once the monolayer was established, Transferrin-ProSNAs, Scr-ProSNAs, or native β-Gal were applied to the apical side (**Figure 33C**). The fluorescence of the media on the basolateral side was measured over time using a plate reader fluorimeter as a proxy for protein transcytosis. The fluorescence intensity of the media in wells treated with both ProSNA constructs increased steadily as a function of time and at a much faster rate than the native protein (**Figure 33D**). It is to be expected that the Scr-ProSNA would exhibit some degree of transcytosis capability, as it has been previously shown in a clinical trial that SNAs synthesized with gold cores cross the BBB and accumulate in glioblastoma brain tumors following systemic injection, presumably facilitated by scavenger-mediated movement.[30, 32] Regardless, the Transferrin-ProSNAs exhibited a

significantly faster rate of transcytosis (k= 0.44 ± 0.08 hr $^{-1}$) than the Scr-ProSNAs (k = 0.28 ± 0.04 hr $^{-1}$), which we conclude is due to their increased affinity to the transferrin receptor.

3.2.4. Transferrin ProSNAs Significantly Increase the *In Vivo* Accumulation of Proteins in the Brain.

By employing TfR aptamers as the DNA shell, we hypothesized that Transferrin-ProSNAs can target the BBB, affect transcytosis and enter the brain. Therefore, to study the brain targeting efficiency of Transferrin-ProSNAs, CD-1 mice (*n* = 6) were injected intravenously (IV) with either

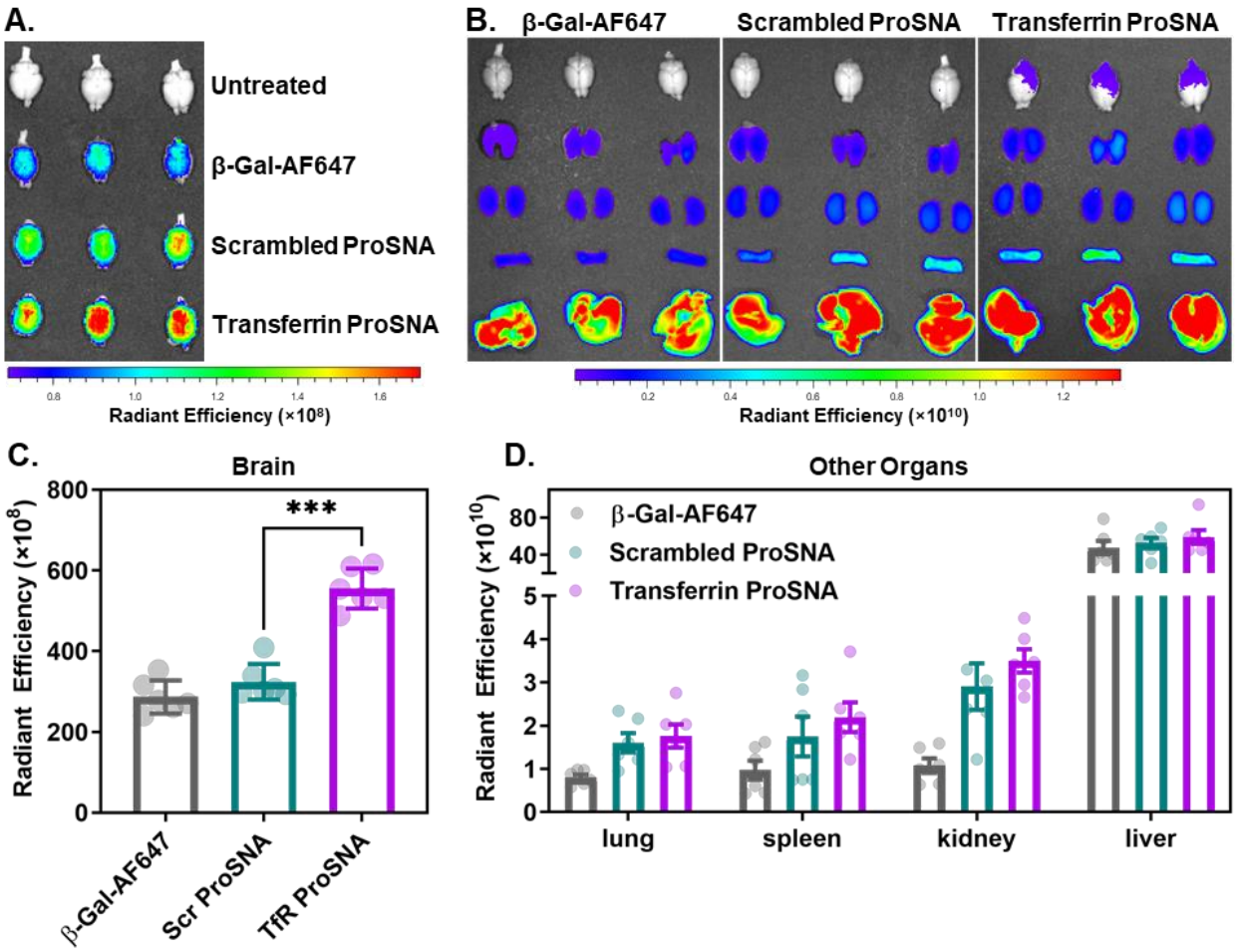

Figure 34. Biodistribution of β-Gal Following Systemic Injection in Mice. After a 1 h treatment with 6.5 mg of β-Gal/kg mouse via a tail-vein injection; mice (*n* = 6) were sacrificed, perfused, and their organs dissected and fixed. (A, B) Using IVIS, the fluorescence from the protein's AF647 tag was measured in the brain and other filtration organs. (C, D) A region of interest was drawn around each organ, and the fluorescence counts were quantified. Each dot represents an individual mouse, the bars represent the mean, and the error bars show SD.

Transferrin-ProSNAs, Scr-ProSNAs, or native β-Gal at a dosage of 6.5 mg/kg with respect to protein concentration. At 1-h post-injection, the biodistribution of each construct was assessed using an *in vivo* imaging system (IVIS) to measure the fluorescence signal in each organ (**Figure 34**) following sacrifice and perfusion. Excitingly, Transferrin-ProSNAs show a significant increase in brain accumulation (p = 0.0001, **Figure 34A**) as compared to the Scr-ProSNAs, which only differs in sequence by four bases. Moreover, the targeting by Transferrin-ProSNAs is specific to the brain, as there was no observed increase in accumulation in other filtration organs (**Figure 34B**). Together, this indicates that the DNA aptamers remain folded and recognize their target receptor in a living system.

3.2.5. Transferrin-ProSNAs Visualized Throughout the Brain via Confocal Microscopy.

Encouraged by the increased brain accumulation of Transferrin-ProSNAs on a whole-organ level, we evaluated the tissue and cellular distribution of all materials using immunofluorescent histochemistry (IFC) of brain tissue slices. CD-1 mice (n = 3) were injected intravenously with either Transferrin-ProSNAs, Scr-ProSNAs, or native β-Gal at a dosage of 6.5 mg/kg with respect to protein concentration. At 1-h post-injection, animals were sacrificed and perfused, then brain tissues were sectioned and incubated with a DAPI nucleus stain. Strikingly, the AF647 signal originating from the protein conjugated fluorophore was present throughout the entirety of the brain and not sequestered in a single region. Intense, punctate red fluorescence signals present in the same z-plane as DAPI signals, indicating that Transferrin-ProSNAs are taken up by cells within the brain (**Figure 35**). Conversely, there was no detectable signal in brain tissue slices of animals administered the native protein or Scr-ProSNA. This is in agreement with the whole-organ-level data, where minimal brain accumulation was observed via IVIS for these two systems. Together, this shows that not only to Transferrin-ProSNAs increase the accumulation of protein

in the brain via enhanced BBB penetration, but also enable the efficient cellular entry in cells present throughout the brain and CNS.

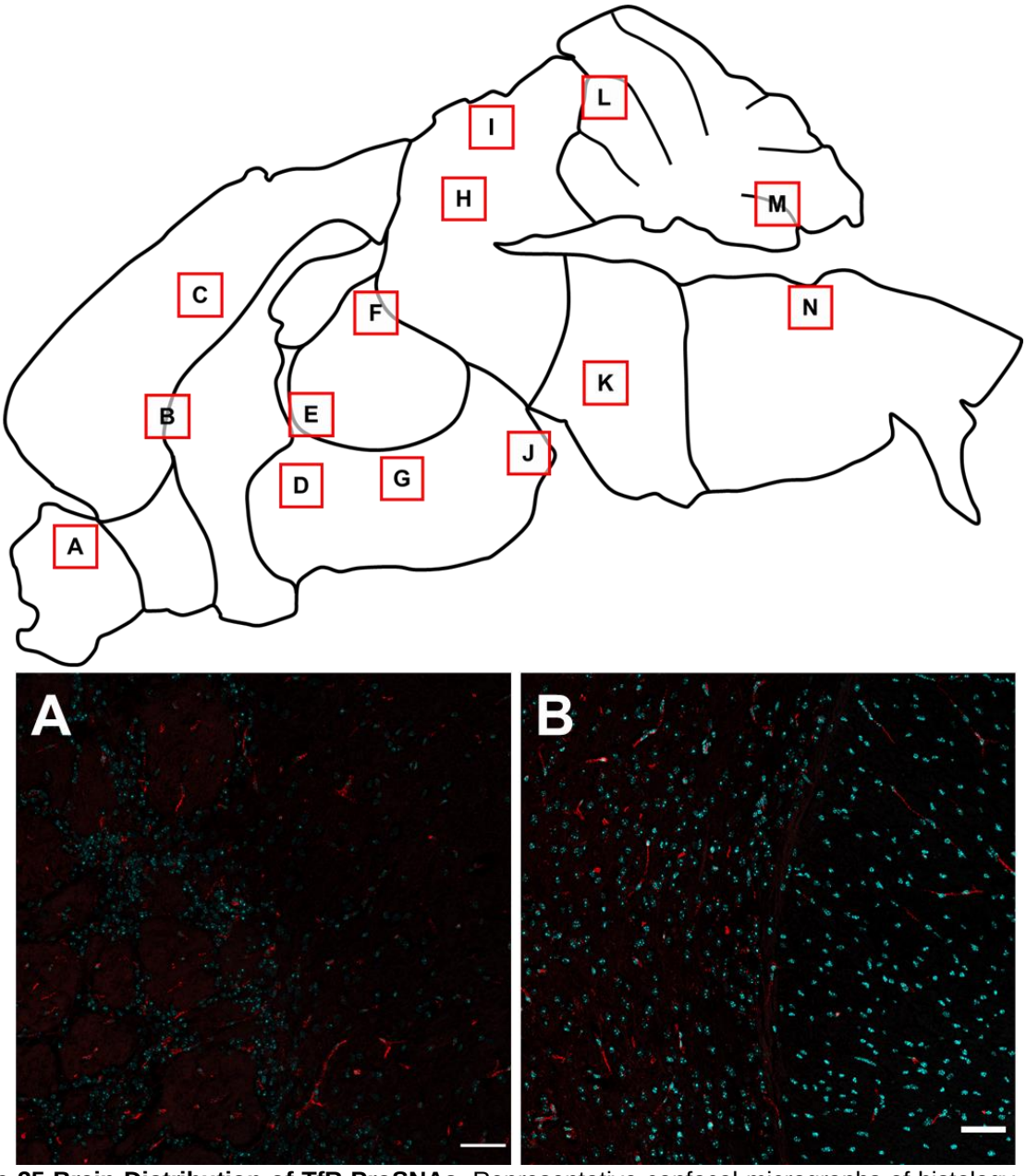

Figure 35 Brain Distribution of TfR-ProSNAs. Representative confocal micrographs of histology slides after injection of fluorolabled TrF ProSNA (6.5 mg β-Gal/kg mouse). Punctate red fluorescence signal (ProSNA) is present throughout the brain, in regions such as: (A) olfactory bulb, (B) caudate putamen, (C) cerebral cortex, (D) basal forebrain, (E, F) thalamus, (G, J) hypothalamus, (H, I) midbrain, (K) pons, (L, M) cerebellum, and (N) midbrain. Nuclei are stained with DAPI (cyan) to approximate the location within the cell. Scale bar = 50 μm.

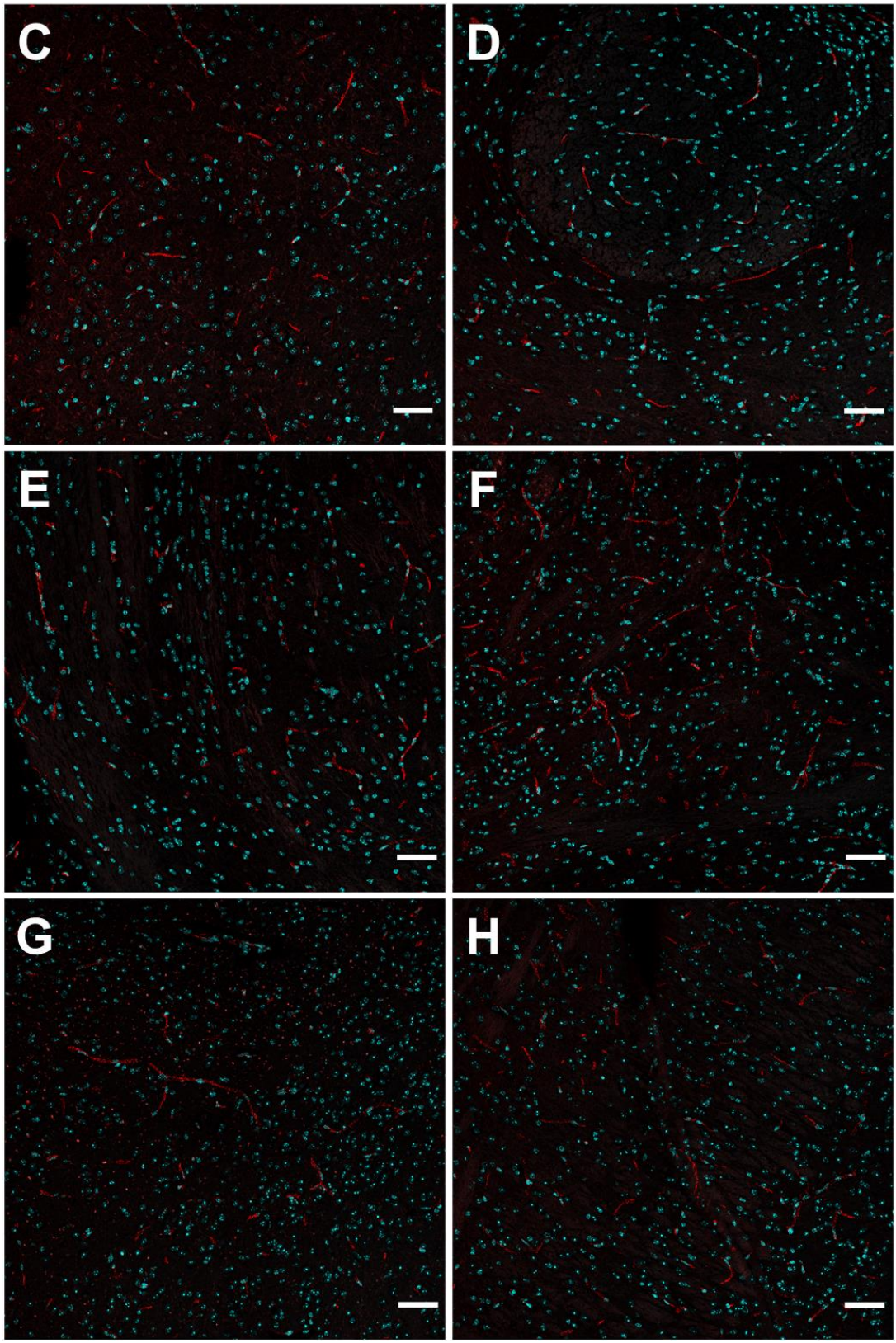
C
D
E
F
G
H

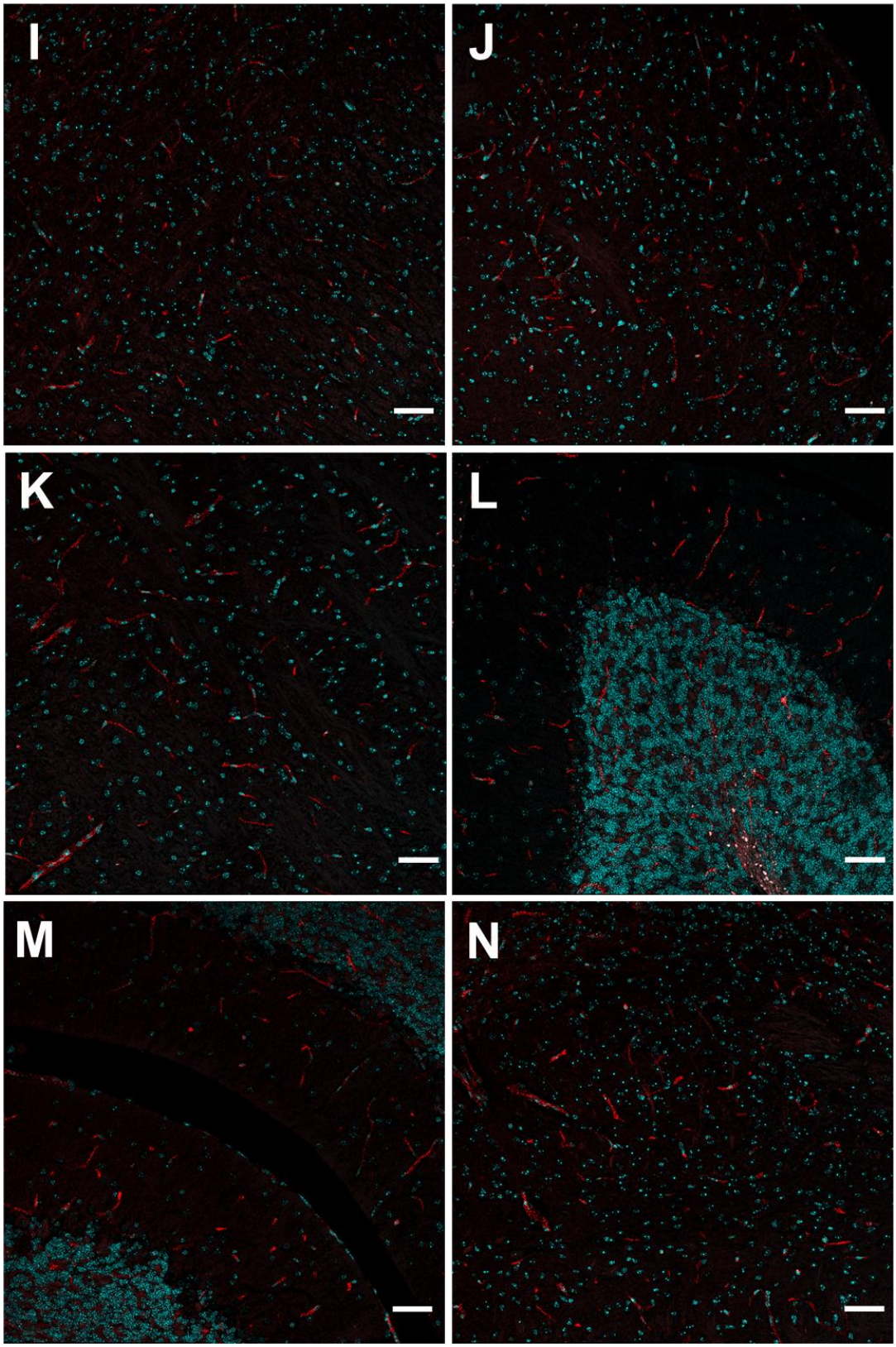
I
J
K
L
M
N

3.3. Intranasal Administration

TfR-ProSNAs can successfully target the brain and promotes active transport from the blood into the CNS; however, most of the injected dose is quickly eliminated by filtration organs. Therefore, to sidestep blood clearance of administrated ProSNAs, we experimented with alternative administration routes to bypass the BBB. The nasal passage is one such route to direct delivery to the CNS. The mechanism of delivery from the nasal mucosa to the brain has not been fully elucidated; however, it is hypothesized that compounds are transported transcellularly (through either sustentacular (support) cells or exposed olfactory sensory neurons) or extracellularly (between cells that lack tight junctions).[135] Predominantly used to increase the delivery of steroids, hormones[136, 137], vaccine antigens, and antibodies, we believe that this will be a less invasive and less expensive way of increasing the delivery of ProSNAs to the brain.

β-Gal-ProSNAs were synthesized according to previously established protocols with a G-quadruplex (GQ) DNA shell design. In **Chapter 2,** I established that G-rich sequences—which can gold into unique secondary structures—resulted in the highest *in vitro* cellular uptake due to its high binding affinity to SR-A. In this experiment, β-Gal-AF647 or GQ-ProSNAs (100 μg β-Gal / mouse) were either systemically injected via the tail-vein or administered intranasally in CD-1

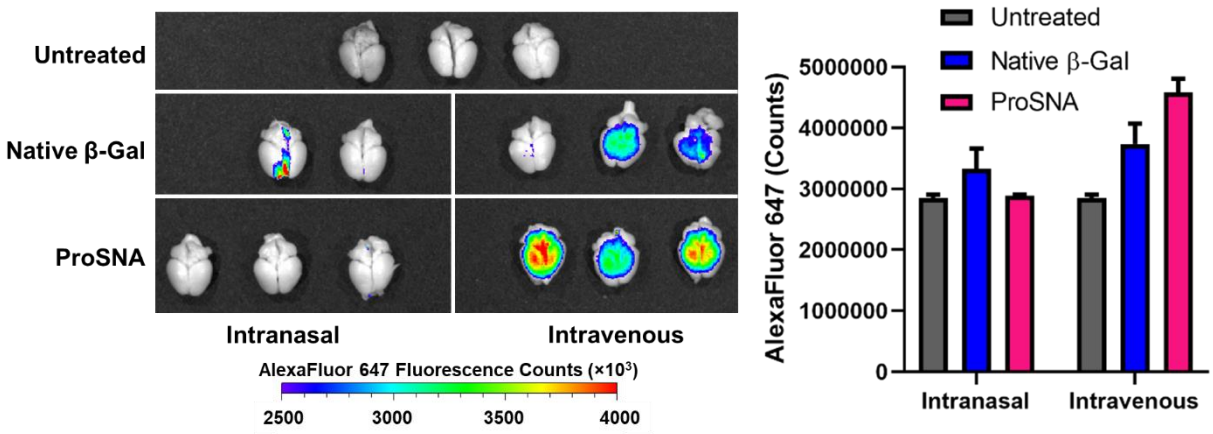

Figure 36. Intravenous Administration Demonstrates Higher Brain Delivery Compared to Intranasal. CD-1 mice were injected intravenously or administered intranasally with 100 μg native β-Gal or T_4GGT_{10} ProSNA per mouse. Following a 1-h treatment, the mice were sacrificed, perfused, and the fluorescence intensity in each organ was quantified and graphed using IVIS.

mice (*n* = 3). One hour post-treatment, the mice were sacrificed, perfused, and their organs were fixed and subsequently imaged using IVIS. The amount of protein delivered to the brain was assessed by the fluorescence from the AF647 protein tag. Based on the fluorescence counts from each brain, proteins reach the brain better using an intravenous injection compared to intranasal administration (**Figure 36**). We hypothesize that both the native protein and ProSNA remain stuck in the mucus layer due to the sample's negative charge or their inherently large size. For example, biologics delivered intranasally currently undergoing clinical trials range in size from 980 Da to 5.8 kDa[135]; therefore, intranasal administration is more suitable for smaller proteins.

3.4. Intrathecal Injection

Intrathecal (IT) administration is the delivery of drugs directly into the cerebrospinal fluid (CSF), and it is a pathway that has gained renewed attention to circumvent the BBB. CSF flows in the subarachnoid space (SAS), which surrounds the brain and spinal cord (**Figure 37A**). Therefore, we hypothesized that by intrathecally injecting the ProSNA into the CSF, proteins would circulate through the SAS, bypassing the BBB, improving access to the brain, and minimizing off-target exposure.[110, 111, 113, 138, 139]There is evidence that incorporating macromolecules into nanocarriers will differentiate the pharmacokinetics and toxicity of injected drugs.[140, 141] Compared to freely administered molecules, IT administered nanomedicines are

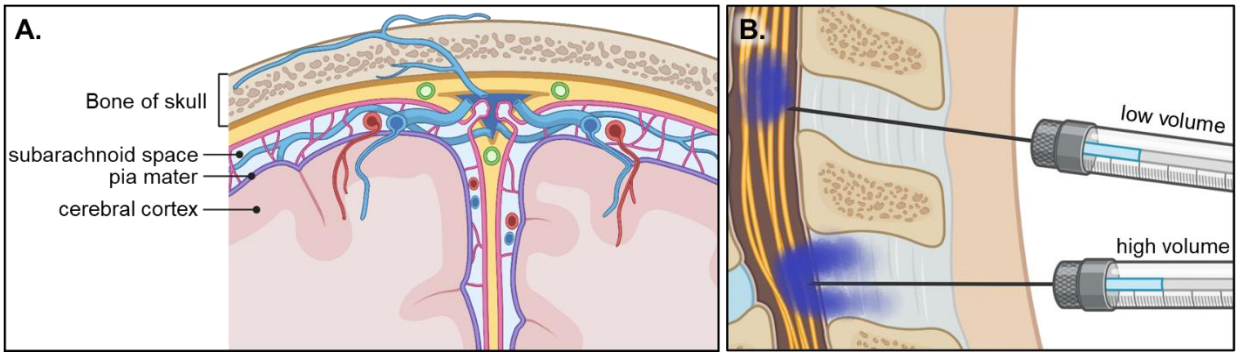

Figure 37. Schematic of Intrathecal Injection into Subarachnoid Space. (A) The subarachnoid space surrounds the brain and spinal cord which is (B) accessed by the correct needle placement during an intrathecal injection (top). Misposition of the needle lowers delivery dosage into the cerebrospinal fluid in the subarachnoid space (bottom) and increases retention in the epidural space.

well-retained within the CNS, and encapsulated payloads experience slower clearance, which can enhance brain exposure.

To test this, we administered AF647 labeled ProSNAs to healthy mice via direct injection into the spine. Two different ProSNAs—T-rich and GQ—were tested based on prior cellular

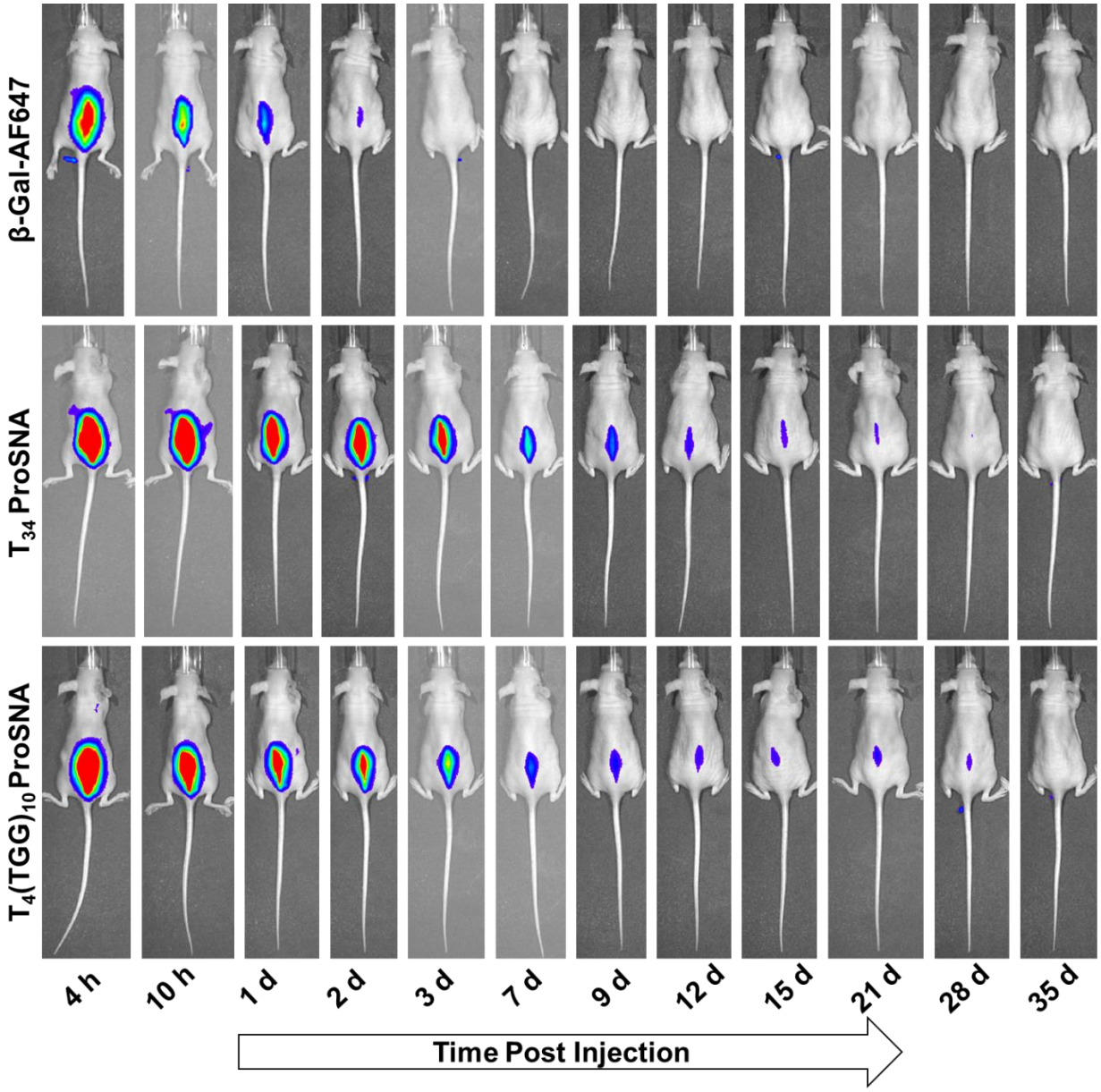

Figure 38. Intrathecal Injection at Higher Volume of Protein and ProSNA in Mice. Athymic nude mice were injected intravenously with 30 µL sample/mouse. Biodistribution was monitored by IVIS and fluorescence intensity from the AF647 fluorescence protein tag is visualized. Both ProSNAs are visualized in the spine at least 10x longer than the native protein, indicative of enhanced stability when using the ProSNA system.

uptake and biodistribution differences when injected intravenously (see **Chapter 2**). To evaluate broad patterns of protein delivery following IT injection, distribution was monitored *in vivo* in athymic nude mice over five weeks using an IVIS imaging system. In a first trial, 30 µL of native protein or the ProSNAs was injected into the intervertebral space between the L5-L6 spinal segments (**Figure 38**). For this injection, the majority of the treatment remained at the injection site. We hypothesize that our injection volume was too high (**Figure 37B**). Rather than injecting in the SAS, the material spilled into the epidural space, predominantly composed of adipose tissue (fat). Nevertheless, we observed a significant enhancement in the conservation of the AF647 signal for the ProSNAs compared to the native protein in the lower spine. The native protein is cleared 72h post-injection. However, the T-rich ProSNA is visualized in the spine for up to three weeks, and the GQ-ProSNA is detected in the spine after four weeks.

We repeated the IT injection with a lower volume (10 µL, **Figure 39**) and visualized a significant increase in brain delivery. Once again, the fluorescence signal from GQ-ProSNA treated mice persists in the brain significantly longer (>3 days). In contrast, the native protein is cleared after 24 h, a result of high clearance rates of the CSF and protease

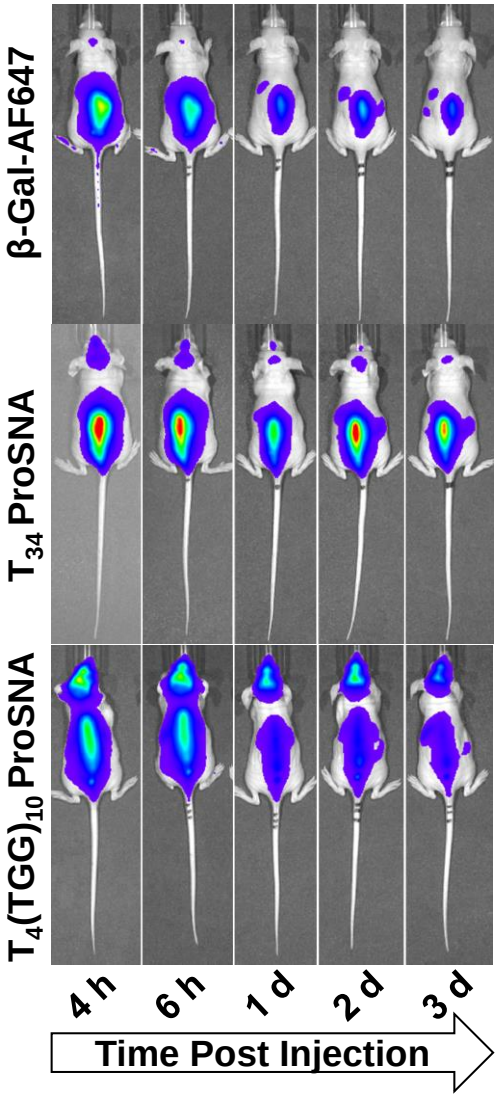

Figure 39. Intrathecal Injection at Lower Volume Increases Brain Delivery for ProSNAs. Athymic nude mice were injected intravenously with 10 µL sample/mouse. Biodistribution was monitored by IVIS and fluorescence intensity from the AF647 fluorescence protein tag is visualized. Both ProSNAs are visualized in the brain significantly longer than the native protein, indicative of enhanced stability and a unique cerebral spinal fluid distribution when using the ProSNA system.

degradation. We propose that the extended brain fluorescence signal for ProSNA treated mice results from extended protein stability and favorable interaction between the DNA shell's and cells lining the leptomeningeal. Unfortunately, the experiment was cut short due to an unrelated dermatitis infection in the mice after three days. Although successful in some mice, the IT injection is technically challenging in small animals, given the relatively small size of the SAS. Nevertheless, these pilot experiments demonstrate promising evidence that the DNA shell's presentation plays a significant role in governing CSF mobility following IT delivery. Further studies would be needed to directly probe how ProSNAs interact will cells lining the perivascular space, the sample's pharmacokinetics, and whether injected proteins retain enzymatic activity following brain penetration. Moreover, different injection volumes or techniques (injection of protein followed by a flush of PBS) may have a significant impact on the spread of macromolecules through the CSF.

3.5. Conclusions

Herein, we show that the delivery of proteins to the brain is enhanced through their transformation into ProSNAs comprised of DNA aptamers that bind the TfR receptor. This is significant, because although it has been previously shown that adding a DNA shell changes the biodistribution of proteins[81], this is the first demonstration of using the oligonucleotide sequence as a tissue targeting moiety. This is especially exciting when one considers the vast number of targets and disease sites that aptamers can be easily designed against[142-144]. Moreover, DNA aptamers have been previously successfully employed in ProSNAs as nucleic acid recognition elements to probe pH or glucose levels in living cells.[145] As such, it may be possible to design systems that simultaneously target to disease sites (using a targeting aptamer) and probe intracellular conditions upon localization (using a recognition aptamer). Taken together, this work illustrates that DNA shell design can have a profound impact on the resulting distribution of SNAs

and can be used to target hard-to-reach organs through intelligent sequence design. Moreover, we performed a new injection strategy—intrathecal administration—to circumvent the BBB and visualized an increase in brain delivery and stability with the ProSNA when compared to the native protein. This pilot study suggest that the intrathecal route may be useful for the delivery of ProSNAs to the CNS. Further experimentation on the impact of injection volume, animal model, and SNA-perivascular cell interactions is necessary in order to ultimately apply this procedure to therapeutically relvant SNAs.

3.6. Methods and Materials

3.6.1. Synthesis and Characterization of β-Galactosidase Protein Spherical Nucleic Acids

3.6.1.1. Oligonucleotide synthesis

Oligonucleotides were synthesized using standard phosphoramidite chemistry protocols on an ABI 392 using 1000 Å universal CPG solid supports (ChemGenes) and phosphoramidites, as well as coupling reagents purchased from Glen Research. A mild oxidizing agent ((1S)-(+)-(10-Camphorsulfonyl)-oxaziridine, CSO) was used to increase coupling efficiency and preserve the integrity of the DBCO-dT phosphoramidite. Synthesized strands were cleaved using 30% aqueous ammonia (Sigma Aldrich) for 16 h at room temperature and purified by HPLC using a reverse-phase C4 column (Shimadzu) running a gradient from 0 to 100% acetonitrile in triethylammonium acetate buffer (Sigma Aldrich) over 45 min. After HPLC purification, the final dimethoxytrityl group was removed in 20% acetic acid (Sigma Aldrich) for 2 h and extracted in ethyl acetate (Sigma Aldrich). The masses of the oligonucleotides were confirmed using matrix-assisted laser desorption ionization-time of flight (MALDI-MS) mass spectroscopy on a Bruker AutoFlex-III using 2’,6’-dihydroxyacetophenone (Sigma Aldrich) as the matrix. Molecular weights

and extinction coefficients were calculated based on estimates using the IDT OligoAnalyzer tool (**Table 6**)[96].

Table 6. Oligonucleotide sequences, molecular weights, and extinction coefficients

Experiment	Name	Sequence (5' to 3')	MW Expected [Da]	MW Observed [Da]	ε_{260} [$M^{-1}cm^{-1}$]
RMT	TfR	GCG TGG TAC CAC GCT TTT T DBCO-dT	6864	6878	196700
RMT	Scr	GCG TGT GCT CAC GCT TTT T DBCO-dT	6855	6867	190600
Intranasal administration	GQ	DBCO-dT T TTT $(TGG)_{10}$	11515	11459	340400
Intrathecal injection	T-rich	DBCO-dT T TTT $(TTT)_{10}$	11015	11033	294800

3.6.1.2. Synthesis of β-Galactosidase (β-Gal) Protein Spherical Nucleic Acids

ProSNA synthesis was established based on literature precedence.[8, 81] Molecular weights and extinction coefficients pertaining to synthesis and characterization of β-Gal ProSNAs are detailed in **Table 7**.

Table 7. Molecular weights and extinctions for chemical modifications onto β-Gal

Name	MW [Da]	ε_{max} [$M^{-1}cm^{-1}$]
β-Galactosidase	464,000	1,142,000 (280nm) 596,268 (260nm)
Alexa Fluor® 647 dye	1250	265,000 (650nm)
NHS-PEG_4-azide	388	N/A
DBCO-dT	774	18,800 (260 nm)

3.6.1.2.1. Reaction of Surface-Accessible Cysteines with Alexa Fluor 647 (AF647).

β-Gal from an *E. coli* overproducer was purchased from Roche. The lyophilized protein was first dissolved in 1X phosphate-buffered saline (1X PBS; Thermo Fisher Scientific) and washed via 3 rounds of centrifugation using a 100 kDa centrifugal filter (Millipore), resuspending

the protein in 1X PBS after each wash. Protein concentration was determined from its 280 nm absorbance peak collected on a Cary-5000 UV-Vis spectrophotometer in a 1 cm pathlength cuvette. Then, 10 equivalents of Alexa Fluor 647-C_2-maleimide (Thermo Fisher Scientific), dissolved in DMSO, were added to ~19 μM β-Gal in 1500 μL 1X PBS and the reaction was shaken (900 rpm) for 2 hours at 25 °C. Unconjugated Alexa Fluor 647 was removed by repeated rounds of centrifugation using a 100 kDa filter until the filtrate did not have a detectable absorbance at 650 nm by UV-Vis. The number of Alexa Fluor 647 modifications per protein was calculated based on UV-Vis spectroscopy.

3.6.1.2.2. Reaction of Surface-Accessible Lysines with NHS-PEG_4-Azide.

350 equivalents of NHS-PEG_4-azide crosslinker (Thermo Fisher Scientific), dissolved in anhydrous DMSO at a concentration of 100 mM, were added to ~ 45 μM β-Gal-AF647 in 550 μL 1X PBS. The reaction was shaken (900 rpm) overnight at 25°C. Unconjugated linker was removed by 10 rounds of centrifugation using a 100 kDa filter. The number of azide modifications was assessed by MALDI-MS using sinapinic acid (Thermo Fisher Scientific) as a matrix in a Bruker AutoFlex-III.

3.6.1.2.3. Functionalization with DBCO-dT Terminated Oligonucleotides.

350 equivalents of DBCO-dT terminated DNA strands were first lyophilized, then 6.5 μM β-Gal-AF647-azide in 450 μL 1X PBS was added to rehydrate the DNA. This solution was allowed to incubate for 72 h at 25 °C with shaking (900 rpm). Unreacted DNA strands were removed by successive rounds of centrifugation in a 100 kDa filter until the filtrate did not have a detectable absorbance at 260 nm. Typically, complete removal of DNA required 30-40 washing steps. The number of DNA strands per protein was calculated based on UV-Vis spectroscopy (**Figure 40**). Loading densities from ProSNAs described in this work appear in **Table 8**.

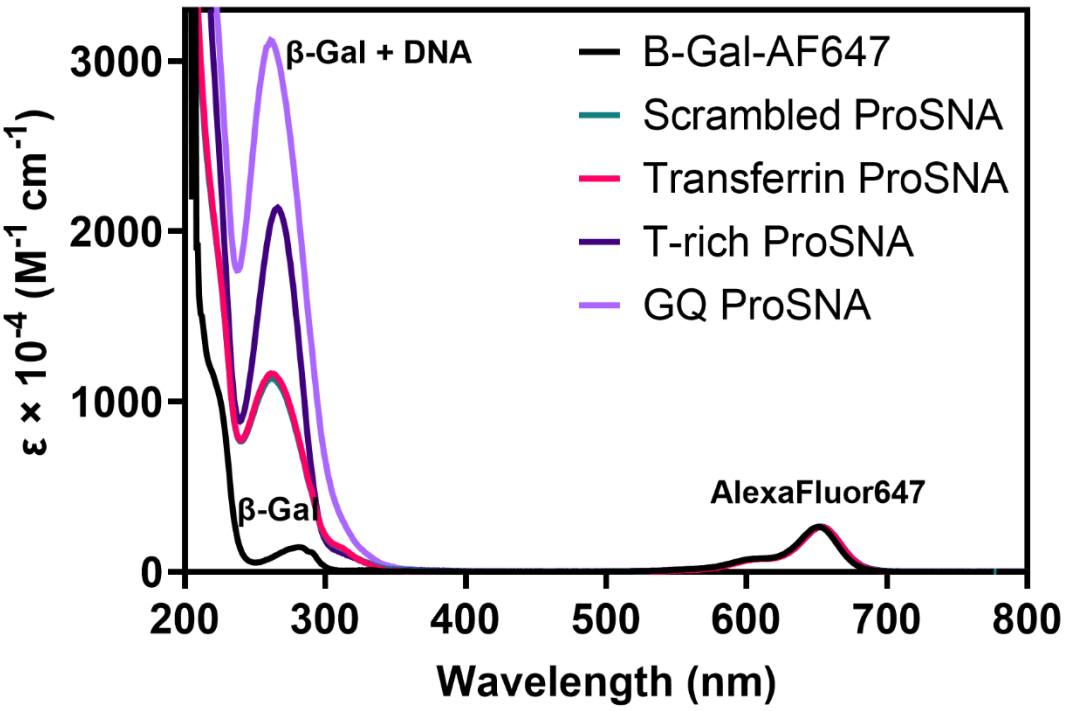

Figure 40. UV-Vis spectra of protein spherical nucleic acids. UV-Vis spectra of ProSNAs with different sequence identities used to quantify DNA loading. Spectra were collected at ambient temperature with a 1 cm pathlength cuvette on a Cary5000 spectrophotometer.

3.6.1.2.4. Functionalization with DBCO-dT Terminated GQ Oligonucleotides.

β-Gal-AF647-azide was first buffer exchanged in lithium phosphate buffer (10 mM LiH2PO4, Sigma-Aldrich, pH 7.4) using five successive rounds of centrifugation in a 100 kDa filter. 350 equivalents of DBCOdT terminated GQ DNA were lyophilized, then 6.5 μM β-Gal-AF647-azide in 450 μL $LiPO_4$ buffer were added to rehydrate the DNA. This solution was allowed to incubate for 72 h at 25°C with shaking (900 rpm). Unreacted DNA strands were removed by successive rounds ofcentrifugation in a 100 kDa filter using the LiPO4 buffer as the washing buffer until the filtrate did not have a detectable absorbance at 260 nm. Typically, complete removal of DNA required 30-40 washing steps. The number of DNA strands per protein was calculated based on UV-Vis spectroscopy. Loading densities from ProSNAs described in this work appear in **Table**

8. After complete removal of unconjugated DNA strands, ProSNAs were buffer exchanged back into 1X PBS buffer using five successive rounds of centrifugation in a 100 kDa filter.

Table 8. Oligonucleotide loading of ProSNA constructs

Experiment	Name	Sequence (5' to 3')	DNA per β-Gal
RMT	TfR	GCG TGG TAC CAC GCT TTT T	39
RMT	Scr	GCG TGT GCT CAC GCT TTT T	37
Intranasal administration	GQ	DBCO-dT T TTT $(TGG)_{10}$	40
Intrathecal injection	T-rich	DBCO-dT T TTT $(TTT)_{10}$	40

3.6.1.3. SDS-PAGE Analysis of ProSNAs.

Protein samples (2 pmol) were incubated at 80 °C for 5 min in 1X Laemmli Sample Buffer (Bio-Rad) and 355 mM 2-mercaptoethanol (Sigma-Aldrich) before loading. Samples were run on a 4-15% TGX mini-Protean pre-cast gradient gel (Bio-Rad) for 30 min at 200 V in 1X

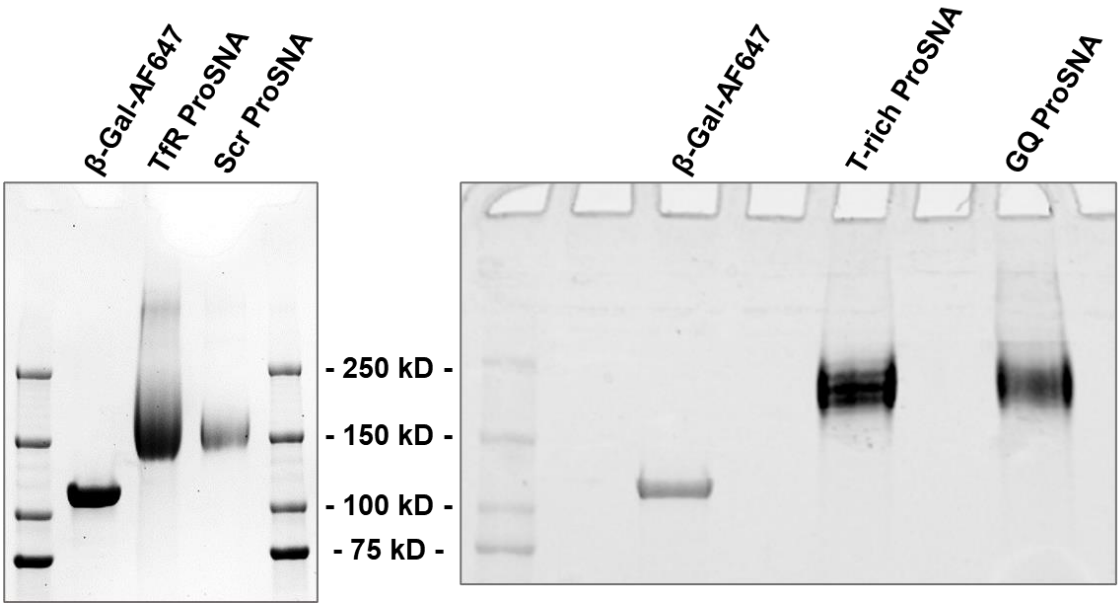

Figure 41. 4-15% SDS PAGE gel of native β-gal and ProSNA variants. Gel was run for 30 min at 200 V in 1X Tris/Glycine/SDS running buffer. Lower mobility bands are indicative of higher molecular weights for ProSNA variants and confirm the succesful conjugation of DNA strands onto the protein.

Tris/Glycine/SDS running buffer (Bio-Rad). Gels were stained using SimplyBlue SafeStain (Invitrogen) before imaging on a ChemiDoc™ MP Imaging System (**Figure 41**).

3.6.1.4. Circular Dichrosim Spectra of TfR-ProSNA, Scr-ProSNA and Native Protein.

Circular dichroism (CD) spectra were recorded in a 10 mm pathlength cuvette at 25°C with a Jasco J-1700 spectropolarimeter equipped with a temperature controller at a concentration of 11.7 μM DNA or 300 nM β-Gal in 1X PBS buffer (pH 7.4). The instrument parameters to record the CD spectra were: 200-350 nm measurement range, 0.1 nm data pitch, 1 nm bandwidth, 50 nm/min scanning speed, and 5 accumulations. Calculated theoretical spectra of the ProSNA were obtained by adding the spectra of β-Gal-AF647 to the spectra of the DNA (**Figure 42**). For CD spectra of T-rich and GQ ProSNA see **Chapter 2**.

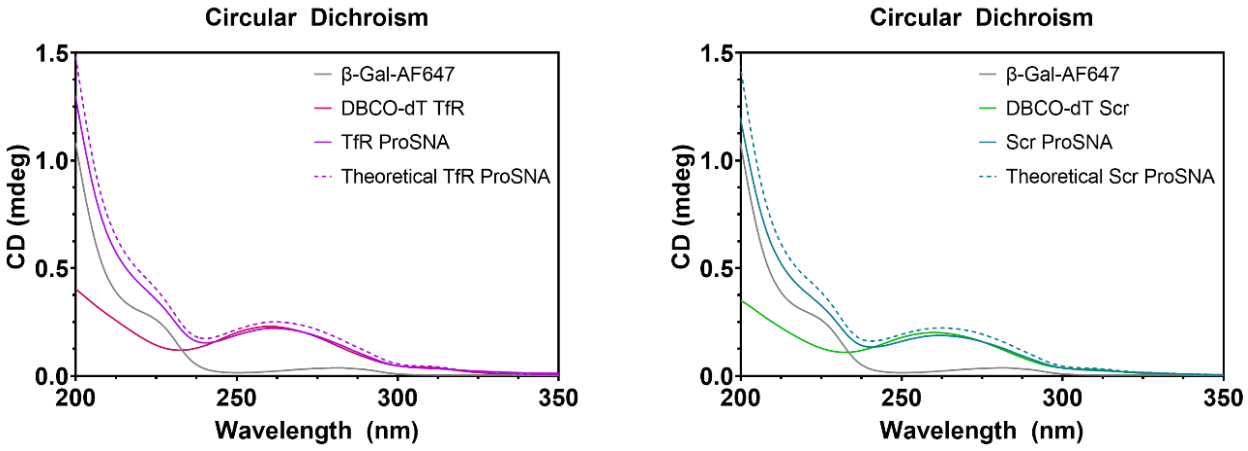

Figure 42. Circular Dichroism (CD) spectra of protein, DNA, and ProSNA. CD spectra of either 300 nM β-Gal (fluorophore modified protein or ProSNA) or 11.7μM DBCO-dT terminated DNA in 1X PBS. Theoretical spectra of ProSNAs (dotted line) were calculated by adding the mdeg values of β-Gal-AF647 and DBCO-dT DNA.

3.6.2. Receptor-Mediated Transcytosis ProSNA Binding or In Vitro Assays

3.6.2.1. BioLayer Interferometry

Receptor-aptamer association studies were performed on a BLItz instrument (ForteBio) in 'Advanced Kinetics' mode at 25˚C using a drop holder (4 uL) for the loading and association steps and a tube (500 uL 1X PBS) for the background and dissociation steps. Recombinant mouse

transferrin receptor (CD71) extracellular domain (Cys89 – Phe763) with a polyhistidine tag at the N-terminus was obtained from Sino Biological. Steps were performed according to the parameters listed in **Table 9** using Anti-Penta-HIS (HIS1K) biosensors (Sartorius):

Table 9. Instrument parameters for Advanced Kinetics experiment on BLI

Step	Sample	Concentration	Time (s)
Initial Baseline	1X PBS	N/A	30
Loading	Transferrin Receptor ECD-His Tag	0.5 mg/mL	400
Baseline	1X PBS	N/A	30
Association	Aptamer	0.25 mM – 2.5 mM	400
Dissociation	1X PBS	N/A	120

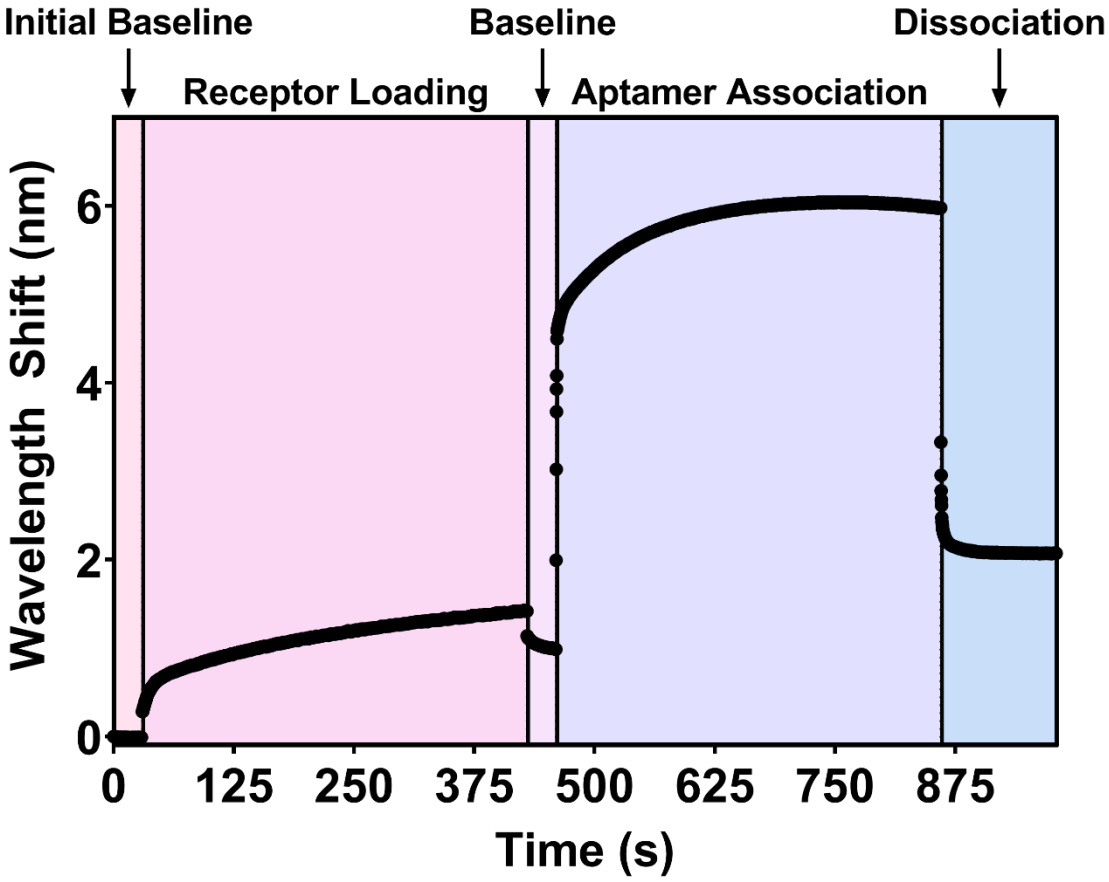

Figure 43. Advanced Kinetics Run of 2.5 mM Transferrin Aptamer. Example of typical run of transferrin aptamers associating with the transferrin receptor. First a baseline is taken in 1X PBS, then the receptor is loaded onto the biosensor. Next another baseline is taken in 1X PBS, followed by aptamer association and dissocation.

Measurements were performed a total of three times with increasing transferrin aptamer concentrations (0.25 mM – 2.5 mM) or 2.5 mM scrambled aptamer (**Figure 43**). Processing of data was performed using BLItz software.

3.6.2.2. *In Vitro* Blood Brain Barrier Model

6.5 mm Transwell®-COL collagen-coated 0.4 µm Pore PTFE membrane inserts (Corning) were first placed in a 24-well plate and pre-incubated with full cell culture media overnight at 37˚C. Full cell culture media consists of DMEM (Gibco) supplemented with 10% fetal bovine serum (Atlanta Biologicals) and 1% penicillin-streptomycin (Gibco). The next day, bEnd.3 *mus musculus* endothelial cells (ATCC) were seeded in the apical side of the transwell insert at 1.25 x 10^5 cells per well and cultured at 37˚C in 5% CO_2. Media was exchanged every other day for a total of 9 days to ensure the growth of a full monolayer. After 9 days, media was removed from both the insert and well. Then, 0.5 mL of fresh media was added to each well and 0.1 mL of treatment was carefully added to the appropriate insert. The treatment consisted of 100 nM of either Alexa Fluor 647-modified native β-Gal or ProSNA variants diluted in full cell culture media. Cells were incubated at 37 C in 5% CO2, and at each time point 75 uL of media was removed from the well. The fluorescence was measured using a BioTek Cytation 5 plate reader at 640 nm excitation / 681 nm emission. After each measurement the 75 uL of media was returned back to its respective well. To determine initial rate of transcytosis, the data points were fit to an exponential plateau according to the following equation and analyzed using GraphPad Prism:

$$\mathrm{Fluoresence}_{\mathrm{time}} = \mathrm{Fluoresence}_{\mathrm{max}} - (\mathrm{Fluoresence}_{\mathrm{max}} - \mathrm{Fluoresence}_{\mathrm{time}}) \times \mathrm{e}^{-\mathrm{rate}\times\mathrm{time}}$$

where $\mathrm{Fluoresence}_{\mathrm{time}}$ is the fluorescence measurement at each time point and $\mathrm{Fluoresence}_{\mathrm{max}}$ is the steady-state fluorescence at the curve's plateau. A summary of the calculated values are in **Table 10**.

Table 10. Summary of results from exponential plateau non-linear regression curve

Sample	$Fluorescence_{max}$	Rate (hr^{-1})
Transferrin ProSNA	751.4 ± 44.1	0.44 ± 0.08
Scrambled ProSNA	745.7 ± 43.5	0.28 ± 0.04

3.6.3. *In Vivo* Investigations of ProSNA Distribution

Female CD-1 mice (strain code: 022) were procured from Charles River Laboratory at 8 weeks of age and maintained in conventional housing. All animal experiments were carried out in accordance with the approved IACUC protocol issued by Northwestern University.

3.6.3.1. Receptor-Mediated Trancytosis ProSNA *In Vivo* Evaluation

3.6.3.1.1. *Ex Vivo* Near-Infrared Fluorescence (NIRF) Imaging

NIRF imaging studies were performed using a Caliper Life Sciences *In Vivo* Imaging System (IVIS) to determine the extent of protein accumulation in main organs post-injection. Female CD1 mice (28-30 g) were administered a single injection via tail vein at a dose of 6.5 mg β-Gal / kg body weight. At 1-hour post-injection, mice (n = 6) were humanely euthanized by cardiac perfusion with 1X PBS while anesthetized. Tissues were harvested and fixed in 4% paraformaldehyde for 1 h at 4 °C. Post-fixation, organs were washed three times with 1X PBS and stored in 1X PBS at 4 °C. Finally, organs were imaged using an IVIS system using 650 nm/700 nm excitation/emission filters and data was quantified by measuring fluorescence counts with the Living Image software.

3.6.3.1.2. Brain Histology and Imaging

Female CD1 mice (29-35 g) were administered a single injection via tail vein at a dose of 6.5 mg β-Gal / kg body weight. One-hour post-injection, mice (n = 3) were humanely euthanized by cardiac perfusion while anesthetized. Each mouse was first perfused with 20 mL of 1X PBS, then 20 mL of 4% paraformaldehyde (PFA; Thermo Fisher Scientific), and the brains were

dissected and stored in 4% PFA with shaking at 4 °C for 2 h. Organs were rinsed in many changes of 1X PBS and equilibrated overnight in 15% sucrose (Sigma Aldrich) in 1X PBS solution at 4 °C. The organs were subsequently transferred to a 30% sucrose in 1X PBS solution and stored at 4 °C until the organs sunk to the bottom of their respective container. Each organ was then embedded in optimal cutting temperature compound and cryo-sectioned in the sagittal plane at the midline at a 10 µm thickness. Slides were stained with DAPI to visualize nuclei. A Leica TCS SP8 Confocal Microscope was used to image different regions of each slide at a 40X magnification.

3.6.3.2. Intranasal Administration *In Vivo* Evaluation

3.6.3.2.1. *Ex Vivo* Near-Infrared Fluorescence (NIRF) Imaging

NIRF imaging studies were performed using a Caliper Life Sciences *In Vivo* Imaging System (IVIS) to determine the extent of protein accumulation in main organs post-injection. Female CD1 mice (28-30 g) were administered a single injection via tail vein or intranasal administation at a dose of 9.3 µg β-Gal / mouse. For intranasal administration, CD-1 mice were first anesthetized while in a supine position, and samples were inhaled into alternating nares every minute for 10 minutes total. The mouse remained anesthetized for an additional 15 minutes after the last intranasal dose. At 1-hour post-injection, mice (n = 3) were humanely euthanized by cardiac perfusion with 1X PBS while anesthetized. Tissues were harvested and fixed in 4% paraformaldehyde for 1 h at 4 °C. Post-fixation, organs were washed three times with 1X PBS and stored in 1X PBS at 4 °C. Finally, organs were imaged using an IVIS system using 650 nm/700 nm excitation/emission filters and data was quantified by measuring fluorescence counts with the Living Image software.

3.6.3.3. Intrathecal Administration *In Vivo* Evaluation

3.6.3.3.1. *Ex Vivo* Near-Infrared Fluorescence (NIRF) Imaging

NIRF imaging studies were performed using a Caliper Life Sciences *In Vivo* Imaging System (IVIS) to determine the extent of protein accumulation in main organs. Female athymic nude mice (20-23 g) were administered a single injection into the intervertebral space between the L5-L6 spinal segments at a dose of 85 µg β-Gal / mouse for 30 µL injection or 45 µg β-Gal / mouse for 10 µL injection. Periodically, mice—while anesthetized—were imaged using an IVIS system using 650 nm/700 nm excitation/emission filters and data was quantified by measuring fluorescence counts with the Living Image software.

CHAPTER 4. IMMUNOSTIMULATORY SPHERICAL NUCLEIC ACIDS AS CANCER VACCINES FOR TRIPLE NEGATIVE BREAST CANCER

Material in this chapter is based upon published work:

Callmann C.E.; Cole L.E.; Kusmierz C.D.; Huang Z.; Horiuchi D.; Mirkin C.A. "Tumor Cell Lysate-Loaded Immunostimulatory Spherical Nucleic Acids as Therapeutics for Triple Negative Breast Cancer." *Proc. Natl. Acad. Sci. USA* **2020**, *117*, 17543-17550

Callmann C.E.; Kusmierz C.D.; Dittmar J.; Broger L.; Mirkin C.A. “Impact of Liposomal Spherical Nucleic Acid Structure on Immunotherapeutic Function.” *ACS Central Sci*. **2021**, *7, 892-899.*

4.1. Introduction

Mobilizing the immune system against tumors is a central goal of personalized cancer treatments. Indeed, the identification of tumor-associated antigens (TAAs) and the advent of cell-based therapies represent significant progress towards achieving this aim[146-150]. However, these approaches, including the use of dendritic cell (DC) vaccines[65] and CAR-T cell therapies[66], are expensive and labor-intensive, as they require the extraction of immature immune cells from patients, expansion of cells *ex vivo*, incubation with TAAs, and reinfusion to the patient. Furthermore, these therapies are restricted to the subset of patients whose tumors express known TAAs[151], and raising an immune response with single-antigen vaccines may ultimately have limited efficacy due to tumor heterogeneity and loss of antigen expression over time[64, 152, 153].

An attractive alternative to single-antigen vaccines is to use lysates isolated from a patient's own tumor as the TAA source[68-70, 72, 73, 154]. Exploiting tumor cell lysates as antigens broadens the set of proteins that can be processed and targeted by immune cells – in principle, the entire tumor proteome can be accessed[67]. Therefore, this also addresses several potential limitations of using a finite set of well-defined TAAs, including: 1) the challenge of identifying immunogenic epitopes from tumors, 2) epitope restriction by the major histocompatibility complex (MHC), and 3) loss of targeted antigens in tumors. However, direct vaccination using tumor lysates has been met with limited success due to low cellular uptake and bioavailability after injection, resulting in minimal immunogenicity[155]. Oxidizing tumor cells prior to lysate isolation and preparation significantly increases immunogenicity when the lysates are utilized as the antigen source in DC vaccines[74, 75, 155]. Importantly, protein chlorination by hypochlorous acid (HOCl), an oxidant produced by neutrophils as part of the adaptive immune response, increases the immunogenicity of antigens several-fold[156], potentially due to their increased proteolytic susceptibility[157]. In addition, HOCl oxidation generates aldehyde-modified antigens that are more immunogenic than their unmodified counterparts[158]. However, the underlying mechanism of how

these changes facilitate antigen presentation and alter the tumor microenvironment (TME) remains unclear. Moreover, a major challenge in immunotherapeutic development is the selection of the appropriate vehicle for delivering both adjuvant and antigen[159], as the way components are formulated can significantly influence delivery to the immune system and thus, activation of immunostimulatory pathways[160, 161]. Nanoscale therapeutics have shown promise in this regard, enhancing antigen-presenting cell (APC) activation over mixtures of adjuvant and antigen[162].

Spherical nucleic acids (SNAs) are a novel class of nucleic acids that exhibit completely different behavior from their linear analogs[4], including rapid cellular uptake without the use of ancillary transfection reagents[82]. The SNA architecture is defined by a dense, highly oriented packing of nucleic acids into a spherical morphology, which imparts new chemical, biological, and physical properties to the nucleic acids from which SNAs are derived. To date, SNAs have been formed from a variety of nanoparticle cores, including gold and other inorganic nanoparticles[4, 7, 33, 82, 163-166], liposomes[9, 11, 12, 37, 49], polymers[86, 167, 168], and proteins[8]. Liposomes are an especially attractive scaffold for SNA templating because the resulting systems are biodegradable and biocompatible, and liposomes are a validated, FDA-approved nanoscale formulation for drug delivery[169]. In addition, the hollow core of liposomal SNAs can encapsulate TAAs and other cargo.

Regarded as one of the more successful biomolecule packing systems to date[170], liposomes are useful in a wide variety of biomedical applications, including drug delivery[171, 172], biosensing[173, 174], diagnostics[175, 176], gene delivery[177], and immunomodulation[11, 12, 16, 178, 179]. The chemical composition of liposomes determines their performance in biological systems[180]. Indeed, it has been well established that the phase transition temperature (T_C) of the constituent lipids dictates the phospholipid bilayer membrane fluidity, which heavily influences the liposome's biological properties, including permeability and lipid exchange[181]. The T_C of a phospholipid is determined by the chemical identity and charge of the hydrophilic head group, as well as the chain length and degree of saturation of the diacyl lipid tail[182]. At temperatures at or below the T_C,

liposomes exist in a gel phase, where lipid exchange is limited and membrane fluidity is low. At temperatures exceeding the T_C, liposomes exist in a liquid-crystalline phase, where the membrane is more fluid and the dynamics of lipid exchange are increased. In general, the T_C increases as the diacyl lipid chain length increases, due to increased Van der Waals forces between the acyl chains[183]. However, introducing double bonds into the diacyl lipid tail decreases the T_C, as the packing of the hydrophobic chains is disrupted by structural kinks introduced by the unsaturated bonds[184]. Together, these subtle changes to the chemical structure of the individual lipid components dictate the supramolecular properties of the liposome and are important to consider when designing liposome-scaffolded materials.

Because of their biocompatibility, modularity, and favorable physical properties[170, 185-189], liposomes are attractive scaffolds for synthesizing spherical nucleic acids (SNAs). Diverse L-SNA constructs with tunable properties can be rapidly generated by changing the lipophilic oligonucleotide anchor[11, 133] or altering the sequence, backbone, and surface density of the oligonucleotide[48]. Liposomal SNAs have been previously observed to initiate antigen presentation, activate immune cells, and induce production of proinflammatory cytokines for cancer treatment and other applications[11, 15, 49, 190, 191]. In many of these examples, the sequence of the oligonucleotide shell is comprised of an unmethylated cytosine-guanosine sequence called CpG-1826. CpG-1826 mimics microbial genomes and acts as a pathogen-associated molecular pattern (PAMP)[192], which is recognized by toll-like receptor 9 (TLR9), a component of the innate immune system located in the endosome of antigen-presenting cells (APCs), including DCs[193].

Given these facts, we reasoned that SNAs containing tumor cell lysates could be used to develop potent nanoscale immunotherapeutics for the treatment of cancers without known TAAs, such as triple negative breast cancer (TNBC). Accounting for the majority of all breast cancer-related mortality[194, 195], TNBC is a highly heterogeneous and aggressive disease that lacks functional expression of both estrogen and progesterone receptors and no overexpression of

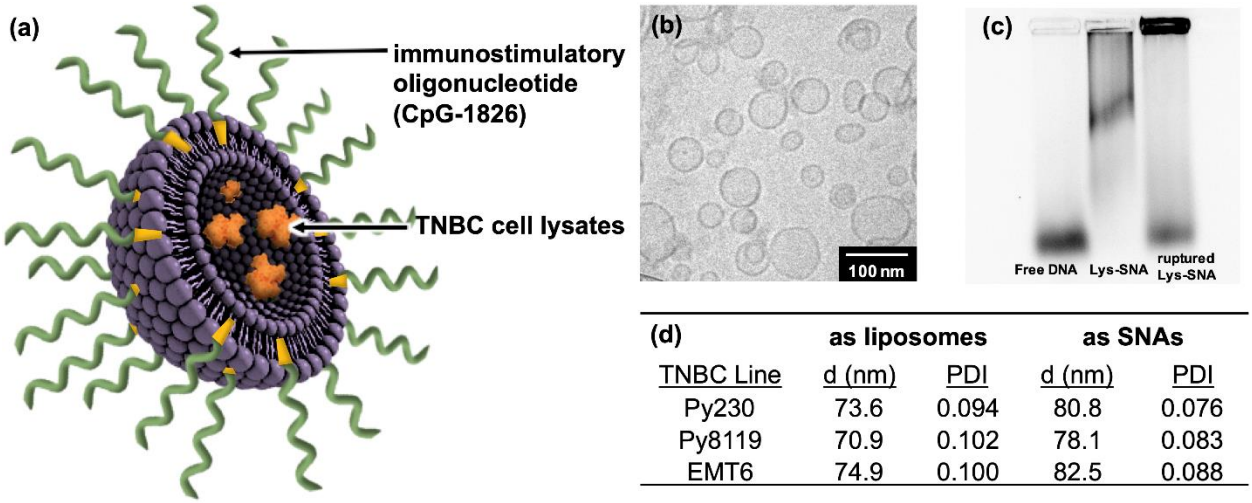

(d)	as liposomes		as SNAs	
TNBC Line	d (nm)	PDI	d (nm)	PDI
Py230	73.6	0.094	80.8	0.076
Py8119	70.9	0.102	78.1	0.083
EMT6	74.9	0.100	82.5	0.088

Figure 44. A lysate-loaded, immunostimulatory spherical nucleic acid (Lys-SNA). (a) A schematic of a Lys-SNA. TNBC lysates (orange) from either oxidized or non-oxidized TNBC cells are encapsulated in the core of a liposome (purple), which is functionalized with cholesterol-modified nucleic acids (green) to generate the SNA. (b) Cryo-TEM of Lys-SNAs. (c) Gel electrophoresis of free CpG-1826 (left lane), Lys-SNAs (middle lane), and Lys-SNAs after exposure to Triton-X to break apart liposomes (right lane). (d) Hydrodynamic diameter of lysate-loaded liposomes and SNAs, as measured by DLS.

human epidermal growth factor receptor 2 (HER2) protein[194-197]. Paradoxically, TNBC primary tumors often initially respond well to chemotherapy; yet, there is a high incidence of relapse and metastasis. The early and aggressive nature of TNBC recurrence is exemplified by significantly decreased rates of progression-free and three-year overall survival vs. other breast cancer subtypes[195, 198, 199], necessitating the development of new and effective treatment options.

In an effort to explore the potential of SNAs as a therapeutic for treating TNBC, we synthesized liposomal SNAs that encapsulate lysates derived from TNBC cell lines in their core and present CpG-1826 on their surfaces (Lys-SNAs, **Figure 44**), as well as analogs that contain lysates from TNBC cells that were oxidized with HOCl prior to lysis (OxLys-SNAs), and evaluated their immunomodulatory activity and antitumor properties in syngeneic, orthotopic mouse models of TNBC. Moreover, we sought to determine whether the molecular identity of the lipids comprising L-SNAs could be used as an additional handle for controlling their biological properties and immunotherapeutic function. Towards this end, we synthesized a series of L-SNAs using liposomes comprised of lipids with varying T_C. In this approach, the hydrophilic headgroup of the

phospholipids remained unchanged, while the chemical identity of the hydrophobic acyl chains was systematically varied (**Figure 45B**). In this way, the surface chemistry remained the same, but the bilayer composition differed. We evaluated the resulting L-SNAs for their *in vitro* serum stability, cellular uptake, immune cell activation, and immunotherapeutic function in mouse models of TNBC.

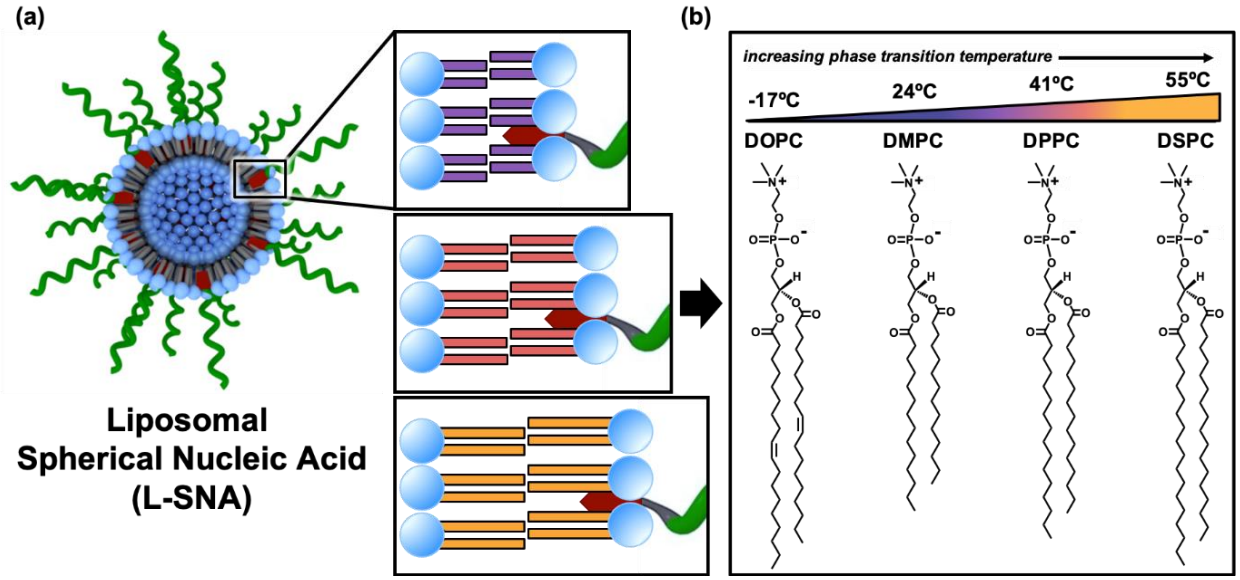

Figure 45. Liposomal SNA (L-SNA) design parameters. (a) Schematic representation of the L-SNA, wherein DNA (green) is embedded into the outer phospholipid membrane of a liposome core using a hydrophobic DNA anchor (depicted in red). The modularity of the L-SNA architecture allows for the rapid generation of diverse constructs by using different phospholipids. (b) Chemical structure and phase transition temperature (T_C) of the phospholipids used in the synthesis of L-SNAs employed in these studies.

4.2. Tumor Cell Lysate-Loaded Immunostimulatory Spherical Nucleic Acids as Therapeutics for Triple Negative Breast Cancer

4.2.1. Lysates from TNBC Cell Lines can be Compartmentalized in Lys-SNAs

To assess the feasibility of using TNBC lysates as antigen sources, we utilized three murine mammary carcinoma cell lines to recapitulate the heterogeneity of TNBC[71, 200]. Towards this end, we utilized Py230, a luminal cell line[201-203], and Py8119, a basal cell line[201-203], derived from the mouse mammary tumor virus-polyoma middle tumor antigen (MMTV-PyMT) mouse model of breast cancer, which loses expression of estrogen and progesterone as it progresses[204].

We chose the EMT6 cell line as a third model, as this syngeneic line has been recently recognized as a valuable model to study immune response in TNBC[205, 206]. Cells were grown to confluency in monolayer cell culture, dissociated and subjected to several freeze-thaw cycles to induce cell necrosis and rupture cell membranes, and centrifuged to remove cellular debris. The soluble protein fraction was encapsulated in ~70 nm liposomes prepared from 1,2-dioleoyl-sn-glycero-3-phosphocholine (DOPC). After purification to remove unencapsulated lysate, the liposomes were incubated with 3'-cholesteryl-modified CpG-1826 to generate Lys-SNAs (**Figure 44A**), whose single-lamellar spherical morphologies were validated by cryogenic transmission electron microscopy (cryo-TEM, **Figure 44B**). The average ratio of protein to DNA was determined to be 1.1 ± 0.7 mg protein per µmol DNA from three independent batches of EMT6 Lys-SNAs. Analysis via gel electrophoresis (**Figure 44C**) and the observed increase in hydrodynamic diameter, as measured by dynamic light scattering (DLS, **Figure 44D**) are consistent with DNA functionalization and SNA generation.

4.2.2. Lys-SNAs Increase Codelivery of Lysates and CpG DNA to DCs *In Vitro* and *In Vivo*

Codelivery of antigen and adjuvant to the same APC is vital for maximal antigen processing and presentation, as well as inducing the most potent antigen-specific immune response[207]. Thus, we investigated the codelivery of lysate and DNA to APCs *in vitro* and *in vivo*. Towards this end, Lys-SNAs containing fluorophore-labeled lysate (fluorescein and Oregon Green 488) and CpG-1826 (Cy5) were synthesized. Purified lysates were incubated with an Oregon Green 488-succinimidyl ester (OR488-NHS) dye and fluorescein-5-maleimide (FITC-maleimide) dye to label both the free amines and thiols in the bulk protein solution. Following removal of any unreacted dye, FITC/OR488-labeled lysates and Cy5-modified DNA were used to generate dual fluorophore-labeled Lys-SNAs. Bone marrow-derived dendritic cells (BMDCs) were isolated from C57Bl/6 mice and incubated with either fluorophore-labeled Lys-SNAs or a mixture

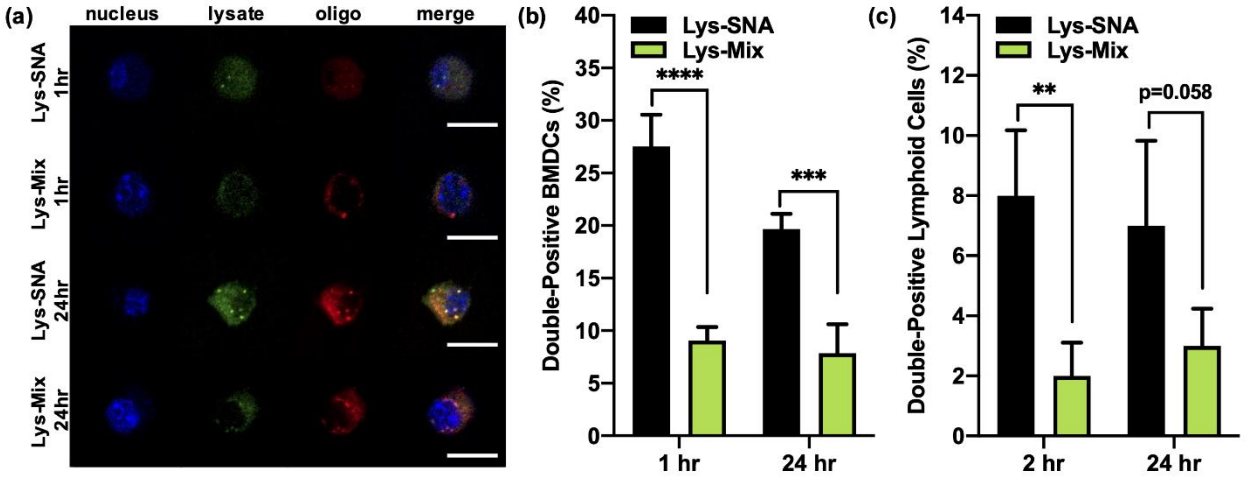

Figure 46. Delivery of FITC-labeled lysate within Cy5-labeled SNAs. (a) Confocal microscopy images of BMDCs incubated with dual fluorophore-labeled Lys-SNA and Lys-Mix for 1 and 24 hr (scale bar = 10 μm). (b) Codelivery of lysate and DNA by Lys-SNA (n=3, black bars) and Lys-Mix (n=3, green bars) to BMDCs *in vitro* after 1 and 24 hr incubations as assessed via flow cytometry. (c) Codelivery of lysate and DNA by Lys-SNA (n=3, black bars) and Lys-Mix (n=3, green bars) to lymphoid cells *in vivo* 2 and 24 hr following subcutaneous injection. Lymph nodes were isolated and CD11c+ lymphoid cells were analyzed by flow cytometry. Statistical analysis was performed using an ordinary one-way ANOVA, where "*" represents a p-value of < 0.05, "**" represents a p-value of < 0.01, and "***" represents a p-value of < 0.001.

of fluorophore-labeled lysate and CpG-1826 (**Figure 46**) at the same protein and DNA concentrations as Lys-SNAs. At set timepoints, cells were collected and analyzed by both confocal microscopy (**Figure 46A**) and flow cytometry (**Figure 46B**) to determine the number of cells positive for both FITC/OR488 and Cy5. At all timepoints, Lys-SNAs showed higher codelivery to immune cells *in vitro* than the simple mixture of lysate with CpG-1826 (Lys-Mix), showing a 3-fold and 2.5-fold enhancement in codelivery after 2 and 24 hr incubation, respectively. To evaluate codelivery of antigen and adjuvant *in vivo*, C57Bl/6 mice were subcutaneously administered Lys-SNA or Lys-Mix containing fluorophore-labeled lysate and CpG-1826 (n=3 per group). At 2 and 24 hr post-injection, animals were sacrificed, inguinal lymph nodes were isolated and dissociated into single-cell suspensions, and then analyzed by flow cytometry (**Figure 46C**). In agreement with the *in vitro* data, codelivery to CD11c+ immune cells *in vivo* was enhanced 4-fold when lysates and adjuvant DNA were formulated as Lys-SNAs at 2 hr post-injection, with over 2.3-fold enhancement still observed at 24 hr.

Encapsulating tumor cell lysates into the core of liposomal SNAs increases the codelivery of lysate and adjuvant DNA to immune cells relative to simple mixtures, both *in vitro* and *in vivo*. This highlights the importance of structural arrangement in the design of immunotherapeutics, as the maximal immune response is achieved when both adjuvant and antigen are delivered to the same target cell[207]. Indeed, formulation of lysate and CpG-1826 into SNAs leads to higher codelivery of both immunomodulatory components to the same CD11c+ cells in the draining lymph node *in vivo* at 2 hr post-injection, as compared to a simple mixture of linear CpG-1826 and bare liposomes containing lysate. Importantly, the percent of CD11c+ cells staining positive for both Cy5-labeled DNA and fluorophore-labeled lysate is maintained up to 24 hr after *in vivo* delivery with Lys-SNAs, whereas the percentage of double positive cells increased when treated with the simple mixture, but not to the level of Lys-SNAs.

4.2.3. Lys-SNAs Show Antitumor Activity in Multiple TNBC Models

To assess the antitumor activity of Lys-SNAs *in vivo*, we established orthotopic syngeneic models of TNBC by inoculating mice with ~10^6 TNBC cells (Py230, Py8119, or EMT6) in the left inguinal mammary fat pad. At days 6, 10, and 15 post-inoculation, animals were peritumorally administered Lys-SNA, Lys-Mix, or saline as a negative control at a dose of 10 nmol CpG-1826

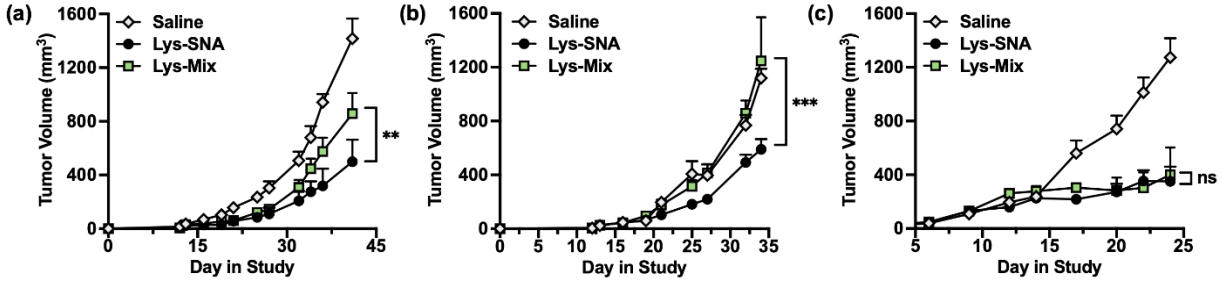

Figure 47. Antitumor effects of Lys-SNA and Lys-Mix *in vivo*. (a) Antitumor efficacy of mice bearing orthotopic syngeneic (a) Py230 tumors, (b) Py8119 tumors, or (c) EMT6 tumors when administered Lys-SNA (black circles), Lys-Mix (green squares), or saline (white diamonds). Treatment initiation began at day 6 post-inoculation and was repeated on days 10 and 15. Statistical analysis was performed using an ordinary one-way ANOVA, where "*" represents a p-value of < 0.05, "**" represents a p-value of < 0.01, "***" represents a p-value of < 0.001, and "n.s." represents a p-value > 0.05, which is considered not significant.

and 20 μg lysate. In the Py230 and Py8119 models, animals administered Lys-SNAs showed a 42% and 53% reduction in tumor volume, respectively, relative to animals administered Lys-Mix at day 30 of the study (**Figure 47A-B**), suggesting that packaging lysates into the core of SNAs increases their antitumor efficacy. In the EMT6 model, administration Lys-SNA stalled tumor growth relative to saline, showing a 73% reduction in tumor growth at day 25; however, no significant difference in tumor growth was observed between animals administered Lys-SNA and Lys-Mix (**Figure 47C**). Based on previous reports of using tumor lysates as antigen sources[156-158], we hypothesized that the lysates generated in the EMT6 model were poorly immunogenic, thus leading to suboptimal T cell priming and subsequent antitumor activity. Therefore, we investigated the use of lysates derived from oxidized tumor cells in this model.

4.2.4. Oxidizing Tumor Cells Prior to Lysis Increases Observed Immunogenicity

Since it has been reported that oxidation increases the immunogenicity of tumor lysates, we sought to determine whether lysates derived from oxidized tumor cells could be utilized as potent antigen sources following incorporation into SNAs. We generated oxidized tumor cell lysates by incubating EMT6 cells in 60 μM HOCl for 1 hr to ensure complete cell death[208]. Oxidized lysates were then prepared by subjecting the cells to several freeze-thaw cycles and centrifugation to remove cellular debris. The total amount of protein lysate collected from oxidized tumor cells (herein referred to as “oxidized lysate”) was similar to that of protein lysate collected from non-oxidized tumor cells (herein referred to as “non-oxidized lysate”);

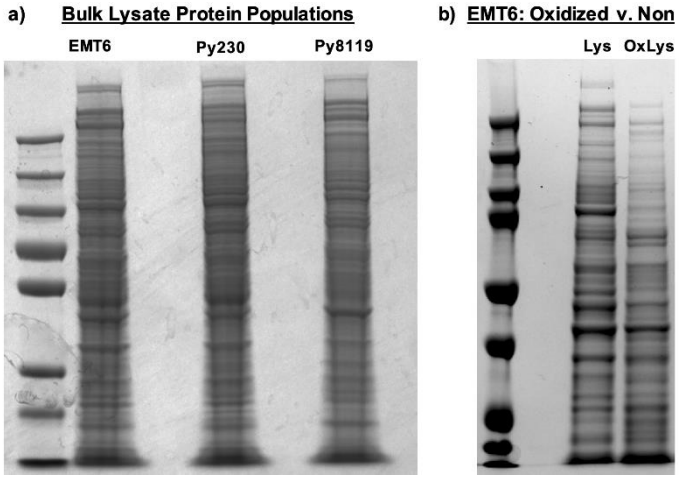

Figure 48. SDS PAGE gel of (a) lysates isolated from EMT6, Py230, and Py8119, and (b) lysates isolated from non-oxidized (left lane) and oxidized EMT6 cells (right lane).

however, the bulk protein population of oxidized lysate differed from that of non-oxidized lysate, with larger protein bands appearing in the oxidized sample (**Figure 48**). This finding confirms that cellular oxidation prior to lysate generation changes the available antigen pool, which is in agreement with published studies on the use of oxidized lysates in DC vaccines[74, 75].

To determine whether oxidation prior to lysate generation increases the immunogenicity of the isolated lysate, we incubated BMDCs with CpG-1826 (0.1 nmol) and either non-oxidized lysate or oxidized lysate at equivalent protein concentrations (1 µg total protein). The expression of maturation markers CD40, CD80, and CD86 was significantly elevated in BMDCs incubated with oxidized lysates (**Figure 49A-C**) relative to treatment with non-oxidized lysates alone, showing a 75%, 20%, and 34% increase in CD40, CD80, and CD86 marker expression over non-oxidized lysates, respectively, as well as a 160%, 47%, and 98% increase over CpG-1826 alone. Furthermore, expression of the MHC-II was elevated by 47% in BMDCs incubated with oxidized lysate as compared to those incubated with CpG-1826 alone (**Figure 49D**). This finding suggests

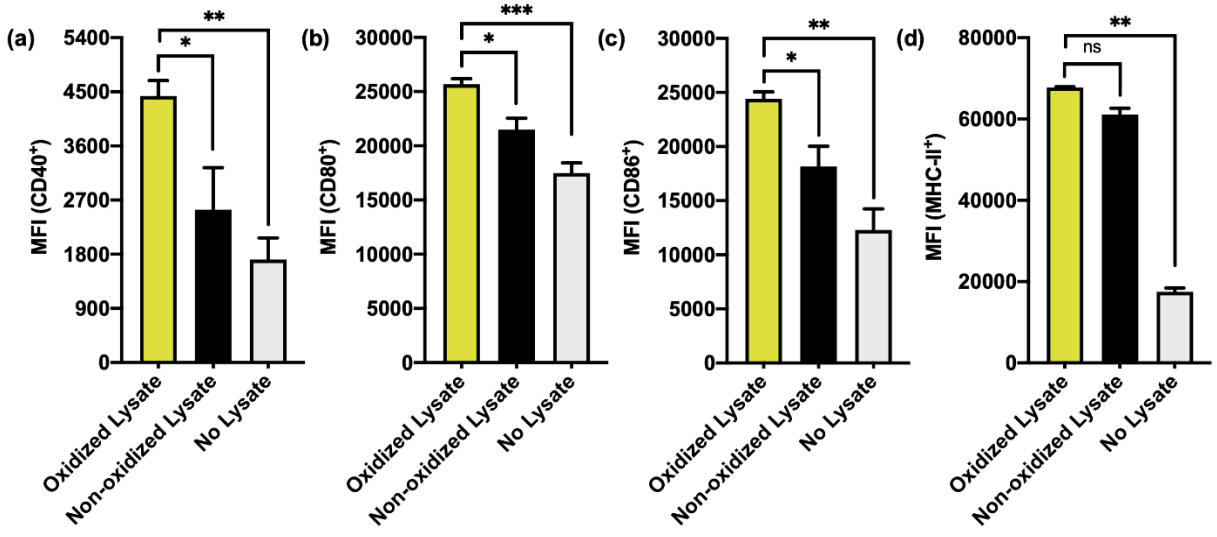

Figure 49. Activation of BMDCs *in vitro* following incubation. Cells isolated from C57BL6 mice were purified and cocultured with CpG-1826 and oxidized lysates (yellow bars), non-oxidized lysates (black bars), or no lysate (grey bars). After two days, DC activation was measured by flow cytometry for expression levels of (a) CD40, (b) CD80, (c) CD86, and (d) MHC-II. Statistical analysis was performed using an ordinary one-way ANOVA, where "*" represents a p-value of < 0.05, "**" represents a p-value of < 0.01, "***" represents a p-value of < 0.001,and "n.s." represents a p-value > 0.05, which is considered not significant.

that inducing cell death via oxidation leads to lysate populations that have elevated adjuvant behavior as well as antigenic behavior, as DC maturation is primarily dictated by activation with adjuvants[209].

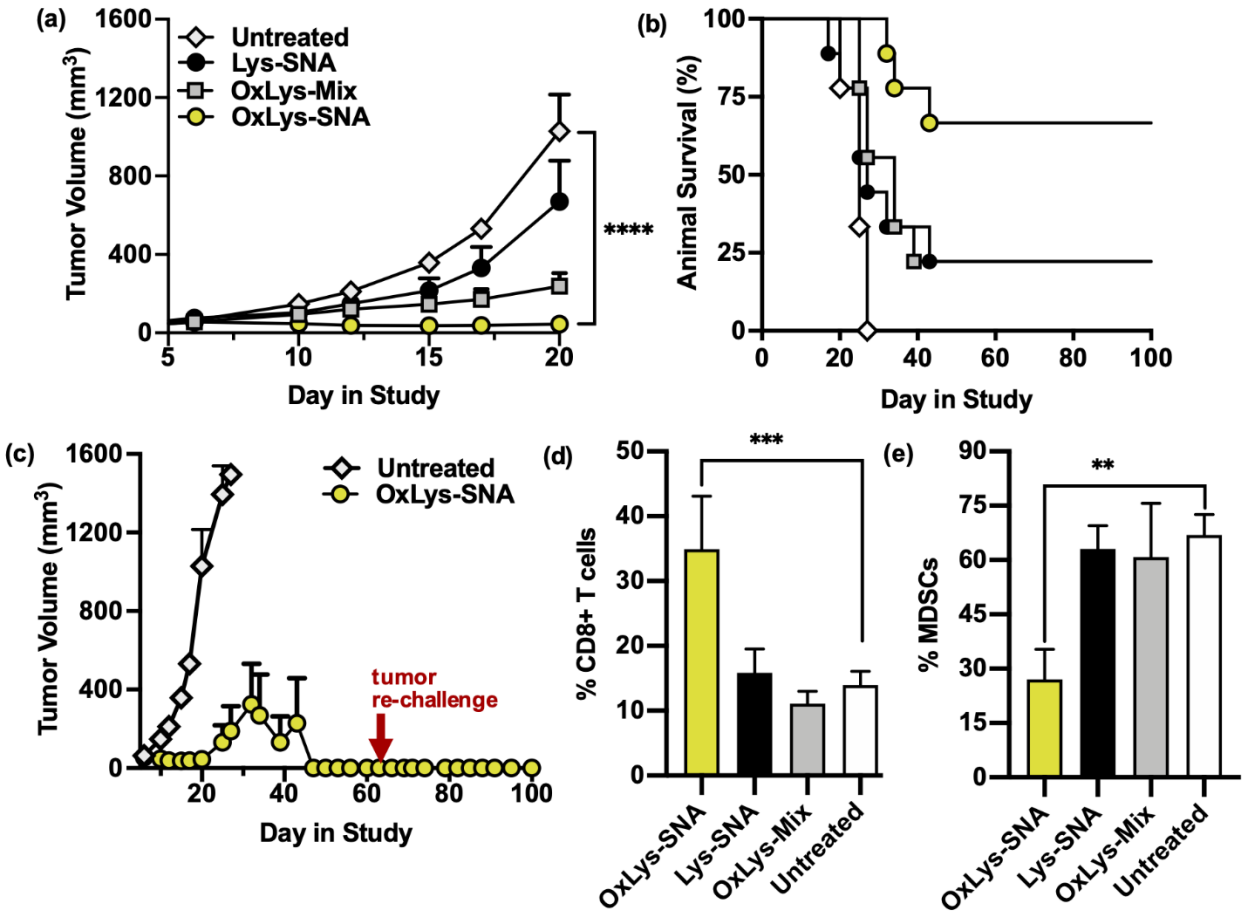

Figure 50. OxLys-SNA *in vivo* analyses. (a) Antitumor efficacy and (b) corresponding survival curve of Balb/c mice (n=9 per group) bearing orthotopic syngeneic EMT6 tumors when administered OxLys-SNA (yellow circles), OxLys-Mix (grey squares), Lys-SNA (black circles), or saline (white diamonds). Treatment initiation began at day 6 post-inoculation and was repeated on days 10 and 15. (c) Full tumor growth curve of animals administered OxLys-SNA (yellow circles) or saline (white diamonds). A subset of animals that had been administered OxLys-SNAs (n=3) were re-challenged by inoculation with ~10^6 EMT6 cells in the right inguinal mammary fat pad at day 65 (red arrow) and tumor growth monitored out to day 100. Population of (d) cytotoxic CD8+T cells and (e) MDSCs isolated from the TME of EMT6-bearing mice at day 11 post-inoculation, following treatment on days 6 and 15 with OxLys-SNA (yellow bars), Lys-SNA (black bars), OxLys-Mix (grey bars), or saline (white bars). Statistical analysis was performed using an ordinary one-way ANOVA, where "*" represents a p-value of < 0.05, "**" represents a p-value of < 0.01, "***" represents a p-value of < 0.001, and "****" represents a p-value of < 0.0001.

4.2.5. OxLys-SNAs Significantly Inhibit Tumor Growth and Extend Survival *In Vivo*

To evaluate the function of OxLys-SNAs as cancer immunotherapeutics, the *in vivo* antitumor activity of OxLys-SNAs was compared to Lys-SNAs and mixtures of oxidized lysate with CpG-1826 (OxLys-Mix) in the EMT6 model of TNBC. Balb/C mice were inoculated with ~10^6 tumor cells in the left inguinal mammary fat pad and at day 6 post-inoculation, treatment was initiated via peritumoral subcutaneous injection of OxLys-SNA, Lys-SNA, OxLys-Mix, (n=9 per group) at a dose of 5 nmol DNA and 20 µg protein. Saline-treated animals were used as a negative control. Injections were repeated at day 10 and 15. Tumor mass and animal survival were monitored for 100 days post-inoculation. Animals administered OxLys-SNA responded remarkably well to treatment as compared to all other treatment groups (**Figure 50A**), with 7 out of 9 OxLys-SNA treated animals experiencing complete tumor remission at day 20 (**Figure 51A**). Furthermore, animal survival was significantly extended when administered OxLys-SNA (**Figure 50B**), with 6 out of 9 animals OxLys-SNA treated animals surviving beyond day 100 post-inoculation. Indeed, the first OxLys-SNA treated animal to succumb to tumor burden (tumor volume exceeding 1500 mm3) survived longer than all saline-treated animals (**Figure 51B**). To assess the ability of OxLys-SNAs to induce an immunological memory response, a small cohort of animals administered OxLys-SNAs were re-challenged by implanting ~10^6 EMT6 cells in the inguinal mammary fat pad on day 60 following initial tumor implantation (**Figure 50C**). All animals (n=3) remained tumor free following re-challenge with EMT6 cells, indicating that vaccination with OxLys-SNAs not only eradicates existing tumors but also prevents new tumors from forming.

4.2.6. OxLys-SNAs Alter the Immune Cell Population Within the Tumor Microenvironment

To determine the effect of OxLys-SNA administration on the immune cell population at the tumor site, Balb/c mice were inoculated with EMT6 cells in the left inguinal mammary fat pad. At days 6 and 10 post-inoculation, animals were administered OxLys-SNA, Lys-SNA, OxLys-Mix, or

saline (n=3 per group) via peritumoral subcutaneous injection. On day 11, animals were sacrificed. Tumors were dissociated into single cell suspensions and split into two fractions. One cell fraction was incubated with antibodies against CD45, CD3, and CD8 to identify CD8+ (cytotoxic) T cells present in the TME. The second cell fraction was incubated with CD45, CD11b, and Gr1 to identify myeloid derived suppressor cells (MDSCs) present in the TME. Following antibody incubation, cells were fixed and analyzed via flow cytometry. Excitingly, the population of CD8+ T cells at the tumor site was significantly elevated in animals administered OxLys-SNAs (**Figure 50D**) relative to all other treatment groups, showing a 2.3-fold increase relative to saline-treated controls. Concurrently, the population of MDSCs in animals administered OxLys-SNAs (**Figure 50E**) was decreased 2.5-fold relative to saline-treated controls. High levels of cytotoxic T cells in the microenvironment of breast tumors have been shown to be correlated with positive antitumor effects[210, 211], while high levels of MDSCs promote immune evasion[212]. Therefore, this finding provides insight on the mechanism responsible for the observed antitumor efficacy of OxLys-SNAs.

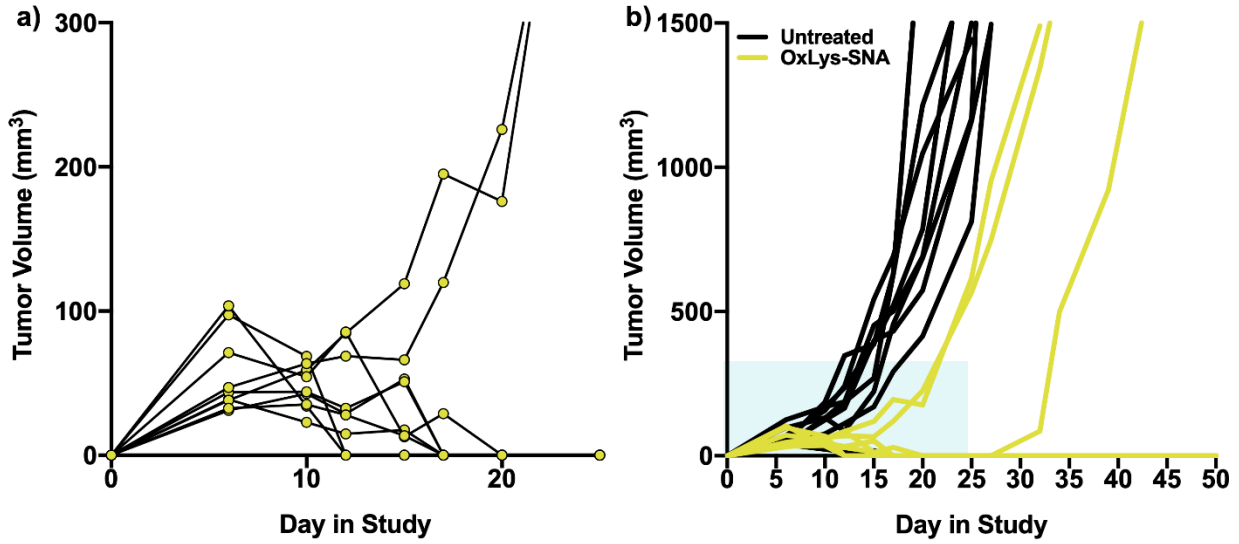

Figure 51. OxLys-SNA *in vivo* analyses. (a) Individual tumor growth (spider) plots of animals administered OxLys-SNA from day 0 to day 25 post-inoculation. At day 20, all but 2 animals receiving OxLys-SNA treatment experienced complete tumor remission. (b) Spider plots of animals administered OxLys-SNA (yellow lines) or saline (black lines) out to day 50 post-inoculation. All saline-treated animals succumbed to tumor burden before the first OxLys-SNA treated animal. Blue box denotes the region in panel a.

4.3. Impact of Liposomal Spherical Nucleic Acid Structure on Immunotherapeutic Function

4.3.1. Synthesis of L-SNAs with Lipids of Varying Phase Transition Temperatures

To assess the effect of liposome composition on the properties of L-SNAs, 80-nm liposomes comprised of lipids with varying T_C (**Figure 45B**) were synthesized using 1,2-dioleylphosphatidylcholine (DOPC, T_C = -17 °C), 1,2-dimyristoyl- phosphatidylcholine (DMPC, T_C = 24 °C), 1,2-dipalmitoylphosphatidylcholine (DPPC, T_C = 41 °C), or 1,2-distearoyl-phosphatidylcholine (DSPC, T_C = 55 °C)[182]. Following overnight incubation with DNA that is doubly functionalized with cholesterol and Cy5 (**Table 12**, entry 1) at $T > T_C$ for all lipids, colloidally stable L-SNAs formed on all liposome scaffolds. The maximum DNA loading per particle was observed for L-SNAs synthesized with DOPC, as evidenced by the absence of free unincorporated DNA by gel electrophoresis at the highest liposome to DNA ratios (**Figure 52**).

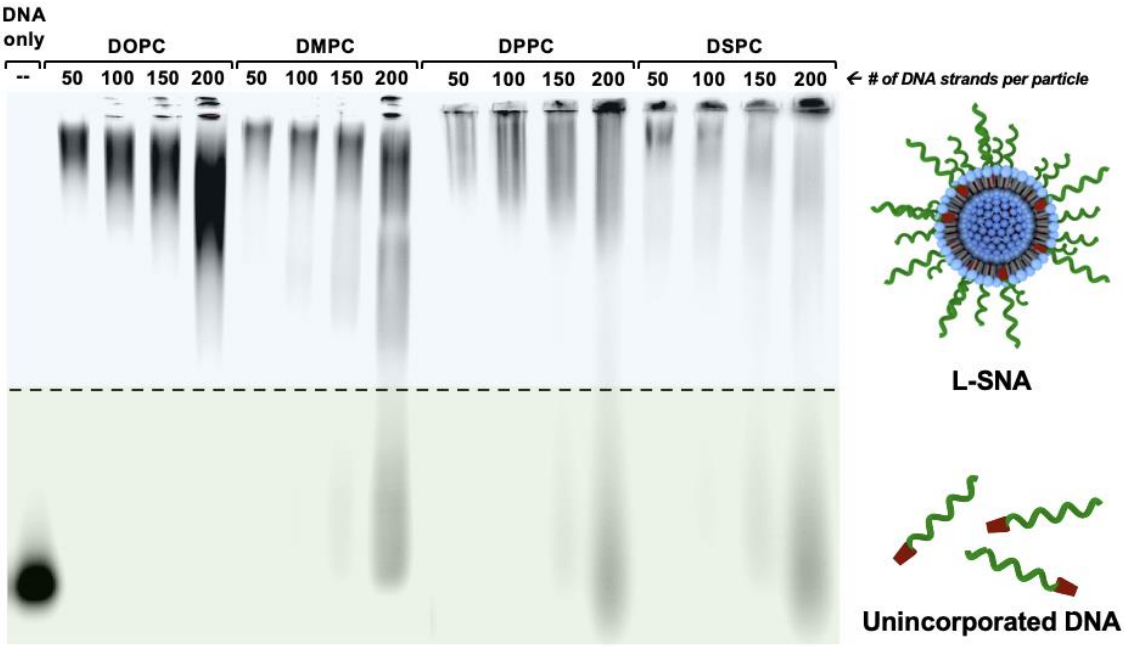

Figure 52. DNA loading capacity of various liposome scaffolds. The DNA loading of liposomes was assessed using native gel electrophoresis and Cy5-labeled DNA. L-SNAs can be successfully formed using liposomes comprised of all phospholipids tested (DOPC, DMPC, DPPC, and DSPC) at DNA loadings of up to 100 strands per particle, as evidenced by the reduction in DNA mobility without the presence of unincorporated DNA, following incubation of cholesterol-functionalized, Cy5-labeled DNA with liposomes at $T > T_C$ for all constructs.

We hypothesize that this is because cholesterol is more readily intercalated into the membrane bilayer of DOPC-based liposomes than those comprised of fully saturated phospholipids, due to conformational rearrangement of lipids in the liquid crystalline phase.[213, 214] Indeed, the maximum DNA loading per particle was reduced in L-SNAs comprised of lipids with higher T_C values (i.e., DMPC, DPPC, and DSPC), as evidenced by the presence of free DNA at loadings exceeding 150 strands per particle (0.31 pmol/cm^2, **Figure 52**). This is presumably due to decreased membrane fluidity of liposomes comprised of lipids with higher T_C.[214] Dynamic light scattering (DLS) analysis confirmed that the L-SNA hydrodynamic diameter was identical regardless of core composition (**Table 13**).

4.3.2. Serum Stability Increases with L-SNAs Formulated with DSPC Lipids

To evaluate the DNA dissociation from the L-SNA scaffold in biological media, L-SNAs were synthesized using liposomes containing 1% rhodamine-labeled lipids (**Figure 62**) and DNA doubly functionalized with cholesterol and Cy5 (**Table 12**, entry 1). On the L-SNA scaffold, Cy5 and rhodamine are within the radius required for Förster resonance energy transfer (FRET), with the FRET signal indicative of the presence of intact L-SNAs. FRET-capable L-SNAs were incubated in 10% fetal bovine serum (FBS) at 37ºC, and their stability was evaluated as a function of the decrease in FRET signal over time (**Figure 54**). To account for any potential variations in dye incorporation per particle and to normalize the data for comparison, the apparent rate constant, k, was calculated for each L-SNA using a one-phase exponential decay equation (**Figure 54**) to determine the initial rate of FRET decrease. The calculated k-values of the L-SNAs decrease as a function of increasing T_C (**Figure 53A**), indicating that the DNA dissociation rate is

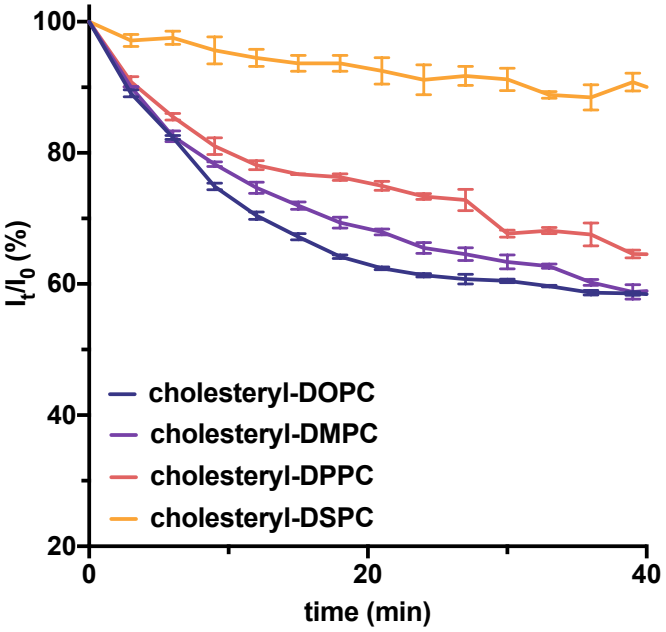

Figure 54. Representative serum stability plots of L-SNA stability. The decrease in FRET signal overtime of L-SNAs composed with different liposomes cores is measured relative to the initial FRET signal. The intial rate is fast for liposomes formulated with lower T_C lipids indicative of less stability.

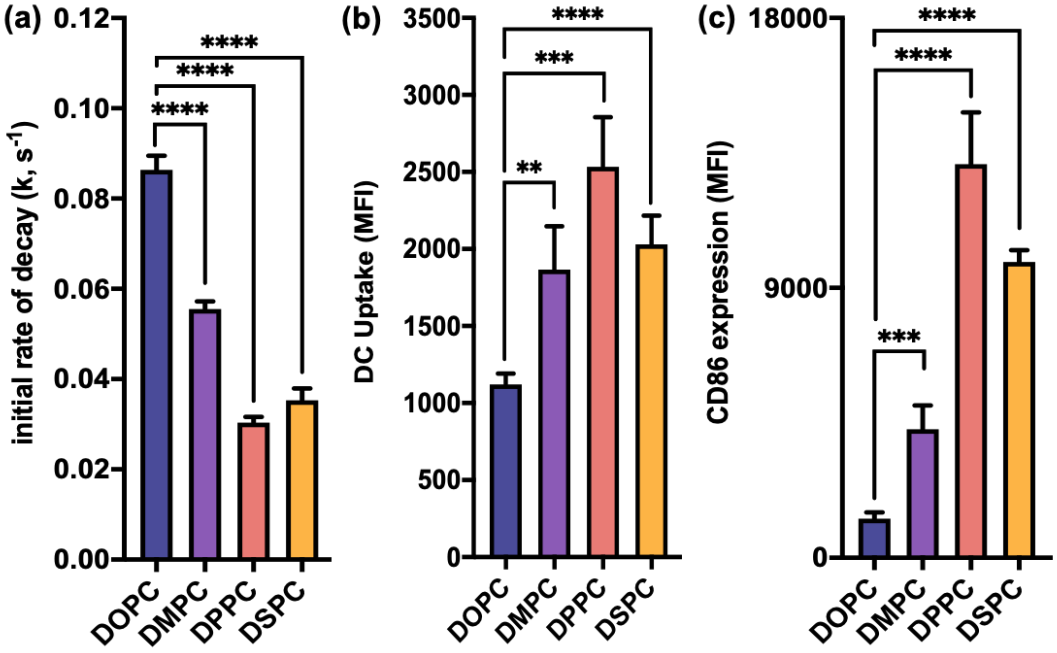

Figure 53. *In vitro* serum stability, cellular uptake, and immune activation by L-SNAs. (a) Plot of the initial rate of decay, k, as a function of decrease in FRET signal over time. Changing the liposome scaffold from DOPC to one comprising phospholipids of higher T_C significantly decreases the rate of DNA dissociation from L-SNAs, thus increasing the stability of the overall construct. (b) Cellular uptake of L-SNAs by DCs as a function of liposome scaffold. Uptake is significantly increased by synthesizing L-SNAs from all higher T_C lipids. (c) DC activation as a function of L-SNA composition. Changing the liposome scaffold from DOPC to one comprising phospholipids of higher T_C significantly increases the observed expression of CD86. Statistical analysis was performed using an unpaired t-test, where "**" represents a p-value of < 0.01, "***" represents a p-value of < 0.001, and "****" represents a p-value of <0.0001. Error bars represent standard deviation. MFI represents median fluorescence intensity.

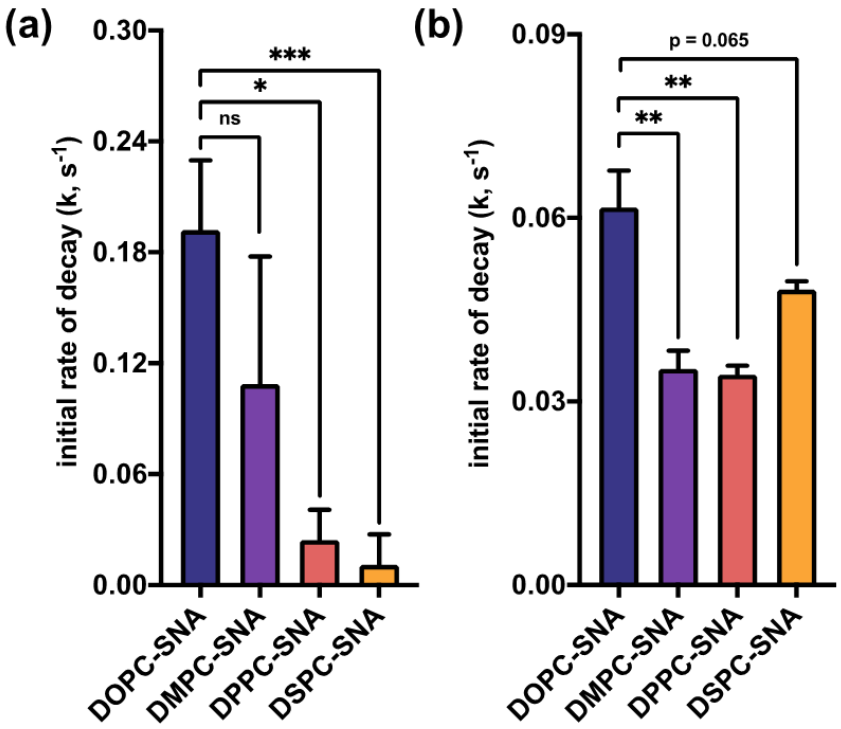

Figure 55. *In vitro* serum stability of L-SNAs at various temperatures. Shown is a plot of the initial rate of decay, k, as a function of the decrease in FRET signal over time when measured at (a) 65 ºC or (b) 20 ºC. Statistical analysis was performed using an unpaired t-test, where "*" represents a p-value of < 0.05, "**" represents a p-value of < 0.01, and "***" represents a p-value of < 0.001. ns represents not significant. Error bars represent standard deviation. *In vitro* serum stability at 20 ºC as a function of liposome composition.

slower in higher T_C L-SNAs and that these L-SNAs are more stable. Indeed, the initial rate of FRET decay for L-SNAs synthesized with DSPC was determined to be approximately 60% lower than those synthesized with DOPC at 37ºC. Importantly, the trends in the rate of DNA dissociation from the SNA scaffold as a function of T_C become more pronounced at increased temperatures (**Figure 55A**). The rate of DNA dissociation from L-SNAs synthesized with DSPC is ~ 95% lower than L-SNAs synthesized from DOPC when serum stability is assessed 65 ºC. Moreover, the differences in DNA dissociation rate become negligible when L-SNAs are incubated at 20 ºC (**Figure 55B**), due to decreased membrane fluidity of all L-SNA constructs.

4.3.3. L-SNAs Composed of DPPC Exhibit Higher Cellular Uptake and Immune Activation

To correlate the *in vitro* serum stability with biological outcomes, the cellular uptake of all L-SNAs by primary immune cells was evaluated as a function of liposome scaffold. Increased cellular uptake as a function of T_C was observed in bone marrow derived dendritic cells (DCs), with an overall upward trend between T_C and cellular uptake, showing an approximately 80% increase in uptake of L-SNAs comprised of DSPC as compared to DOPC (**Figure 53B**). Intriguingly, the cellular uptake by DCs was consistently highest for L-SNAs synthesized from DPPC in biological replicates (n = 3). We hypothesize that this is because the T_C of DPPC (41 °C) is close to the incubation temperature used for these assays (37 °C) and it is known that liposomes become increasingly permeable at temperatures close to the T_C,[215] thus allowing for increased L-SNA membrane flexibility and greater association with cell surfaces.

The effect of L-SNA composition on downstream biological processes was assessed via *in vitro* DC activation, as these cells are functional antigen-presenting cells and have been shown to be efficiently activated by immunostimulatory L-SNAs.[12, 15, 16, 49] L-SNAs were synthesized using immunostimulatory oligonucleotides (CpG-1826)[216] functionalized with cholesterol (**Table 12**, entry 2), and liposomes comprised of DOPC, DMPC, DPPC, or DSPC. Following incubation with L-SNAs, DC activation was evaluated as a function of CD86 expression, which is a surface protein present on mature immune cells that promotes T cell differentiation and survival.[217] A dramatic increase in immune activation was observed when DCs were incubated with the more stable L-SNAs (**Figure 53C**), revealing a 6.5-fold increase in CD86 expression by L-SNAs synthesized with DSPC, as compared to those synthesized with DOPC. Consistent with the cellular uptake trends observed in DCs, L-SNAs comprised of DPPC induced the highest expression of CD86, resulting in a nearly 10-fold increase in CD86 expression as compared to L-SNAs comprised of DOPC (**Table 14**).

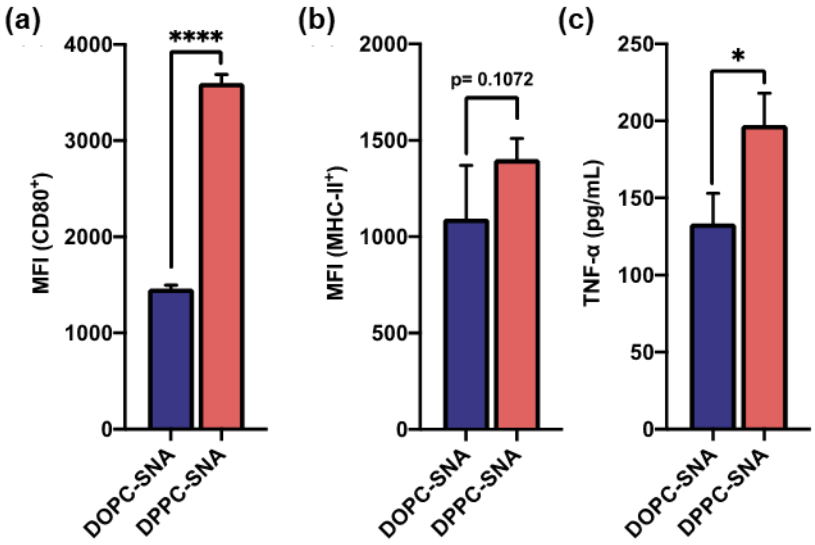

Figure 56. Expression of (a) CD80, (b) MHC-II, and (c) TNF-α *in vitro* by DCs, following a 24-h incubation with either DOPC-SNAs (blue bars) or DPPC-SNAs (pink bars). Statistical analysis was performed using an unpaired t-test, where "*" represents a p-value of < 0.05 and "****" represents a p-value of <0.0001. Error bars represent standard deviation. MFI represents median fluorescence intensity.

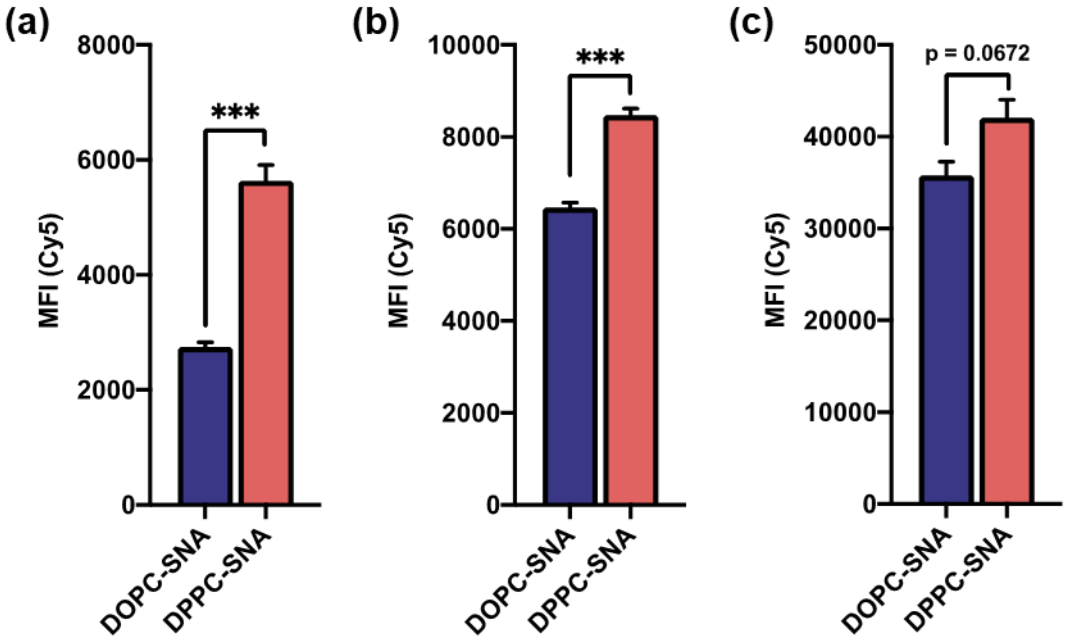

Figure 57. Time-course analysis of L-SNA uptake by DCs *in vitro*. DPPC-SNAs (pink bars) were taken up by DCs to a higher extent than DOPC-SNAs (blue bars) after a (a) 30 min, (b) 2 h, and (c) 24 h incubation. Statistical analysis was performed using an unpaired t-test, where "***" represents a p-value of < 0.001. Error bars represent standard deviation. MFI represents median fluorescence intensity.

Because immunostimulatory L-SNAs synthesized with DPPC (henceforth referred to as "DPPC-SNAs") showed the highest *in vitro* stability, uptake, and CD86 expression, the immune uptake and responses generated by this construct were more comprehensively analyzed and compared to the standard L-SNA construct, which is synthesized with DOPC (henceforth referred to as "DOPC-SNA"). DPPC-SNAs were consistently taken up to a greater extent by DCs than DOPC-SNAs at all timepoints analyzed (**Figure 57**). In addition, DPPC-SNAs showed increased immune activation over DOPC-SNAs, as measured by the expression of surface proteins CD80 and MHC-II (**Figure 56A-B**) and the secretion of the cytokine TNF-α (**Figure 56C**) following 24 h incubation.

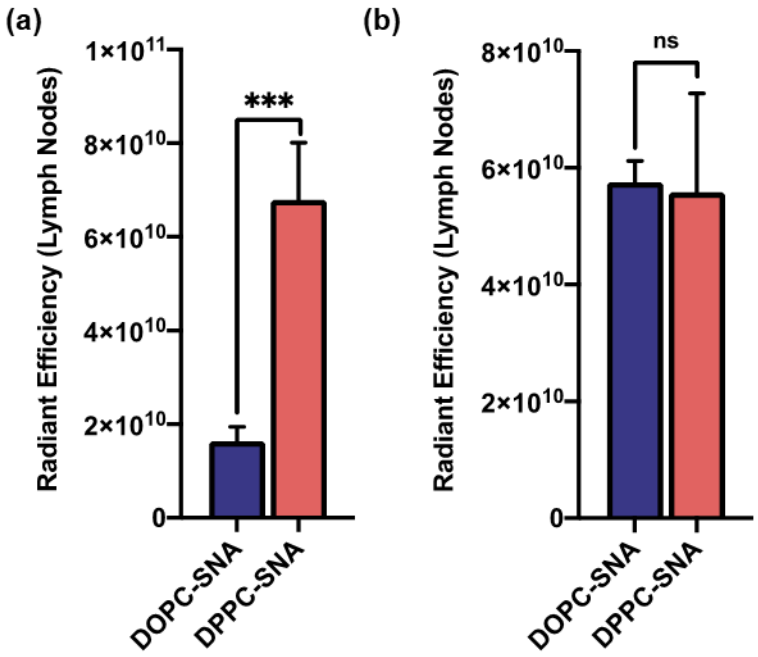

Figure 58. Accumulation of L-SNAs in lymph nodes is significantly different at shorter time points. (a) 2 h or (b) 24 h following subcutaneous administration of DOPC-SNAs (blue bars) or DPPC-SNAs (pink bars) the rhodamine signal from the liposome was measured by *in vivo* imaging system. Statistical analysis was performed using an unpaired t-test, where "***" represents a p-value of < 0.001 and ns represents not significant. Error bars represent standard deviation.

4.3.4. Synergy Between Lysate Preparation Method and Liposome Composition in Antitumor Activity

To determine whether superior *in vitro* DC uptake correlates with higher *in vivo* lymph node targeting, the accumulation of DPPC-SNAs in the lymph nodes was compared to that of DOPC-SNAs as a function of time. To achieve this, healthy mice were administered fluorophore-labeled SNAs via subcutaneous injection at a dose of 2.5 nmol DNA per construct (n=3). The lymph node accumulation of DPPC-SNAs was 4-fold higher than DOPC-SNAs at 2 h post-injection (**Figure 58A**), while the concentration was equivalent at 24 h post-injection (**Figure 58B**). Together, this indicates that DPPC-SNAs are shuttled more rapidly to the lymph nodes *in vivo*, without a loss in long-term retention.

The administration of CpG-1826 in the 4T1 model of TNBC can suppress the spontaneous formation of lung metastases, as a form of "adjuvant only" immunotherapy[218, 219]. Thus, to evaluate whether L-SNA stability and *in vitro* immunostimulatory activity correlated with *in vivo* outcomes, the activity of DOPC-SNAs was compared to DPPC-SNAs in the 4T1 mouse model (**Figure 59**).

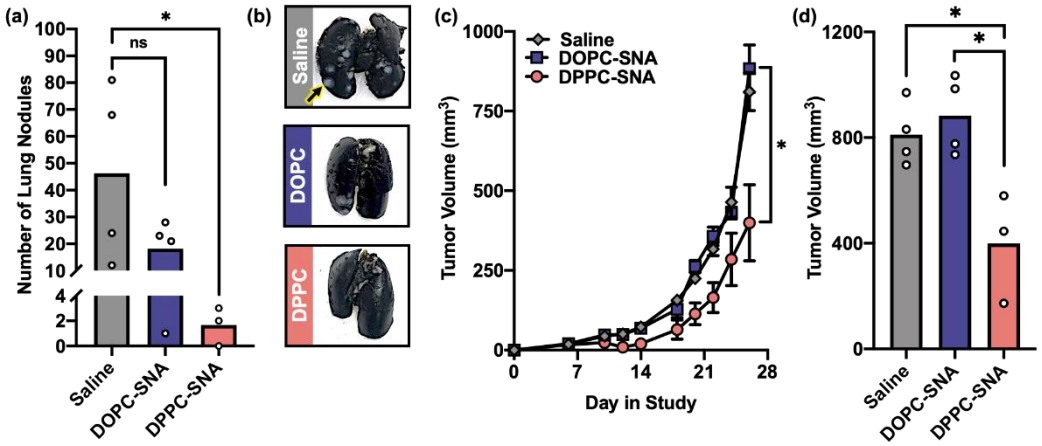

Figure 59. *In vivo* antimetastic and antitumor activity of L-SNAs in the 4T1 TNBC model. (a) Lung metastasis production, as measured by the number of lung nodules identified at day 28 in the study, following administration of saline (grey bar), DOPC-SNAs (blue bar), or DPPC-SNAs (pink bar). White dots represent individual animals in each group. (b) Representative photos of lungs excised from each group. (c) Primary tumor growth in the 4T1 model following administration of saline (grey diamonds), DOPC-SNAs (blue square), or DPPC-SNAs (pink circle). Error bars represent standard error of the mean. (d) Comparison of tumor volume between treatment groups at day 28 in the study. White dots represent individual animals in each group. Statistical analysis was performed using an unpaired t-test, where "*" represents a p-value of < 0.05, and "ns" represents a p-value of >0.05.

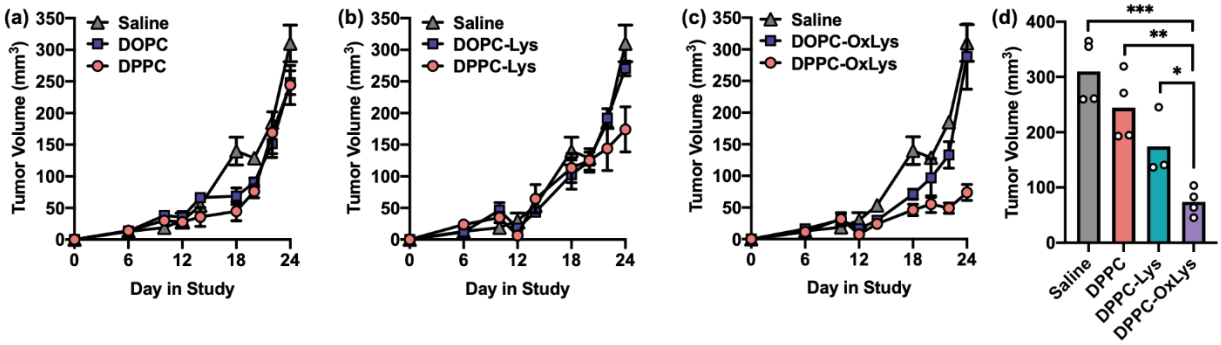

Figure 60. *In vivo* antitumor activity of L-SNAs in the Py8119 TNBC model. (a) Antitumor efficacy of "adjuvant only" L-SNAs as a function of liposome stability, following administration of saline (grey triangle) DOPC-SNAs (blue square), or DPPC-SNAs (pink circle). (b) Antitumor efficacy of L-SNAs encapsulating Py8119 lysates as a function of liposome stability. Animals were administered saline (grey triangle), DOPC-Lys-SNAs (blue square), or DPPC-Lys-SNAs (pink circle). (c) Antitumor efficacy of L-SNAs encapsulating oxidized Py8119 lysates as a function of liposome stability. Animals were administered saline (grey triangle), DOPC-OxLys-SNAs (blue square), or DPPC-OxLys-SNAs (pink circle). ((d) Comparison of tumor volume between DPPC-containing treatment groups at day 28 in the study. White dots represent individual animals in each group. Error bars represent standard error of the mean. Statistical analysis was performed using an unpaired t-test, where "*" represents a p-value of < 0.05, "**" represents a p-value of < 0.01, "***" represents a p-value of < 0.001, and "ns" represents a p-value of > 0.05.

Mice bearing 4T1 tumors were peritumorally administered DOPC-SNAs and DPPC-SNAs via subcutaneous injection at a dose of 5 nmol of CpG-1826 on days 6, 10, and 15 post-inoculation (n = 4 per group). As a negative control, an additional set of animals (n = 4) was administered saline. At day 28 of the study, animals were sacrificed, lungs perfused per literature protocol,[220] and number of lung nodules counted. DPPC-SNAs significantly inhibited the formation of lung metastases (**Figure 59A-B**), whereas DOPC-SNAs were ineffective. Interestingly, this trend held when evaluating primary tumor growth (**Figure 59C-D**), with DPPC-SNAs significantly suppressing tumor growth, while DOPC-SNAs had no effect on primary tumor growth throughout the duration of the study. Consistent with *in vitro* results (vide supra), L-SNA potency in the 4T1 model directly correlates with liposome stability.

To evaluate whether the observed differences in L-SNA activity were tumor model-dependent, the antitumor activity of L-SNAs in the Py8119 model of TNBC was also evaluated. Unsurprisingly, administration of DPPC-SNAs and DOPC-SNAs as "adjuvant only" immunotherapeutics was ineffective in this model (**Figure 60A**), as immunostimulation alone is

often insufficient at raising an antitumor immune response,[219] with a few notable exceptions that include the aforementioned 4T1 model. Since no TAAs have been identified for TNBC, lysates from Py8119 cells were generated and then utilized as antigen sources. These lysates were encapsulated into L-SNAs comprised of DOPC (DOPC-Lys-SNAs) or DPPC (DPPC-Lys-SNAs). The antitumor efficacy of both constructs was compared *in vivo* following L-SNA administration at days 6, 10, and 15 at a dose of 5 nmol of CpG-1826 and 10 μg of lysate. Excitingly, there was a ~60% reduction in tumor growth when DPPC-Lys-SNAs were administered as compared to animals administered saline, whereas there was no difference in tumor growth in animals administered DOPC-Lys-SNAs (**Figure 60B**), again showing the dependence of antitumor efficacy on L-SNA stability.

Oxidizing cancer cells prior to lysate generation often increases their immunogenicity[74, 75, 155] and thus incorporating oxidized lysates into the core of L-SNAs leads to dramatic increases in antitumor efficacy in mouse models of TNBC.[178] Therefore, to determine whether the effects of tumor cell oxidation and L-SNA stability were additive, L-SNAs containing lysates from oxidized Py8119 cells were synthesized using DOPC (DOPC-OxLys-SNAs) and DPPC (DPPC-OxLys-SNAs). Strikingly, DPPC-OxLys-SNAs significantly suppressed tumor growth over the duration of the study (**Figure 60C**), while DOPC-OxLys-SNAs were ineffective at these doses of DNA and lysate. Collectively, these data indicate that the effects of lysate preparation method and L-SNA stability are synergistic, a trend which becomes clearer when the study endpoint for all DPPC-based L-SNAs is compared (**Figure 60D**). While DPPC-SNAs are ineffective at reducing tumor growth in the Py8119 model, the inclusion of lysates into the L-SNA (DPPC-Lys-SNAs) renders these materials effective, and maximum antitumor efficacy is observed when lysates from oxidized cells are used as the antigen sources (DPPC-OxLys-SNAs), revealing the importance of both antigen processing method and liposome stability in these constructs.

4.4. Conclusions

This work is important because it describes a new class of potent vaccines based upon the compartmentalization of antigens in the form of oxidized lysate within a novel nanotherapeutic. These structures, in three TNBC tumor models, show very promising activity with respect to codelivery of lysate and adjuvant and DNA, antitumor efficacy, extended animal survival, and alteration of the immune cell population within the TME. Importantly, this is only one way to compartmentalize lysates in SNA-type architectures, and when one considers recent work that shows single antigen presentation on the outside of SNAs can increase vaccine performance[16], there is a path forward for identifying new structures with vaccine performance superior to those presented herein. Indeed, if one could present the lysate components on the outside of such structures, even better responses may be possible. Taken together, these results show that the method in which tumor cell lysates are generated, as well as the way adjuvant and antigen(s) are packaged and delivered to the immune system, has a profound impact on the resulting antitumor efficacy. Therefore, these results have important implications in the development of personalized immunotherapies for TNBC and other cancers.

Synthesizing L-SNAs from liposomes comprised of lipids with identical phosphatidylcholine headgroups, but varied diacyl lipid tail, allows for single variable analysis of biological properties. Through these studies, we have determined that the serum stability, cellular uptake, immune activation, and antitumor activity of L-SNAs can be augmented by using liposome scaffolds comprised of lipids with higher T_C values, while keeping the nanoparticle size and surface chemistry identical. The dynamics of lipid exchange in liposomes are a function of membrane fluidity, which decreases as T_C increases. Thus, synthesizing L-SNAs from lipids with higher T_C produces structures whose dynamics of lipid exchange are slower. In turn, the rate of DNA dissociation from the L-SNA scaffold is significantly decreased when SNAs are synthesized from lipids with higher T_C, leading to greater interactions between the oligonucleotides and

liposome core and an overall increased structural stability. Because the L-SNA architecture drives its biological properties, prolonged preservation of this structure in biological media leads to the observed enhancements in cellular uptake, immune cell activation, and *in vivo* lymph node accumulation. These results indicate that the biological interactions of nanomaterials are not solely determined by nanoscale size and surface chemistry, but rather that the chemical identity of the components of noncovalent assemblies also plays a substantial role.

We have previously shown that seemingly small chemical and structural changes to the L-SNA platform can have profound impacts on resulting SNA biological properties and functions. For example, changing the chemistry used to anchor DNA into the L-SNA affects the *in vitro* serum stability, immune activation, and *in vivo* tissue distribution due to differences in L-SNA stability.[11, 133] Moreover, altering the chemical bond that releases peptide antigens from immunostimulatory L-SNAs enhances immune activation[49] and modifying the chemical composition and structural arrangement of antigenic cargo within immunostimulatory L-SNAs dramatically affects downstream antitumor efficacy because of differences in signaling kinetics[16, 178]. In line with these findings, we now show that the composition of the liposomal core can be used to modulate the biological properties of L-SNAs, providing another tunable handle in their rational design as immunotherapeutics.

In the 4T1 TNBC mouse model, administration of immunostimulatory L-SNAs synthesized with DPPC significantly decreased tumor growth and lung metastasis formation, as compared to L-SNAs synthesized with DOPC, indicating that more stable L-SNA constructs are required for maximal immunostimulation *in vivo*. Moreover, in TNBC models where “adjuvant only” therapy is ineffective, the inclusion of tumor cell lysates in the core of the L-SNAs reveals a significant dependence on L-SNA composition with respect to antitumor efficacy, where structural stability determines potency. In the Py8119 mouse model, lysates encapsulated in L-SNAs synthesized with DPPC were more effective than their DOPC analogues at stalling tumor growth; a trend that

became more pronounced when incorporating lysates from oxidized Py8119 cells into the L-SNA scaffold, revealing synergy between lysate incorporation method and L-SNA stability.

Taken together, this work convincingly shows that seemingly subtle changes to the chemical structure of nanoscale immunotherapeutics can profoundly impact their performance, and that liposome stability can be used as a variable to control the biological properties of L-SNAs. These results have important implications for the development of therapeutic L-SNAs that extend beyond cancer immunotherapy. For example, in applications where SNAs are systemically administered (e.g., gene regulation), L-SNAs synthesized using high T_C lipids may maximize the serum stability and blood circulation. Furthermore, in applications where high stability is not advantageous, such as those where encapsulated cargo needs to be released from the core of the L-SNA following cellular uptake[13, 178], L-SNAs with intermediate stability may be the most useful. Therefore, it is critical to carefully consider the liposome scaffold when designing both L-SNAs, as well as other liposome-based nanoparticle systems, for biomedical applications.

4.5. Materials and Methods

4.5.1. Tumor Cell Lysate-Loaded Immunostimulatory Spherical Nucleic Acids as Therapeutics for Triple Negative Breast Cancer

4.5.1.1. Generation and Characterization of Cell Lysates

All animal protocols were approved by the Institutional Animal Care and Usage Committee at Northwestern University. EMT6 cell lines were obtained from ATCC and grown in Minimum Essential Media supplemented with 10% heat-inactivated fetal bovine serum (FBS) and 1% penicillin−streptomycin. Py230 and Py8119 were grown in F-12K Medium (ATCC), 5% FBS, 0.1% MITO+ serum extender (Corning), 2.5 μg/mL amphotericin B (Gibco), and 50 μg/mL gentamycin (Gibco). All lysates were prepared from cells under passage number six. For lysate preparation, cells were trypsinized, washed, collected, and resuspended at 106 cells per milliliter in Dulbecco's

phosphate-buffered saline (DPBS), then subjected to five freeze−thaw cycles in liquid nitrogen and a 37 °C water bath. Cellular debris was removed by centrifugation at 10,000 relative centrifugal force (RCF) units for 10 min, and the supernatant was then collected as the protein lysate. Total protein concentration was measured using the bicinchoninic acid (BCA) assay with albumin as the protein standard (Pierce, ThermoFisher Scientific). Protein content was characterized using 4 to 12% sodium dodecyl sulfate (SDS)/ polyacrylamide gel electrophoresis at 100 V for 1 h and loading 20 µg of total protein.

To prepare oxidized lysates, EMT6 cells were grown to confluence in a Petri dish. Cells were washed with DPBS (3×) and then incubated with 60 µM HOCl in DPBS for 1 h at 37 °C. Following the incubation, cells were collected and washed with DPBS to remove any unreacted HOCl. Following centrifugation at 500 RCF for 5 min, cells were resuspended in DPBS at a density of 1 × 107 cells per mL. Cells were subjected to five freeze−thaw cycles using liquid nitrogen and a 37 °C water bath, followed by centrifugation for 10 min at 10,000 RCF. The soluble fraction was collected as the oxidized lysate.

Purified cell lysates were fluorophore-labeled for *in vitro* and *in vivo* uptake experiments. One milligram each of Oregon Green 488-NHS (Thermo Fisher) and FITC-maleimide (Thermo Fisher) dye were incubated with 1 mg/mL lysate in PBS (pH 7.5) for 16 h at 4 °C. The unreacted dye was removed by washing the lysate with 10 mL of PBS 10 times using 50 kDa cutoff centrifugation filters (4,000 × g, 10 min). Fluorophore-labeled lysate was subsequently used to make lysate-SNAs.

4.5.1.2. DNA Synthesis

Cholesteryl-modified CpG-1826 (5′-TCC ATG ACG TTC CTG ACG TT (Sp18)2 Chol-3′) and Cholesteryl-Cy5-modified CpG-1826 (5′-TCC ATG ACG TTC CTG ACG TT -Cy5-(Sp18)2 Chol-3′) were synthesized with phosphorothioate backbones via automated solid-phase DNA

synthesis using an MerMade 12 Synthesizer (Bioautomation), using 4,5-dicyanoimidazole as an activator and 3-((Dimethylamino-methylidene)amino)-3H-1,2,4-dithiazole-3-thione as the sulfurizing agent. Following synthesis, DNA strands were cleaved from solid support via overnight incubation with 30% ammonium hydroxide at room temperature (RT). Excess ammonia was removed through evaporation under nitrogen, and oligonucleotides were purified using an Agilent high-pressure liquid chromatography system using a C4 or C18 column, using a gradient of triethylammonium acetate and acetonitrile (10 to 100% acetonitrile) over 30 min. Purified oligonucleotides were collected and lyophilized. Powdered oligonucleotides were reconstituted in 5 mL of acetic acid and incubated at RT for 1 h, then extracted with ethyl acetate (7 mL, 3×). The purified, deprotected DNA was then lyophilized, resuspended in 1 mL of deionized water, and analyzed by matrix-assisted laser desorption ionization time-of-flight and native gel electrophoresis.

4.5.1.3. Synthesis of Lysate-Loaded SNAs

Tumor cell lysate (either oxidized or not) was encapsulated within DOPC liposomes using the thin-film rehydration method (55). Solutions were adjusted to 1 mg/mL (with respect to protein concentration) in PBS, which was used to rehydrate 5 mg of DOPC for 1 h at RT. After the rehydration period, liposomes were formed through five freeze−thaw cycles, using liquid nitrogen and sonication in a 37 °C water bath. Liposomes were then diluted with PBS such that the highest concentration of lipid was no greater than 2 mg/mL lipid for extrusion, as measured by the commercially available phosphotidylcholine (PC) assay (Sigma). Liposome size was controlled through sequential high-pressure extrusion using polycarbonate filters (T&T Scientific) with pore sizes of 200, 100, 80, and 50 nm. Liposomes were passed through each filter size 10 times. Following the final extrusion, tangential flow filtration with a pore size of 500 kDa (Spectrum) was used to remove any nonencapsulated proteins, and the sample was repeatedly washed with PBS

until no protein was detected in the flow-through, as monitored by measuring the absorption of the flow-through at 280 nm with ultraviolet visible (UV-vis) spectroscopy (Cary) and BCA assay. The amount of protein encapsulated within the liposomes was measured using the BCA assay after disruption of the liposome with 1% SDS to release encapsulated protein. The phospholipid concentration was measured using a commercially available PC assay kit.

To form SNAs, cholesterol-terminated oligonucleotides (3′) were embedded into the outer membrane of the liposomes by mixing 20 µM oligonucleotides with a solution of liposomes at 1.63 mM lipid at 25 °C overnight. The oligonucleotide concentration was determined by measuring the absorption at 260 nm with UV-vis. The resulting SNAs (both OxLys-SNAs and Lys-SNAs) were then concentrated to 20 µM by DNA using centrifugation filter units (Millipore), which also removed any unbound DNA. The resulting structures were analyzed by zeta potential (Malvern Zetasizer), gel electrophoresis, and DLS (**Figure 44**).

4.5.1.4. Characterization of Lysate-Loaded SNAs

Lysate-loaded SNAs were characterized using cryo-TEM, gel electrophoresis, DLS (**Figure 44D**), and zeta potential (**Table 11**). Cryo-EM samples were prepared by FEI Vitrobot Mark III by dropping 4 µL on a 200-mesh copper TEM grid with lacey carbon film, blotted for 5 s and then plunged into liquid ethane before transfer to a cryo-holder and storage in liquid nitrogen prior to imaging. Cryo-EM imaging was performed using a Hitachi HT7700 transmission electron microscope with a Gatan cryo-transfer holder under 120-kV accelerating voltage, and images were taken with a Gatan imaging camera at 30,000× magnification. Confirmation of DNA loading was done using gel electrophoresis, DLS, and zeta potential measurements. Cy5-labeled, cholesteryl-modified oligonucleotides, Cy5-labeled Lys-SNAs, and Cy5-labeled Lys-SNAs that had been incubated with Triton-X to dissociate liposomes (50 pmol each) were loaded into a 1% agarose gel on ice and run at 100 V for 45 min (**Figure 44C**).

Table 11. **Zeta Potential Analyses of Lys-SNAs and OxLys-SNAs.**

TNBC Cell Line	as liposomes		as SNAs	
	Zeta-Potential (mV)	St. Dev.	Zeta-Potential (mV)	St. Dev.
Py230	-7.05	1.42	-23.45	2.75
Py8119	-4.28	3.80	-27.83	1.68
EMT6	-5.37	1.14	-28.01	1.52
Ox-EMT6	-5.66	1.84	-35.25	0.08

4.5.1.5. Uptake of Lys-SNAs and Lys-Mix by BMDCs *In Vitro*

Bone marrow was isolated from femurs of Balb/C or C57BL/6 mice and cultured in Roswell Park Memorial Institute (RPMI)-1640 media, supplemented with 10% heat-inactivated FBS, 1% penicillin−streptomycin, and 20 ng/mL granulocyte-macrophage colony-stimulating factor. Media was replenished on day 3, and cells were harvested on day 6. SNAs were prepared by encapsulating AlexaFluor488-labeled lysate within the liposomal core and functionalizing Cy5-labeled DNA using the same methods as described above. Fluorophore-labeled SNAs were used to measure the uptake of particles in BMDCs. BMDCs were added to 24-well plates at 500,000 cells per well, and immediately treated with 1 μM Cy5-labeled DNA and AlexaFluor488-labeled lysate, or doubly labeled SNAs, for 1 or 24 h. Cells were washed, fixed with 4% paraformaldehyde for 10 min at RT, and either resuspended in DPBS for flow cytometry (BD LSRFortessa) or stained with 4′,6-diamidino-2-phenylindole and imaged with confocal microscopy (Zeiss LSM 800) using a 63× objective.

4.5.1.6. Uptake of Lys-SNAs and Lys-Mix by Lymphoid Cells *In Vivo*

Female C57BL/6 mice (n = 3, 8 wk to 10 wk old) were injected s.c. (flank) with 200 μL of 50 μM fluorophore-labeled Lys-SNAs or a mixture of CpG-1826 and lysate (Lys-Mix). Mice were killed 2 h or 24 h post-injection, and draining lymph nodes were excised. Lymph nodes were

dissociated into single cells using a cell strainer. Single-cell suspensions were stained with antibodies for CD11c (PE-Cy7) as well as a live/dead stain, and analyzed using flow cytometry.

4.5.1.7. Lys-SNA Antitumor Efficacy

Female mice (age 8 wk to 10 wk) were inoculated with 1 × 106 TNBC cells (C57BL/6 mice for Py230 and Py8119; Balb/C mice for EMT6) via s.c. injection into the right inguinal mammary fat pad. On days 6, 10, and 15, animals were administered Lys-SNA, Lys-Mix, or saline (n = 5 per group) via peritumoral injection (50 μM, 200 μL). Tumor volumes were calculated by measuring the length and width with calipers and applying the formula V = L × W × W/2. Studies were stopped and animals killed when tumor burden of saline-treated animals exceeded 1,200 mm3.

4.5.1.8. OxLys-SNA Antitumor Efficacy

Female Balb/C mice (age 8 wk to 10 wk) were inoculated with 1 × 106 EMT6 cells via s.c. injection into the right inguinal mammary fat pad. On days 6, 10, and 15, animals were administered OxLys-SNA, OxLys-Mix, Lys-SNA, or saline (n = 9 per group) via peritumoral at a dose of 5 nmol DNA and 20 μg of protein. Tumor volumes were calculated by measuring the length and width with calipers and applying the formula V = L × W × W/2. Animal survival was monitored up to 100 d, and animals were killed when tumor burden exceeded 1,500 mm3. At day 60 post-inoculation, a subset of surviving OxLys-SNA animals (n = 3) was rechallenged by inoculation with ∼106 EMT6 cells in the right inguinal mammary fat pad, and monitored for evidence of tumor growth for an additional 40 d.

4.5.1.9. BMDC Activation

BMDCs were isolated and cultured as described above. On day 6, BMDCs were harvested and incubated (100,000 BMDCs/sample) with CpG-1826 (0.1 nmol) plus oxidized lysates, nonoxidized lysates, or saline (1 μg of total protein) to induce BMDC maturation. After 48 h incubation, cells were washed with DPBS (3×) and stained with antibodies against CD40, CD80,

CD86, and MHC-II, as well as with a live/dead stain, by incubation with the appropriate antibodies for 20 min at RT. Cells were then washed with DPBS (3×) and fixed with paraformaldehyde prior to analysis using flow cytometry. Immune cells were identified by gating for CD11b+/CD11c+ double-positive cells, followed by gating for the appropriate marker (CD40, CD80, CD86, or MHC-II).

4.5.1.10. Analysis of Immune Cell Populations at EMT6 Tumor Site

Female Balb/C mice (age 8 wk to 10 wk) were inoculated with ∼106 EMT6 cells via injection into the right inguinal mammary fat pad. At days 6 and 10 post-inoculation, animals (n = 3 per group) were administered OxLys-SNA, OxLys-Mix, Lys-SNA, or saline via peritumoral injection. On day 11, animals were killed, and tumors were harvested for immune cell population analysis. Tumors were washed with DPBS and dissociated into single-cell suspensions using a cell strainer. Tumor cells were then split into two samples. One sample was stained with antibodies against CD45, CD3, and CD8 to identify CD8+ cytotoxic T cells. The second sample was incubated with CD45, CD11b, and Gr1 to identify MDSCs. After incubation for 20 min at RT, cells were washed with DPBS (3×) and fixed with paraformaldehyde prior to analysis via flow cytometry. CD8+ T cells were identified by first gating for CD45+ cells, followed by gating for CD3+/CD8+ double-positive cells (**Figure 61A**).MDSCs were identified by first gating for CD45+ cells, followed by gating for CDllb+/Gr1+ double-positive cells (**Figure 61B**).

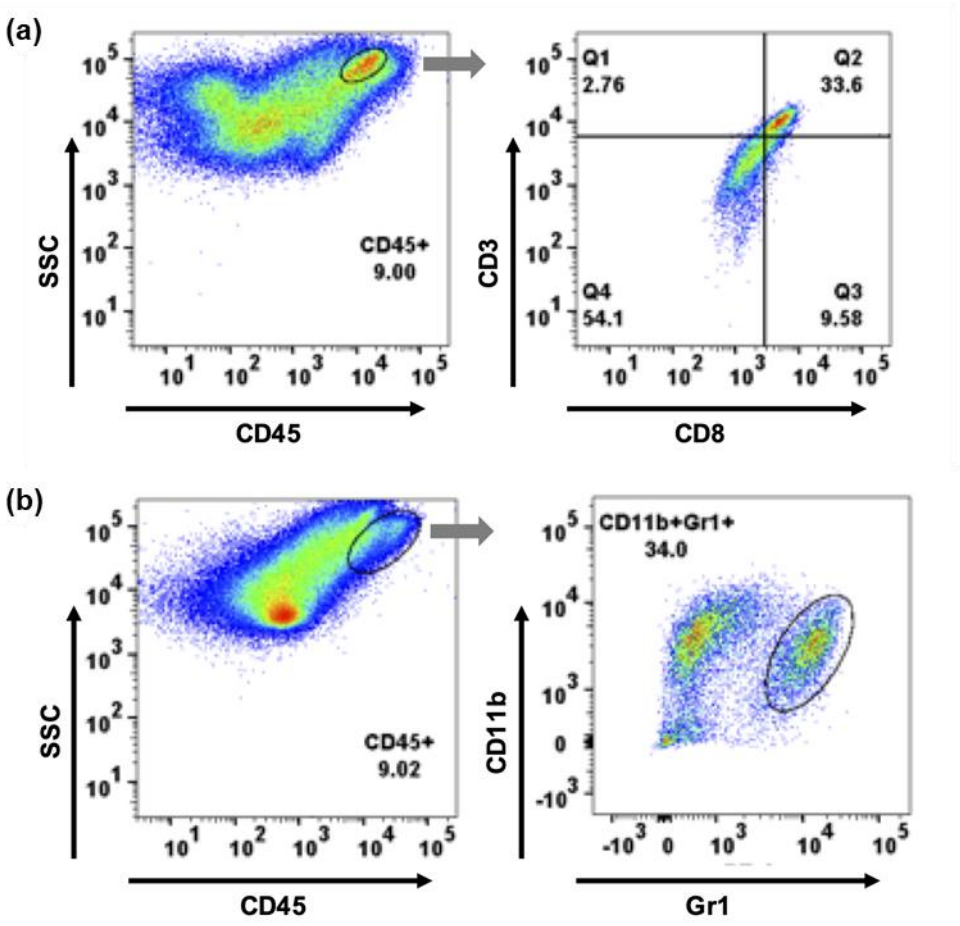

Figure 61. Tumor immune cell flow cytometry gating strategy. (a) Representative example of the CD8+ (cytotoxic) T cell population at the tumor site at day 11 post-inoculation. (b) Representative example of the MDSC population at the tumor site at day 11 post-inoculation.

4.5.2. Impact of Liposomal Spherical Nucleic Acid Structure on Immunotherapeutic Function

4.5.2.1. DNA Synthesis

All DNA sequences (**Table 12**) were synthesized with phosphorothioate (PS) backbones via automated solid-phase DNA synthesis using an MerMade 12 Synthesizer (Bioautomation). 4,5-dicyanoimidazole (DCI) was used as an activator and 3-[(Dimethylamino-methylidene)amino]-3H-1,2,4-dithiazole-3-thione was used as the sulfurizing agent. Completed DNA strands were cleaved from solid support via overnight incubation with 30% NH_4OH at ambient temperature. Excess ammonia was removed through evaporation under a stream of nitrogen. All

oligonucleotides were purified using HPLC (Agilent) on a C4 column with acetonitrile and triethylammonium acetate (TEAA), using a gradient of 10% to 100% acetonitrile over 30 min. Purified oligonucleotides were collected, lyophilized, and then reconstituted in 5 mL acetic acid. Following incubation at RT for 1 h, the oligonucleotides were extracted with ethyl acetate three times, and then lyophilized. Following resuspension in 1 mL deionized water, the oligonucleotides were analyzed by matrix-assisted laser desorption/ionization mass spectrometry (MALDI-MS) and native gel electrophoresis. To generate lipid-modified oligonucleotides (**Table 12**, entries 2 and 4), azide-modified 1,2-dipalmitoylphosphoethanolamine (DPPE) was incubated with the appropriate DBCO-containing DNA sequence overnight at RT and purified via gel electrophoresis.

Table 12. DNA Sequences

Entry	Sequence (5' to 3')
1	TTT TTT TTT TTT TTT TTT TT $(Spacer18)_2$ Cholesterol
2	TTT TTT TTT TTT TTT TTT TT $(Spacer18)_2$ DBCO-dT
3	TCC ATG ACG TTC CTG ACG TT $(Spacer18)_2$ Cholesterol
4	TCC ATG ACG TTC CTG ACG TT $(Spacer18)_2$ DBCO-dT

4.5.2.2. Synthesis of L-SNAs of Varying T_C

Thin films of DOPC, DMPC, DPPC, or DSPC were formed by adding the appropriate volume of lipid in a solution of chloroform into a glass vial and evaporating the solvent via nitrogen stream, followed by lyophilization overnight to remove any residual chloroform. Thin films were rehydrated with Dulbecco's phosphate buffered saline (DPBS) at $T > T_C$ for all lipids (RT for DOPC, 45ºC for DMPC and DPPC, and 60ºC for DSPC), and liposomes initially formed by several cycles of freeze-thaw/sonication in a 50ºC water bath until all suspensions became clear. These liposome solutions were then serially extruded using polycarbonate filters (T&T Scientific) with pore sizes of 200, 100, and 80 nm at $T > T_C$ for all liposomes. Liposomes were passed through each filter 20 times. Following the final extrusion, the liposomes were split into batches, the

phospholipid concentration was determined using the commercially available phosphatidylcholine assay kit, and the particle concentration was calculated using previously reported methods.[11] To generate L-SNAs, liposome stocks were split into several aliquots and 50, 100, 150, or 200 strands of cholesterol-modified DNA (**Table 12**, entries 1 and 3) or lipid-modified DNA (**Table 12**, entries 2 and 4) per particle was added to each aliquot and incubated overnight at $T > T_C$ for all lipids. The resulting constructs were subjected to native gel electrophoresis using 2% agarose at 160V for 45 min to analyze L-SNA formation and DNA loading capability by tracking DNA using either GelRed DNA stain or endogenous Cy5 signal. As a control, free oligonucleotides were run in their own lane to monitor for any unincorporated oligonucleotides into the L-SNA structures. Evidence of L-SNA formation was seen by the change in migration rate, relative to free oligonucleotide and confirmed by an increase in hydrodynamic diameter via dynamic light scattering (DLS) using a Wyatt DynaPro® plate reader system (**Table 13**).

Table 13. **Representative hydrodynamic diameter of liposomes and L-SNAs. (D = hydrodynamic diameter; PDI = polydispersity index)**

Lipid Core	Lipsomes		SNA (50 strands/particle)		SNA (100 strands/particle)	
	D (nm)	PDI	D (nm)	PDI	D (nm)	PDI
DOPC	89.9	0.19	110.0	0.12	127.5	0.24
DMPC	81.8	0.15	115.6	0.22	120.3	0.23
DPPC	83.6	0.06	129.1	0.027	127.7	0.01
DSPC	94.3	0.05	125.7	0.19	129.8	0.17

To prepare FRET-capable L-SNAs, lipid thin films were prepared as described above, but with the addition of 1% Rhodamine B-labelled phosphothenolamine lipid with an identical diacyl tail. Rhodamine-modified lipids (Rho-DOPE, Rho-DMPE, and Rho-DPPE) were purchased from commercial sources, while Rho-DSPE was synthesized in house (*vide infra*). The rhodamine-

incorporated thin films were formed into liposomes in the same manner as described above, followed by formation into SNAs by incubating Cy5-labelled DNA (**Table 12**, entries 1 and 2) with labelled liposomes at 100 strands per particle overnight at $T > T_C$.

4.5.2.3. Synthesis of Rhodamine-modified DSPE

To synthesize rhodamine-modified lipids with distearoyl-lipid tails for the generation of fluorescent DSPC liposomes (**Figure 62**), sulforhodamine B acid chloride (77 mg, 0.1335 nmol, 1.0 equivalent) was dissolved in 250 mL anhydrous dichloromethane (DCM) in a 500 mL round bottom flask (RBF) at RT. In a separate RBF, DSPE (100 mg, 0.1336 nmol, 1.0 equivalent) and triethylamine (27 mg, 0.267 nmol, 2.0 equivalents) were taken up in a solution of anhydrous DCM and stirred at RT for 10 min to form a homogenous mixture. To this, the sulforhodamine B solution was added dropwise. The reaction was stirred for 1 h at RT while maintaining a pH between 7.0 and 8.0, with the solution becoming clear over the course of the reaction, indicating that DSPE was reacting with the fluorophore and forming a soluble product. Solvent was then removed using a rotary evaporator. The crude product was dissolved in DCM, washed with 5% HCl (3x), washed with distilled water (3x), and dried over magnesium sulfate. Following filtration to remove desiccant, the product was purified using a CombiFlash® automated purification system (Teledyne ISCO), with a mobile phase of 2% methanol in DCM. The purified product was collected, solvent evaporated via rotary evaporation, and stored at -20ºC until use. Product identity was confirmed by NMR and MALDI-MS ([M+Na] identified, MW =1329.17).

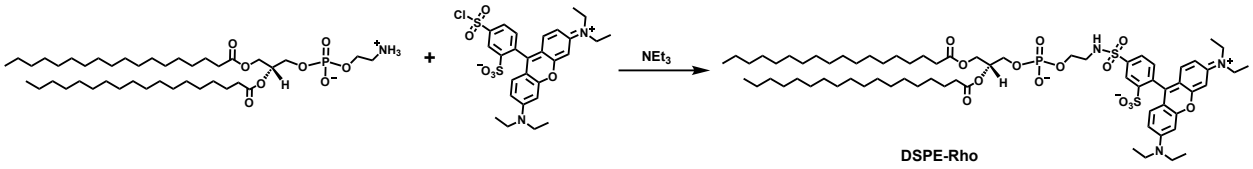

Figure 62. Synthesis of Rhodamine-modified DSPE.

4.5.2.4. Uptake of L-SNAs by HeLa Cells

In a typical experiment, HeLa cells (ATCC) were cultured in a 96-well plate in DMEM (Gibco) supplemented with 10% FBS (Atlanta Biologicals) and 1% penicillin-streptomycin (Gibco). Once 80% confluent, cells were treated with L-SNA variants (20 µL, 2.4 µM DNA) for 2 h in serum-containing media in triplicate. Post-treatment, cells were washed with 1X PBS, trypsinized (Gibco), and fixed in 4% paraformaldehyde (Thermo Fisher Scientific) and subsequently analyzed by flow cytometry using a BD LSRFortessa measuring the fluorescence (excitation 640 nm, emission 655-685 nm) of at least 10,000 single-cell events per sample. Raw FCS files were gated based on forward and side scatter intensities and analyzed on FlowJo.

4.5.2.5. Uptake of L-SNAs by DCs

DCs were isolated from femoral bone marrow of C57BL/6 mice and cultured in RPMI-1640 supplemented with 10% heat-inactivated FBS, 1% penicillin-streptomycin, and 20 ng/mL of mouse granulocyte-macrophage colony-stimulating factor (GM-CSF). Media was replenished on day three and cells were harvested on day six. DCs were added to 24-well plates at 300,000 cells per well, and immediately treated with FRET-capable L-SNAs at 0.1 µM for 30 min. Cells were washed, fixed with 4% paraformaldehyde for 10 min at room temperature, and resuspended in DPBS for flow cytometry (BD LSRFortessa).

4.5.2.6. *In Vitro* Serum stability of L-SNAs

FRET-capable L-SNAs (50 µL each at same particle concentration) at either 50 or 100 strands of DNA per particle were added to a 96-well plate in triplicate. 50 µL DPBS was added to each well, followed by 10 µL FBS. The well-plate was incubated at 37ºC and fluorescence measured every 3 min for a total of 180 min with the Cytation™ 5 fluorescence reader (BioTek Instruments), using an excitation wavelength of 565 nm and emission wavelength of 690 nm. The rate of FRET signal disappearance was evaluated as a function of starting fluorescence, plotted

in GraphPad Prism, and the initial rate of decay was calculated for each plot using the built-in analysis function.

4.5.2.7. *In Vivo* Blood Clearance of L-SNAs

FRET-capable L-SNAs comprised of either DOPC or DSPC were prepared at a concentration of 5 nmol DNA per 200 uL solution in DPBS. Balb/C mice were anesthetized with isoflurane and administered L-SNAs via intravenous injection through the tail vein. At 4, 20, 40, and 90 min post-injection, blood was collected from the retroorbital sinus and serum isolated by spin centrifugation at 1000×g for 10 min and stored on ice for transportation. Serum samples were immediately analyzed for FRET signal using the Cytation™ 5 fluorescence reader, using an excitation wavelength of 565 nm and emission wavelength of 690 nm. The serum half-life was evaluated by plotting the change in fluorescence (I_t / I_0) as a function in time using Microsoft Excel, fitting the data to a one phase decay (R^2 = 0.9952 for DSPC and 0.9808 for DOPC), and using the generated equation to calculate the time at which 50% of the initial fluorescence intensity remained.

4.5.2.8. Activation of DCs by L-SNAs

DCs were isolated and cultured as described above. On day 6, DCs were harvested and incubated (300,000 DCs/sample) with L-SNAs. After 24 h, cells were washed with DPBS (3x) and stained with antibodies against CD11b, CD11c, and CD86, as well as with a live/dead stain, by incubation with the appropriate antibodies for 20 min at RT. Cells were washed with DPBS (3x) and fixed with paraformaldehyde prior to analysis using flow cytometry. Immune cells were identified by gating for $CD11b^+/CD11c^+$ double-positive cells, followed by gating for $CD86^+$ cells.

***Table 14*. Calculated Increase in CD86 Expression for L-SNAs**

DNA Anchor	Lipid Core	CD86		
		Average MFI	St. Dev.	Fold-Increase over DOPC-SNA
cholesterol	DOPC	1304	212	n/a
cholesterol	DMPC	4288	791	3.3
cholesterol	DPPC	12411	2003	9.5
cholesterol	DSPC	9862	393	7.6

CHAPTER 5. SPHERICAL NUCLEIC ACIDS AS A PLATFORM FOR INFECTIOUS DISEASE VACCINES

Material in this chapter is based upon on-going work:

Teplensky, M.H.; Kusmierz, C.D.; Distler, M.E.; Mirkin C.A. “Spherical Nucleic Acids as a Platform for Infectious Disease Vaccines.” *In preparation*.

5.1. Introduction

In late 2019 a novel coronavirus (COVID-19, SARS-CoV-2) emerged.[221, 222] The resulting pandemic had disastrous health, social, and economic ramifications, of which the impacts have yet to be fully realized. The integration of social distancing and heightened hygiene efforts minimized the virus's effects; yet, the rapid development of vaccines turned the tide for this pandemic. Through a partnership between public and private sectors, vaccine development, testing, and distribution was vastly accelerated, resulting in Pfizer/BioNTech and Moderna being given an emergency use authorization by the FDA in December 2020.[223, 224] These COVID19 vaccines—lipid nanoparticle-encapsulated mRNA that encodes the spike protein—are prime examples of nanotechnology's value for preventing infectious diseases and gives credence for its future development.[225] One particular extension is the subunit vaccine, formulations that co-deliver recombinant viral proteins to serve as an antigen source combined with adjuvants to mount an immune response.[226] Like mRNA vaccines, subunit vaccines are safer than live-attenuated vaccines; additionally, they are more stable and less reliant on cold chain distribution, making them practical for distribution in third-world and developing settings.[227, 228] The COVID-19 pandemic cemented the need for various vaccine platforms that can be easily applied to evolving variants and different infectious diseases.

Vaccines elicit protective immunity and memory to a pathogen by activating T and B cells accompanied by the formation of memory cells (**Figure 63**). Subunit vaccines consist of specific, purified macromolecules derived from pathogens.[229] For example, the first antigen vaccine used clinically was for hepatitis B, developed by recombinantly expressing the surface antigen of the virus in yeast cells.[230] Inoculation with the pathogenic proteins induces protective immunity, and as a result, viral infection has decreased 95% after the institution of vaccination programs.[231] However, with other infectious diseases, the antigen alone is not immunogenic enough to raise a protective immune response against these proteins. Instead, adjuvants such as alum, CpG, LPS,

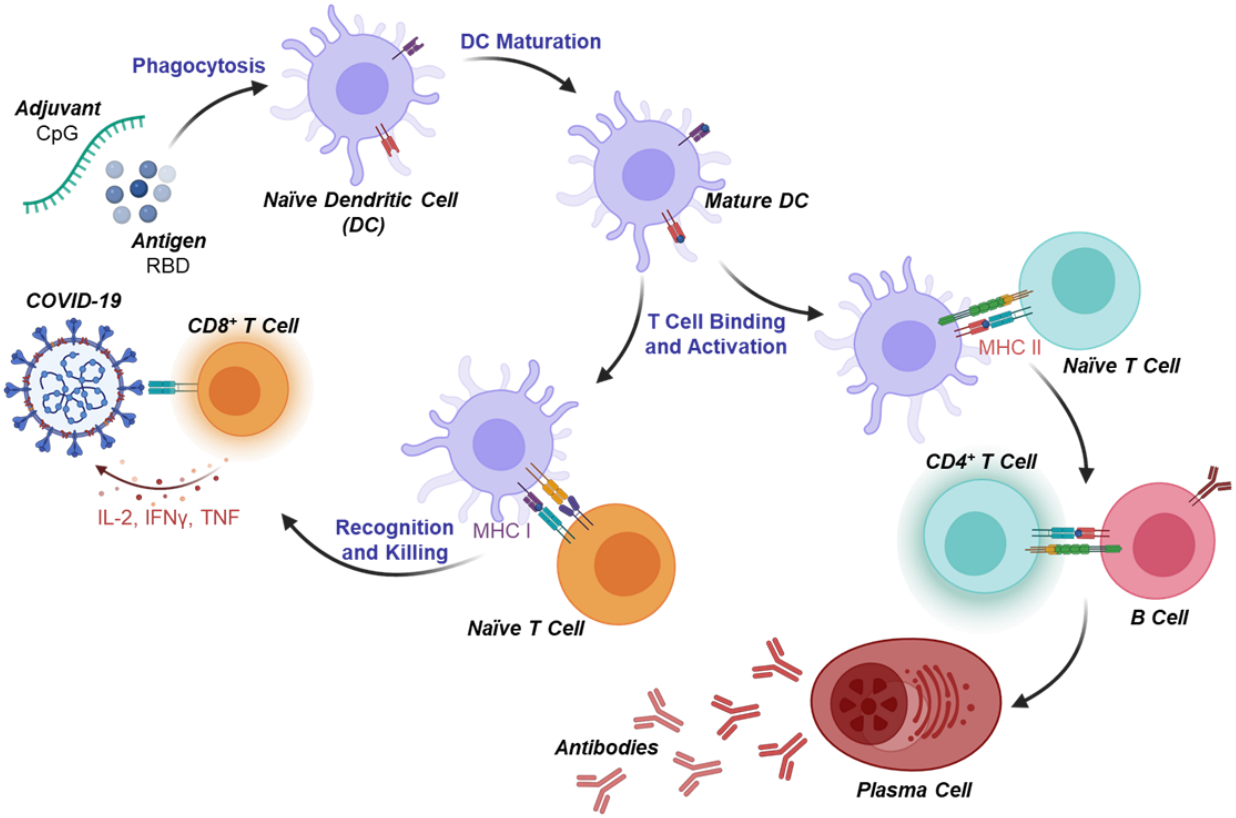

Figure 63. Immune Response to Subunit Vaccines. Dendritic cells endocytose the subunit vaccine and process the antigen, presenting the protein on MHC-I or MHC-II, which allow recognition by T-cells. If a $CD8^+$ T cell binds MHC-I, it will undergo clonal expansion and directly target the pathogen, secreting inflammatory mediators. If a $CD4^+$ T cell binds MHC-II, it can activate B cells which in turn differentiate into plasma cells. These cells secrete antibodies which specifically target the pathogen, preventing infection.

or Freund's complete are included to activate dendritic cells and macrophages via Toll-like receptors, which mobilize the adaptive immune response.[232]

The spike (S) protein is a glycoprotein that decorates the surface of SARS-CoV-2 and is in charge of the host cell recognition and cell membrane fusion.[78] A portion of the S protein—on the S1 subunit—contains the receptor-binding domain (RBD), which recognizes and binds to the cell's angiotensin-converting enzyme 2 (ACE-2) receptor.[78, 233] The S protein is essential for viral infectivity. Moreover, immunity to this protein correlates with COVID-19 protection; thus, both the RBD and S proteins are attractive antigen sources.[234-236] When considering scalability and cost,

the RBD is a particularly appealing target because it exhibits higher expression levels (on an mg protein/L scale) than the spike trimer in mammalian host systems.[237]

A combination of efficient lymph node draining, enhanced stability, and high codelivery of adjuvant and antigen to antigen-presenting cells (APCs) are all elements to maximize humoral responses. The Mirkin Group has demonstrated the utility of rational vaccinology in designing effective cancer vaccines (see **Chapter 4**) and demonstrated that the immune response is dependent on the SNA's privileged architecture.[12, 16, 178, 238, 239] Therefore, we sought to push the boundaries of the SNA, beyond oncology, into a new platform for infectious disease vaccines. As a first step, SNAs were designed to incorporate RBD proteins in a liposomal core and decorated with CpG immunostimulatory sequences (**Figure 64**). These vaccines activate B-cells in human peripheral blood mononuclear cells (hPBMCs) *in vitro*. Furthermore, in a mouse model, inoculation with SNA vaccines generated specific and robust neutralizing antibodies on par with current commercial alternatives. These results suggest that SNA structure matters and can be

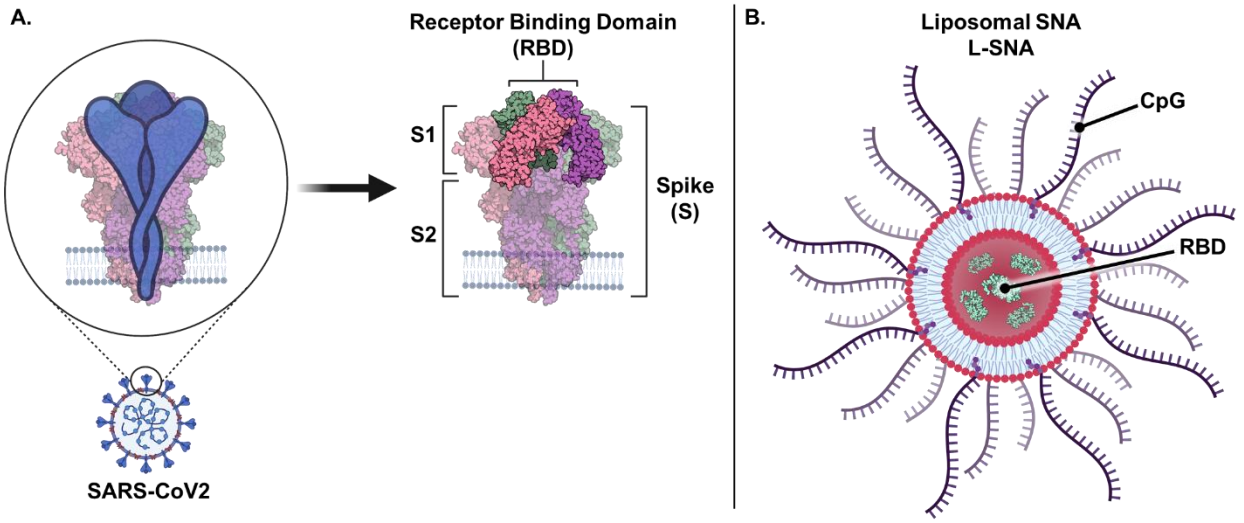

Figure 64. Encapsulating RBD into SNA Architecture will Improve Immunogenic Responses. A) The spike (S) protein is an attractive antigen sources of SARS-CoV2. In the S1 subunit, the receptor binding domain (RBD) recognizes and binds to a host's ACE2 receptor. B) Liposomal-SNAs (L-SNAs) are composed a liposomal core which encapsulates RBD proteins and have a DNA shell of CpG which serves as a immunostimulatory adjuvant. The representation was adapted from PDB ID 6VXX and made using BioRender.com.

leveraged to co-deliver viral proteins and CpG DNA at fixed stoichiometries to trigger a humoral immune response for infectious diseases.

5.2. SNA Design and Characterization

To generate COVID-19 SNA vaccines, we utilized the modular nature of the liposomal SNA (L-SNA) to simultaneously deliver both protein antigens (encapsulated within the liposome) and CpG adjuvants (adsorbed on the liposome's surface). In this way, the ratio of adjuvant to antigen could be varied to assess the optimal ratio of the vaccine's constituents as it relates to downstream immune function. L-SNAs were synthesized using protocols previously established by our group. Protein antigens were first encapsulated in 80-nm liposomes prepared from 1,2-dioleoyl-*sn*-glycero-3-phosphocholine (DOPC) and subsequently incubated with 3'-cholesteryl-modified CpG sequences to generate L-SNAs. Successful DNA incorporation was confirmed by both dynamic light scattering (DLS) or agarose gel electrophoresis, which shows shifts commensurate with the increased size upon DNA addition (**Figure 65**). The average protein loading per liposome is 5.6 ± 1.9 RBD (n = 5) and CpG DNA loadings were varied from either 75 to 200 DNA strands per liposome.

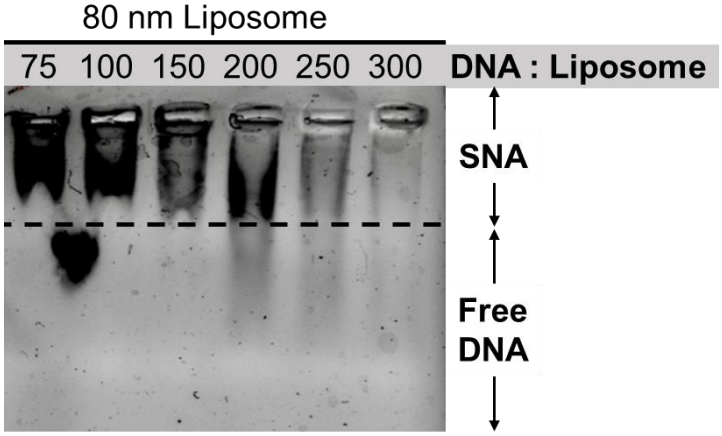

Figure 65. DNA Loading Capacity onto 80 nm Liposomes. DNA intercalation into DOPC liposomes was assessed using agarose gel electrophoresis. A maximum loading of 200 for 80 nm liposomes is evidenced by lower mobility into the gel and lack of free DNA signal.

5.3. B-Cell Activation in hPBMCs

The principle of vaccination for disease prevention depends entirely on the immunological memory carried by memory B cells and memory T cells. SNAs have repeatedly been shown to activate dendritic cells (DCs)—through the expression of CD86—which in turn prime cytotoxic ($CD8^+$) T cells for cancer immunotherapy.[16] However, there has yet to be a demonstration of whether SNAs can activate B cells. To test this, we treated human-derived peripheral blood mononuclear cells (hPBMCs) with L-SNAs composed of an RBD-encapsulated liposomal core and CpG7909 adjuvant (human TLR-9 agonist) DNA shell. After one day of incubation, cells were stained with a memory B cell marker (CD27) to assess whether SNAs can activate B cells. CD27 is a key marker for memory B cells, and its signaling promotes further differentiation into plasma

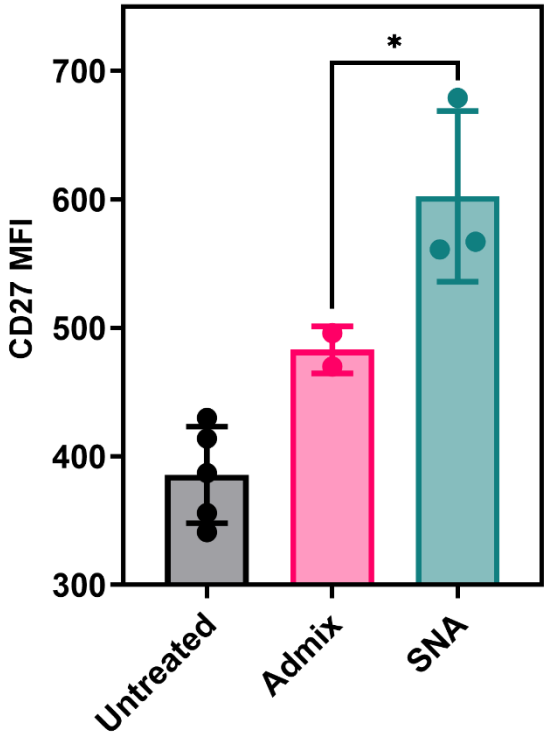

Figure 66. L-SNA Vaccine Activates B-cells in hPBMCs. hPBMCs were treated for 24 h with RBD encapsulated SNAs or a simple mixture of RBD and CpG at 25 nM by protein and 5 μM by DNA. CD27 expression—a memory B-cell marker—is significantly increased for the SNA group which demonstrates an SNA's ability to induce B-cell activation. Each dot is a single replicate, the bars represent the mean, and the error bars show standard deviation. Groups were compared by ANOVA where * is $p < 0.1$.

cells.[240] We quantified a significant difference in CD27 expression for SNAs when compared to simple mixtures of RBD and CpG, likely due to an SNA's superior biological properties such as higher cellular uptake, stability, and greater codelivery of both components (**Figure *66***). This more prominent B-cell activation demonstrates that SNAs can affect the adaptive immune system and bodes well for downstream *in vivo* analyses.

5.4. Response to SNA Vaccination in Mouse Models

5.4.1. Antibody Production

To evaluate whether COVID-19 SNA vaccines can elevate the humoral response to an encapsulated antigen, we quantified RBD-IgG specific antibody production and neutralization following a subcutaneous injection in C57BL/6 mice (n = 3 - 6). An indirect ELISA assay on mouse sera collected two weeks post-injection demonstrate a 3000-fold enhancement in the production of antigen-specific antibodies in SNA-treated mice when compared to the control (**Figure 67C**). Furthermore, after performing a neutralizing assay, the SNA-treated mice exhibited a pronounced 17-fold increase in neutralizing titers after one dose and 558-fold difference after two doses (**Figure 67D**). The neutralizing assay validated that antibodies produced can recognize the RBD domain and block its binding to the ACE-2 receptor. These trends compound following a second injection two weeks later. This showcases the importance of structuring components into an SNA architecture. RBD proteins and CpG DNA alone exhibit poor biodistribution to draining lymph nodes and rapid clearance.[241] By contrast, these results uphold that SNAs distribute to lymph nodes and exhibit high uptake and codelivery of cargo to immune cells *in vivo*. Moreover, high neutralizing antibody levels correlate with protection against infection; therefore, these results establish that SNA vaccines could be a viable vaccination strategy for COVID-19.[242] When compared to end-point titers in mice inoculated with the Moderna vaccine, the SNA matches in antibody production and increases in neutralizing antibodies titers (reciprocal [IC50] titer for

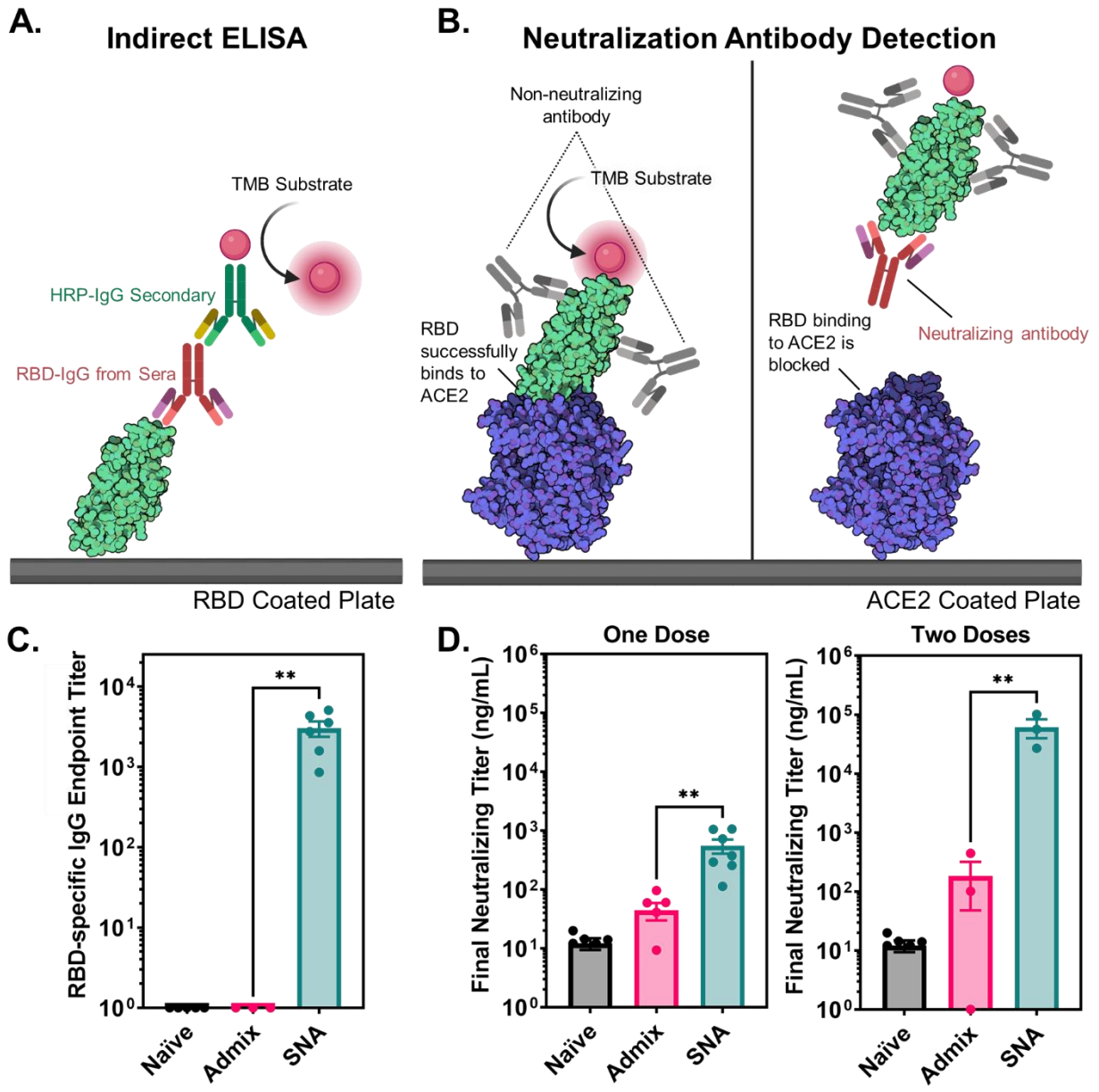

Figure 67. Robust Production of Antigen Specific Antibodies Following L-SNA Inoculation. A) Schematic of an indirect ELISA assay which is used to quantify RBD IgG titers in mouse serum. In this assay, a plate coated with RBD is first incubated with mouse serum. Antibodies in sera specific to RBD specifically bind to the target antigen. Incubation with HRP-conjugated IgG secondary antibody followed by a HRP colorimetric enzyme reaction indicates the quantity of RBD-specific antibodies present in each blood sample. B) In a neutralization assay, RBD-HRP solution is first incubated with serum samples, and antibodies specific to RBD are able to bind. In a subsequent incubation of mixtures to an ACE2 coated plate, when neutralizing antibodies are present, the RBD-HRP binding to ACE2 is blocked. The lack of HRP-RBD binding to wells is correlated to low absorbance signal following an HRP colorimetric enzymatic reaction. C) Following an indirect ELISA assay, serum from SNA-treated mice has significantly higher levels of RBD-specific antibodies when compared to a simple mixture of RBD and CpG. D) Likewise, antibodies produced in SNA-treated mice inhibit RBD binding to ACE2, indicating that antibodies are capable of inhibiting viral entry via a host cell's ACE2 receptor. Each dot is a single replicate, the bars represent the mean, and the error bars show SEM . Groups were compared by ANOVA where ** is $p<0.001$.

of mRNA delivered with the Moderna vaccine, these approximations validate that the SNA produces an immune response comparable to vaccines currently on the market.

5.4.2. Comparison to Commercial Adjuvants

As previously discussed, to increase the immunogenicity of the RBD protein, we incorporated CpG1826 DNA as an adjuvant source. In addition to its immunostimulatory activity, when adjuvant DNA is presented in a densely packed, multivalent, and radially orientated fashion around the liposome core, this SNA architecture enables the ability to enter cells without the need for auxiliary transfection agents. To assess the influence adjuvant identity has on vaccine

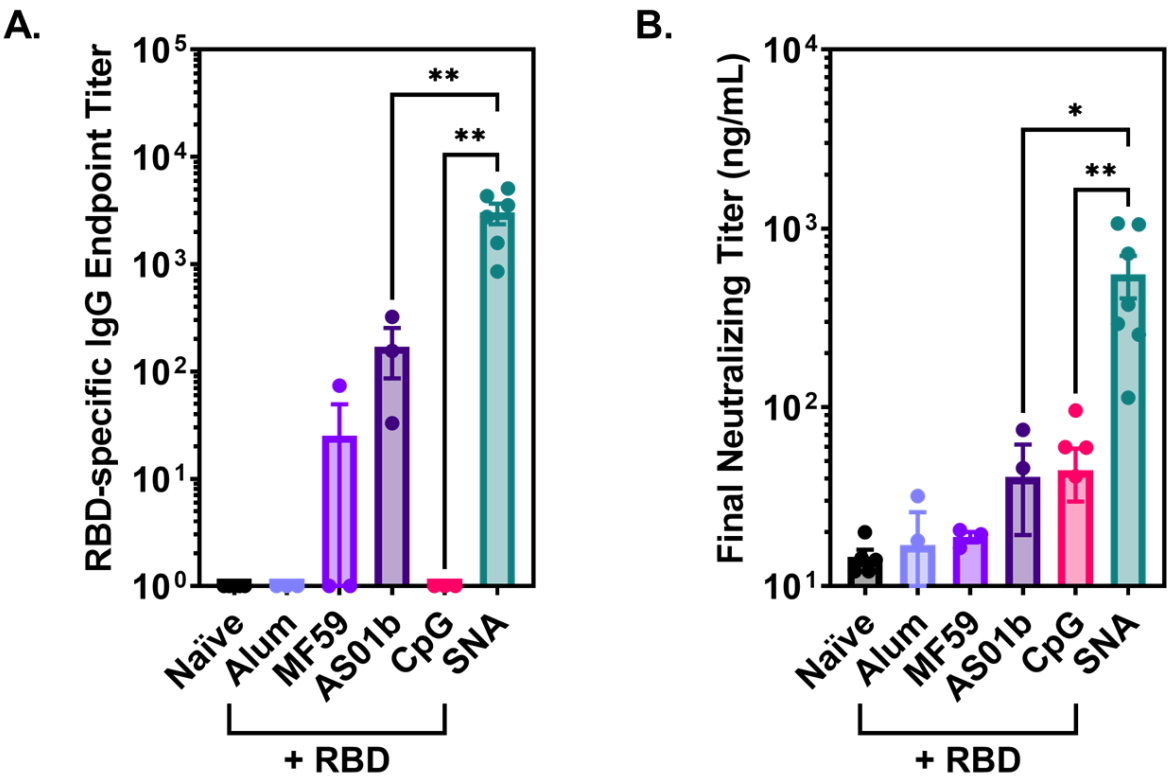

Figure 68. Antibody production following inoculation of RBD with other clinically-relevant adjuvants. The importance of the SNA architecture and anchoring CpG adjuvants to a liposome core emerges when comparing SNA-treated mice to mice inoculated with RBD mixed with commercial adjuvant alternatives. The antibodies produced by SNAs–which have a dense, radial orientation of CpG into a multivalent DNA shell—is significantly more than a linear mixture of CpG and RBD, demonstrating that structure matters when formulating vaccines. Mice were injected subcutaneously with either SNA or a mixture of components at a concentration of 1.4 nmol by RBD. Each bar represents the mean of n = 5-6 replicates and the error bars is the SEM. Groups were compared by ANOVA where * is $p < 0.1$ and ** is $p < 0.001$.

performance, we compared the SNA platform against other alternatives. We evaluated vaccine performance in mice treated with mixtures of RBD and commercial adjuvants such as Alum, MF59, and AS01b and compared their antibody production to mice vaccinated with the SNA. By both ELISA and neutralizing assays, SNAs outperform other adjuvants in the production of RBD-specific antibodies, doubling titers of the best performing commercial adjuvant AS01b (**Figure 68**). Worthy of mention, when CpG is not formulated as an SNA—instead injected as a mixture with RBD—the oligonucleotide adjuvant fails to compete. This tells us that by restructuring this adjuvant as an SNA, we can significantly increase its efficacy, affirming the power of the SNA's structure.

5.4.3. Adjuvant-Antigen Stoichiometries Impact Immune Response

To evaluate the effect DNA loading has on vaccine efficacy, we varied both the liposome's size and the DNA surface coverage. L-SNAs were synthesized with adjuvant loading ranging from 75 to 200 per liposome, while RBD encapsulation remained similar. We hypothesize this will have a two-prong effect: 1) higher cellular uptake correlates with more DNA loading[1], 2) increased adjuvant delivery will result in a better immune response. To test this, mice were inoculated with vaccine variants, and two weeks post-injection, end-point IgG-RBD antibody and neutralizing titers in mouse sera were quantified and plotted against adjuvant loading (**Figure 69**). The positive correlation between adjuvant loading and immune response (R^2 = 0.99) is likely due to the increased adjuvant and antigen delivery with larger liposomes and increased DNA surface coverage. In future vaccine designs, we can include more hydrophobic DNA intercalation linkers and more stable liposome formulations to increase CpG loading, which was previously shown to be efficacious for cancer vaccines.[11, 239]

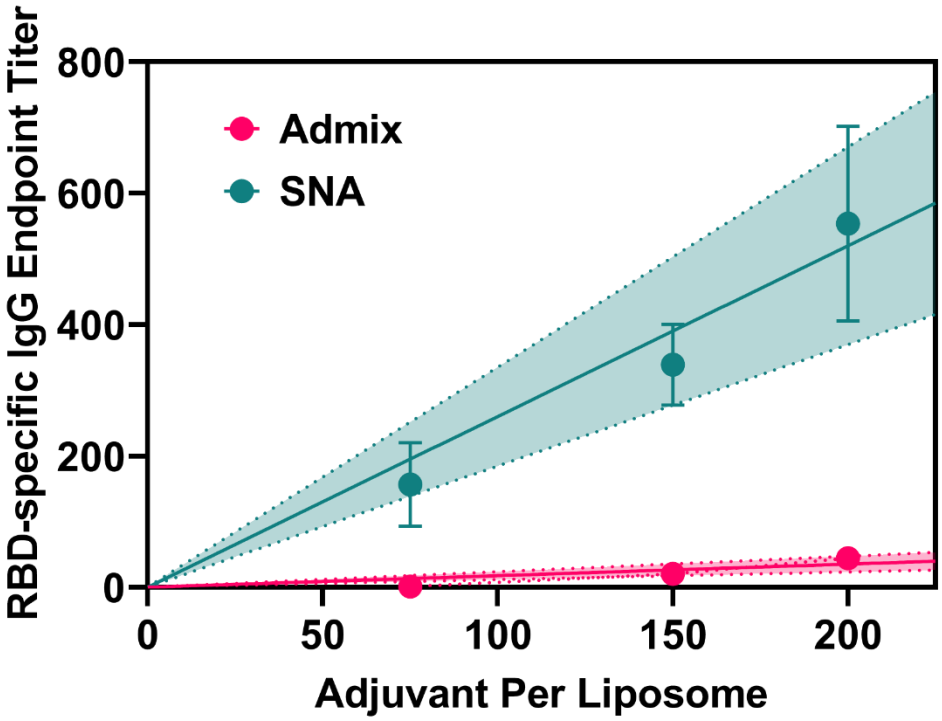

Figure 69. Adjuvant Loading Correlates with Immune Response. The quantity of neutralizing, RBD-specific antibodies produced in SNA-treated mice correlates with the SNA's CpG DNA loading. This may be a combination of higher dendritic cell uptake due to higher valency of DNA and more immunostimulation as a result of increased adjuvant delivery. Mice were injected subcutaneously with either SNA or a mixture of linear components at a concentration of 1.4 nmol by RBD. Each point represents the mean of n = 5-6 replicates and the error bars is the standard deviation. The line is a trendline which was fit using GraphPad Prism and for the SNA group the R^2 is 0.99.

5.4.4. Identification of Ig Classes Using Proteomics

In addition to RBD antibody titers, we identified different antibody classes and subclasses present in SNA-treated mouse sera to get a holistic representation of immunoglobulins present. Eighteen different immunoglobulins were identified using proteomics among different SNA formulations (75, 150, or 200 adjuvant strands/liposome), with an additional five distinct Ig proteins present in 200 DNA per liposome L-SNA treatment group. Furthermore, the quantity of these proteins increases as the DNA loading increases (**Figure 70**). The IgM antibody was among the proteins present in all SNA vaccine groups and is the first immunoglobulin class produced in the primary response to antigens. It is involved in the early stages of the immune response and

serves to recognize and eliminate pathogens. Other proteins secreted include the IgG subclass IgG2b and Igκ, which are produced by mature B-cells and participate in antigen recognition. At the time of writing, we continue to identify proteins present in mouse sera several weeks after inoculation. We expect Ig profiles to change and anticipate quantifying their expression over a long duration.

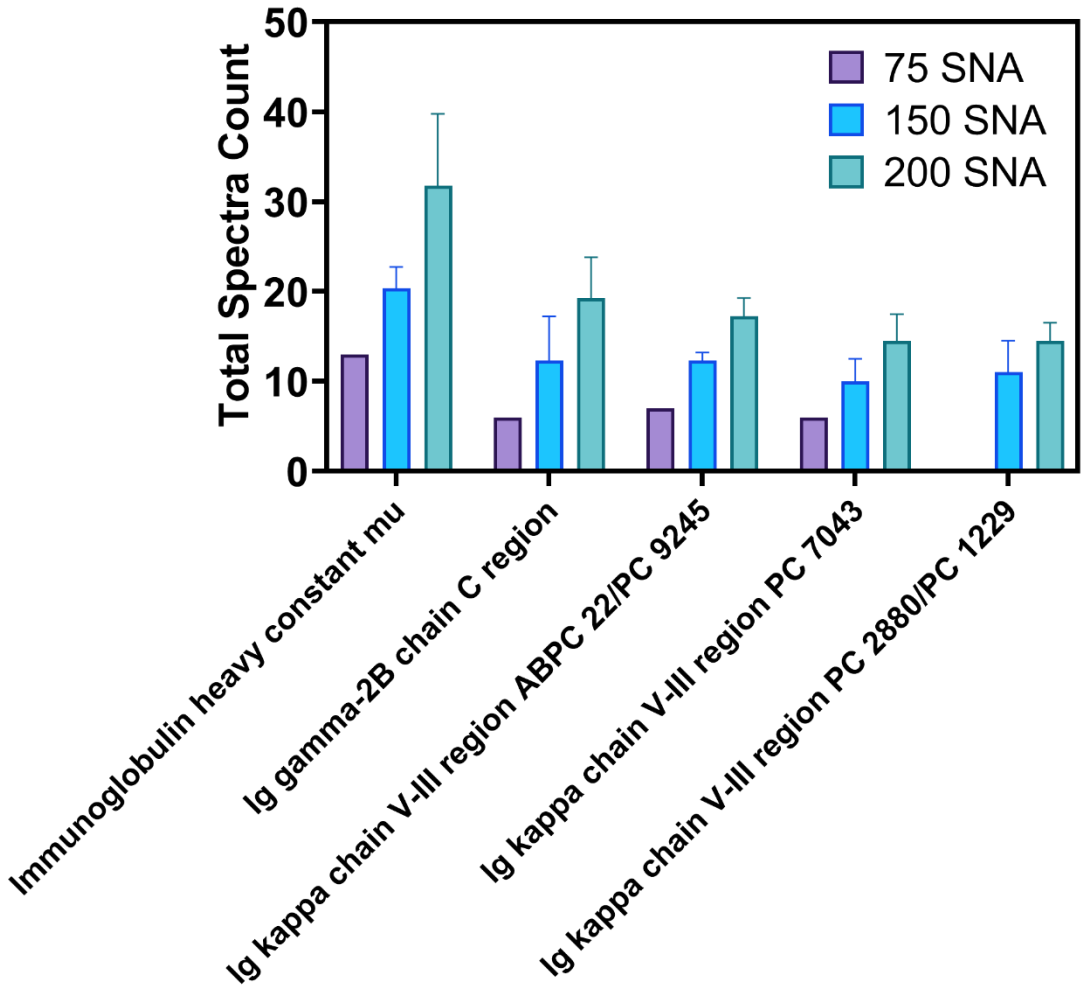

Figure 70. SNA Vaccines Formulated with Different Adjuvant DNA Loadings Result in Differential Protein Expression. Upregulated immunoglobulin proteins present in sera samples from mice two weeks post first SNA vaccine inoculation. When SNAs have higher CpG DNA loadings, there is an upregulation in proteins present in sera correlating with a larger immune response. Each bar represents the mean of n = 1-3 replicates and the error bars is the SEM.

5.5. Conclusions and Outlook

This work is the first representation of utilizing SNAs as a vaccine candidate for an infectious disease. After incorporating COVID-19 specific antigenic proteins into liposomes decorated with a shell of CpG-1826 DNA, these SNA structures demonstrate high antigen-specific, neutralizing antibody production in an animal model. Importantly, this is only antigen source and adjuvant sequence, and when one considers the modularity and programmability of the SNA architecture, the rapid translation to variant antigens and human adjuvant sequences (CpG7909) is possible. All in all, these initial results have broad implications in the development of nano vaccines for COVID-19 and beyond.

5.6. Methods and Materials

5.6.1. Synthesis and Characterization of Liposomal Spherical Nucleic Acids COVID-19 Vaccines

5.6.1.1. Receptor Binding Domain (RBD) Protein Expression

Proteins were expressed using standard protocols in Expi293 system (Thermo Fisher Scientific). A vector for the receptor-binding domain (RBD) from SARS-CoV-2 (a.a. 319-541) was obtained from BEI Resources (NR-52309). The sequence was designed by fusing the RBD sequence with a C-terminal hexahistidine tag and is intended for pCAGGS mammalian expression under the AG promoter. Successful expression was confirmed by SDS-PAGE gel (**Figure 71**).

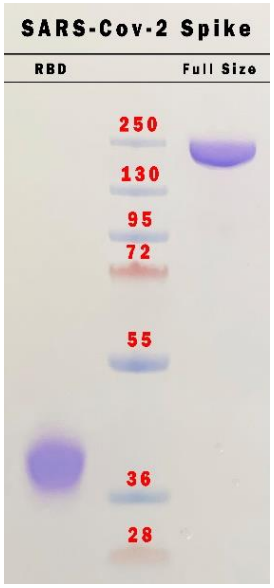

Figure 71. SDS PAGE gel of RBD and full-size Spike protein from which it derives.

5.6.1.2. Oligonucleotide Synthesis

Oligonucleotides (**Table 15**) were generated using an ABI-392 automated DNA synthesizer. 3'-cholesteryl-TEG CPG solid supports and phosphoramidites were obtained from Glen Research. Sequences were synthesized with a phosphorothioate backbone per manufacturer's specifications using 4,5-dicyanoimidazole as an activator and 3-((Dimethylamino-methylidene)amino)-3H-1,2,4-dithiazole-3-thione as the sulfurizing agent. Following synthesis, sequences were cleaved from the solid support using ammonium hydroxide (30%, Sigma-Aldrich) at room temperature for 24 hours and purified by reverse-phase HPLC (Shimadzu) on a C18 column, using a gradient of Buffer A (0.1M triethylammonium acetate [Sigma-Aldrich] and 3% acetonitrile [Sigma-Aldirch] in water) to pure acetonitrile over 45 minutes. Purified oligonucleotides were deprotected in 20% acetic acid (Sigma-Aldrich) for 1 hour and extracted following three washed with ethyl acetate (Sigma-Aldrich). To ensure proper DNA synthesis, the molecular weight of the sequences was measured by matrix-assisted laser desorption time of flight (MALDI-TOF) with a Bruker AutoFlex-III and compared to calculated molecular weight estimates via the IDT OligoAnalyzer Tool.

Table 15. **DNA Adjuvant Sequences**

Name	Sequence (5' to 3')
CPG1826	TCC ATG ACG TTC CTG ACG TT $(Spacer18)_2$ Cholesterol
CPG7909	TCG TCG TTT TGT CGT TTT GTC GTT $(Spacer18)_2$ Cholesterol

5.6.1.3. Synthesis of RBD-Loaded Liposomal SNAs (L-SNAs)

50mg of DOPC (Avanti Polar Lipids) was reconstituted in chloroform (Sigma-Aldrich) and evaporated to a thin film using a MULTIVAP nitrogen evaporator. 2.5 mL of an RBD-solution (7 mg/mL) in Dulbecco's phosphate buffer saline (DPBS, Gibco) was used to rehydrate the film. Liposomes were formed following 20 freeze-thaw cycles (liquid nitrogen and sonication in a 37˚C

water bath), followed by extrusion to 80 nm. Unencapsulated RBD was removed by performing three rounds of tangential flow filtration (TFF) using a filter with a pore size of 500 kDa (Spectrum). The amount of RBD encapsulated was measured using a BCA assay (Thermo-Fisher) after bursting liposomes with 1% SDS. The liposome concentration was measured using a phosphatidylcholine (PC) assay (Sigma-Aldrich). To form SNAs, 3' cholesterol-terminated CPG1826 or CPG7909 DNA strands were added to the liposomes in a 75:1, 150:1, or 200:1 oligonucleotide to liposome ratio—depending on the experiment—and incubated at 37˚C overnight. L-SNAs were stored 4˚C.

5.6.1.4. Characterization of RBD-Loaded Liposomal SNAs (L-SNAs)

Successful SNA formation was characterized by dynamic light scattering (DLS, Malvern Zetasizer) as previously described[9] and visualized by agarose gel electrophoresis. Free linear DNA and SNAs were loaded into a 1% agarose gel on ice and run at 100V for 45 min (**Figure 65**).

5.6.2. *In Vitro* Human Peripheral Blood Mononuclear Cell (hPBMC) B-Cell Activation

Human peripheral blood mononuclear cells (hPBMCs) were purchased from Zenbio and thawed at the start of the experiment. The cell suspension was added to 3 mL of RPMI media (Gibco) supplemented with 10% heat-inactivated fetal bovine serum (Atlanta Biologicals) and 1% Penicillin-Streptomycin (Gibco). Cells were concentrated by centrifugation (300 x g for 10 min), resuspended in media, counted, and diluted to 1 x 10^6 cells/mL. Next, cells were treated with L-SNAs and the appropriate controls at [RBD] = 25 nM and [CpG7909] = 5 μM. After 24-h, samples were stained with antibodies (Live marker, UV; CD19, BV421; HLA-DR, PerCP Cy 5.5; CD27, BV605; CD40, BB515) and fixed in 4% paraformaldehyde (Thermo Fisher Scientific). Cells were analyzed by flow cytometry using a BD FACSymphony flow cytometer, and cell events were gated and analyzed on FlowJo.

5.6.3. *In Vivo* Immune Activation in Mouse Model

Female C57BL/6J mice (strain code: 027) were procured from Charles River Laboratory at 8 weeks of age and maintained in conventional housing. All animal experiments were carried out in accordance with the approved IACUC protocol issued by Northwestern University.

5.6.3.1. Injection of L-SNAs and Blood Collection

Mice were injected subcutaneously with 1.4 nmol RBD (L-SNA and corresponding linear mixture). In two-week increments following injection, blood was collected via a retro-orbital blood draw. Animals were anesthetized with isoflurane, and once asleep, a heparin (Sigma-Aldrich) lined pipette is inserted through the conjunctiva and into the orbital sinus by quickly rotating the tube. Approximately 100 uL of blood is drawn and stored at room temperature for at least 30 min to allow the blood to clot. The blood is then centrifuged at 1000 x g for 10min, and the supernatant (serum) is carefully removed and transferred to a 96 well plate for downstream analysis. If not used immediately, serum was stored at -80˚C in 0.5 mL sterilized tubes.

5.6.3.2. ELISA for RBD-Specific IgG Antibodies

A Biolegend Nunc™ Maxi Sorp™ ELISA Uncoated Plate was coated with 2.5 μg/mL of RBD protein diluted in 1X Biolegend ELISA Coating Buffer for 2 h at 37°C. After coating, the plate was washed and subsequently blocked for 2 h at 37°C with 200 uL of DPBS-T, which consists of Dulbecco's phosphate buffer saline (DPBS, Gibco) supplemented with 10% fetal bovine serum (Atlanta Biologicals) and 0.1% Tween-20 (Sigma-Aldrich). In the meantime, mouse sera were diluted to various dilution concentrations (50x, 100x, 500x, 1000x, 2500x, and/or 5000x) in 5X ELISA dilution buffer (eBioscience). After the blocking step, the blocking solution was removed, and 100uL of each diluted sample was added to their respective well. The plate was incubated for 1 h at 37°C and subsequently washed three times with DPBS-T. Next, 100 μL of a secondary antibody (Goat anti-mouse IgG-HRP, Abcam), diluted 1:4000 in 5X ELISA dilution buffer, was added to each well and incubated at room temperature for 1 h. Following three wash cycles with DPBS-T, 100uL of a 1:1

mixture of TMB Reagent A and TMB Reagent B (BioLegend)—made immediately before addition—was added to each well. The plate was incubated at room temperature for 3 min. Next, 100µl of TMB Stop Solution (BioLegend) was added, and absorbance at 450nm was immediately read using a BioTek Cytation 5.

5.6.3.3. Neutralizing Antibody Binding Assay

Neutralization titers were determined using a GenScript SARS-CoV-2 Surrogate Virus Neutralization Test (sVNT) Kit. First, the following dilutions were made:

- Negative Matrix Control (NMC): Naïve serum was diluted 10-fold with sample dilution buffer.
- 1X Wash Solution: 20X stock wash solution was diluted 20-fold in sterile water.
- Standard Curve: Monoclonal antibody (MAB, A02051) was first diluted to a final working concentration of 3 µg/mL with sterile water. A standard curve was created by diluting the MAB in NMC at the following concentrations: [MAB] = 300, 150, 75, 37.5, 18.75, 9.38, 4.7 ng/mL.
- Samples: Serum samples were first diluted 10-fold in sample dilution buffer. A 1:3 serial dilution was then performed in sample dilution buffer resulting in the following dilution ratios: [Sample] = 1:10, 1:30, 1:90, 1:270, 1:810, 1:2430.
- Positive and Negative Controls: Samples were provided by the kit and diluted ten-fold in sample dilution buffer.
- HRP functionalized RBD (RBD-HRP) Working Solution: RBD-HRP was provided by the kit and diluted 1000-fold in HRP dilution buffer.

In a 96-well plate, 120 uL of the standard curve solutions and 60 uL of samples and positive/negative controls were added to their respective wells. Quickly, an equal volume of RBD-HRP solution (120 uL for standard curve solutions and 60 uL for samples and positive/negative controls) was added to all wells, and the plate was incubated at 37°C for 30 min. Next, 100uL of these mixtures were transferred

to the provided ELISA plate pre-coated with ACE2 receptors, and the plate was sealed and incubated at 37°C for 15 min. Wells were washed four times with 1X wash solution, then 100uL of TMB solution was added to each well and incubated at room temperature for 15 min, protected from light. Finally, 50uL of Stop Solution was added to all wells to quench the reaction, and the absorbance at 450nm was immediately read using a BioTek Cytation 5.

References

1. Giljohann, D. A.; Seferos, D. S.; Patel, P. C.; Millstone, J. E.; Rosi, N. L.; Mirkin, C. A., Oligonucleotide Loading Determines Cellular Uptake of DNA-Modified Gold Nanoparticles. *Nano Letters* **2007,** *7* (12), 3818-3821.

2. Hurst, S. J.; Lytton-Jean, A. K. R.; Mirkin, C. A., Maximizing DNA Loading on a Range of Gold Nanoparticle Sizes. *Analytical Chemistry* **2006,** *78* (24), 8313-8318.

3. Narayan, S. P.; Choi, C. H. J.; Hao, L.; Calabrese, C. M.; Auyeung, E.; Zhang, C.; Goor, O. J. G. M.; Mirkin, C. A., The Sequence-Specific Cellular Uptake of Spherical Nucleic Acid Nanoparticle Conjugates. **2015,** *11* (33), 4173-4182.

4. Mirkin, C. A.; Letsinger, R. L.; Mucic, R. C.; Storhoff, J. J., A DNA-based method for rationally assembling nanoparticles into macroscopic materials. *Nature* **1996,** *382* (6592), 607-609.

5. Patel, P. C.; Giljohann, D. A.; Daniel, W. L.; Zheng, D.; Prigodich, A. E.; Mirkin, C. A., Scavenger Receptors Mediate Cellular Uptake of Polyvalent Oligonucleotide-Functionalized Gold Nanoparticles. *Bioconjugate Chemistry* **2010,** *21* (12), 2250-2256.

6. Choi, C. H. J.; Hao, L.; Narayan, S. P.; Auyeung, E.; Mirkin, C. A., Mechanism for the endocytosis of spherical nucleic acid nanoparticle conjugates. *Proceedings of the National Academy of Sciences* **2013,** *110* (19), 7625-7630.

7. Cutler, J. I.; Zheng, D.; Xu, X.; Giljohann, D. A.; Mirkin, C. A., Polyvalent Oligonucleotide Iron Oxide Nanoparticle “Click” Conjugates. *Nano Letters* **2010,** *10* (4), 1477-1480.

8. Brodin, J. D.; Sprangers, A. J.; McMillan, J. R.; Mirkin, C. A., DNA-Mediated Cellular Delivery of Functional Enzymes. *Journal of the American Chemical Society* **2015,** *137* (47), 14838-14841.

9. Banga, R. J.; Chernyak, N.; Narayan, S. P.; Nguyen, S. T.; Mirkin, C. A., Liposomal Spherical Nucleic Acids. *Journal of the American Chemical Society* **2014,** *136* (28), 9866-9869.

10. Cutler, J. I.; Zhang, K.; Zheng, D.; Auyeung, E.; Prigodich, A. E.; Mirkin, C. A., Polyvalent Nucleic Acid Nanostructures. *Journal of the American Chemical Society* **2011,** *133* (24), 9254-9257.

11. Meckes, B.; Banga, R. J.; Nguyen, S. T.; Mirkin, C. A., Enhancing the Stability and Immunomodulatory Activity of Liposomal Spherical Nucleic Acids through Lipid-Tail DNA Modifications. *Small* **2017**, 1702909.

12. Radovic-Moreno, A. F.; Chernyak, N.; Mader, C. C.; Nallagatla, S.; Kang, R. S.; Hao, L.; Walker, D. A.; Halo, T. L.; Merkel, T. J.; Rische, C. H.; Anantatmula, S.; Burkhart, M.; Mirkin, C. A.; Gryaznov, S. M., Immunomodulatory spherical nucleic acids. *Proceedings of the National Academy of Sciences* **2015,** *112* (13), 3892-3897.

13. Ferrer, J. R.; Wertheim, J. A.; Mirkin, C. A., Dual Toll-Like Receptor Targeting Liposomal Spherical Nucleic Acids. *Bioconjugate Chemistry* **2019,** *30* (3), 944-951.

14. Wu, X. A.; Choi, C. H. J.; Zhang, C.; Hao, L.; Mirkin, C. A., Intracellular Fate of Spherical Nucleic Acid Nanoparticle Conjugates. **2014,** *136* (21), 7726-7733.

15. Huang, Z. N.; Cole, L. E.; Callmann, C. E.; Wang, S.; Mirkin, C. A., Sequence Multiplicity within Spherical Nucleic Acids. *ACS Nano* **2020,** *14* (1), 1084-1092.

16. Wang, S.; Qin, L.; Yamankurt, G.; Skakuj, K.; Huang, Z.; Chen, P.-C.; Dominguez, D.; Lee, A.; Zhang, B.; Mirkin, C. A., Rational vaccinology with spherical nucleic acids. *Proceedings of the National Academy of Sciences* **2019,** *116* (21), 10473-10481.

17. Callmann, C. E.; Cole, L. E.; Kusmierz, C. D.; Huang, Z.; Horiuchi, D.; Mirkin, C. A., Tumor cell lysate-loaded immunostimulatory spherical nucleic acids as therapeutics for triple-negative breast cancer. *Proceedings of the National Academy of Sciences* **2020,** *117* (30), 17543.

18. Demers, L. M.; Mirkin, C. A.; Mucic, R. C.; Reynolds, R. A.; Letsinger, R. L.; Elghanian, R.; Viswanadham, G., A Fluorescence-Based Method for Determining the Surface Coverage and Hybridization Efficiency of Thiol-Capped Oligonucleotides Bound to Gold Thin Films and Nanoparticles. *Analytical Chemistry* **2000,** *72* (22), 5535-5541.

19. Zhang, C.; Hao, L.; Calabrese, C. M.; Zhou, Y.; Choi, C. H. J.; Xing, H.; Mirkin, C. A., Biodegradable DNA-Brush Block Copolymer Spherical Nucleic Acids Enable Transfection Agent-Free Intracellular Gene Regulation. **2015,** *11* (40), 5360-5368.

20. Li, H.; Zhang, B.; Lu, X.; Tan, X.; Jia, F.; Xiao, Y.; Cheng, Z.; Li, Y.; Silva, D. O.; Schrekker, H. S.; Zhang, K.; Mirkin, C. A., Molecular spherical nucleic acids. *Proceedings of the National Academy of Sciences* **2018,** *115* (17), 4340-4344.

21. Doi, T.; Higashino, K.; Kurihara, Y.; Wada, Y.; Miyazaki, T.; Nakamura, H.; Uesugi, S.; Imanishi, T.; Kawabe, Y.; Itakura, H.; Yazaki, Y.; Matsumoto, A.; Kodama, T., Charged Collagen Structure Mediates the Recognition of Negatively Charged Macromolecules by Macrophage Scavenger Receptors. *The Journal of Biological Chemistry* **1993,** *268* (3), 2126-2133.

22. Suzuki, K.; Doi, T.; Imanishi, T.; Kodama, T.; Tanaka, T., Oligonucleotide aggregates bind to the macrophage scavenger receptor. **1999,** *260* (3), 855-860.

23. Chinen, A. B.; Guan, C. M.; Mirkin, C. A., Spherical Nucleic Acid Nanoparticle Conjugates Enhance G-Quadruplex Formation and Increase Serum Protein Interactions. *Angewandte Chemie International Edition* **2014**, n/a-n/a.

24. Chinen, A. B.; Guan, C. M.; Ko, C. H.; Mirkin, C. A., The Impact of Protein Corona Formation on the Macrophage Cellular Uptake and Biodistribution of Spherical Nucleic Acids. **2017**, 1603847.

25. Guan, C. M.; Chinen, A. B.; Ferrer, J. R.; Ko, C. H.; Mirkin, C. A., Impact of Sequence Specificity of Spherical Nucleic Acids on Macrophage Activation in Vitro and in Vivo. *Molecular Pharmaceutics* **2019,** *16* (10), 4223-4229.

26. Rosi, N. L.; Giljohann, D. A.; Thaxton, C. S.; Lytton-Jean, A. K. R.; Han, M. S.; Mirkin, C. A., Oligonucleotide-Modified Gold Nanoparticles for Intracellular Gene Regulation. *Science* **2006,** *312* (5776), 1027-1030.

27. Hao, L.; Patel, P. C.; Alhasan, A. H.; Giljohann, D. A.; Mirkin, C. A., Nucleic Acid-Gold Nanoparticle Conjugates as Mimics of microRNA. *Small* **2011,** *7* (22), 3158-3162.

28. Giljohann, D. A.; Seferos, D. S.; Prigodich, A. E.; Patel, P. C.; Mirkin, C. A., Gene Regulation with Polyvalent siRNA−Nanoparticle Conjugates. *Journal of the American Chemical Society* **2009,** *131* (6), 2072-2073.

29. Rouge, J. L.; Sita, T. L.; Hao, L.; Kouri, F. M.; Briley, W. E.; Stegh, A. H.; Mirkin, C. A., Ribozyme–Spherical Nucleic Acids. **2015**, 150814061116009.

30. Jensen, S. A.; Day, E. S.; Ko, C. H.; Hurley, L. A.; Luciano, J. P.; Kouri, F. M.; Merkel, T. J.; Luthi, A. J.; Patel, P. C.; Cutler, J. I.; Daniel, W. L.; Scott, A. W.; Rotz, M. W.; Meade, T. J.; Giljohann, D. A.; Mirkin, C. A.; Stegh, A. H., Spherical Nucleic Acid Nanoparticle Conjugates as an RNAi-Based Therapy for Glioblastoma. *Science Translational Medicine* **2013,** *5* (209), 209ra152-209ra1.

31. Zheng, D.; Giljohann, D. A.; Chen, D. L.; Massich, M. D.; Wang, X.-Q.; Iordanov, H.; Mirkin, C. A.; Paller, A. S., Topical delivery of siRNA-based spherical nucleic acid nanoparticle conjugates for gene regulation. *Proceedings of the National Academy of Sciences* **2012,** *109* (30), 11975-11980.

32. Kumthekar, P.; Ko, C. H.; Paunesku, T.; Dixit, K.; Sonabend, A. M.; Bloch, O.; Tate, M.; Schwartz, M.; Zuckerman, L.; Lezon, R.; Lukas, R. V.; Jovanovic, B.; McCortney, K.; Colman, H.; Chen, S.; Lai, B.; Antipova, O.; Deng, J.; Li, L.; Tommasini-Ghelfi, S.; Hurley, L. A.; Unruh, D.; Sharma, N. V.; Kandpal, M.; Kouri, F. M.; Davuluri, R. V.; Brat, D. J.; Muzzio, M.; Glass, M.; Vijayakumar, V.; Heidel, J.; Giles, F. J.; Adams, A. K.; James, C. D.; Woloschak, G. E.; Horbinski, C.; Stegh, A. H., A first-in-human phase 0 clinical study of RNA interference–

based spherical nucleic acids in patients with recurrent glioblastoma. *Science Translational Medicine* **2021,** *13* (584), eabb3945.

33. Seferos, D. S.; Prigodich, A. E.; Giljohann, D. A.; Patel, P. C.; Mirkin, C. A., Polyvalent DNA Nanoparticle Conjugates Stabilize Nucleic Acids. *Nano Letters* **2009,** *9* (1), 308-311.

34. Krishnamoorthy, K.; Hoffmann, K.; Kewalramani, S.; Brodin, J. D.; Moreau, L. M.; Mirkin, C. A.; Olvera De La Cruz, M.; Bedzyk, M. J., Defining the Structure of a Protein–Spherical Nucleic Acid Conjugate and Its Counterionic Cloud. *ACS Central Science* **2018,** *4* (3), 378-386.

35. Krishnamoorthy, K.; Kewalramani, S.; Ehlen, A.; Moreau, L. M.; Mirkin, C. A.; Olvera De La Cruz, M.; Bedzyk, M. J., Enzymatic Degradation of DNA Probed by In Situ X-ray Scattering. *ACS Nano* **2019**.

36. Seferos, D. S.; Giljohann, D. A.; Rosi, N. L.; Mirkin, C. A., Locked Nucleic Acid–Nanoparticle Conjugates. **2007,** *8* (11), 1230-1232.

37. Sprangers, A. J.; Hao, L.; Banga, R. J.; Mirkin, C. A., Liposomal Spherical Nucleic Acids for Regulating Long Noncoding RNAs in the Nucleus. **2016**, 1602753.

38. Barnaby, S. N.; Lee, A.; Mirkin, C. A., Probing the inherent stability of siRNA immobilized on nanoparticle constructs. *Proceedings of the National Academy of Sciences* **2014,** *111* (27), 9739-9744.

39. Yamankurt, G.; Stawicki, R. J.; Posadas, D. M.; Nguyen, J. Q.; Carthew, R. W.; Mirkin, C. A., The effector mechanism of siRNA spherical nucleic acids. *Proceedings of the National Academy of Sciences* **2020,** *117* (3), 1312-1320.

40. Skakuj, K.; Bujold, K. E.; Mirkin, C. A., Mercury-Free Automated Synthesis of Guanidinium Backbone Oligonucleotides. *Journal of the American Chemical Society* **2019,** *141* (51), 20171-20176.

41. Dhar, S.; Daniel, W. L.; Giljohann, D. A.; Mirkin, C. A.; Lippard, S. J., Polyvalent Oligonucleotide Gold Nanoparticle Conjugates as Delivery Vehicles for Platinum(IV) Warheads. *Journal of the American Chemical Society* **2009,** *131* (41), 14652-14653.

42. Guo, C.; Manjili, M. H.; Subjeck, J. R.; Sarkar, D.; Fisher, P. B.; Wang, X.-Y., Therapeutic Cancer Vaccines. Elsevier: 2013; pp 421-475.

43. Waldman, A. D.; Fritz, J. M.; Lenardo, M. J., A guide to cancer immunotherapy: from T cell basic science to clinical practice. *Nature Reviews Immunology* **2020,** *20* (11), 651-668.

44. Jordan, K. R.; McMahan, R. H.; Kemmler, C. B.; Kappler, J. W.; Slansky, J. E., Peptide vaccines prevent tumor growth by activating T cells that respond to native tumor antigens. *Proceedings of the National Academy of Sciences* **2010,** *107* (10), 4652-4657.

45. Schmidt, W.; Buschle, M.; Zauner, W.; Kirlappos, H.; Mechtler, K.; Trska, B.; Birnstiel, M. L., Cell-free tumor antigen peptide-based cancer vaccines. *Proceedings of the National Academy of Sciences* **1997,** *94* (7), 3262-3267.

46. Pamer, E.; Cresswell, P., Mechanisms of MHC Class I–Restricted Antigen Processing. *Annual Review of Immunology* **1998,** *16* (1), 323-358.

47. Allison, J. P.; Hurwitz, A. A.; Leach, D. R., Manipulation of costimulatory signals to enhance antitumor T-cell responses. *Current Opinion in Immunology* **1995,** *7* (5), 682-686.

48. Yamankurt, G.; Berns, E. J.; Xue, A.; Lee, A.; Bagheri, N.; Mrksich, M.; Mirkin, C. A., Exploration of the nanomedicine-design space with high-throughput screening and machine learning. *Nature Biomedical Engineering* **2019,** *3* (4), 318-327.

49. Skakuj, K.; Wang, S.; Qin, L.; Lee, A.; Zhang, B.; Mirkin, C. A., Conjugation Chemistry-Dependent T-Cell Activation with Spherical Nucleic Acids. *Journal of the American Chemical Society* **2018,** *140* (4), 1227-1230.

50. Urquhat, L. *Top companies and drugs by sales in 2019*; Nature Reviews Drug Discovery, 2020.

51. Leader, B.; Baca, Q. J.; Golan, D. E., Protein therapeutics: a summary and pharmacological classification. *Nature Reviews Drug Discovery* **2008,** *7* (1), 21-39.

52. Desnick, R. J.; Schuchman, E. H., Enzyme Replacement Therapy for Lysosomal Diseases: Lessons from 20 Years of Experience and Remaining Challenges. *Annual Review of Genomics and Human Genetics* **2012,** *13* (1), 307-335.

53. Brock, D. J.; Kondow-Mcconaghy, H. M.; Hager, E. C.; Pellois, J.-P., Endosomal Escape and Cytosolic Penetration of Macromolecules Mediated by Synthetic Delivery Agents. *Bioconjugate Chemistry* **2019,** *30* (2), 293-304.

54. Guidotti, G.; Brambilla, L.; Rossi, D., Cell-Penetrating Peptides: From Basic Research to Clinics. *Trends in Pharmacological Sciences* **2017,** *38* (4), 406-424.

55. Veronese, F. M., Peptide and protein PEGylation. *Biomaterials* **2001,** *22* (5), 405-417.

56. Martins, S.; Sarmento, B.; Ferreira, D. C.; Souto, E. B., Lipid-based colloidal carriers for peptide and protein delivery--liposomes versus lipid nanoparticles. *Int J Nanomedicine* **2007,** *2* (4), 595-607.

57. Jefferies, W. A.; Brandon, M. R.; Hunt, S. V.; Williams, A. F.; Gatter, K. C.; Mason, D. Y., Transferrin receptor on endothelium of brain capillaries. *Nature* **1984,** *312* (5990), 162-163.

58. Johnsen, K. B.; Burkhart, A.; Melander, F.; Kempen, P. J.; Vejlebo, J. B.; Siupka, P.; Nielsen, M. S.; Andresen, T. L.; Moos, T., Targeting transferrin receptors at the blood-brain barrier improves the uptake of immunoliposomes and subsequent cargo transport into the brain parenchyma. *Scientific Reports* **2017,** *7* (1).

59. Chen, C. H. B.; Dellamaggiore, K. R.; Ouellette, C. P.; Sedano, C. D.; Lizadjohry, M.; Chernis, G. A.; Gonzales, M.; Baltasar, F. E.; Fan, A. L.; Myerowitz, R.; Neufeld, E. F., Aptamer-based endocytosis of a lysosomal enzyme. *Proceedings of the National Academy of Sciences* **2008,** *105* (41), 15908-15913.

60. Macdonald, J.; Houghton, P.; Xiang, D.; Duan, W.; Shigdar, S., Truncation and Mutation of a Transferrin Receptor Aptamer Enhances Binding Affinity. *Nucleic Acid Therapeutics* **2016,** *26* (6), 348-354.

61. Macdonald, J.; Denoyer, D.; Henri, J.; Jamieson, A.; Burvenich, I. J. G.; Pouliot, N.; Shigdar, S., Bifunctional Aptamer–Doxorubicin Conjugate Crosses the Blood–Brain Barrier and Selectively Delivers Its Payload to EpCAM-Positive Tumor Cells. *Nucleic Acid Therapeutics* **2020,** *30* (2), 117-128.

62. Vinay, D. S.; Ryan, E. P.; Pawelec, G.; Talib, W. H.; Stagg, J.; Elkord, E.; Lichtor, T.; Decker, W. K.; Whelan, R. L.; Kumara, H. M. C. S.; Signori, E.; Honoki, K.; Georgakilas, A. G.; Amin, A.; Helferich, W. G.; Boosani, C. S.; Guha, G.; Ciriolo, M. R.; Chen, S.; Mohammed, S. I.; Azmi, A. S.; Keith, W. N.; Bilsland, A.; Bhakta, D.; Halicka, D.; Fujii, H.; Aquilano, K.; Ashraf, S. S.; Nowsheen, S.; Yang, X.; Choi, B. K.; Kwon, B. S., Immune evasion in cancer: Mechanistic basis and therapeutic strategies. *Seminars in Cancer Biology* **2015,** *35*, S185-S198.

63. Zitvogel, L.; Apetoh, L.; Ghiringhelli, F.; Kroemer, G., Immunological aspects of cancer chemotherapy. *Nature Reviews Immunology* **2008,** *8* (1), 59-73.

64. Slingluff, C. L., The Present and Future of Peptide Vaccines for Cancer. *The Cancer Journal* **2011,** *17* (5), 343-350.

65. John M. Timmerman, M.; Ronald Levy, M., Dendritic Cell Vaccines for Cancer Immunotherapy. *Annual Review of Medicine* **1999,** *50* (1), 507-529.

66. Brown, C. E.; Mackall, C. L., CAR T cell therapy: inroads to response and resistance. *Nature Reviews Immunology* **2019,** *19* (2), 73-74.

67. Chiang, C.; Coukos, G.; Kandalaft, L., Whole Tumor Antigen Vaccines: Where Are We? *Vaccines* **2015,** *3* (2), 344-372.

68. Kawahara, M.; Takaku, H., A tumor lysate is an effective vaccine antigen for the stimulation of CD4+T-cell function and subsequent induction of antitumor immunity mediated by CD8+T cells. *Cancer Biology & Therapy* **2015,** *16* (11), 1616-1625.

69. González, F. E.; Gleisner, A.; Falcón-Beas, F.; Osorio, F.; López, M. N.; Salazar-Onfray, F., Tumor cell lysates as immunogenic sources for cancer vaccine design. *Human Vaccines & Immunotherapeutics* **2014,** *10* (11), 3261-3269.

70. Moyer, J. S.; Maine, G.; Mulé, J. J., Early Vaccination with Tumor Lysate-Pulsed Dendritic Cells after Allogeneic Bone Marrow Transplantation Has Antitumor Effects. *Biology of Blood and Marrow Transplantation* **2006,** *12* (10), 1010-1019.

71. Meade, K. J.; Sanchez, F.; Aguayo, A.; Nadales, N.; Hamalian, S. G.; Uhlendorf, T. L.; Banner, L. R.; Kelber, J. A., Secretomes from metastatic breast cancer cells, enriched for a prognostically unfavorable LCN2 axis, induce anti-inflammatory MSC actions and a tumor-supportive premetastatic lung. *Oncotarget* **2019,** *10* (32), 3027-3039.

72. Fields, R. C.; Shimizu, K.; Mulé, J. J., Murine dendritic cells pulsed with whole tumor lysates mediate potent antitumor immune responsesin vitroandin vivo. *Proceedings of the National Academy of Sciences* **1998,** *95* (16), 9482-9487.

73. Kim, J.; Mooney, D. J., In vivo modulation of dendritic cells by engineered materials: Towards new cancer vaccines. *Nano Today* **2011,** *6* (5), 466-477.

74. Grant, M. L.; Shields, N.; Neumann, S.; Kramer, K.; Bonato, A.; Jackson, C.; Baird, M. A.; Young, S. L., Combining dendritic cells and B cells for presentation of oxidised tumour antigens to CD8+ T cells. *Clinical & Translational Immunology* **2017,** *6* (7), e149.

75. Chiang, C. L.-L.; Kandalaft, L. E.; Tanyi, J.; Hagemann, A. R.; Motz, G. T.; Svoronos, N.; Montone, K.; Mantia-Smaldone, G. M.; Smith, L.; Nisenbaum, H. L.; Levine, B. L.; Kalos, M.; Czerniecki, B. J.; Torigian, D. A.; Powell, D. J.; Mick, R.; Coukos, G., A Dendritic Cell Vaccine Pulsed with Autologous Hypochlorous Acid-Oxidized Ovarian Cancer Lysate Primes

Effective Broad Antitumor Immunity: From Bench to Bedside. *Clinical Cancer Research* **2013,** *19* (17), 4801-4815.

76. Organization, W. H. *COVID-19 Weekly Epidemiological Update*; December 27, 2020, 2020.

77. Nanomedicine and the COVID-19 vaccines. *Nature Nanotechnology* **2020,** *15* (12), 963-963.

78. Lan, J.; Ge, J.; Yu, J.; Shan, S.; Zhou, H.; Fan, S.; Zhang, Q.; Shi, X.; Wang, Q.; Zhang, L.; Wang, X., Structure of the SARS-CoV-2 spike receptor-binding domain bound to the ACE2 receptor. *Nature* **2020,** *581* (7807), 215-220.

79. Tai, W.; He, L.; Zhang, X.; Pu, J.; Voronin, D.; Jiang, S.; Zhou, Y.; Du, L., Characterization of the receptor-binding domain (RBD) of 2019 novel coronavirus: implication for development of RBD protein as a viral attachment inhibitor and vaccine. *Cellular & Molecular Immunology* **2020,** *17* (6), 613-620.

80. Dejnirattisai, W.; Zhou, D.; Ginn, H. M.; Duyvesteyn, H. M. E.; Supasa, P.; Case, J. B.; Zhao, Y.; Walter, T. S.; Mentzer, A. J.; Liu, C.; Wang, B.; Paesen, G. C.; Slon-Campos, J.; López-Camacho, C.; Kafai, N. M.; Bailey, A. L.; Chen, R. E.; Ying, B.; Thompson, C.; Bolton, J.; Fyfe, A.; Gupta, S.; Tan, T. K.; Gilbert-Jaramillo, J.; James, W.; Knight, M.; Carroll, M. W.; Skelly, D.; Dold, C.; Peng, Y.; Levin, R.; Dong, T.; Pollard, A. J.; Knight, J. C.; Klenerman, P.; Temperton, N.; Hall, D. R.; Williams, M. A.; Paterson, N. G.; Bertram, F. K. R.; Siebert, C. A.; Clare, D. K.; Howe, A.; Radecke, J.; Song, Y.; Townsend, A. R.; Huang, K.-Y. A.; Fry, E. E.; Mongkolsapaya, J.; Diamond, M. S.; Ren, J.; Stuart, D. I.; Screaton, G. R., The antigenic anatomy of SARS-CoV-2 receptor binding domain. *Cell* **2021**.

81. Kusmierz, C. D.; Bujold, K. E.; Callmann, C. E.; Mirkin, C. A., Defining the Design Parameters for in Vivo Enzyme Delivery Through Protein Spherical Nucleic Acids. *ACS Central Science* **2020**.

82. Cutler, J. I.; Auyeung, E.; Mirkin, C. A., Spherical Nucleic Acids. *Journal of the American Chemical Society* **2012,** *134* (3), 1376-1391.

83. Seferos, D. S.; Giljohann, D. A.; Hill, H. D.; Prigodich, A. E.; Mirkin, C. A., Nano-Flares: Probes for Transfection and mRNA Detection in Living Cells. *Journal of the American Chemical Society* **2007,** *129* (50), 15477-15479.

84. Prigodich, A. E.; Randeria, P. S.; Briley, W. E.; Kim, N. J.; Daniel, W. L.; Giljohann, D. A.; Mirkin, C. A., Multiplexed Nanoflares: mRNA Detection in Live Cells. *Analytical Chemistry* **2012,** *84* (4), 2062-2066.

85. Samanta, D.; Ebrahimi, S. B.; Mirkin, C. A., Nucleic-Acid Structures as Intracellular Probes for Live Cells. *Advanced Materials* **2020,** *32* (13), 1901743.

86. Zhu, S.; Xing, H.; Gordiichuk, P.; Park, J.; Mirkin, C. A., PLGA Spherical Nucleic Acids. *Advanced Materials* **2018,** *30* (22), 1707113.

87. Harris, J. M.; Martin, N. E.; Modi, M., Pegylation. *Clinical Pharmacokinetics* **2001,** *40* (7), 539-551.

88. Roberts, M. J.; Bentley, M. D.; Harris, J. M., Chemistry for peptide and protein PEGylation. *Advanced Drug Delivery Reviews* **2002,** *54* (4), 459-476.

89. Fishburn, C. S., The Pharmacology of PEGylation: Balancing PD with PK to Generate Novel Therapeutics. *Journal of Pharmaceutical Sciences* **2008,** *97* (10), 4167-4183.

90. Pearson, A. M.; Rich, A.; Krieger, M., Polynucleotide Binding to Macrophage Scavenger Receptors Depends on the Formation of Base-quartet-stabilized Four-stranded Helice. *The Journal of Biological Chemistry* **1993,** *268* (5), 3546-3554.

91. Tsoi, K. M.; Macparland, S. A.; Ma, X.-Z.; Spetzler, V. N.; Echeverri, J.; Ouyang, B.; Fadel, S. M.; Sykes, E. A.; Goldaracena, N.; Kaths, J. M.; Conneely, J. B.; Alman, B. A.; Selzner, M.; Ostrowski, M. A.; Adeyi, O. A.; Zilman, A.; McGilvray, I. D.; Chan, W. C. W.,

Mechanism of hard-nanomaterial clearance by the liver. *Nature Materials* **2016,** *15* (11), 1212-1221.

92. Schwarze, S. R.; Ho, A.; Vocero-Akbani, A.; Dowdy, S. F., In Vivo Protein Transduction: Delivery of a Biologically Active Protein into the Mouse. *Science* **1999,** *285* (5433), 1569.

93. Du, B.; Yu, M.; Zheng, J., Transport and interactions of nanoparticles in the kidneys. *Nature Reviews Materials* **2018,** *3* (10), 358-374.

94. Mebius, R. E.; Kraal, G., Structure and function of the spleen. *Nature Reviews Immunology* **2005,** *5* (8), 606-616.

95. Murphy, J. E.; Tedbury, P. R.; Homer-Vanniasinkam, S.; Walker, J. H.; Ponnambalam, S., Biochemistry and cell biology of mammalian scavenger receptors. *Atherosclerosis* **2005,** *182* (1), 1-15.

96. IDT PrimerQuest program. https://www.idtdna.com/SciTools.

97. Del Villar-Guerra, R.; Trent, J. O.; Chaires, J. B., G-Quadruplex Secondary Structure Obtained from Circular Dichroism Spectroscopy. *Angewandte Chemie International Edition* **2018,** *57* (24), 7171-7175.

98. Lim, K. W.; Amrane, S.; Bouaziz, S.; Xu, W.; Mu, Y.; Patel, D. J.; Luu, K. N.; Phan, A. T. N., Structure of the Human Telomere in K+Solution: A Stable Basket-Type G-Quadruplex with Only Two G-Tetrad Layers. *Journal of the American Chemical Society* **2009,** *131* (12), 4301-4309.

99. Marchand, A.; Gabelica, V., Native Electrospray Mass Spectrometry of DNA G-Quadruplexes in Potassium Solution. *Journal of The American Society for Mass Spectrometry* **2014,** *25* (7), 1146-1154.

100. Fu, A.; Tang, R.; Hardie, J.; Farkas, M. E.; Rotello, V. M., Promises and Pitfalls of Intracellular Delivery of Proteins. *Bioconjugate Chemistry* **2014,** *25* (9), 1602-1608.

101. Joseph; Xu, Y.-H.; Sun, Y.; Adam; Pamela; Guy; Sidransky, E.; Gregory; Krainc, D., Gaucher Disease Glucocerebrosidase and α-Synuclein Form a Bidirectional Pathogenic Loop in Synucleinopathies. *Cell* **2011,** *146* (1), 37-52.

102. Mazzulli, J. R.; Zunke, F.; Tsunemi, T.; Toker, N. J.; Jeon, S.; Burbulla, L. F.; Patnaik, S.; Sidransky, E.; Marugan, J. J.; Sue, C. M.; Krainc, D., Activation of -Glucocerebrosidase Reduces Pathological -Synuclein and Restores Lysosomal Function in Parkinson's Patient Midbrain Neurons. **2016,** *36* (29), 7693-7706.

103. Mazzulli, J. R.; Zunke, F.; Isacson, O.; Studer, L.; Krainc, D., α-Synuclein–induced lysosomal dysfunction occurs through disruptions in protein trafficking in human midbrain synucleinopathy models. *Proceedings of the National Academy of Sciences* **2016,** *113* (7), 1931-1936.

104. Pardridge, W. M., Blood-Brain Barrier and Delivery of Protein and Gene Therapeutics to Brain. *Frontiers in Aging Neuroscience* **2020,** *11*.

105. Yi, X.; Manickam, D. S.; Brynskikh, A.; Kabanov, A. V., Agile delivery of protein therapeutics to CNS. *Journal of Controlled Release* **2014,** *190*, 637-663.

106. Salameh, T. S.; Banks, W. A., Delivery of Therapeutic Peptides and Proteins to the CNS. Elsevier: 2014; pp 277-299.

107. Chang, E.-L.; Ting, C.-Y.; Hsu, P.-H.; Lin, Y.-C.; Liao, E.-C.; Huang, C.-Y.; Chang, Y.-C.; Chan, H.-L.; Chiang, C.-S.; Liu, H.-L.; Wei, K.-C.; Fan, C.-H.; Yeh, C.-K., Angiogenesis-targeting microbubbles combined with ultrasound-mediated gene therapy in brain tumors. *Journal of Controlled Release* **2017,** *255*, 164-175.

108. Gasca-Salas, C.; Fernández-Rodríguez, B.; Pineda-Pardo, J. A.; Rodríguez-Rojas, R.; Obeso, I.; Hernández-Fernández, F.; Del Álamo, M.; Mata, D.; Guida, P.; Ordás-Bandera, C.; Montero-Roblas, J. I.; Martínez-Fernández, R.; Foffani, G.; Rachmilevitch, I.; Obeso, J. A.,

Blood-brain barrier opening with focused ultrasound in Parkinson's disease dementia. *Nature Communications* **2021,** *12* (1).

109. Abrahao, A.; Meng, Y.; Llinas, M.; Huang, Y.; Hamani, C.; Mainprize, T.; Aubert, I.; Heyn, C.; Black, S. E.; Hynynen, K.; Lipsman, N.; Zinman, L., First-in-human trial of blood–brain barrier opening in amyotrophic lateral sclerosis using MR-guided focused ultrasound. *Nature Communications* **2019,** *10* (1).

110. Calias, P.; Papisov, M.; Pan, J.; Savioli, N.; Belov, V.; Huang, Y.; Lotterhand, J.; Alessandrini, M.; Liu, N.; Fischman, A. J.; Powell, J. L.; Heartlein, M. W., CNS Penetration of Intrathecal-Lumbar Idursulfase in the Monkey, Dog and Mouse: Implications for Neurological Outcomes of Lysosomal Storage Disorder. *PLoS ONE* **2012,** *7* (1), e30341.

111. Papisov, M. I.; Belov, V. V.; Gannon, K. S., Physiology of the Intrathecal Bolus: The Leptomeningeal Route for Macromolecule and Particle Delivery to CNS. *Molecular Pharmaceutics* **2013,** *10* (5), 1522-1532.

112. Householder, K. T.; Dharmaraj, S.; Sandberg, D. I.; Wechsler-Reya, R. J.; Sirianni, R. W., Fate of nanoparticles in the central nervous system after intrathecal injection in healthy mice. *Scientific Reports* **2019,** *9* (1).

113. Calias, P.; Banks, W. A.; Begley, D.; Scarpa, M.; Dickson, P., Intrathecal delivery of protein therapeutics to the brain: A critical reassessment. *Pharmacology & Therapeutics* **2014,** *144* (2), 114-122.

114. Pizzo, M. E.; Wolak, D. J.; Kumar, N. N.; Brunette, E.; Brunnquell, C. L.; Hannocks, M.-J.; Abbott, N. J.; Meyerand, M. E.; Sorokin, L.; Stanimirovic, D. B.; Thorne, R. G., Intrathecal antibody distribution in the rat brain: surface diffusion, perivascular transport and osmotic enhancement of delivery. *The Journal of Physiology* **2018,** *596* (3), 445-475.

115. Terstappen, G. C.; Meyer, A. H.; Bell, R. D.; Zhang, W., Strategies for delivering therapeutics across the blood–brain barrier. *Nature Reviews Drug Discovery* **2021,** *20* (5), 362-383.

116. Schuster, J.; Koulov, A.; Mahler, H.-C.; Detampel, P.; Huwyler, J.; Singh, S.; Mathaes, R., In Vivo Stability of Therapeutic Proteins. *Pharmaceutical Research* **2020,** *37* (2).

117. Langen, U. H.; Ayloo, S.; Gu, C., Development and Cell Biology of the Blood-Brain Barrier. *Annual Review of Cell and Developmental Biology* **2019,** *35* (1), 591-613.

118. Daneman, R.; Prat, A., The Blood–Brain Barrier. *Cold Spring Harbor Perspectives in Biology* **2015,** *7* (1), a020412.

119. Kadry, H.; Noorani, B.; Cucullo, L., A blood–brain barrier overview on structure, function, impairment, and biomarkers of integrity. *Fluids and Barriers of the CNS* **2020,** *17* (1).

120. Zhang, W.; Liu, Q. Y.; Haqqani, A. S.; Leclerc, S.; Liu, Z.; Fauteux, F.; Baumann, E.; Delaney, C. E.; Ly, D.; Star, A. T.; Brunette, E.; Sodja, C.; Hewitt, M.; Sandhu, J. K.; Stanimirovic, D. B., Differential expression of receptors mediating receptor-mediated transcytosis (RMT) in brain microvessels, brain parenchyma and peripheral tissues of the mouse and the human. *Fluids and Barriers of the CNS* **2020,** *17* (1).

121. Pulgar, V. M., Transcytosis to Cross the Blood Brain Barrier, New Advancements and Challenges. *Frontiers in Neuroscience* **2019,** *12*.

122. Boado, R. J.; Ka-Wai Hui, E.; Zhiqiang Lu, J.; Pardridge, W. M., Insulin receptor antibody-iduronate 2-sulfatase fusion protein: Pharmacokinetics, anti-drug antibody, and safety pharmacology in Rhesus monkeys. *Biotechnology and Bioengineering* **2014,** *111* (11), 2317-2325.

123. Giugliani, R.; Giugliani, L.; De Oliveira Poswar, F.; Donis, K. C.; Corte, A. D.; Schmidt, M.; Boado, R. J.; Nestrasil, I.; Nguyen, C.; Chen, S.; Pardridge, W. M., Neurocognitive and somatic stabilization in pediatric patients with severe Mucopolysaccharidosis Type I after 52

weeks of intravenous brain-penetrating insulin receptor antibody-iduronidase fusion protein (valanafusp alpha): an open label phase 1-2 trial. *Orphanet Journal of Rare Diseases* **2018,** *13* (1).

124. Anraku, Y.; Kuwahara, H.; Fukusato, Y.; Mizoguchi, A.; Ishii, T.; Nitta, K.; Matsumoto, Y.; Toh, K.; Miyata, K.; Uchida, S.; Nishina, K.; Osada, K.; Itaka, K.; Nishiyama, N.; Mizusawa, H.; Yamasoba, T.; Yokota, T.; Kataoka, K., Glycaemic control boosts glucosylated nanocarrier crossing the BBB into the brain. *Nature Communications* **2017,** *8* (1).

125. Zhang, Y.; Pardridge, W. M., Delivery of β-Galactosidase to Mouse Brain via the Blood-Brain Barrier Transferrin Receptor. *Journal of Pharmacology and Experimental Therapeutics* **2005,** *313* (3), 1075-1081.

126. Banerjee, D.; Liu, A. P.; Voss, N. R.; Schmid, S. L.; Finn, M. G., Multivalent Display and Receptor-Mediated Endocytosis of Transferrin on Virus-Like Particles. *ChemBioChem* **2010,** *11* (9), 1273-1279.

127. Cabezón, I.; Manich, G.; Martín-Venegas, R.; Camins, A.; Pelegrí, C.; Vilaplana, J., Trafficking of Gold Nanoparticles Coated with the 8D3 Anti-Transferrin Receptor Antibody at the Mouse Blood–Brain Barrier. *Molecular Pharmaceutics* **2015,** *12* (11), 4137-4145.

128. Li, X.; Yang, Y.; Zhao, H.; Zhu, T.; Yang, Z.; Xu, H.; Fu, Y.; Lin, F.; Pan, X.; Li, L.; Cui, C.; Hong, M.; Yang, L.; Wang, K. K.; Tan, W., Enhanced in Vivo Blood–Brain Barrier Penetration by Circular Tau–Transferrin Receptor Bifunctional Aptamer for Tauopathy Therapy. *Journal of the American Chemical Society* **2020,** *142* (8), 3862-3872.

129. Ullman, J. C.; Arguello, A.; Getz, J. A.; Bhalla, A.; Mahon, C. S.; Wang, J.; Giese, T.; Bedard, C.; Kim, D. J.; Blumenfeld, J. R.; Liang, N.; Ravi, R.; Nugent, A. A.; Davis, S. S.; Ha, C.; Duque, J.; Tran, H. L.; Wells, R. C.; Lianoglou, S.; Daryani, V. M.; Kwan, W.; Solanoy, H.; Nguyen, H.; Earr, T.; Dugas, J. C.; Tuck, M. D.; Harvey, J. L.; Reyzer, M. L.; Caprioli, R. M.; Hall, S.; Poda, S.; Sanchez, P. E.; Dennis, M. S.; Gunasekaran, K.; Srivastava, A.; Sandmann,

T.; Henne, K. R.; Thorne, R. G.; Di Paolo, G.; Astarita, G.; Diaz, D.; Silverman, A. P.; Watts, R. J.; Sweeney, Z. K.; Kariolis, M. S.; Henry, A. G., Brain delivery and activity of a lysosomal enzyme using a blood-brain barrier transport vehicle in mice. *Science Translational Medicine* **2020,** *12* (545), eaay1163.

130. Kariolis, M. S.; Wells, R. C.; Getz, J. A.; Kwan, W.; Mahon, C. S.; Tong, R.; Kim, D. J.; Srivastava, A.; Bedard, C.; Henne, K. R.; Giese, T.; Assimon, V. A.; Chen, X.; Zhang, Y.; Solanoy, H.; Jenkins, K.; Sanchez, P. E.; Kane, L.; Miyamoto, T.; Chew, K. S.; Pizzo, M. E.; Liang, N.; Calvert, M. E. K.; Devos, S. L.; Baskaran, S.; Hall, S.; Sweeney, Z. K.; Thorne, R. G.; Watts, R. J.; Dennis, M. S.; Silverman, A. P.; Zuchero, Y. J. Y., Brain delivery of therapeutic proteins using an Fc fragment blood-brain barrier transport vehicle in mice and monkeys. *Science Translational Medicine* **2020,** *12* (545), eaay1359.

131. Barnaby, S. N.; Perelman, G. A.; Kohlstedt, K. L.; Chinen, A. B.; Schatz, G. C.; Mirkin, C. A., Design Considerations for RNA Spherical Nucleic Acids (SNAs). **2016,** *27* (9), 2124-2131.

132. Chinen, A. B.; Ferrer, J. R.; Merkel, T. J.; Mirkin, C. A., Relationships between Poly(ethylene glycol) Modifications on RNA–Spherical Nucleic Acid Conjugates and Cellular Uptake and Circulation Time. **2016**.

133. Ferrer, J. R.; Sinegra, A. J.; Ivancic, D.; Yeap, X. Y.; Qiu, L.; Wang, J.-J.; Zhang, Z. J.; Wertheim, J. A.; Mirkin, C. A., Structure-Dependent Biodistribution of Liposomal Spherical Nucleic Acids. *ACS Nano* **2020**.

134. Khan, A. I.; Liu, J.; Dutta, P., Iron transport kinetics through blood-brain barrier endothelial cells. *Biochimica et Biophysica Acta (BBA) - General Subjects* **2018,** *1862* (5), 1168-1179.

135. Lochhead, J. J.; Thorne, R. G., Intranasal delivery of biologics to the central nervous system. *Advanced Drug Delivery Reviews* **2012,** *64* (7), 614-628.

136. Born, J.; Lange, T.; Kern, W.; McGregor, G. P.; Bickel, U.; Fehm, H. L., Sniffing neuropeptides: a transnasal approach to the human brain. *Nature Neuroscience* **2002,** *5* (6), 514-516.

137. Craft, S., Intranasal Insulin Therapy for Alzheimer Disease and Amnestic Mild Cognitive Impairment. *Archives of Neurology* **2012,** *69* (1), 29.

138. Papisov, M. I.; Belov, V.; Fischman, A. J.; Belova, E.; Titus, J.; Gagne, M.; Gillooly, C., Delivery of proteins to CNS as seen and measured by positron emission tomography. *Drug Delivery and Translational Research* **2012,** *2* (3), 201-209.

139. Papisov, M. I.; Belov, V.; Belova, E.; Fischman, A. J.; Fisher, R.; Wright, J. L.; Gannon, K. S.; Titus, J.; Gagne, M.; Gillooly, C. A., Investigation of intrathecal transport of NPT002, a prospective therapeutic based on phage M13, in nonhuman primates. *Drug Delivery and Translational Research* **2012,** *2* (3), 210-221.

140. Umbrain, V.; D'Haese, J.; Alafandy, M.; Roover, E.; Schoutens, A.; Gansbeke, B.; Albert, A.; Goffinet, G.; Camu, F.; Legros, F. J., Scintigraphic visualization of intrathecal liposome biodistribution. *Acta Anaesthesiologica Scandinavica* **1997,** *41* (1), 25-34.

141. Vinogradov, S. V.; Batrakova, E. V.; Kabanov, A. V., Nanogels for Oligonucleotide Delivery to the Brain. *Bioconjugate Chemistry* **2004,** *15* (1), 50-60.

142. Keefe, A. D.; Pai, S.; Ellington, A., Aptamers as therapeutics. *Nature Reviews Drug Discovery* **2010,** *9* (7), 537-550.

143. Tan, W.; Wang, H.; Chen, Y.; Zhang, X.; Zhu, H.; Yang, C.; Yang, R.; Liu, C., Molecular aptamers for drug delivery. *Trends in Biotechnology* **2011,** *29* (12), 634-640.

144. Zhou, J.; Rossi, J. J., Cell-type-specific, Aptamer-functionalized Agents for Targeted Disease Therapy. *Molecular Therapy - Nucleic Acids* **2014,** *3* (6), e169.

145. Samanta, D.; Ebrahimi, S. B.; Kusmierz, C. D.; Cheng, H. F.; Mirkin, C. A., Protein Spherical Nucleic Acids for Live-Cell Chemical Analysis. *Journal of the American Chemical Society* **2020,** *142* (31), 13350-13355.

146. Ali, S. A.; Shi, V.; Maric, I.; Wang, M.; Stroncek, D. F.; Rose, J. J.; Brudno, J. N.; Stetler-Stevenson, M.; Feldman, S. A.; Hansen, B. G.; Fellowes, V. S.; Hakim, F. T.; Gress, R. E.; Kochenderfer, J. N., T cells expressing an anti–B-cell maturation antigen chimeric antigen receptor cause remissions of multiple myeloma. *Blood* **2016,** *128* (13), 1688-1700.

147. Maude, S. L.; Laetsch, T. W.; Buechner, J.; Rives, S.; Boyer, M.; Bittencourt, H.; Bader, P.; Verneris, M. R.; Stefanski, H. E.; Myers, G. D.; Qayed, M.; De Moerloose, B.; Hiramatsu, H.; Schlis, K.; Davis, K. L.; Martin, P. L.; Nemecek, E. R.; Yanik, G. A.; Peters, C.; Baruchel, A.; Boissel, N.; Mechinaud, F.; Balduzzi, A.; Krueger, J.; June, C. H.; Levine, B. L.; Wood, P.; Taran, T.; Leung, M.; Mueller, K. T.; Zhang, Y.; Sen, K.; Lebwohl, D.; Pulsipher, M. A.; Grupp, S. A., Tisagenlecleucel in Children and Young Adults with B-Cell Lymphoblastic Leukemia. *New England Journal of Medicine* **2018,** *378* (5), 439-448.

148. Neelapu, S. S.; Locke, F. L.; Bartlett, N. L.; Lekakis, L. J.; Miklos, D. B.; Jacobson, C. A.; Braunschweig, I.; Oluwole, O. O.; Siddiqi, T.; Lin, Y.; Timmerman, J. M.; Stiff, P. J.; Friedberg, J. W.; Flinn, I. W.; Goy, A.; Hill, B. T.; Smith, M. R.; Deol, A.; Farooq, U.; McSweeney, P.; Munoz, J.; Avivi, I.; Castro, J. E.; Westin, J. R.; Chavez, J. C.; Ghobadi, A.; Komanduri, K. V.; Levy, R.; Jacobsen, E. D.; Witzig, T. E.; Reagan, P.; Bot, A.; Rossi, J.; Navale, L.; Jiang, Y.; Aycock, J.; Elias, M.; Chang, D.; Wiezorek, J.; Go, W. Y., Axicabtagene Ciloleucel CAR T-Cell Therapy in Refractory Large B-Cell Lymphoma. *New England Journal of Medicine* **2017,** *377* (26), 2531-2544.

149. Park, J. H.; Rivière, I.; Gonen, M.; Wang, X.; Sénéchal, B.; Curran, K. J.; Sauter, C.; Wang, Y.; Santomasso, B.; Mead, E.; Roshal, M.; Maslak, P.; Davila, M.; Brentjens, R. J.;

Sadelain, M., Long-Term Follow-up of CD19 CAR Therapy in Acute Lymphoblastic Leukemia. *New England Journal of Medicine* **2018,** *378* (5), 449-459.

150. Schuster, S. J.; Svoboda, J.; Chong, E. A.; Nasta, S. D.; Mato, A. R.; Anak, Ö.; Brogdon, J. L.; Pruteanu-Malinici, I.; Bhoj, V.; Landsburg, D.; Wasik, M.; Levine, B. L.; Lacey, S. F.; Melenhorst, J. J.; Porter, D. L.; June, C. H., Chimeric Antigen Receptor T Cells in Refractory B-Cell Lymphomas. *New England Journal of Medicine* **2017,** *377* (26), 2545-2554.

151. Kuai, R.; Ochyl, L. J.; Bahjat, K. S.; Schwendeman, A.; Moon, J. J., Designer vaccine nanodiscs for personalized cancer immunotherapy. *Nature Materials* **2017,** *16* (4), 489-496.

152. Fang, J.; Hu, B.; Li, S.; Zhang, C.; Liu, Y.; Wang, P., A multi-antigen vaccine in combination with an immunotoxin targeting tumor-associated fibroblast for treating murine melanoma. *Molecular Therapy - Oncolytics* **2016,** *3*, 16007.

153. Balkwill, F. R.; Capasso, M.; Hagemann, T., The tumor microenvironment at a glance. *Journal of Cell Science* **2012,** *125* (23), 5591-5596.

154. Win, S. J.; McMillan, D. G. G.; Errington-Mais, F.; Ward, V. K.; Young, S. L.; Baird, M. A.; Melcher, A. A., Enhancing the immunogenicity of tumour lysate-loaded dendritic cell vaccines by conjugation to virus-like particles. *British Journal of Cancer* **2012,** *106* (1), 92-98.

155. Chiang, C. L.-L.; Benencia, F.; Coukos, G., Whole tumor antigen vaccines. *Seminars in Immunology* **2010,** *22* (3), 132-143.

156. Marcinkiewicz, J., Neutrophil chloramines: missing links between innate and acquired immunity. *Immunology Today* **1997,** *18* (12), 577-580.

157. Marcinkiewicz, J.; Chain, B. M.; Olszowska, E.; Olszowski, S.; Zgliczyński, J. M., Enhancement of immunogenic properties of ovalbumin as a result of its chlorination. *International Journal of Biochemistry* **1991,** *23* (12), 1393-1395.

158. Allison, M. E. D.; Fearon, D. T., Enhanced immunogenicity of aldehyde-bearing antigens: a possible link between innate and adaptive immunity. *European Journal of Immunology* **2000,** *30* (10), 2881-2887.

159. Coulie, P. G.; Van Den Eynde, B. J.; Van Der Bruggen, P.; Boon, T., Tumour antigens recognized by T lymphocytes: at the core of cancer immunotherapy. *Nature Reviews Cancer* **2014,** *14* (2), 135-146.

160. Frey, S.; Castro, A.; Arsiwala, A.; Kane, R. S., Bionanotechnology for vaccine design. *Current Opinion in Biotechnology* **2018,** *52*, 80-88.

161. Irvine, D. J.; Hanson, M. C.; Rakhra, K.; Tokatlian, T., Synthetic Nanoparticles for Vaccines and Immunotherapy. *Chemical Reviews* **2015,** *115* (19), 11109-11146.

162. Kemp, J. A.; Shim, M. S.; Heo, C. Y.; Kwon, Y. J., "Combo" nanomedicine: Co-delivery of multi-modal therapeutics for efficient, targeted, and safe cancer therapy. *Advanced Drug Delivery Reviews* **2016,** *98*, 3-18.

163. Lytton-Jean, A. K. R.; Mirkin, C. A., A Thermodynamic Investigation into the Binding Properties of DNA Functionalized Gold Nanoparticle Probes and Molecular Fluorophore Probes. *Journal of the American Chemical Society* **2005,** *127* (37), 12754-12755.

164. Lee, J.-S.; Lytton-Jean, A. K. R.; Hurst, S. J.; Mirkin, C. A., Silver Nanoparticle−Oligonucleotide Conjugates Based on DNA with Triple Cyclic Disulfide Moieties. *Nano Letters* **2007,** *7* (7), 2112-2115.

165. Mitchell, G. P.; Mirkin, C. A.; Letsinger, R. L., Programmed Assembly of DNA Functionalized Quantum Dots. *Journal of the American Chemical Society* **1999,** *121* (35), 8122-8123.

166. Young, K. L.; Scott, A. W.; Hao, L.; Mirkin, S. E.; Liu, G.; Mirkin, C. A., Hollow Spherical Nucleic Acids for Intracellular Gene Regulation Based upon Biocompatible Silica Shells. **2012,** *12* (7), 3867-3871.

167. Li, Z.; Zhang, Y.; Fullhart, P.; Mirkin, C. A., Reversible and Chemically Programmable Micelle Assembly with DNA Block-Copolymer Amphiphiles. *Nano Letters* **2004,** *4* (6), 1055-1058.

168. Calabrese, C. M.; Merkel, T. J.; Briley, W. E.; Randeria, P. S.; Narayan, S. P.; Rouge, J. L.; Walker, D. A.; Scott, A. W.; Mirkin, C. A., Biocompatible Infinite-Coordination-Polymer Nanoparticle-Nucleic-Acid Conjugates for Antisense Gene Regulation. **2014**, n/a-n/a.

169. Bulbake, U.; Doppalapudi, S.; Kommineni, N.; Khan, W., Liposomal Formulations in Clinical Use: An Updated Review. *Pharmaceutics* **2017,** *9* (4), 12.

170. Bozzuto, G.; Molinari, A., Liposomes as nanomedical devices. *Int J Nanomedicine* **2015**, 975.

171. Allen, T. M.; Cullis, P. R., Liposomal drug delivery systems: From concept to clinical applications. *Advanced Drug Delivery Reviews* **2013,** *65* (1), 36-48.

172. Sercombe, L.; Veerati, T.; Moheimani, F.; Wu, S. Y.; Sood, A. K.; Hua, S., Advances and Challenges of Liposome Assisted Drug Delivery. *Frontiers in Pharmacology* **2015,** *6*.

173. Bally, M.; Bailey, K.; Sugihara, K.; Grieshaber, D.; Vörös, J.; Städler, B., Liposome and Lipid Bilayer Arrays Towards Biosensing Applications. *Small* **2010,** *6* (22), 2481-2497.

174. Liu, Q.; Boyd, B. J., Liposomes in biosensors. *The Analyst* **2013,** *138* (2), 391-409.

175. Gregoriadis, G.; Florence, A. T., Liposomes in Drug Delivery. *Drugs* **1993,** *45* (1), 15-28.

176. Xia, Y.; Xu, C.; Zhang, X.; Ning, P.; Wang, Z.; Tian, J.; Chen, X., Liposome-based probes for molecular imaging: from basic research to the bedside. *Nanoscale* **2019,** *11* (13), 5822-5838.

177. Balazs, D. A.; Godbey, W. T., Liposomes for Use in Gene Delivery. *Journal of Drug Delivery* **2011,** *2011*, 326497.

178. Callmann, C. E.; Cole, L. E.; Kusmierz, C. D.; Huang, Z.; Horiuchi, D.; Mirkin, C. A., Tumor cell lysate-loaded immunostimulatory spherical nucleic acids as therapeutics for triple-

negative breast cancer. *Proceedings of the National Academy of Sciences* **2020,** *117* (30), 17543-17550.

179. Vangasseri, D. P.; Cui, Z.; Chen, W.; Hokey, D. A.; Falo, L. D.; Huang, L., Immunostimulation of dendritic cells by cationic liposomes. *Molecular Membrane Biology* **2006,** *23* (5), 385-395.

180. Lian, T.; Ho, R. J. Y., Trends and Developments in Liposome Drug Delivery Systems. *Journal of Pharmaceutical Sciences* **2001,** *90* (6), 667-680.

181. Kučerka, N.; Nieh, M.-P.; Katsaras, J., Fluid phase lipid areas and bilayer thicknesses of commonly used phosphatidylcholines as a function of temperature. *Biochimica et Biophysica Acta (BBA) - Biomembranes* **2011,** *1808* (11), 2761-2771.

182. Beltrán-Gracia, E.; López-Camacho, A.; Higuera-Ciapara, I.; Velázquez-Fernández, J. B.; Vallejo-Cardona, A. A., Nanomedicine review: clinical developments in liposomal applications. *Cancer Nanotechnology* **2019,** *10* (1).

183. Kheyfets, B.; Galimzyanov, T.; Mukhin, S., Microscopic Description of the Thermodynamics of a Lipid Membrane at a Liquid–Gel Phase Transition. *JETP Letters* **2018,** *107* (11), 718-724.

184. Bruce Alberts, A. J., Julian Lewis, Martin Raff, Keith Roberts, Peter Walter, *Molecular Biology of the Cell*. 4th ed.; Garland Science: New York, 2002.

185. Hong, J. S.; Vreeland, W. N.; Depaoli Lacerda, S. H.; Locascio, L. E.; Gaitan, M.; Raghavan, S. R., Liposome-Templated Supramolecular Assembly of Responsive Alginate Nanogels. *Langmuir* **2008,** *24* (8), 4092-4096.

186. Lockhart, J. N.; Beezer, D. B.; Stevens, D. M.; Spears, B. R.; Harth, E., One-pot polyglycidol nanogels via liposome master templates for dual drug delivery. *Journal of Controlled Release* **2016,** *244*, 366-374.

187. Tan, G.; Xu, P.; He, J.; Lawson, L.; McPherson, G. L.; John, V. T., Highly aspherical silica nanoshells by templating tubular liposomes. *Soft Matter* **2009,** *5* (16), 3006.

188. Lestini, B. J.; Sagnella, S. M.; Xu, Z.; Shive, M. S.; Richter, N. J.; Jayaseharan, J.; Case, A. J.; Kottke-Marchant, K.; Anderson, J. M.; Marchant, R. E., Surface modification of liposomes for selective cell targeting in cardiovascular drug delivery. *Journal of Controlled Release* **2002,** *78* (1-3), 235-247.

189. Turánek, J.; Mašek, J.; Raška, M.; Ledvina, M.; Paulovičová, E.; Hubatka, F.; Kotouček, J., 13 - Modification of liposomal surface by polysaccharides: Preparation, characterization, and application for drug targeting. In *Functional Polysaccharides for Biomedical Applications*, Maiti, S.; Jana, S., Eds. Woodhead Publishing: 2019; pp 433-467.

190. Guan, C.; Chernyak, N.; Dominguez, D.; Cole, L.; Zhang, B.; Mirkin, C. A., RNA-Based Immunostimulatory Liposomal Spherical Nucleic Acids as Potent TLR7/8 Modulators. *Small* **2018,** *14* (49), 1803284.

191. Vollmer, J.; Weeratna, R.; Payette, P.; Jurk, M.; Schetter, C.; Laucht, M.; Wader, T.; Tluk, S.; Liu, M.; Davis, H. L.; Krieg, A. M., Characterization of three CpG oligodeoxynucleotide classes with distinct immunostimulatory activities. *European Journal of Immunology* **2004,** *34* (1), 251-262.

192. Kumagai, Y.; Takeuchi, O.; Akira, S., TLR9 as a key receptor for the recognition of DNA☆. *Advanced Drug Delivery Reviews* **2008,** *60* (7), 795-804.

193. Gross, B. P.; Wongrakpanich, A.; Francis, M. B.; Salem, A. K.; Norian, L. A., A Therapeutic Microparticle-Based Tumor Lysate Vaccine Reduces Spontaneous Metastases in Murine Breast Cancer. *The AAPS Journal* **2014,** *16* (6), 1194-1203.

194. Li, Z.; Qiu, Y.; Lu, W.; Jiang, Y.; Wang, J., Immunotherapeutic interventions of Triple Negative Breast Cancer. *Journal of Translational Medicine* **2018,** *16* (1).

195. Stagg, J.; Allard, B., Immunotherapeutic approaches in triple-negative breast cancer: latest research and clinical prospects. *Therapeutic Advances in Medical Oncology* **2013,** *5* (3), 169-181.

196. Anders, C.; Carey, L. A., Understanding and treating triple-negative breast cancer. *Oncology (Williston Park)* **2008,** *22* (11), 1233-1243.

197. André, F.; Zielinski, C. C., Optimal strategies for the treatment of metastatic triple-negative breast cancer with currently approved agents. *Annals of Oncology* **2012,** *23*, vi46-vi51.

198. Anders, C. K.; Carey, L. A., Biology, Metastatic Patterns, and Treatment of Patients with Triple-Negative Breast Cancer. *Clinical Breast Cancer* **2009,** *9*, S73-S81.

199. Fedele, M.; Cerchia, L.; Chiappetta, G., The Epithelial-to-Mesenchymal Transition in Breast Cancer: Focus on Basal-Like Carcinomas. *Cancers* **2017,** *9* (12), 134.

200. Su, Y.; Hopfinger, N. R.; Nguyen, T. D.; Pogash, T. J.; Santucci-Pereira, J.; Russo, J., Epigenetic reprogramming of epithelial mesenchymal transition in triple negative breast cancer cells with DNA methyltransferase and histone deacetylase inhibitors. *Journal of Experimental & Clinical Cancer Research* **2018,** *37* (1).

201. Ellies, L. G.; Kuo, C., Abstract C91: PyVmT luminal and EMT cell lines exhibit characteristic patterns of orthotopic and tail vein metastasis. *Cancer Research* **2013,** *73* (3 Supplement), C91.

202. Biswas, T.; Yang, J.; Zhao, L.; Sun, L., Abstract P2-04-07: Modeling orthotopic and metastatic progression of mammary tumors to evaluate the efficacy of TGF-β inhibitors in a pre-clinical setting. *Cancer Research* **2012,** *72* (24 Supplement), P2-04-07-P2-04-07.

203. Christenson, J. L.; Butterfield, K. T.; Spoelstra, N. S.; Norris, J. D.; Josan, J. S.; Pollock, J. A.; McDonnell, D. P.; Katzenellenbogen, B. S.; Katzenellenbogen, J. A.; Richer, J. K., MMTV-PyMT and Derived Met-1 Mouse Mammary Tumor Cells as Models for Studying the Role of the

Androgen Receptor in Triple-Negative Breast Cancer Progression. *Hormones and Cancer* **2017,** *8* (2), 69-77.

204. Ouzounova, M.; Lee, E.; Piranlioglu, R.; El Andaloussi, A.; Kolhe, R.; Demirci, M. F.; Marasco, D.; Asm, I.; Chadli, A.; Hassan, K. A.; Thangaraju, M.; Zhou, G.; Arbab, A. S.; Cowell, J. K.; Korkaya, H., Monocytic and granulocytic myeloid derived suppressor cells differentially regulate spatiotemporal tumour plasticity during metastatic cascade. *Nature Communications* **2017,** *8* (1), 14979.

205. Barnes, S., EMT-6 Syngeneic Breast Tumor Model – A Powerful Tool For Immuno-oncology Studies *Covance* **2019**.

206. Liu, L. N.; Shivakumar, R.; Allen, C.; Fratantoni, J. C., Delivery of Whole Tumor Lysate into Dendritic Cells for Cancer Vaccination. Humana Press: 2008; pp 139-153.

207. Krishnamachari, Y.; Salem, A. K., Innovative strategies for co-delivering antigens and CpG oligonucleotides. *Advanced Drug Delivery Reviews* **2009,** *61* (3), 205-217.

208. Prokopowicz, Z. M.; Arce, F.; Biedron, R.; Chiang, C. L. L.; Ciszek, M.; Katz, D. R.; Nowakowska, M.; Zapotoczny, S.; Marcinkiewicz, J.; Chain, B. M., Hypochlorous Acid: A Natural Adjuvant That Facilitates Antigen Processing, Cross-Priming, and the Induction of Adaptive Immunity. *The Journal of Immunology* **2010,** *184* (2), 824-835.

209. Ho, N. I.; Huis In 'T Veld, L. G. M.; Raaijmakers, T. K.; Adema, G. J., Adjuvants Enhancing Cross-Presentation by Dendritic Cells: The Key to More Effective Vaccines? *Frontiers in Immunology* **2018,** *9*.

210. Maimela, N. R.; Liu, S.; Zhang, Y., Fates of CD8+ T cells in Tumor Microenvironment. *Computational and Structural Biotechnology Journal* **2019,** *17*, 1-13.

211. Kim, P. S.; Ahmed, R., Features of responding T cells in cancer and chronic infection. *Current Opinion in Immunology* **2010,** *22* (2), 223-230.

212. Lesokhin, A. M.; Merghoub, T.; Wolchok, J. D., Myeloid-derived suppressor cells and the efficacy of CD8+T-cell immunotherapy. *OncoImmunology* **2013,** *2* (2), e22764.

213. Smaby, J. M.; Momsen, M. M.; Brockman, H. L.; Brown, R. E., Phosphatidylcholine acyl unsaturation modulates the decrease in interfacial elasticity induced by cholesterol. *Biophysical Journal* **1997,** *73* (3), 1492-1505.

214. McMullen, T. P. W.; Lewis, R. N. A. H.; McElhaney, R. N., Differential scanning calorimetric study of the effect of cholesterol on the thermotropic phase behavior of a homologous series of linear saturated phosphatidylcholines. *Biochemistry* **1993,** *32* (2), 516-522.

215. Chen, W.; Duša, F.; Witos, J.; Ruokonen, S.-K.; Wiedmer, S. K., Determination of the Main Phase Transition Temperature of Phospholipids by Nanoplasmonic Sensing. *Scientific Reports* **2018,** *8* (1).

216. Ramirez-Ortiz, Z. G.; Specht, C. A.; Wang, J. P.; Lee, C. K.; Bartholomeu, D. C.; Gazzinelli, R. T.; Levitz, S. M., Toll-Like Receptor 9-Dependent Immune Activation by Unmethylated CpG Motifs in Aspergillus fumigatus DNA. *Infection and Immunity* **2008,** *76* (5), 2123-2129.

217. Sansom, D. M.; Manzotti, C. N.; Zheng, Y., What's the difference between CD80 and CD86? *Trends in Immunology* **2003,** *24* (6), 313-318.

218. Hu, J.; Xu, J.; Li, M.; Zhang, Y.; Yi, H.; Chen, J.; Dong, L.; Zhang, J.; Huang, Z., Targeting Lymph Node Sinus Macrophages to Inhibit Lymph Node Metastasis. *Molecular Therapy - Nucleic Acids* **2019,** *16*, 650-662.

219. Bodogai, M.; Lee Chang, C.; Wejksza, K.; Lai, J.; Merino, M.; Wersto, R. P.; Gress, R. E.; Chan, A. C.; Hesdorffer, C.; Biragyn, A., Anti-CD20 Antibody Promotes Cancer Escape via Enrichment of Tumor-Evoked Regulatory B Cells Expressing Low Levels of CD20 and CD137L. *Cancer Research* **2013,** *73* (7), 2127-2138.

220. Wexler, H., Accurate Identification of Experimental Pulmonary Metastases2. *JNCI: Journal of the National Cancer Institute* **1966,** *36* (4), 641-645.

221. Huang, C.; Wang, Y.; Li, X.; Ren, L.; Zhao, J.; Hu, Y.; Zhang, L.; Fan, G.; Xu, J.; Gu, X.; Cheng, Z.; Yu, T.; Xia, J.; Wei, Y.; Wu, W.; Xie, X.; Yin, W.; Li, H.; Liu, M.; Xiao, Y.; Gao, H.; Guo, L.; Xie, J.; Wang, G.; Jiang, R.; Gao, Z.; Jin, Q.; Wang, J.; Cao, B., Clinical features of patients infected with 2019 novel coronavirus in Wuhan, China. *The Lancet* **2020,** *395* (10223), 497-506.

222. Chan, J. F.-W.; Yuan, S.; Kok, K.-H.; To, K. K.-W.; Chu, H.; Yang, J.; Xing, F.; Liu, J.; Yip, C. C.-Y.; Poon, R. W.-S.; Tsoi, H.-W.; Lo, S. K.-F.; Chan, K.-H.; Poon, V. K.-M.; Chan, W.-M.; Ip, J. D.; Cai, J.-P.; Cheng, V. C.-C.; Chen, H.; Hui, C. K.-M.; Yuen, K.-Y., A familial cluster of pneumonia associated with the 2019 novel coronavirus indicating person-to-person transmission: a study of a family cluster. *The Lancet* **2020,** *395* (10223), 514-523.

223. FDA Takes Key Action in Fight Against COVID-19 By Issuing Emergency Use Authorization for First COVID-19 Vaccine. *U.S. Food & Drug Administration* December 11, 2020, 2020.

224. FDA Takes Additional Action in Fight Against COVID-19 By Issuing Emergency Use Authorization for Second COVID-19 Vaccine. *U.S. Food & Drug Administration* December 18, 2020, 2020.

225. Corbett, K. S.; Edwards, D. K.; Leist, S. R.; Abiona, O. M.; Boyoglu-Barnum, S.; Gillespie, R. A.; Himansu, S.; Schäfer, A.; Ziwawo, C. T.; Dipiazza, A. T.; Dinnon, K. H.; Elbashir, S. M.; Shaw, C. A.; Woods, A.; Fritch, E. J.; Martinez, D. R.; Bock, K. W.; Minai, M.; Nagata, B. M.; Hutchinson, G. B.; Wu, K.; Henry, C.; Bahl, K.; Garcia-Dominguez, D.; Ma, L.; Renzi, I.; Kong, W.-P.; Schmidt, S. D.; Wang, L.; Zhang, Y.; Phung, E.; Chang, L. A.; Loomis, R. J.; Altaras, N. E.; Narayanan, E.; Metkar, M.; Presnyak, V.; Liu, C.; Louder, M. K.; Shi, W.; Leung, K.; Yang, E. S.; West, A.; Gully, K. L.; Stevens, L. J.; Wang, N.; Wrapp, D.; Doria-

Rose, N. A.; Stewart-Jones, G.; Bennett, H.; Alvarado, G. S.; Nason, M. C.; Ruckwardt, T. J.; McLellan, J. S.; Denison, M. R.; Chappell, J. D.; Moore, I. N.; Morabito, K. M.; Mascola, J. R.; Baric, R. S.; Carfi, A.; Graham, B. S., SARS-CoV-2 mRNA vaccine design enabled by prototype pathogen preparedness. *Nature* **2020,** *586* (7830), 567-571.

226. Shin, M. D.; Shukla, S.; Chung, Y. H.; Beiss, V.; Chan, S. K.; Ortega-Rivera, O. A.; Wirth, D. M.; Chen, A.; Sack, M.; Pokorski, J. K.; Steinmetz, N. F., COVID-19 vaccine development and a potential nanomaterial path forward. *Nature Nanotechnology* **2020,** *15* (8), 646-655.

227. Hotez, P. J.; Bottazzi, M. E., Developing a low-cost and accessible COVID-19 vaccine for global health. *PLOS Neglected Tropical Diseases* **2020,** *14* (7), e0008548.

228. Vetter, V.; Denizer, G.; Friedland, L. R.; Krishnan, J.; Shapiro, M., Understanding modern-day vaccines: what you need to know. *Annals of Medicine* **2018,** *50* (2), 110-120.

229. Moyle, P. M.; Toth, I., Modern Subunit Vaccines: Development, Components, and Research Opportunities. *ChemMedChem* **2013,** *8* (3), 360-376.

230. Valenzuela, P.; Medina, A.; Rutter, W. J.; Ammerer, G.; Hall, B. D., Synthesis and assembly of hepatitis B virus surface antigen particles in yeast. *Nature* **1982,** *298* (5872), 347-350.

231. Excler, J.-L.; Saville, M.; Berkley, S.; Kim, J. H., Vaccine development for emerging infectious diseases. *Nature Medicine* **2021,** *27* (4), 591-600.

232. Coffman, R. L.; Sher, A.; Seder, R. A., Vaccine Adjuvants: Putting Innate Immunity to Work. *Immunity* **2010,** *33* (4), 492-503.

233. Letko, M.; Marzi, A.; Munster, V., Functional assessment of cell entry and receptor usage for SARS-CoV-2 and other lineage B betacoronaviruses. *Nature Microbiology* **2020,** *5* (4), 562-569.

234. Zost, S. J.; Gilchuk, P.; Case, J. B.; Binshtein, E.; Chen, R. E.; Nkolola, J. P.; Schäfer, A.; Reidy, J. X.; Trivette, A.; Nargi, R. S.; Sutton, R. E.; Suryadevara, N.; Martinez, D. R.; Williamson, L. E.; Chen, E. C.; Jones, T.; Day, S.; Myers, L.; Hassan, A. O.; Kafai, N. M.; Winkler, E. S.; Fox, J. M.; Shrihari, S.; Mueller, B. K.; Meiler, J.; Chandrashekar, A.; Mercado, N. B.; Steinhardt, J. J.; Ren, K.; Loo, Y.-M.; Kallewaard, N. L.; McCune, B. T.; Keeler, S. P.; Holtzman, M. J.; Barouch, D. H.; Gralinski, L. E.; Baric, R. S.; Thackray, L. B.; Diamond, M. S.; Carnahan, R. H.; Crowe, J. E., Potently neutralizing and protective human antibodies against SARS-CoV-2. *Nature* **2020,** *584* (7821), 443-449.

235. Shi, R.; Shan, C.; Duan, X.; Chen, Z.; Liu, P.; Song, J.; Song, T.; Bi, X.; Han, C.; Wu, L.; Gao, G.; Hu, X.; Zhang, Y.; Tong, Z.; Huang, W.; Liu, W. J.; Wu, G.; Zhang, B.; Wang, L.; Qi, J.; Feng, H.; Wang, F.-S.; Wang, Q.; Gao, G. F.; Yuan, Z.; Yan, J., A human neutralizing antibody targets the receptor-binding site of SARS-CoV-2. *Nature* **2020,** *584* (7819), 120-124.

236. Voss, W. N.; Hou, Y. J.; Johnson, N. V.; Delidakis, G.; Kim, J. E.; Javanmardi, K.; Horton, A. P.; Bartzoka, F.; Paresi, C. J.; Tanno, Y.; Chou, C.-W.; Abbasi, S. A.; Pickens, W.; George, K.; Boutz, D. R.; Towers, D. M.; McDaniel, J. R.; Billick, D.; Goike, J.; Rowe, L.; Batra, D.; Pohl, J.; Lee, J.; Gangappa, S.; Sambhara, S.; Gadush, M.; Wang, N.; Person, M. D.; Iverson, B. L.; Gollihar, J. D.; Dye, J.; Herbert, A.; Finkelstein, I. J.; Baric, R. S.; McLellan, J. S.; Georgiou, G.; Lavinder, J. J.; Ippolito, G. C., Prevalent, protective, and convergent IgG recognition of SARS-CoV-2 non-RBD spike epitopes. *Science* **2021**, eabg5268.

237. Stadlbauer, D.; Amanat, F.; Chromikova, V.; Jiang, K.; Strohmeier, S.; Arunkumar, G. A.; Tan, J.; Bhavsar, D.; Capuano, C.; Kirkpatrick, E.; Meade, P.; Brito, R. N.; Teo, C.; McMahon, M.; Simon, V.; Krammer, F., SARS-CoV-2 Seroconversion in Humans: A Detailed Protocol for a Serological Assay, Antigen Production, and Test Setup. *Current Protocols in Microbiology* **2020,** *57* (1).

238. Qin, L.; Wang, S.; Dominguez, D.; Long, A.; Chen, S.; Fan, J.; Ahn, J.; Skakuj, K.; Huang, Z.; Lee, A.; Mirkin, C.; Zhang, B., Development of Spherical Nucleic Acids for Prostate Cancer Immunotherapy. *Frontiers in Immunology* **2020,** *11*.

239. Callmann, C. E.; Kusmierz, C. D.; Dittmar, J. W.; Broger, L.; Mirkin, C. A., Impact of Liposomal Spherical Nucleic Acid Structure on Immunotherapeutic Function. *ACS Central Science* **2021**.

240. Agematsu, K.; Hokibara, S.; Nagumo, H.; Komiyama, A., CD27: a memory B-cell marker. *Immunology Today* **2000,** *21* (5), 204-206.

241. Ezan, E., Pharmacokinetic studies of protein drugs: Past, present and future. *Advanced Drug Delivery Reviews* **2013,** *65* (8), 1065-1073.

242. Lau, E. H. Y.; Tsang, O. T. Y.; Hui, D. S. C.; Kwan, M. Y. W.; Chan, W.-H.; Chiu, S. S.; Ko, R. L. W.; Chan, K. H.; Cheng, S. M. S.; Perera, R. A. P. M.; Cowling, B. J.; Poon, L. L. M.; Peiris, M., Neutralizing antibody titres in SARS-CoV-2 infections. *Nature Communications* **2021,** *12* (1).

VITA

CAROLINE DANIELLE KUSMIERZ
Department of Chemistry, Northwestern University
2145 Sheridan Rd. Evanston, IL 60208
carolinekusmierz2015@u.northwestern.edu

EDUCATION

Northwestern University, Evanston, IL 2015 – 2021
Ph.D. in Chemistry
Advisor: Prof. Chad A. Mirkin

University of Texas at Austin, Austin, TX 2010 – 2015
B.S. in Chemistry with Honors

RESEARCH EXPERIENCE

Northwestern University, Evanston, IL 2015 – 2021
Advisor: Prof. Chad A. Mirkin
Dissertation: Advancing the Delivery and Therapeutic Potential of Biologics with Spherical Nucleic Acids

University of Texas at Austin, Austin, TX 2013 – 2015
Advisor: Prof. Keith Stevenson
Research: Synthesis of Janus platinum-iron oxide nanoparticles for impact electrochemistry.

Lawrence Livermore National Laboratory, Livermore, CA Summer 2014
Advisor: Yong-Jin Han
Research: Facile bulk synthesis of cuprous oxide nanoparticles.

University of Texas at Austin, Austin, TX 2011 – 2013
Advisor: Prof. Brad Holliday
Research: Synthesis of Europium metal complexes for integration into photovoltaic devices.

PUBLICATIONS

10. Teplensky MH; **Kusmierz, CD**; Distler, ME; Mirkin CA “Spherical Nucleic Acids as a Platform for Infectious Disease Vaccines.” *In preparation*.

9. **Kusmierz CD**, Callmann, CE, Mirkin CA. “Transferrin Aptamers Increase the In Vivo Blood-Brain Barrier Penetration of Protein Spherical Nucleic Acids.” *Bioconjug. Chem.* 2021, *Submitted.*

8. Ebrahimi SE*, Samanta D*, **Kusmierz CD**, Mirkin CA. “Protein Transfection Via Spherical Nucleic Acids.” *Nat. Protoc*. 2021, *In review*.

7. Distler, ME; Teplensky, MH; Bujold, KE; **Kusmierz, CD**; Mirkin, CA. “DNA Dendrons as Universal Agents for Intracellular Delivery.” *J. Am. Chem. Soc.* 2021, *In review*.

6. Ebrahimi SE*, Samanta D*, Partridge BE, **Kusmierz CD**, Cheng HF, Grigorescu AA, Chavez JL, Mirau PA, Mirkin CA. “Programming Fluorogenic DNA Probes for Rapid Detection of Steroids.” *Angew. Chem. Int. Ed*. 2021, *60*, 1-7.

5. Callmann CE, **Kusmierz CD**, Dittmar J, Broger L, Mirkin CA. “Impact of Liposomal Spherical Nucleic Acid Structure on Immunotherapeutic Function.” *ACS Central Sci*. 2021, *7, 892-899.*

4. Samanta D*, Ebrahimi SB*, **Kusmierz CD**, Cheng HF, Mirkin CA. “Protein Spherical Nucleic Acids for Live-Cell Chemical Analysis.” *J. Am. Chem. Soc.* 2020, *142*, 13350-13355.

3. Callmann CE, Cole LE, **Kusmierz CD**, Huang Z, Horiuchi D, Mirkin CA "Tumor Cell Lysate-Loaded Immunostimulatory Spherical Nucleic Acids as Therapeutics for Triple Negative Breast Cancer." *Proc. Natl. Acad. Sci. USA* 2020, *117*, 17543-17550.

2. **Kusmierz CD**, Bujold KE, Callmann CE, Mirkin CA. "Defining the Design Parameters for *in Vivo* Enzyme Delivery Through Protein Spherical Nucleic Acids." *ACS Central Sci.* 2020, *6*, 815-822.

1. Shen Y, Kuddes, DD, Naquin CA, Hesterberg TW, **Kusmierz CD**, Holliday BJ, Slinker JD. "Improving light-emitting electrochemical cells with ionic additives." *Appl. Phys. Lett.* 2013*, 102*, 203305.

*denotes equal contribution

PATENT APPLICATION

Mirkin, CA, Teplensky MH, Dister ME, Kusmierz CD, Callmann CE. “Antiviral Vaccines using Spherical Nucleic Acids. “US provisional application number 63/160,600.

Mirkin, CA, Bujold, KE, Distler, ME, Kusmierz, CD. “Spherical Nucleic Acids with Dendritic Ligands.” US provisional application number 62/923,923.